DEVELOPMENT, CHARACTERIZATION AND OPTIMIZATION OF ELECTROLESS Ni-W-P-Ce COATINGS FOR MULTIFUNCTIONAL APPLICATIONS

Thesis submitted by

VIKASH KUMAR

Doctor of Philosophy

(Engineering)

DEPARTMENT OF MECHANICAL ENGINEERING

FACULTY COUNCIL OF ENGINEERING & TECHNOLOGY

JADAVPUR UNIVERSITY

KOLKATA, INDIA

2025

INDEX NO.: 277/21/E

REGISTRATION NO: 1022111001

1. **Title of the thesis:**

Development, characterization and optimization of electroless Ni-W-P-Ce coatings for multifunctional applications.

2. **Name, Designation & Institution of the Supervisors:**

i. Dr. Buddhadeb Oraon
Professor
Department of Mechanical Engineering
Jadavpur University, Kolkata-700032

ii. Dr. Sumanta Mukherjee
Assistant Professor
Department of Production & Industrial Engineering
Birsa Institute of Technology Sindri, Dhanbad- 828123

3. **List of Publications (Refereed Journals)**

i. **Vikash Kumar**, Biplab Baran Mandal, Surajit Das, Buddhadeb Oraon, Sumanta Mukherjee. "Tailoring electroless Ni-W-P polyalloy coatings: Unveiling the synergistic impact of cerium addition and annealing on surface functional properties." Surface and Coatings Technology 485 (2024): 130874. https://doi.org/10.1016/j.surfcoat.2024.130874

ii. **Vikash Kumar**, Biplab Baran Mandal, Buddhadeb Oraon. "Statistical analysis of activator and poly-alloy electroless coating on plain carbon steel by full factorial design." NeuroQuantology 20, no. 10 (2022): 9396-9405. https://doi.org/10.14704/nq.2022.20.10.NQ55917

iii. **Vikash Kumar**, Biplab Baran Mandal, Buddhadeb Oraon. "Synthesis and characterization of electroless Ni-W-Ce-P coating on AISI 1010 substrate." Materials Today: Proceedings 59 (2022): 1183-1188. https://doi.org/10.1016/j.matpr.2022.03.267

Vikash Kumar
16-06-2025

17/6/25
Prof. [illegible]
Dept. of Mechanical Engineering
Jadavpur University, Kolkata-32

Sumanta Mukherjee
16-06-25
Assistant Professor
Production & Industrial Engg. Dept.
BIT Sindri, Dhanbad

iv. **Vikash Kumar**, Biplab Baran Mandal, Buddhadeb Oraon, Sumanta Mukherjee. "Preliminary insights into the effects of bath loading and substrate texture on electroless deposition of Ni-W-Ce-P." International Journal of Materials Research. **(Under review)**

v. **Vikash Kumar**, Buddhadeb Oraon, Sumanta Mukherjee. "Comparative analysis of RSM and hybrid ANN-metaheuristic approaches for multiobjective optimization of electroless Ni-W-P-Ce coatings." **(Under preparation)**

4. **List of Patents:**

Nil

5. **List of Presentations in National/International Conferences**

i. January 17-20, 2024, Young Scientist Conference (India International Science Festival), Translational Health Science and Technology Institute, Faridabad, Haryana.

ii. December 8-10, 2023, 5th International Conference on Processing and Characterization of Materials, NIT Rourkela.

iii. December 1, 2023, Young Scientists Colloquium, Materials Research Society of India, Jadavpur University.

iv. January 22-24, 2023, Young Scientist Conference (India International Science Festival), MANIT, Bhopal.

v. November 25-26, 2021, 3rd International Conference on Recent Advances in Materials and Manufacturing, D Y Patil College of Engineering and Technology, Kolhapur, Maharashtra.

Vikash Kumar
16-06-2025

17/6/25

Professor
Dept. of Mechanical Engineering
Jadavpur University, Kolkata-32

Sumanta Mukherjee
16.06.25

Assistant Professor
Production & Industrial Engg. Dept.
BIT Sindri, Dhanbad

STATEMENT OF ORIGINALITY

I, **VIKASH KUMAR** registered on 21.01.2021, do hereby declare that this thesis entitled "**Development, characterization and optimization of electroless Ni-W-P-Ce coatings for multifunctional applications**" contains literature survey and original research work done by the undersigned candidate as part of Doctoral studies.

All information in this thesis have been obtained and presented in accordance with existing academic rules and ethical conduct. I declare that, as required by these rules and conduct, I have fully cited and referred all materials and results that are not original to this work.

I also declare that I have checked this thesis as per the "Policy on Anti Plagiarism, Jadavpur University, 2019", and the level of similarity as checked by iThenticate software is **9%**.

Signature of Candidate: Vikash Kumar

(VIKASH KUMAR)

Date: 16-06-2025

Certified by Supervisor(s):

(Signature with date, seal)

1. 15/6/25

(Dr. Buddhadeb Oraon)

Professor
Dept. of Mechanical Engineering
Jadavpur University, Kolkata-32

2. Sumanta Mukherjee 16.06.25

(Dr. Sumanta Mukherjee)

Assistant Professor
Production & Industrial Engg. Dept.
BIT Sindri, Dhanbad

CERTIFICATE FROM THE SUPERVISORS

This is to certify that the thesis entitled "**Development, characterization and optimization of electroless Ni-W-P-Ce coatings for multifunctional applications**" submitted by Shri VIKASH KUMAR, who got his name registered on 21.01.2021 for the award of Ph.D. (Engineering) degree of Jadavpur University is absolutely based upon his own work under our supervision and that neither his thesis nor any part of the thesis has been submitted for any degree/diploma or any other academic award anywhere before.

1. _____

(Dr. Buddhadeb Oraon)

Signature of the Supervisor
and date with Office Seal

Professor
Dept. of Mechanical Engineering
Jadavpur University, Kolkata-32

2. _____

(Dr. Sumanta Mukherjee)

Signature of the Supervisor
and date with Office Seal

Assistant Professor
Production & Industrial Engg. Dept.
BIT Sindri, Dhanbad

ACKNOWLEDGEMENT

I come from a humble background where my parents run a small shop in our village. Despite their challenges, they supported me selflessly throughout my academic journey. Their sacrifices are beyond words, and I dedicate this achievement to my Mummy, Papa, Brother, and Dadi, without their constant support, this Ph.D. would not have been possible.

I am deeply thankful to my supervisor, Prof. Buddhadeb Oraon Sir, for his unwavering support and constant guidance throughout my Ph.D. journey. It was a privilege to pursue my doctoral studies under his mentorship. Despite my frequent queries, he has always been patient, approachable, and encouraging. His disciplined approach, especially in documentation, has been a great source of inspiration for me.

I would also like to express my sincere gratitude to my co-supervisor, Dr. Sumanta Mukherjee Sir, for his invaluable contribution to my research. Sumanta Sir has invested significant time and effort in guiding me, and I owe much of my research knowledge and confidence to him. As my M.Tech supervisor and Ph.D. co-supervisor, he has been a constant source of support and mentorship. His help in understanding characterization techniques, manuscript preparation, research presentations, and overall personality development has profoundly shaped my academic growth and research capabilities.

I am also sincerely grateful to Prof. Gautam Majumdar Sir, Prof. Goutam Nandi Sir, and the esteemed members of my Research Advisory Committee, Prof. Rajat Subhra Sen Sir and Prof. Partha Sarathi Chakraborty Sir, for their valuable guidance and insights.

A heartfelt thank you goes to my labmates and roommates, Chandra Sekhar Rauta and Biplab Da, for their constant moral and financial support. I am especially thankful to Binod Barai, whose encouragement during my most challenging days has helped me stay strong and focused. I will always remember the support and motivation provided by Rupam, Sovan, Subhasish Da, Ambikesh Da, Sovan Da, and Srinath Da. Their kindness and encouragement kept me through this journey, and I am thankful to all of them.

Lastly, I am truly grateful to all the Professors and staff of Jadavpur University for the love, respect, and support they have shown me throughout my academic journey.

_____

(Vikash Kumar)

ABSTRACT

Electroless coating is a chemical deposition technique that allows for uniform application of metal or alloy coatings onto a wide range of substrates, both metallic and non-metallic, regardless of their shape or complexity. Unlike electroplating, it operates without the need for an external electric current and relies on controlled redox reactions to reduce metal ions from the solution onto the substrate. This thesis focuses on the development, characterization, and optimization of electroless Ni-W-P-Ce coatings on low-carbon steel (AISI 1010) for multifunctional applications.

For development of the coating, different coating conditions were explored, and a neutral bath (pH 7.5) stabilized with thiourea was identified to exhibit superior performance in terms of bath stability, deposition rate, coating microstructure, and microhardness. Next, the bath composition was optimized to maximize the overall coating performance, and a novel hybrid multi-objective optimization approach was adapted by combining an artificial neural network (ANN) with a metaheuristic algorithm. Among the evaluated algorithms, red fox optimization (RFO) proved most effective, yielding an optimized coating with a surface roughness of 0.12 µm, microhardness of 726 HV, 64% reduced fouling weight, surface free energy of 15.97 J/m2, and 98.73% corrosion protection efficiency.

Next, a comprehensive suite of characterization techniques, including microhardness, surface roughness, deposition rate, scratch and wear resistance, corrosion resistance, biofilm formation, surface morphology, structural analysis, and compositional analysis, were employed to thoroughly investigate the influence of cerium incorporation in Ni-W-P-Ce coatings. An optimal Ce concentration of 8 mg/L was identified, which significantly enhanced the functional performance of the coatings. Subsequent annealing at various temperatures revealed a trade-off among the properties, indicating that careful thermal treatment can balance the mechanical, chemical, and structural attributes. Further studies explored the effects of substrate surface preparation methods, including activation with different agents (HCl and PdCl2), polishing to various surface roughness levels, and modifying bath loading conditions. Among these, HCl activation was more effective than PdCl2 activation, enhancing adhesion through micro-roughening. Polishing with finer grit (1500 grit) promoted controlled nucleation and uniform coating growth, resulting in superior adhesion and enhanced mechanical properties. Additionally, an optimal bath loading of 0.88 dm2·L-1 was identified, effectively balancing the deposition rate and bath stability.

CONTENTS

LIST OF FIGURES

LIST OF TABLES

ABBREVIATIONS

ENC	Electroless nickel coating
CVD	Chemical vapor deposition
PVD	Physical vapor deposition
HER	Hydrogen evolution reaction
PCB	Printed circuit board
DoE	Design of experiments
RSM	Response surface methodology
ANN	Artificial neural network
GA	Genetic Algorithm
ABC	Artificial bee colony
FA	Firefly algorithm
TLBO	Teaching learning-based optimization
WOA	Whale optimization algorithm
RFO	Red fox optimization
UBM	Under bump metallization
REEs	Rare earth elements
CCD	Central composite design
BBD	Box-Behnken design
ANOVA	Analysis of variance
BPNN	Back-propagation neural network
AHA	Artificial hummingbird algorithm
SA	Simulated annealing
NSGA	Non-dominated sorting genetic algorithm
MWCNT	Multi-walled carbon nanotube

AI	Artificial intelligence
ML	Machine learning
UTS	Ultimate tensile strength
FESEM	Field-emission scanning electron microscopy
EDS	Energy-dispersive X-ray spectroscopy
XRD	X-ray diffraction
TDS	Total dissolved solids
OCP	Open circuit potential
LP	Linear potentiodynamic polarization
HV	Microhardness
FW	Fouling weight
SFE	Surface free energy
PE	Protection efficiency
MSE	Mean squared error
FWHM	Full width at half maximum
EIS	Electrochemical impedance spectroscopy
OHL	Outer Helmholtz layer
IHL	Inner Helmholtz layer
BE	Binding energy
EG	Ethylene glycol
SFC	Scratch friction coefficient
SV	Scratch volume
CoF	Coefficient of friction
SWR	Specific wear rate
CPE	Constant phase element
FTIR	Fourier transform infrared spectroscopy

Chapter 1 Introduction

This chapter provides an in-depth overview of electroless coatings and covers their principles, types, industrial applications, and emerging research trends. This highlights the increasing demand for multifunctional coatings and the development of electroless polyalloy coatings on low-carbon steels and concludes with a summary of the thesis structure and research objectives.

1.1 Background

Surface modification techniques play a crucial role in enhancing the properties of materials, with applications spanning multiple industries. These techniques can be broadly classified into two categories: coating and surface treatment. Coatings involve the application of thin layers to improve corrosion resistance, wear resistance, and thermal stability. In contrast, surface treatments, such as diffusion and plasma treatments, modify surfaces without adding layers, thereby enhancing the mechanical and chemical properties of the material at the surface level [1].

Coating techniques can be classified based on the state of the coating material during the deposition (Figure 1.1). Gaseous functional coating methods such as chemical vapor deposition (CVD) and physical vapor deposition (PVD) are vacuum-based processes that form thin films with enhanced mechanical and optical properties. These methods modify the near-surface structure and improve the performance in various applications.

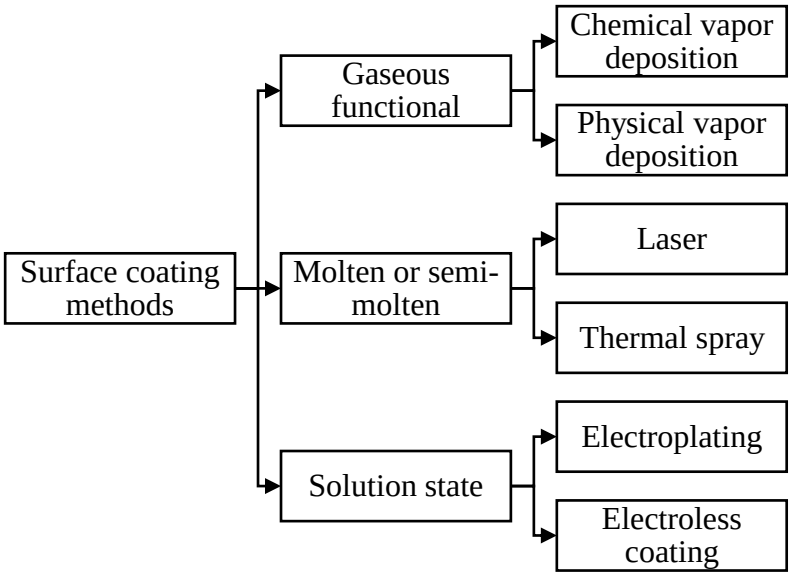

Figure 1.1. Classification of coating techniques based on deposition state.

Molten or semi-molten techniques, such as laser cladding and thermal spraying, involve heating materials until they reach a molten state before deposition onto a substrate. Although these processes offer excellent thermal and wear resistance, their effectiveness is sometimes limited because of their poor adhesion properties. Solution-based coating techniques, including electroplating and electroless coating, are cost-effective and versatile [2]. In this study, electroless coatings are investigated.

1.2 Electroless coatings

Among the various coating methods, electroless coatings have garnered significant attention because of their ability to uniformly deposit metal layers via autocatalytic chemical reactions. Electroless coatings are chemical deposition processes that allow for uniform application of metal or compound coatings onto various substrates without the use of an external electric current. This method is valued for its versatility, as it can effectively coat both conductive and non-conductive materials, making it ideal for diverse applications including electronics, energy storage devices, and anti-corrosion solutions. The advantages of electroless deposition include the ability to produce high-quality, consistent coatings with exceptional anti-corrosion properties and excellent wear resistance, while avoiding issues related to current density uniformity typical of electroplating. However, this method also has some disadvantages, such as a limited bath life that requires regular monitoring and replenishment, potential environmental concerns associated with the disposal of alkaline and acidic baths, and the necessity for surface pre-treatments to ensure adhesion on certain substrates [3]. The best part of electroless coating is that it can be performed professionally in large batches, making the entire process more cost-effective and generating significant long-term savings.

Electroless coating is an autocatalytic process, in which the deposited metal acts as a catalyst for continuous deposition, creating a self-sustaining reaction. The process begins with the reduction of metal ions in a solution containing a suitable reducing agent that donates electrons to form a solid metallic layer on the substrate surface. In an electrochemical process, an active catalytic surface is required to facilitate the oxidation and reduction reactions that are essential for metal deposition. The effectiveness of deposition depends on the compatibility between the metal and the reducing agent, as some metals may not react efficiently, leading to incomplete deposition or side reactions. For instance, Pd exhibits a high catalytic activity across various reducing agents, making it

versatile under different deposition conditions. Similarly, copper effectively catalyzes formaldehyde oxidation, whereas nickel and cobalt can oxidize a broader range of reducing agents but are ineffective for formaldehyde oxidation [3–5].

Electroless deposition offers several advantages over traditional coating methods such as electroplating, PVD, and CVD. Its cost-effectiveness stems from the use of simpler and less expensive equipment and materials compared to electroplating, which requires precise control of the electrical parameters [6,7]. This makes electroless deposition ideal for large-scale applications, where the cost is a concern.

A key advantage is its ability to produce uniform coatings, even in complex geometries, owing to its autocatalytic nature [8]. Unlike electroplating, which struggles with uniform thickness on intricate parts, electroless deposition ensures consistent coverage without requiring a conductive substrate [9]. In addition, it is highly versatile, allowing coatings to be deposited on metals, polymers, and ceramics, unlike PVD and CVD, which have substrate limitations [10,11]. This broad compatibility expands its industrial application and requires less specialized equipment and expertise [12,13].

Electroless deposition also offers environmental benefits because certain formulations use less hazardous reducing agents and produce less toxic waste than electroplating, which often involves harmful chemicals, such as cyanides [14]. The development of sugar-based coating solutions further highlights their potential for sustainable manufacturing [6]. As industries prioritize cost, uniformity, and eco-friendliness, electroless deposition continues to be a valuable surface engineering technology.

Electroless coatings primarily consist of Ni-based alloys, particularly Ni-P and Ni-B coatings. Ni-P coatings are widely recognized for their exceptional corrosion resistance, which varies depending on the phosphorus content. A higher phosphorus content enhanced the corrosion resistance, whereas a lower phosphorus content increased the hardness. Conversely, Ni-B coatings exhibit superior hardness and wear resistance, but lower corrosion protection than Ni-P coatings. Furthermore, electroless composite coatings incorporating micro- and nanoscale reinforcements, such as SiC and TiO_2, significantly enhance the surface properties, including hardness, wear resistance, and lubricity [2].

1.2.1 Application of electroless coatings

Electroless coatings are extensively used industrially because of their durability and superior performance in harsh environments. As depicted in Figure 1.2, these coatings have applications in the automotive and electronics sectors, accounting for approximately 20% of the total usage. The oil and chemical (15%), machinery (11%), and aerospace (10%) industries rely heavily on electroless coatings for their corrosion and wear resistance. Other specialized industries, including food processing and printing, also benefit from electroless coatings, owing to their hygienic and protective properties [2]. Recent advancements in electroless coating technology include the development of a 24/7 helpline for troubleshooting and technical support, thereby highlighting the growing significance of this coating technique in industrial applications [15].

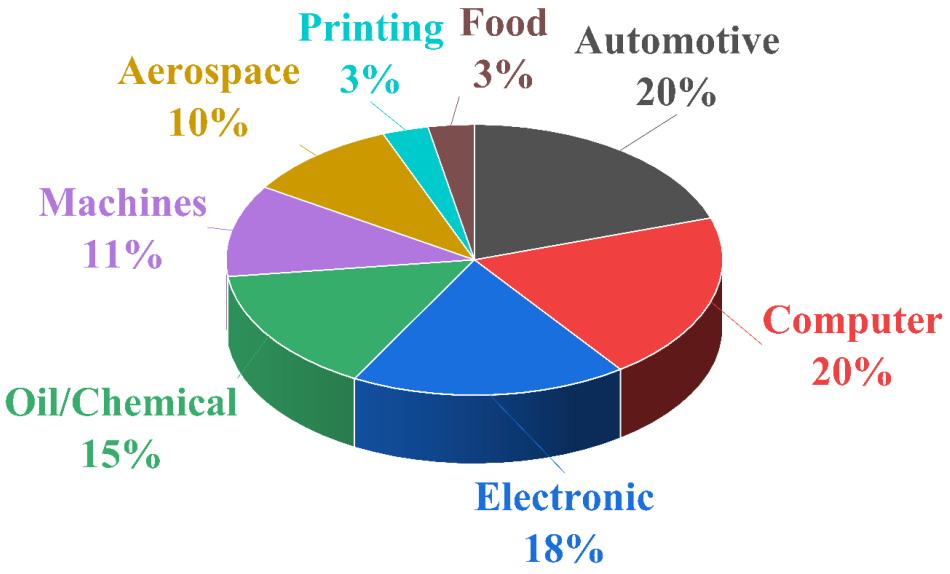

Figure 1.2. Industrial applications of electroless coatings across various sectors.

Electroless nickel coatings (ENC) have been proven to significantly extend the service life of components for up to 30 years in some cases and are extensively used across multiple industries. In power electronics, ENC is applied to protect cold copper plates and heat sinks, whereas in aerospace, oil and gas processing, and hydraulic systems, it safeguards actuator bodies and critical equipment subjected to extreme conditions. The automotive sector benefits from ENC by improving the durability and corrosion resistance of brake pistons, as well as preventing galvanic corrosion in electric vehicle busbars, thereby ensuring stable performance in hybrid and electric vehicles. The most commonly coated industrial components are illustrated in Figure 1.3 [16–22]. Notably, electroless coatings, such as Ni-

B and Ni-P/B, play a vital role in enhancing the durability and performance of components such as gears, bearings, valves, carburetors, and fuel injection systems, especially in environments involving alternative fuels [23,24]. Their excellent friction-reducing and wear-resistant properties extend the lifespan of various engine components [25,26].

Figure 1.3. Common industrial components benefiting from ENC.

Aerospace applications also benefit significantly because electroless coatings provide protective finishes for landing gear components, engine mounts, and hydraulic fittings, ensuring reliability under harsh environmental conditions [24,27]. Additionally, these coatings help to achieve lightweight and corrosion-resistant surfaces, which are essential for improving aircraft performance and safety [25].

In the electronics industry, electroless nickel and palladium coatings are widely applied to printed circuit boards (PCBs) to enhance their solderability and corrosion resistance [25,28]. Electroless silver coatings are used to improve the conductivity of circuit interconnects, whereas nickel coatings contribute to semiconductor manufacturing and metallization of plastics, enabling miniaturization and intricate designs [27,29].

Biomedical applications of electroless coatings include their use in medical implants and devices, where biocompatible surfaces facilitate better adhesion and functionality

[27,30]. Furthermore, these coatings play a crucial role in manufacturing composites and magnetic materials, offering superior mechanical strength and thermal conductivity [31].

Another significant advantage of electroless coatings is their ability to provide uniform metal deposition on complex geometries and non-conductive substrates. This makes them indispensable for a wide range of industrial applications, including solid free-form fabricated components, such as prosthetic limbs, which require both performance and aesthetic qualities [3,32].

One of the most significant recent applications of electroless coatings is their role as electrocatalysts in hydrogen evolution reactions (HER). The unique microstructures of these coatings, which often feature amorphous phases and high surface roughness, enhance their catalytic activities. Their superior corrosion resistance, favorable hydrogen adsorption energy, and optimized surface morphology contributed to their efficient and stable HER performance. The introduction of dopants, multilayer coatings, and process optimization further improve catalytic efficiency, making electroless nickel coatings a promising alternative to platinum-based catalysts for hydrogen production [33].

1.2.2 Types of electroless nickel coatings

As shown in Figure 1.4, there are several distinct types of electroless coatings, each designed to deliver specific performance benefits and characteristics that are suitable for a wide range of applications [34,35].

Pure nickel coatings

Pure electroless nickel coatings consist primarily of nickel, without significant additions of other elements such as phosphorus or boron. Hydrazine is commonly used as the reducing agent during deposition. Although pure nickel coatings tend to be softer and less corrosion-resistant than nickel-phosphorus alloys, they still provide excellent electrical conductivity and ductility. These properties make them suitable for specific applications in which conductivity and flexibility are essential [36].

Nickel alloy coatings

Nickel alloy coatings involve the addition of other metals (such as P, B, Zn, Ce, Cu, and W) to nickel, thereby improving the mechanical properties of the coating. These coatings typically exhibit enhanced hardness and wear resistance compared with those of pure

nickel. For instance, nickel-phosphorus and nickel-boron alloys are common variations with distinct attributes. The specific alloy composition can be tailored according to the requirements of the application, providing flexibility in properties, such as thermal stability and electrical conductivity. Variations in the levels of phosphorous and boron can lead to different categorizations.

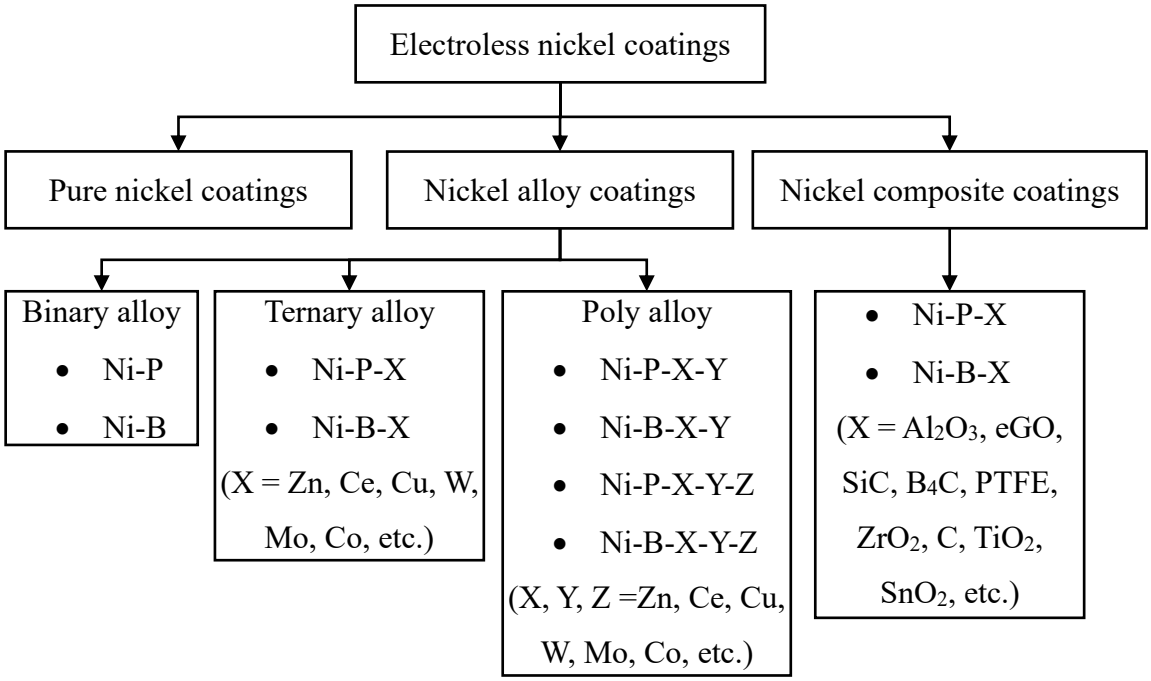

Figure 1.4. Classification of electroless nickel coatings.

High-P coatings (10-13% P) offer superior corrosion resistance, making them ideal for highly corrosive environments. Mid-phosphorus coatings (5-9% P) provide a balance between corrosion and wear resistance while delivering a bright finish, which is commonly used for moving parts, although they may induce tensile stress in certain metals, such as steel. Low-phosphorus coatings (up to 5% P) excel in high-temperature environments and offer enhanced wear resistance but provide lower corrosion protection, especially under acidic conditions.

Boron-based electroless nickel baths are classified into low-boron (0.5-3% B) and high-boron (3-5% B) variants, each offering distinct properties. Low-boron coatings enhance their solderability and conductivity, making them well suited for electronic applications. In contrast, high-boron coatings exhibit increased hardness and improved resilience after heat treatment, making them a viable alternative to chrome coatings in various industries, although they are less effective in corrosive environments. However, both types of coatings

tend to be more porous than the other electroless coatings, which can limit their performance in certain applications.

By adding various elements to electroless nickel coatings, new alloys (such as binary, ternary, or polyalloys) can be formulated to achieve specific properties. This flexibility allows the creation of coatings tailored to meet a wide range of industrial requirements, such as improved corrosion resistance, wear resistance, lubricity, and electrical conductivity. The ability to customize these coatings makes them highly versatile and valuable for diverse industrial applications.

Nickel composite coatings

These coatings incorporate second-phase materials such as ceramic particles (e.g., TiO_2, Al_2O_3, and SiC), minerals (diamond and columbite-tantalite), and polymers (polyvinyl chloride, PTFE) within the nickel matrix, significantly enhancing characteristics such as wear resistance and self-lubricating properties. Nickel composite coatings are gaining traction for applications requiring strong mechanical performance, such as in the aerospace and automotive industries, owing to their ability to withstand extreme conditions and provide additional functionalities.

1.3 Principles of electroless coating deposition

Electroless coating is a non-galvanic metal deposition method that uses a chemical reducing agent to convert metal ions to a solid metal state in an aqueous solution. The process is highly autocatalytic, allowing uniform coating deposition across various substrate geometries [37].

Key components of electroless coating:

i. Metal ion source:

This process typically uses metal salts, with nickel (Ni) being one of the most common salts, often in the form of nickel sulfate ($NiSO_4$). Other metal ions, such as copper (Cu) and silver (Ag), can also be plated.

ii. Reducing agent:

A chemical reducing agent is required to facilitate the transfer of the electrons necessary for the reduction of metal ions. Common reducing agents include sodium hypophosphite (NaH_2PO_2), hydrazine, or glucose.

iii. Complexing agents:

Complexing agents, such as citrates or ammonium salts, are often used to stabilize metal ions in solution and prevent premature precipitation, complexing agents (like citrates or ammonium salts) are often used. These agents help to maintain the metal ion concentration and pH within the desired range.

iv. pH buffering agents:

The pH of the solution affects the deposition rate and quality of the coating. Adjusting agents are used to maintain an optimal pH, usually between 4.5 and 5.5, for nickel coating.

The fundamental reactions in electroless coatings involve oxidation and reduction reactions, which can be broken down as follows:

i. Cathodic reaction (reduction): Ni ions are reduced to form a solid Ni.

$$Ni^{2+} + 2e^{-} \rightarrow Ni\ (s) \tag{1.1}$$

Here, Ni^{2+} ions in the solution gain electrons supplied by the oxidizing agent, forming metallic Ni on the substrate.

ii. Anodic reaction (oxidation): the reducing agent is oxidized to release electrons.

$$NaH_2PO_2 \rightarrow Na^{+} + H_2O + Products + 2e^{-} \tag{1.2}$$

Here, sodium hypophosphite undergoes oxidation, contributing to the electrons needed to reduce nickel ions.

1.3.1 Thermodynamics of electroless coating

Thermodynamics deals with the energy changes associated with chemical reactions and, in the context of electroless coating, provides insights into the feasibility and driving forces of the deposition process. The feasibility is governed by Gibbs free energy (ΔG), where a negative ΔG indicates a spontaneous reaction. The process is also driven by the electrode potentials of the half-cell reactions, that is, the cathodic reaction (Ni^{2+}→ Ni) and the anodic reaction (oxidation of reducing agents). A positive overall cell potential implies favorable deposition.

Mixed Potential Theory explains that the actual deposition potential (mixed potential) results from simultaneous anodic and cathodic reactions. This steady-state potential is vital for understanding and controlling the spontaneity and balance of a reaction.

1.3.2 Kinetics of electroless coating

Kinetics studies the rate of metal deposition influenced by temperature, reactant concentration, nature of the reducing agent, and surface conditions. The rate law is often as follows:

$$R = k[M^{2+}][Red]^n \tag{1.3}$$

where R is the deposition rate, k is the rate constant, $[M^{2+}]$ is the concentration of metal ions, and [Red] is the concentration of the reducing agent.

The temperature dependence of the deposition rate can be understood using the Arrhenius equation:

$$k = Ae^{-\frac{E_a}{RT}} \tag{1.4}$$

where k is the rate constant, A is the pre-exponential factor, E_a is the activation energy, R is the gas constant, and T is temperature (K). A lower activation energy indicates a higher reaction rate.

Mass transport (diffusion) and reaction control play key roles in this process. In diffusion-limited cases, agitation improves the rate. In kinetically controlled systems, the surface reactions are dominant.

Hydrogen evolution can occur as a side reaction, particularly at a certain pH or with specific reducing agents, affecting the coating quality. Managing this is essential for the deposit efficiency and selectivity.

1.3.3 Role of catalysts and surface activation

The substrate surface must be sufficiently activated to facilitate an electroless coating. Activation may involve:

- Surface preparation: Proper cleaning and conditioning of the surface ensure that it is free from contaminants and can bond with the deposited metal.

- Catalytic activation: Palladium and other noble metals are often used as catalysts to provide the initial sites for nickel deposition. The process begins in the activated regions, allowing Ni deposition to proceed in an autocatalytic manner, where the deposit enhances further deposition.

1.3.4 Parameters influencing electroless coating

i. pH control:

The solution pH plays a significant role in controlling the deposition rate and morphology of the deposited film. Lower or higher pH levels can lead to poor deposit quality or the formation of unwanted by-products.

ii. Temperature:

The reaction rate increases with temperature owing to the enhanced diffusion and kinetic energy of the reactants. However, excessively high temperatures can lead to rapid decomposition of the bath or uneven deposition.

iii. Concentration of components:

The concentrations of metal ions, reducing agents, and stabilizers can significantly affect the rate and uniformity of the deposition. Therefore, optimal concentrations are necessary to obtain high-quality deposits with desirable properties.

iv. Time of deposition:

The deposition time affects the thickness and quality of the coating. Controlling the deposition time is necessary to prevent excessive build-up or weak adhesion.

1.4 Engineering multifunctional properties in electroless coatings

1.4.1 Hardness and wear resistance

Electroless coatings reinforced with particles, such as Al_2O_3, SiC, and ZrO_2, exhibit significantly improved hardness and tribological performance. Al_2O_3 is particularly effective owing to its low friction, high wear resistance, and chemical stability when incorporated into Ni-P matrices [38–40]. Refractory metals such as Mo and W further enhance thermal stability and toughness [41], while MWCNTs contribute to self-lubricating properties that reduce friction and wear [42].

The hardness and wear resistance of the composite coatings were strongly influenced by the dispersion and content of reinforcing particles. A higher nanoparticle content in Ni-ZrO_2 and Ni- Al_2O_3 coatings increases the hardness and decreases the wear rates [40]. Similarly, Cu-coated B_4C particles enhance the mechanical strength and wettability of Al2025 alloys [43], and Ni-P-Cu coatings benefit from phase formation (Ni_3P, NiCu), which improves tribo-mechanical behavior through grain refinement and dislocation inhibition [44].

Post-deposition heat treatment at 400 °C promoted the crystallization of Ni-P to Ni and Ni_3P phases, increasing the hardness and wear resistance [45]. However, temperatures above 450 °C can degrade performance owing to oxidation, grain coarsening, and Fe diffusion, leading to reduced adhesion and increased porosity [44].

1.4.2 Corrosion resistance

Electroless composite coatings are known to enhance corrosion resistance. Ni-P/PTFE coatings reduce the corrosion current and increase the corrosion potential, although they may compromise hardness and stiffness [46]. Carbon nanoparticles, such as those from candle soot, improve corrosion resistance cost-effectively in Ni-P coatings [47]. Bi-layer coatings, such as Co/Sn, offer multilayer protection by reducing the corrosion rates [48].

Alloying Ni-P/Ni-B with elements such as W and La^{3+} enhances the corrosion behavior through oxide film formation and grain refinement, although optimal concentrations are critical to avoid performance decline [49,50]. Ni-P-Cu coatings benefit from optimized copper levels and heat treatment, which improve the morphology and protective properties [45].

Ni-Mo-P coatings provide high electrochemical stability in aggressive environments, making them suitable for energy and marine applications [51]. Coatings produced using wastewater also show good corrosion resistance at moderate temperatures, although their performance drops beyond 400 °C owing to oxide-related degradation [52].

1.4.3 Thermal stability

Electroless coatings play a significant role in enhancing the thermal stabilities of various composite materials. The deposition of Ag and Ni onto h-BN and CNTs improves the interfacial bonding and dispersion within the aluminum matrix composites, reducing

agglomeration and oxidation, and improving the high-temperature performance [53]. Similarly, cerium-containing coatings increase the oxidation resistance by forming dense oxide scales and acting as cation diffusion barriers [54].

Ag-coated glass flakes improve the thermal and mechanical performance of PAE composites by increasing their degradation and softening temperatures [55]. In thermoelectric materials, electroless Ag/SnTe coatings enhance the Seebeck coefficient, reduce the thermal conductivity, and improve the overall thermoelectric efficiency (zT = 0.67 at 823 K) [56].

Thermal stability is also improved in Ag nanowire-based electrodes through AgNP deposition, significantly lowering the sheet resistance and preserving the conductivity under heat exposure [57]. Ni-Fe-P coatings on bamboo fibers increase the degradation temperature and reduce pyrolysis, thereby acting as a protective thermal barrier [58]. Additionally, ScF_3 electroless coatings enable near-zero thermal expansion in Cu composites, providing thermal shock resistance ideal for electronic packaging applications [59].

1.4.4 Antimicrobial properties for biomedical and marine applications

Electroless nanocomposite coatings have shown promising antimicrobial performances, making them suitable for applications in biomedical and marine environments. NiP-TiNi coatings reduced E. coli viability by over 80% and inhibited biofilm formation, achieving up to 93% corrosion inhibition in sulfate-reducing bacterial media [60]. Similarly, Ni-P coatings enhanced with ZnO-doped C_3N_4 nanocapsules effectively reduced S. aureus growth, particularly at low ZnO concentrations, with heat treatment further improving bactericidal activity [61].

Silver-based coatings also demonstrate strong antimicrobial effects. Ag-loaded ceramic papers and Ag-coated PA6 fibers showed over 99% bacterial inhibition against S. aureus and E. coli, with durability retained after washing, indicating potential in food preservation and textile applications [62,63]. Electroless Ni-P coatings with ZnO nanoparticles on ABS substrates further reduce bacterial colonization, reinforcing their relevance for medical devices and hygiene-critical surfaces [64].

Cerium- and neodymium-containing coatings also contribute to antimicrobial activity. Cerium compounds disrupt bacterial structures and generate reactive oxygen species,

thereby offering dual corrosion and microbial resistance [65]. Nd_2O_3-Ag nanohybrids exhibit over 98% bactericidal efficiency, combining ion release and membrane disruption mechanisms [66].

1.5 Optimization of electroless coating process parameters

1.5.1 Traditional optimization techniques

Early attempts to optimize the electroless coating processes have been largely empirical. Researchers have systematically varied individual parameters while observing their effects on the resulting coating properties. This "one-factor-at-a-time" approach, while conceptually simple, proved to be highly inefficient and time-consuming. Furthermore, it fails to account for the potential interactions between multiple parameters, leading to suboptimal results. The inherent limitations of this method necessitate a shift towards more statistically rigorous approaches [67,68].

The development of the statistical design of experiments (DoE) has marked a crucial turning point. Techniques, such as orthogonal arrays [69] and the Taguchi method [70], provide frameworks for systematically varying multiple parameters simultaneously, enabling a more efficient exploration of the parameter space. In particular, the Taguchi method has gained significant traction owing to its ability to minimize the number of experiments required, while still providing statistically robust results. By employing orthogonal arrays, researchers can identify significant factors and their optimal levels with fewer experimental runs than traditional full-factorial designs. Studies using the Taguchi method have successfully optimized various aspects of electroless coatings, including the microhardness and deposition rate [71,72]. However, even these advanced DoE methods often struggle to adequately capture the complex interactions between multiple parameters, potentially leading to incomplete or misleading conclusions [73]. This limitation has spurred the development of more sophisticated modelling techniques.

1.5.2 Response surface methodology (RSM)

Response surface methodology (RSM) has emerged as a powerful statistical tool for modelling and optimizing complex processes characterized by multiple interacting variables. RSM utilizes mathematical and statistical techniques to construct response surfaces, which graphically represent the relationship between the process parameters

(independent variables) and the desired coating properties (dependent variables, such as corrosion rate, hardness, or deposition rate) [74,75]. RSM employs various experimental designs, including Box-Behnken [76] and central composite designs [75], to gather data for model construction. These designs were chosen for their efficiency in exploring the parameter space, while minimizing the number of required experiments. The resulting empirical models, often second-order polynomial equations, allow for the prediction of optimal parameter combinations that yield the desired coating characteristics [77].

The CCD structure for the three-factor design is shown in Figure 1.5. It comprises three components: (1) a factorial or fractional factorial design with combinations of factors at two levels (high and low), represented by corner points; (2) center points to estimate experimental error and curvature; and (3) axial (star) points placed at a distance (α) from the center to ensure rotatability, providing uniform precision in all directions.

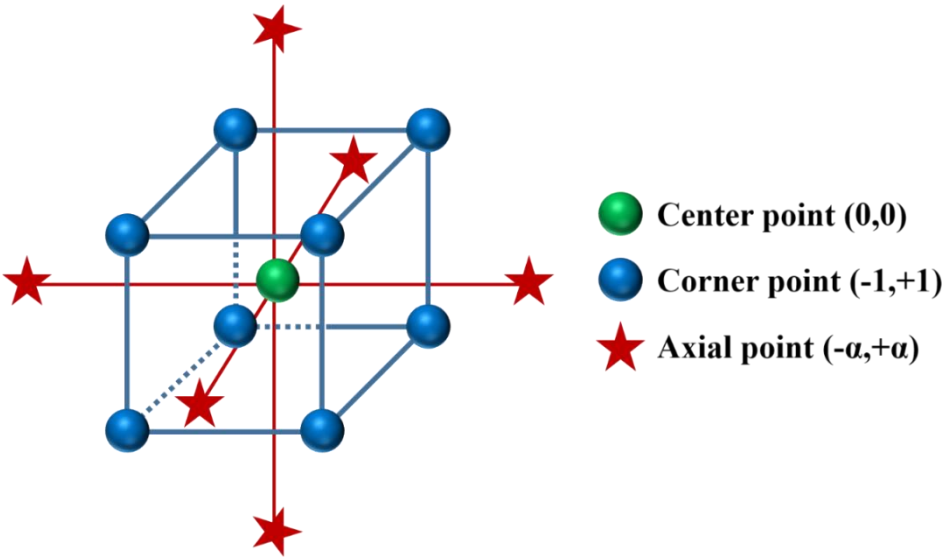

Figure 1.5. Structure of CCD for the three-factor experimental design.

1.5.3 Artificial neural networks (ANNs)

Artificial neural networks (ANNs), inspired by biological neural networks of the brain, provide a powerful machine-learning approach for modelling complex nonlinear systems. Unlike the RSM, which relies on explicitly defined mathematical functions, ANNs can learn complex relationships from data without requiring a priori assumptions regarding the underlying functional form. This makes them well suited for modelling electroless coating processes, where the interplay between parameters can be highly intricate and nonlinear [78].

1.5.4 Metaheuristic algorithms

Metaheuristic algorithms offer a powerful class of optimization methods inspired by natural processes, such as swarm intelligence, biological evolution, and physical phenomena. These algorithms are particularly well-suited for tackling complex multimodal optimization problems, where traditional gradient-based methods may fail to find the global optimum [79]. Their robustness and ability to handle noisy or incomplete data make them attractive for optimizing the electroless coating processes. Several metaheuristic algorithms have been applied to this field, including

Genetic algorithm (GA): Inspired by the principles of natural selection and genetic evolution, GAs have been widely employed for optimization problems across various engineering disciplines [70,77,80]. Their ability to handle complex, multi-objective optimization problems and their robustness to noise make them particularly well-suited for optimizing the electroless coating process. GAs operate by evolving a population of potential solutions and selecting the fittest individuals based on a fitness function that evaluates the quality of the solutions. Through genetic operators such as crossover and mutation, new solutions are generated, and the population evolves towards better solutions over generations [81].

Several other swarm intelligence-based metaheuristic algorithms have also been applied to optimize electroless coating parameters, including the Artificial bee colony (ABC) algorithm, Firefly algorithm (FA), and Teaching-learning-based optimization (TLBO). The ABC algorithm models the foraging behavior of honey bees by utilizing employed bees, onlookers, and scout bees to efficiently explore and exploit the search space for optimal solutions. The Firefly Algorithm is inspired by the mutual attraction among fireflies, where individuals are drawn toward brighter, more attractive solutions, directing the search for optimal outcomes. Meanwhile, TLBO replicates a classroom learning process in which learners enhance their knowledge through interaction with a 'teacher,' representing the best solution and their peers, and progressively improving solution quality through iterative learning phases [76].

1.5.5 Hybrid approaches

The inherent strengths of different optimization techniques have motivated the development of hybrid approaches that combine the capabilities of multiple methods. These

hybrid models aim to leverage the advantages of each component technique, while mitigating their individual limitations. For example, integrating ANNs with metaheuristic algorithms combines the powerful predictive capabilities of ANNs with the global search capabilities of metaheuristics [81,82]. This synergistic approach can lead to a more accurate and efficient optimization of the electroless coating parameters.

Similarly, combining RSM with metaheuristic algorithms can enhance the exploration of the parameter space and improve the robustness of the optimization process [83]. RSM provides a statistical framework for modelling the relationships between process parameters and coating properties, whereas metaheuristics offer a powerful mechanism for searching for optimal solutions in the parameter space defined by the RSM model. The combination of these two approaches can lead to more reliable and accurate predictions of the optimal parameter combinations. Other hybrid methods include gray-fuzzy-based approaches [69] that combine statistical modelling with fuzzy logic to handle uncertainty and vagueness in the optimization process.

1.6 Research motivation and scope

1.6.1 Development of electroless polyalloy coatings on low-carbon steel

Electroless polyalloy coatings, particularly Ni-P-based alloys, offer a promising solution for enhancing the properties of low-carbon steel by incorporating elements such as Mo, W, and Co. These coatings improve hardness, corrosion and wear resistance, thermal stability, frictional properties, and antimicrobial effectiveness, making them suitable for multifunctional applications. Given the widespread industrial use of low-carbon steel and its inherent limitations in corrosion resistance and wear durability, advanced coatings are essential for extending the component lifespan and improving performance in demanding environments. This study aims to develop a novel Ni-P alloy coating tailored for multifunctional applications in marine, biomedical, antifouling, and other industrial sectors.

1.7 Thesis outline and contributions

The thesis entitled “Development, characterization and optimization of electroless Ni-W-P-Ce coatings for multifunctional applications” has been divided into seven chapters, excluding the appendix. An overview of the remainder of this thesis is summarized below.

Chapter 2 presents a literature review focusing on the development of multifunctional electroless polyalloy coatings. It summarizes previous research on polyalloy coatings for various applications and highlights the key findings and advancements. Through this review, existing research gaps were identified, which formed the basis for defining the objectives of this study.

Following that, **Chapter 3** describes the synthesis and characterization of rare earth metal cerium-added electroless Ni-W-P coatings on low-carbon steel. This study examines the effects of varying the chemical concentrations and coating parameters to achieve a stable coating bath and high-quality Ni-W-P-Ce coated samples.

Afterward, in **Chapter 4**, 30 experiments were designed using the central composite design within the response surface methodology, with the lower and upper factor levels derived from the findings of the previous chapter. Subsequently, multi-objective optimization of the electroless Ni-W-P-Ce coating parameters was conducted using a hybrid ANN-metaheuristic optimization technique to simultaneously enhance five key coating properties: roughness, hardness, antifouling ability, surface free energy, and corrosion protection efficiency.

Subsequently, **Chapter 5** explores the microstructural evolution and performance characteristics of cerium-modified electroless Ni-W-P coatings, both before and after heat treatment. The coatings were deposited using optimized parameters, and only the Ce content was varied. This study systematically examined the effect of the cerium concentration on the deposition rate, microstructure, composition, and functional properties.

In continuation, **Chapter 6** examines the influence of key process parameters- activator solution, bath loading, and substrate roughness- on the initiation, growth, and properties of electroless Ni-W-P-Ce coatings deposited on low-carbon steel substrates.

Finally, **Chapter 7** presents a summary of the research work, along with recommendations for future research directions. The references used in this study are listed at the end of this thesis.

Chapter 2 Literature review

This chapter reviews electroless coatings with a focus on their composition, multifunctional properties, and enhancement strategies, including the use of rare earth elements. It also examines optimization techniques, such as statistical methods, machine learning, and metaheuristic algorithms, and concludes with identified research gaps and objectives that frame the study.

2.1 Role of alloying elements in electroless coatings

The incorporation of secondary elements into electroless Ni-P coatings is a proven strategy for enhancing their properties and expanding their applications. Elements such as tungsten (W), zinc (Zn), copper (Cu), chromium (Cr), molybdenum (Mo), and rare earth elements significantly improve mechanical and physical characteristics, including hardness, wear resistance, corrosion resistance, thermal stability, and magnetic properties, depending on their concentration, bath composition, and deposition parameters. Multi-element alloying further enhances the coating performance, enabling customized functionalities for specific applications. For instance, hard particles or lubricating agents improve wear resistance and reduce friction, whereas noble metals enhance corrosion protection in aggressive environments [84,85].

The specific effects of individual elements on the microstructure and performance of Ni-P based polyalloy coatings are discussed in the following subsections.

2.1.1 Role of cobalt

The incorporation of cobalt into electroless Ni-P coatings resulted in 12.67 wt.% cobalt and 14.63 wt.% phosphorus. Co significantly contributed to the magnetic properties of the Ni-Co-P coatings. In a quaternary system, where both cobalt and cerium were introduced into the Ni-P bath, the annealed Ni-Co-P-Ce coating (at 400 °C) exhibited a composition of 21.5 wt.% cobalt, 7.1 wt.% phosphorus, and 1.3 wt.% cerium. The presence of cobalt enhanced nickel ion deposition, facilitated the formation of the ferromagnetic Ni(Co) phase, and suppressed the development of paramagnetic phases, such as Ni_3P and Co_2P. Consequently, the coating demonstrated improved saturation magnetization and coercivity [84,86].

2.1.2 Role of iron

Iron (Fe) plays a pivotal role in shaping the structural and functional characteristics of electroless Ni-Fe-P coatings. The Fe and phosphorus (P) contents of these coatings can vary significantly, with Fe ranging from 3 wt.% to 24 wt.% and P from 4 wt.% to 14 wt.%. The amount of iron directly influences the microstructure; coatings with less than 9 wt.% Fe are typically amorphous; those with Fe content between 9 wt.% and ~12 wt.% exhibit a mixed amorphous-crystalline structure; and above 12 wt.%, the coatings become fully crystalline. This structural evolution contributes to enhanced thermal stability and improved wettability, making Ni-Fe-P coatings suitable candidates for applications such as under-bump metallization (UBM) in high-temperature electronic packaging [87].

In more complex systems, such as quaternary Ni-Co-Fe-P coatings, the introduction of iron exerts a synergistic effect with nickel and cobalt, significantly enhancing the electrocatalytic performance. Iron promotes the formation of a mixed amorphous and nanocrystalline structure, which increases the density of electrochemically active sites and is especially relevant for the hydrogen evolution reaction (HER). Moreover, an optimized atomic ratio of Ni, Co, Fe, and P has been found to correlate with improved HER activity, highlighting the critical role of Fe in tuning the catalyst composition for maximum performance [88].

2.1.3 Role of copper

Copper (Cu) incorporation into electroless Ni-P coatings has been shown to markedly enhance their functional properties, particularly in Ni-P-Cu composite systems. The addition of copper improves corrosion resistance and heat transfer performance owing to its high thermal conductivity. It also refines the microstructure, resulting in a denser coating with an increased mechanical strength. Studies have demonstrated that coatings with an optimal Cu concentration (1 g/L) significantly outperform uncoated mild steel, with cooling rates improved by approximately 25.2%, and notable increases in corrosion resistance were observed within the 100-400 °C range. These enhancements make Ni-P-Cu coatings highly suitable for thermal management applications, such as heat exchangers [45].

In quaternary systems such as Ni-P-Cu-W coatings, copper contributes to modifying the surface texture and grain structure, leading to larger grain sizes and improved mechanical characteristics. After annealing at 500 °C, the coatings exhibited an elastic

modulus of approximately 10.48 GPa. Despite earlier reports suggesting the limited influence of copper on tribological properties compared to tungsten, the presence of copper in these polyalloy coatings resulted in a significant reduction in the wear rate and coefficient of friction. This indicates a synergistic effect, where copper aids in enhancing the tribological performance when combined with tungsten, thus broadening the functional applications of these coatings [89].

2.1.4 Role of zinc

Zinc (Zn) plays a vital role in enhancing the performance of electroless Ni-P-based coatings. In the Ni-Zn-P system, elemental analysis revealed weight percentages of 7.24% Zn, 9.4% P, and 83.36% Ni. The incorporation of Zn significantly improves the mechanical strength and corrosion resistance of the coatings. Notably, Zn doping has been shown to enhance hardness, fatigue life, and electrochemical behavior, making Ni-Zn-P coatings suitable for applications requiring durable and protective surfaces [90].

Zn offers substantial benefits to quaternary Ni-Zn-Cu-P coatings. The elemental composition of the duplex coating was Ni (79.71 wt.%), P (10.25 wt.%), Zn (7.55 wt.%), and Cu (2.5 wt.%). The introduction of Zn in this system contributed to the development of a more compact, uniform granular microstructure, which significantly improved the corrosion resistance compared to conventional Ni-P coatings, particularly under 3.5 wt.% NaCl solution testing. Moreover, while Zn^{2+} ions are known to inhibit plating rates, the addition of Cu^{2+} ions effectively balances this effect, resulting in coating thicknesses comparable to those of binary systems. This synergy highlights the multifaceted role of Zn in improving both the structural integrity and corrosion performance of electroless alloy coatings [91].

2.1.5 Role of molybdenum

Molybdenum (Mo) has a significant influence on the corrosion resistance and mechanical performance of electroless Ni-P coatings. Its incorporation notably improved the resistance to pitting corrosion, particularly in chloride-rich environments, by promoting the formation of a stable passive film on the coating surface. Furthermore, Mo enhances the adhesion of the coating to the magnesium alloy substrates. Optimal results were observed at a Na_2MoO_4 concentration of 0.4 g/L, which provided a balanced Mo and phosphorus (P) content, resulting in improved microstructure and mechanical strength [92].

The presence of Mo further enhanced the thermal stability and structural integrity of Ni-Mo-W-P quaternary coatings. Specifically, Mo helps stabilize the amorphous phase up to 450 °C, effectively delaying the phase transformations that typically result in brittleness. This stabilization preserves the fracture toughness and allows the alloy to achieve higher hardness levels without compromising the ductility. These characteristics make Ni-Mo-W-P coatings especially advantageous for high-temperature applications, including solderable surfaces in integrated circuits, where both durability and thermal resilience are essential [41].

2.1.6 Role of tungsten

Tungsten (W) is a critical alloying element in electroless Ni-P coatings and contributes significantly to corrosion resistance and structural enhancement. Its inclusion in Ni-W-P coatings promotes the formation of a robust passive film that effectively inhibits the ingress of water and oxygen, thereby providing excellent protection to the underlying magnesium alloy substrates. Additionally, tungsten plays a role in refining the grain structure of the coating and increasing the nucleation rate during deposition, which helps to maintain an amorphous structure. These effects result in a more uniform, dense, and protective coating surface with improved durability [93].

Tungsten has been shown to considerably improve the electrocatalytic performance in Ni-W-Mo-Co-P polyalloy coatings. The uniform distribution of W ions throughout the coating enhances its intrinsic electrochemical characteristics and alters its electronic structure, leading to an increased active surface area. This contributes to the superior HER activity, with reported overpotentials of 41 mV at 10 mA/cm^2, 46 mV at 20 mA/cm^2, and 67 mV at 100 mA/cm^2, along with a favorable Tafel slope of 38 $mV \cdot dec^{-1}$. The electroless deposition technique further ensures the chemical stability and durability of the Ni-W-Mo-Co-P coatings, making them excellent candidates for energy-related applications that require robust and efficient HER catalysts [94].

2.1.7 Role of rare earth elements

The incorporation of rare earth elements (REEs) such as lanthanum (La), yttrium (Y), cerium (Ce), and neodymium (Nd) significantly enhances the microstructure, deposition rate, and overall performance of the electroless coatings. REEs improve bath stability, facilitate catalytic reduction, and refine grain structures, leading to denser coatings with

superior corrosion resistance and mechanical properties [50,95]. Optimized concentrations of REEs accelerate deposition rates by increasing the number of nucleation sites, whereas excessive amounts can hinder the process by shielding the catalytically active sites [95]. In Ni-P-B coatings, REEs, such as La^{3+} and Ce^{3+}, promote finer grain structures and self-cleaning superhydrophobic surfaces, enhancing their protective capabilities [50]. Similarly, the addition of Ce and Nd in Ni-W-P and Ni-Mo-P coatings results in improved adhesion, reduced surface defects, and lower corrosion rates, making them ideal for applications in aerospace, automotive, and other industries exposed to harsh environments [96,97]. REEs also contribute to the amorphization of coatings, enhancing their durability and electrochemical stability [96]. In addition to corrosion resistance, REEs improve catalytic activity in the hydrogen evolution reaction (HER), as seen in the Ni-Co-B-RE coatings. Elements such as gadolinium (Gd) optimize the electronic structure and enhance electron transfer, leading to a lower overpotential and improved hydrogen adsorption/desorption kinetics [98]. Furthermore, the incorporation of Ce in Ni-Cu coatings modifies the reduction potential of copper, forming a denser passive film that reduces pitting corrosion and extends the service life of coatings in corrosive environments [99]. Overall, the strategic incorporation of REEs into electroless coatings significantly enhances their structural integrity, tribological properties, and corrosion resistance, rendering them valuable for advanced engineering applications [100].

Role of cerium and its potential benefits in electroless coatings

Cerium (Ce) has been used for the development of advanced functional coatings owing to its exceptional physicochemical properties, including corrosion resistance, self-healing capabilities, superhydrophobicity, and UV shielding. The most common applications of Ce are shown in Figure 2.1. As one of the most abundant rare-earth elements, the dual-valence transformation of cerium (Ce^{3+} and Ce^{4+}) enhances its effectiveness as a corrosion inhibitor, forming protective passive layers on metal surfaces that significantly reduce corrosion rates. The integration of cerium compounds into various coating matrices not only improves their durability and performance but also opens avenues for innovative applications in diverse fields such as aerospace, automotive, and electronics. By fully utilizing the unique characteristics of Ce, researchers aim to address the challenges of resource waste and expand the functional applications of rare-earth elements in coatings, ultimately contributing to more sustainable manufacturing practices and increasing economic value [65].

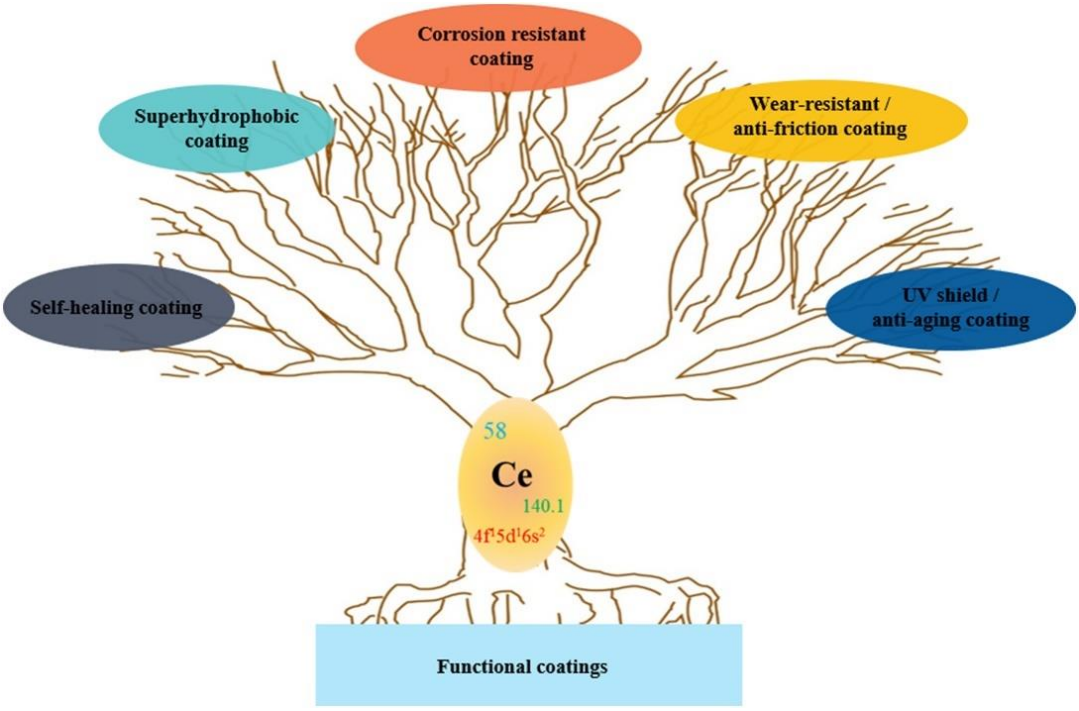

Figure 2.1. Applications of rare earth metal cerium (adapted from [65]).

In electroless coatings, such as Ni-P, the incorporation of cerium oxide (CeO_2) not only promotes structural stability but also improves the electrochemical properties. The presence of Ce enhances charge-transfer kinetics through the formation of oxygen vacancies, which facilitates electron transfer. Furthermore, the defective CeO_2 species contributed to the regulation of the adsorption-desorption processes, thereby improving the overall hydrogen evolution efficiency [101].

Microstructural changes

The incorporation of Ce into the electroless coatings can induce significant microstructural changes. Cerium ions can act as nucleation sites, influencing the growth of the coating and leading to the refinement of the grain size. This grain refinement can enhance the mechanical properties of the coating, such as hardness and wear resistance. The presence of Ce can also affect phase formation in the coating, leading to the formation of different intermetallic compounds or oxide phases [102]. These microstructural changes can significantly affect the overall performance of the coating, thereby affecting its corrosion resistance, thermal stability, and other properties [97]. The specific microstructural changes observed depended on various factors, including the type of coating, cerium concentration, and deposition conditions.

Mechanical properties

The addition of cerium to electroless coatings often leads to improvements in mechanical properties, particularly hardness and wear resistance. This enhancement can be attributed to several factors, including grain refinement, dispersion strengthening [103], and formation of hard intermetallic phases [102]. Studies have shown that optimal Ce concentrations can significantly increase the microhardness of Ni-P [102], Ni-B, and other coatings [104]. This improved hardness translates to enhanced wear resistance, as demonstrated by various tribological tests. However, exceeding the optimum cerium concentration can lead to a decrease in wear resistance, indicating the importance of precise control over cerium content. The underlying mechanisms responsible for the improved wear resistance include increased grain boundary strength and formation of protective oxide layers [105].

Corrosion resistance

The incorporation of Ce into electroless coatings significantly enhanced their corrosion resistance. This improvement could be attributed to several factors. First, cerium forms a passive oxide layer on the coating surface, acting as a barrier against corrosive agents [106]. Second, Ce ions can block the diffusion paths of the corrosive species, preventing them from reaching the substrate. Third, Ce can react with aggressive anions (e.g., chlorides) to form insoluble compounds, further enhancing corrosion protection [54]. Studies have shown that the corrosion resistance of various coatings, including Ni-Ce-P [54], Ni-Mo-P [97], and Ni-B-CeO_2 [105], is significantly improved by the addition of Ce. The optimal cerium concentration for achieving maximum corrosion resistance varies depending on the specific coating system and the corrosive environment. The effectiveness of Ce in enhancing corrosion protection is evident in various environments including saline solutions [97], molten salts [106], and aggressive atmospheric conditions [107]. The formation of protective cerium oxide layers [108] and blocking of diffusion paths contributed to the enhanced corrosion resistance observed in these studies. The type of phosphate post-treatment also plays a crucial role in determining the corrosion resistance of cerium-containing coatings, with different phosphate treatments leading to significant variations in stability against pitting corrosion [107].

Thermal stability

The addition of Ce significantly improves the thermal stability of the electroless coatings. This enhancement was attributed to the ability of Ce to inhibit the diffusion of phosphorus [109] or boron [85] atoms within the coating matrix. These atoms are often responsible for the degradation of the coating at elevated temperatures. The presence of Ce hinders the mobility, thus increasing the temperature at which significant structural changes occur. This improved thermal stability is crucial for applications involving high-temperature exposure, such as thermal barrier coatings [85]. The specific mechanisms of the thermal stability enhancement vary depending on the coating composition and cerium concentration.

Other properties (e.g., magnetic, biofilm inhibition)

Cerium incorporation can also influence other properties of electroless coatings depending on the specific composition and processing parameters. For instance, the addition of Ce to Ni-Co-P coatings enhances their magnetic properties, leading to improved saturation magnetization. The underlying mechanism involves the promotion of ferromagnetic phase formation in the coating [110]. In other cases, Ce has been found to improve the biofilm inhibition capabilities of coatings, making them suitable for applications where microbiologically induced corrosion is a concern [102]. These findings highlight the versatility of Ce as an additive in electroless coatings and its potential to tailor the properties of the coatings to meet specific application requirements.

2.2 Electroless coating process parameter optimization

2.2.1 Process optimization via response surface methodology

Response surface methodology (RSM), often combined with design of experiments (DoE) techniques such as central composite design (CCD) and Box-Behnken design, have been extensively employed to optimize the deposition parameters and enhance the performance of electroless coatings.

Zhang et al. [74] utilized RSM with CCD to optimize the parameters for Ni-Fe-P electroless coatings. A full factorial design involving ten experimental runs was conducted, followed by analysis of variance (ANOVA) to validate the predictive models. The optimal coating performance was achieved at a bath temperature of 85.1 °C and a pH of 7.9, leading

to a significant enhancement in corrosion resistance. The optimized coating exhibited a polarization resistance of 22,180.8 Ω·cm^2, corrosion current density of 3.30 μA/cm^2, and corrosion potential of -0.4253 V.

Similarly, CCD within the RSM framework was applied to investigate the effects of cobalt sulfate, sodium hypophosphite, and bath temperature on the corrosion behavior of Ni-Co-P coatings. The optimal conditions; 15 g/L cobalt sulfate, 30 g/L sodium hypophosphite, and 80 °C bath temperature, yielded a minimum corrosion rate of 0.535 μm/year, representing a 74.76% reduction from the original copper substrate rate of 2.12 μm/year [75].

Further optimization of the Ni-Co-P coatings was explored using the Box-Behnken design across three variables: nickel sulfate, cobalt sulfate, and bath temperature. Fifteen experimental runs were conducted, and the data were analyzed using machine learning algorithms, such as gradient descent with RMSprop, ABC, Firefly, and Teaching-learning-based optimization. The study identified an optimal corrosion rate of 0.435 μm/year, with statistical analysis confirming the strong influence of the cobalt sulfate concentration and its interaction with bath temperature on the coating performance [76].

In the case of electroless Ni-W-P coatings applied to AZ91D magnesium alloys, RSM was employed to develop a quadratic regression model assessing multiple process parameters. Optimal conditions included 20 g/L nickel sulfate, 15 g/L sodium tungstate, 30 g/L sodium hypophosphite, a bath temperature of 65 °C, and a pH of 9.3. Among these, the sodium tungstate concentration was the most influential, with interactions among variables that significantly affected the corrosion resistance of the coating. The optimized coating demonstrated an impressive failure time of 10,200 min in immersion tests, indicating strong protective capabilities [111].

Optimization of the Ni-B-nanodiamond composite coatings was carried out using RSM with a CCD framework involving 15 experiments. The variables included the nanodiamond concentration, reducing agent concentration, and stabilizer levels. The resulting quadratic models accounted for 94.85% of the response variability in the microhardness and thickness. Under optimal conditions, the coatings achieved a maximum microhardness of 871 HK50 and a thickness of up to 15.0 μm, confirming the effectiveness of RSM in tailoring the coating properties [112].

2.2.2 Modeling process-property relationships using artificial neural networks

Vijayanand et al. [113] applied a back-propagation neural network (BPNN) to optimize the hardness of citrate-stabilized electroless nickel-boron coatings by modeling the effects of nickel concentration, reducing agent, and stabilizer. The model was trained using data from 11 experiments and validated using four additional runs. It achieved a high coefficient of determination ($R^2 = 0.9852$), with a predicted maximum hardness of 592 HV, which closely matched the experimental results. Although the ANN model was highly effective, the Box-Behnken design (BBD) offered a slightly better fit, achieving $R^2 = 0.9911$.

Vijayanand et al. [114] in another study used BPNN to explore the relationship between the concentration of an amphoteric surfactant and the average surface roughness (R_a) of electroless Ni-B coatings. Using a multilayer perceptron structure with optimized parameters, the network achieved $R^2 = 0.988$, outperforming traditional regression approaches and effectively capturing the influence of the surfactant concentration on the surface morphology.

In a different dipping and padding coating process, a cascade-forward neural network was used to predict the concentration of silver nanoparticles (AgNPs) coated on dyed silk fabric using bacterial inhibition zones as the input. The network architecture includes multiple hidden layers with neurons connected from all the previous layers to enhance learning. This approach significantly improved the accuracy of AgNP concentration prediction compared with traditional spectrophotometric color matching, achieving a high correlation of 0.994 between the actual and predicted values and a low mean absolute error of 0.46 [115].

ANN modeling was also employed to predict the deposition rate of the Ni-W-P-nanoTiO_2 composite coatings based on parameters optimized using the Taguchi method. The most effective architecture was ANN 4-7-1, which comprised four input neurons, seven hidden neurons, and one output neuron. This configuration achieved a correlation coefficient of $R^2 = 0.9820$, demonstrating strong agreement between the predicted and experimental values and reinforcing the ANN's potential for optimizing electroless deposition parameters [71].

Similarly, a feed-forward BPNN was used to predict the microhardness of the Ni-Zn-Cu-P coatings. After evaluating various neuron configurations, the ANN 3-7-1 model was found to be the most accurate, yielding an RMSE of 8.8475 and R^2 of 0.982. The ANN

model outperformed the predictions obtained using the Taguchi method, highlighting its superior predictive capability for mechanical property optimization [78].

Additionally, an enhanced dendritic neural (DN) network optimized using the artificial hummingbird algorithm (AHA) was developed to model the wear behavior of Cu-Al_2O_3 nanocomposites reinforced with silver. This advanced model accurately predicted both the wear rate and the coefficient of friction. The results revealed that increasing the Al_2O_3 content reduced wear and improved frictional properties, and the DN-AHA hybrid outperformed conventional methods in terms of predictive accuracy [82].

2.2.3 Optimization through metaheuristic algorithms

Hassan et al. [76] utilized metaheuristic optimization algorithms, including ABC, Firefly algorithm, and Teaching-learning-based optimization, to optimize the corrosion rate of electroless Ni-Co-P alloy coatings on copper substrates. The algorithms targeted significant factors, such as cobalt sulfate concentration and bath temperature, resulting in an optimized corrosion rate of 0.435 μm/Y, which is a 79.5% reduction from the corrosion rate of pure copper (2.12 μm/Y). The optimization results were consistent with the experimental data, demonstrating the effectiveness of the algorithms in enhancing the corrosion resistance of the coatings.

Mandal et al. [70] employed several metaheuristic optimization algorithms, including GA, ABC, and ANN with Differential evolution, to optimize the microhardness of electroless Ni-Sn-P coatings. The GA achieved an optimal microhardness of 387.4328 HV, whereas the ANN predicted 376.57 HV. The experimental microhardness was confirmed at 387.43 HV, highlighting the effectiveness of the algorithms. The analysis showed that nickel sulfate and sodium hypophosphite significantly influenced the microhardness, which was supported by surface morphology evaluations using techniques such as SEM and EDX.

In one study, metaheuristic optimization algorithms, including the Plackett-Burman design for screening, Box-Behnken design for local optimization, and GA and simulated annealing (SA) for global optimization, were utilized to refine the process parameters for electroless nickel-boron coatings. The combination of these techniques led to a significant reduction in the average surface roughness, reaching a value of 0.252 ± 0.004 μm [77].

De et al. [116] used the Non-dominated sorting genetic algorithm II (NSGA-II) for multi-objective optimization to maximize the weight percentages of Nickel and Cobalt in

electroless Ni-Co-P coatings while balancing their conflicting nature. By optimizing process parameters, such as cobalt concentration, reducing agent concentration, and bath temperature, NSGA-II produced a Pareto optimal front, presenting several optimal parameter combinations. The results demonstrated a strong correlation between the NSGA-II-predicted values and actual experimental data, thus validating the approach and enhancing the efficiency of the coating process.

2.2.4 Hybrid optimization strategies

Agrawal and Mukhopadhyay [81] integrated an ANN with a GA to identify the optimal parameters for minimizing the wear rate and coefficient of friction. The ANN, trained using the Levenberg-Marquardt algorithm, predicted performance outcomes that were then refined by the GA, employing selection, crossover, and mutation processes over multiple generations. This approach successfully yielded optimal operating conditions of 34.2099 N load, 0.5006 m/s speed, and 726.7243 m distance, achieving a wear rate of 0.1003×10^{-8} $g.N^{-1}.m^{-1}$ and a COF of 0.2099, as confirmed through validation tests.

2.3 Additional factors influencing electroless coating performance

2.3.1 Effect of bath loading on coating properties

Genova et al. [36] reported that in pure electroless nickel coatings, an increase in bath loading (defined as the substrate surface area per volume of solution) leads to a higher nickel deposition rate up to a threshold of approximately 1.5 mm^2/ml. Beyond this point, the deposition rate tends to plateau, which is attributed to the saturation of the catalytically active sites on the substrate surface. Consequently, further increases in the bath loading did not contribute to the additional growth in the coating thickness.

Similarly, Ergul et al. [117] demonstrated that bath loading has a significant impact on the deposition rate of electroless Ni-P coatings on multiwalled carbon nanotubes (MWCNT). They observed that lower bath loading enhanced the deposition rate, whereas higher bath loading combined with the large surface area of MWCNTs reduced it, emphasizing the need for optimized bath loading to achieve effective metal coatings on MWCNTs.

2.3.2 Antifouling behavior and microbiologically influenced corrosion resistance

Electroless Ni-Cu-P-PTFE coatings improved antifouling performance by incorporating PTFE particles that lowered the surface free energy of the deposits, thereby reducing fouling adhesion on heat exchanger surfaces. The key factor for fouling resistance was the reduced surface free energy rather than the surface roughness, as smoother coatings did not significantly enhance the antifouling properties [118].

The Electroless Ni-B/GO superhydrophobic coating provided antifouling performance by creating a robust micro/nanostructured surface with ultralow water adhesion and a high contact angle (162.8°), enabling water droplets to easily roll off and remove contaminants, as explained by the Cassie-Baxter model. This coating maintained cleanliness even after multiple immersions in muddy water owing to its strong adhesion, mechanical durability, chemical stability in acidic and alkaline solutions, and excellent corrosion resistance, collectively preventing pollutant adhesion and fouling buildup on the AZ91 magnesium alloy surfaces [119].

The electroless NiP-TiNi nanocomposite coating improved the resistance to microbiologically influenced corrosion by exhibiting lower porosity, which limits chloride ion penetration, releases Ni^{2+} ions, and forms TiO_2, which possesses strong antimicrobial properties against sulfate-reducing bacteria and significantly increases the charge transfer resistance, as shown by electrochemical impedance spectroscopy. These factors together reduce biofilm and corrosion product formation on the surface, leading to an approximately 93% corrosion inhibition efficiency after 28 d of incubation in SRB media [60].

2.4 Research gaps

Based on a literature survey of the different areas of electroless coatings described above, the following research gaps were found that require further investigation.

One of the key areas requiring attention is the development of polyalloy Ni-P coatings incorporating W and Ce. Tungsten has been shown to enhance the hardness, thermal stability, corrosion resistance, and tribological properties of Ni-P coatings. Similarly, the addition of small amounts of Ce to an electroless bath has been shown to improve oxidation resistance, grain refinement, and catalytic properties. However, there is a lack of comprehensive studies exploring the combined effects of tungsten and cerium addition in polyalloy Ni-P coatings, particularly in the context of multifunctional applications.

Current research on Ce-based compounds reveals several gaps, including the limited compatibility of Ce within coating matrices for long-term corrosion protection and an incomplete understanding of its interactions with both the coating and the substrate.

Most existing research has focused on optimizing individual properties in isolation, such as hardness, wear resistance, and corrosion resistance. There is a significant gap in studies that systematically investigate the simultaneous enhancement of the multiple functional properties of electroless coatings. The interplay between various performance factors, such as corrosion resistance, mechanical strength, and tribological behavior, has not been adequately explored.

In addition, advanced optimization techniques, including artificial intelligence (AI) and machine learning (ML), remain underutilized in electroless coating research. These computational tools offer immense potential for improving the process parameters, predicting the coating performance, and identifying optimal compositions more efficiently.

Another critical research gap lies in the elemental analysis of the electroless coating baths. The chemical composition of the coating bath plays a crucial role in determining the final coating properties; however, there is limited research on systematically analyzing and optimizing the bath chemistry to develop high-performance coatings. More studies are needed to understand how variations in bath composition affect the coating quality, stability, and deposition rates.

Moreover, the effects of bath loading, substrate roughness, and activators on electroless coatings have not been reported extensively. These factors significantly impact the coating adhesion, uniformity, and overall performance; however, research addressing their precise effects remains limited. The preparation and surface treatment of substrates before electroless deposition are often overlooked despite being a crucial step in ensuring coating reliability and durability. More systematic studies are needed to investigate the effects of substrate characteristics on the coating microstructure and performance.

2.5 Research objectives

AISI 1010 steel is a low-carbon steel containing approximately 0.1 wt.% carbon, known for its cost-effectiveness and balanced mechanical properties. It has a high Young's modulus of 200 GPa and maximum ultimate tensile strength (UTS) of approximately 650 MPa. Owing to its favorable characteristics, AISI 1010 steel is widely used in applications,

such as automotive components, machinery, and structural elements, where a combination of strength and ductility is essential [120]. The application of electroless coatings to AISI 1010 steel can enhance its corrosion resistance, hardness, wear resistance, and surface uniformity, making it a cost-efficient solution for various industrial applications.

Based on the research gaps stated above, the following objectives were fixed:

i. Development of multifunctional electroless Ni-W-P-Ce coatings on AISI 1010 steel
ii. Multi-objective optimization of electroless Ni-W-P-Ce coating parameters
iii. Investigation of cerium concentration on microstructural evolution and coating performance
iv. Effect of activator, substrate roughness and bath loading on coating quality

Chapter 3 Development and evaluation of stable electroless Ni-W-P-Ce coating baths

This chapter presents the synthesis and characterization of cerium-added electroless Ni-W-P coatings on AISI 1010 low-carbon steel using four baths with varied compositions and conditions. Mechanical and microstructural analyses were conducted to gain insight into optimizing the coating performance for enhanced durability in demanding applications.

3.1 Experimental details

3.1.1 Substrate preparation

The substrate material used in this study was a 1 mm thick low-carbon steel AISI 1010 sheet procured from the Steel Mart Company, Mumbai, India. The chemical composition of the substrates is listed in Table 3.1. The sheet was sectioned into smaller specimens measuring 15 × 10 × 1 mm^3 using wire EDM and subsequently polished with progressively finer grades of silicon carbide sandpaper (400, 800, 1200, 1500, and 2000) to achieve an improved surface finish. To eliminate tightly adhered contaminants, such as dirt, oil, and grease, the substrate surface was initially cleaned with distilled water, followed by acetone in an ultrasonic cleaner (Make: Apex Instruments, Model: UltraS-L20) for 10 min. Next, the substrate was degreased by immersion in a NaOH solution at 40 °C for 15 min. Finally, the activation process was performed by stirring the substrate in 30% diluted HCl solution for 30 s. To prevent contamination by the residual particles, the substrate was thoroughly rinsed with distilled water before and after each step.

Table 3.1. Chemical composition of AISI 1010 steel.

Element	Iron, Fe	Manganese, Mn	Sulphur, S	Phosphorous, P	Carbon, C
Content (%)	99.18-99.62	0.30-0.60	≤ 0.050	≤ 0.040	0.080-0.13

3.1.2 Coating bath preparation

Initially, various bath formulations were developed to deposit Ni-W-P-Ce coatings on low-carbon steel by varying the concentrations of metal salts, complexing agents, and stabilizers, as well as adjusting the bath pH and temperature. After optimization, the four final bath compositions were identified, and the coated samples obtained from these baths were subsequently characterized. The chemical compositions and operating conditions of each bath are listed in Table 3.2.

Table 3.2. Chemical composition and operating conditions.

Chemicals	Unit	Bath A	Bath B	Bath N1	Bath N2
Nickel sulfate ($NiSO_4.6H_2O$)	g/L	25	15	40	40
Ceric sulfate ($Ce(SO_4)_2.4H_2O$)	mg/L	10	50	6	6
Sodium hypophosphite ($NaH_2PO_2.H_2O$)	g/L	25	40	30	30
Sodium tungstate (Na_2WO_4)	g/L	30	15	15	15
Sodium acetate ($CH_3COONa.3H_2O$)	g/L	20	-	-	-
Trisodium citrate ($Na_3C_6H_5O_7.2H_2O$)	g/L	-	45	20	20
Lactic acid ($C_3H_6O_3$)	ml/L	31	-	-	-
Citric acid ($C_6H_8O_7$)	g/L	5	-	-	-
Lead II acetate ($Pb(C_2H_3O_2)_2$)	mg/L	2	-	-	-
Thiourea (CH_4N_2S)	g/L	-	-	0.001	0.001
pH		5 ± 0.2	9 ± 0.2	7 ± 0.2	7.5 ± 0.2
Coating time	h	1	0.5	1	2
Temperature	°C	85 ± 2	75 ± 2	75 ± 2	75 ± 2

These formulations were selected based on prior research on electroless Ni-P coatings incorporating tungsten and cerium [110,121]. In addition, chemical solutions including acetone (CH_3COCH_3) and sodium hydroxide (NaOH) at a concentration of 0.1 mol/L, hydrochloric acid (HCl) at a concentration of approximately 35%, and an ammonia solution (NH_3) with a concentration of approximately 25% were utilized in this study. All chemicals were sourced from Merck Life Science Pvt. Ltd., and thiourea was procured from Loba Chemie Pvt. Ltd. Precise weighing of the substances was performed using a high-precision weighing machine (Make: Sartorius, Model: BSA224S-CW) with an accuracy of 0.1 mg. The coating process was conducted without mechanical agitation using a magnetic stirrer with a hot plate (Make: REMI, Model: 5 MLH PLUS). An ammonia solution was added to regulate the bath pH, which was monitored using a pH meter (Eutech, CyberScan). The electroless coating setup primarily consisted of beakers, a magnetic stirrer with a hot plate, a pH meter, a thermometer, a thread or wire, and a weighing scale. A schematic representation of the setup is shown in Figure 3.1. Bath N1 and N2 shared nearly identical chemical compositions, with their primary difference being their respective pH values. In the case of Bath N2, sodium tungstate was first dissolved separately in distilled water before being introduced into the final bath containing all the other chemicals once the temperature reached approximately 60 °C. Subsequently, the pH was adjusted using ammonia solution.

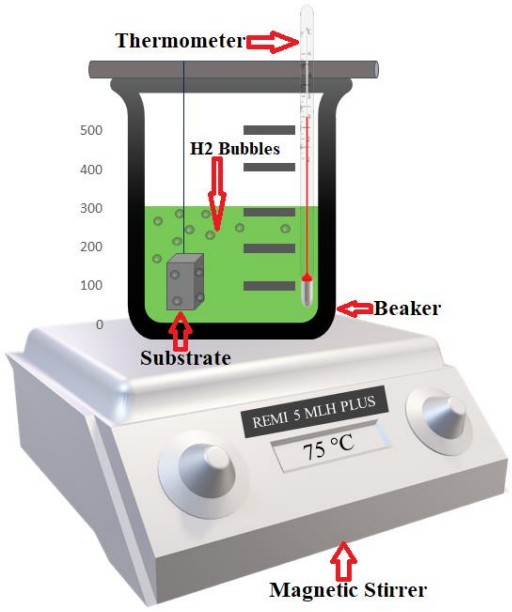

Figure 3.1. Schematic of the electroless coating setup.

3.2 Mechanical and microstructural characterization

After the coating, the rate of deposition was determined by the weight gain method [122] using Equation 3.1.

$$\nu = \frac{W}{A \times t} \; (mg.cm^{-2}.h^{-1}) \tag{3.1}$$

where ν is the deposition rate, W is the increment in weight after coating (mg), A is the total surface area of the substrate (cm^2), and t is the coating time (h).

Vickers microhardness measurements were conducted for both the coated samples and substrate using a microhardness tester (UHL VMHT). These measurements ensured that the hardness of the coating layer, rather than the composite hardness, was obtained by determining the indentation depth using the simple relationship given in Equation 3.2. In this equation, ‘hi’ represents the indentation depth, while ‘d’ denotes the average diagonal length [123]. During the measurements, the indentation load, indentation speed, turret position, and dwell time were maintained at 50 gf, 30 µm/s, 50x magnification, and 10 s, respectively. The indentation load was applied at five different locations on each sample surface, and the average of these five values was considered the final microhardness value for the sample. Additionally, the variation in the diagonal length (ΔD), which represents the tolerance during hardness measurement, was maintained below 5%.

$$h_i = \frac{d}{2\sqrt{2}\,tan\,68°} = \frac{d}{7} \tag{3.2}$$

The surface morphology and coating composition were observed using field-emission scanning electron microscopy (FESEM) Inspect F50 (FEI, Netherlands). During operation, the high voltage (HV), magnification, working distance (WD), and horizontal field width (HFW) were fixed at 20 kV, 5000x, 12.9 mm, and 59.7 μm respectively. First, highly magnified secondary electron images were captured, and elemental mapping was performed using energy-dispersive X-ray spectroscopy (EDS) coupled with FESEM.

Structural and phase analyses of the coated samples were performed using an X-ray diffractometer (Bruker, D8 Advance) with a scan range of 10-80°. The wavelength of X-rays (λ) in the copper tube was 0.15418 nm.

3.3 Results and discussion

3.3.1 Bath stability

The procedure for preparing the acidic coating bath (Bath A) is illustrated in Figure 3.2. Initially, all metal salts (nickel sulfate and ceric sulfate), except sodium tungstate, were dissolved in distilled water in a beaker, whereas sodium tungstate was separately dissolved in another beaker. All other chemicals, including sodium hypophosphite, sodium acetate, lactic acid, citric acid, and lead(II) acetate, were dissolved in a third beaker, as shown in Figure 3.2(a). Sodium hypophosphite functions as a reducing agent and undergoes oxidation to provide electrons for the reduction process, whereas sodium acetate and lead(II) acetate act as stabilizers, mitigating the rapid pH fluctuations caused by hydrogen ion release during nickel reduction [124]. Acetic acid serves as the primary complexing agent, stabilizing nickel ions and regulating the deposition rate, whereas citric acid, acting as an auxiliary complexant, enhances the bath stability but reduces the coating speed at higher concentrations [125]. Separate dissolution of these components is crucial for preventing premature reactions between the metal ions and reducing agents. In electroless coatings, the reduction of metal ions by a reducing agent is the primary reaction requiring strict control. If metal salts and reducing agents are directly mixed as dry components or in concentrated solutions, immediate reactions can occur, leading to uncontrolled metal reduction outside the coating process [126]. Once all chemicals were fully dissolved, they were combined in a single beaker, as depicted in Figure 3.2(b).

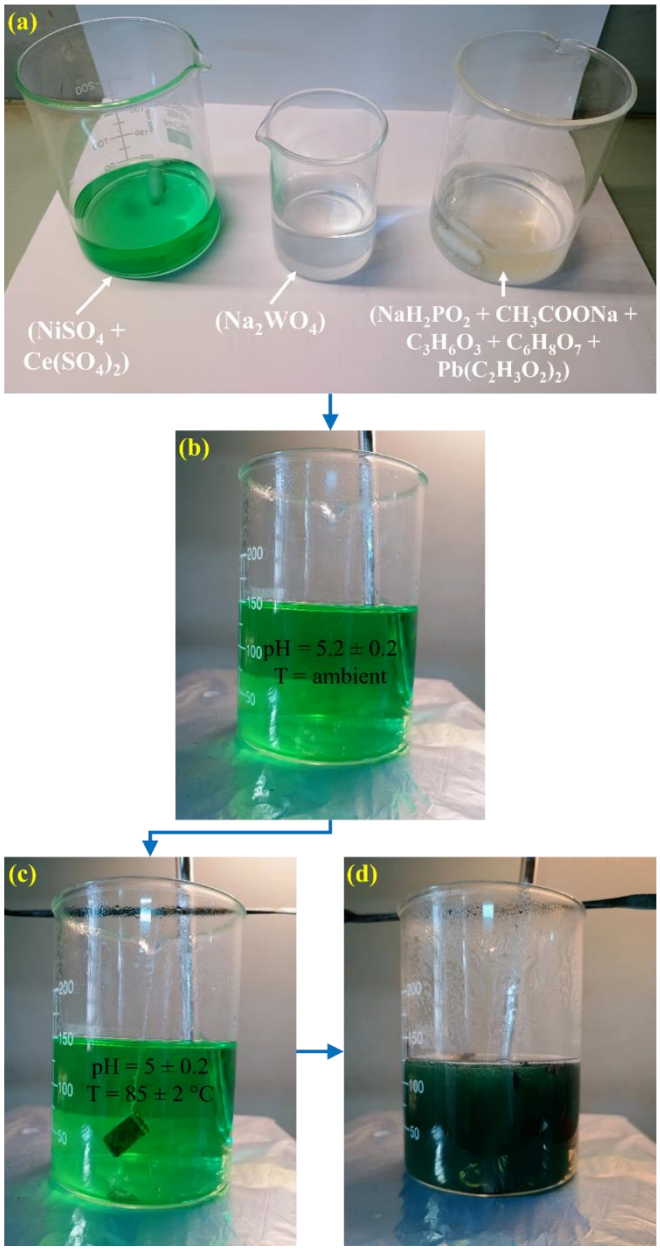

Figure 3.2. Sequential steps for preparation of Bath A.

At this stage, the bath appeared clear and transparent, with a light green color and pH of approximately 5.2. The bath temperature was increased to 85 °C before immersing the substrate, as shown in Figure 3.2(c). During this step, the bath remained transparent and the pH stabilized at approximately 5.

The coating process was performed for approximately one hour. Subsequently, spontaneous bath decomposition was observed, marked by rapid hydrogen bubble generation and a color change from green to black, as illustrated in Figure 3.2(d). The acidic nature of this bath and elevated coating temperature (85 °C) contributed to its

decomposition. This instability can be attributed to the chemical degradation of reducing agents, such as hypophosphite, under acidic conditions, where they tend to oxidize or decompose prematurely. Acidic baths promote a higher rate of hydrogen evolution, which adversely affects the coating reaction by locally depleting active species. Additionally, elevated temperatures accelerate side reactions, further destabilizing the bath [127].

Another basic bath (Bath B) was prepared, which decomposed within just half an hour. This was likely due to the absence of a stabilizer and high concentration of cerium. A high Ce ion concentration promotes particle agglomeration, which blocks catalytically active sites on the substrate surface and increases the surface energy of the coating, thereby inhibiting nucleation and growth. Moreover, the excessive presence of Ce ions destabilizes the coating bath, resulting in a reduced deposition efficiency [121].

A neutral electroless coating bath (Bath N1) was formulated using fewer chemicals than Bath A, which contained two complexing agents. Bath N1 utilizes only one trisodium citrate. Sodium citrate, known for its moderate complexing ability, helps stabilize the coating solution by forming stable complexes with Ni^{2+} ions [128]. This stabilization was essential for maintaining the desired pH and chemical environment during the coating process. Additionally, instead of using two stabilizers, as in Bath A only one stabilizer, thiourea, was used in this formulation. In acidic electroless nickel baths, thiourea plays a critical role in preventing the formation of nickel phosphite precipitates when sodium hypophosphite is used as a reducing agent. Similarly, in alkaline baths, thiourea ensures the solubility of nickel ions, preventing their precipitation as nickel hydroxide and thereby enhancing the overall stability of the coating solution [129].

To prepare Bath N1, all metal salts were dissolved in a beaker with distilled water, whereas the remaining chemicals were dissolved separately in another beaker, as illustrated in Figures 3.3(a) and 3.3(b). After the chemicals were dissolved separately, they were combined in a single beaker, as shown in Figure 3.3(c). Because all the metal salts were dissolved together in a single beaker, the solution appeared nontransparent. At this stage, the solution remained nontransparent with a light blue appearance, and the pH was measured at approximately 7.2. Upon heating the bath to 75 °C, the color of the solution changed from nontransparent light blue to slightly transparent green, as shown in Figure 3.3(d). During this process, pH decreased to 6.2. This decrease in pH with increasing temperature is primarily attributed to the enhanced ionization of water, which increases the

concentration of hydrogen ions (H^+), thereby lowering the pH. Additionally, elevated temperatures influence the solubility of gases and chemical species in the bath, promoting reactions that generate acidic by-products or deplete hydroxide ions (OH^-), further reducing the solution pH [130]. It is important to note that the coating temperature was maintained at 75 °C to avoid issues encountered at higher temperatures in Bath A.

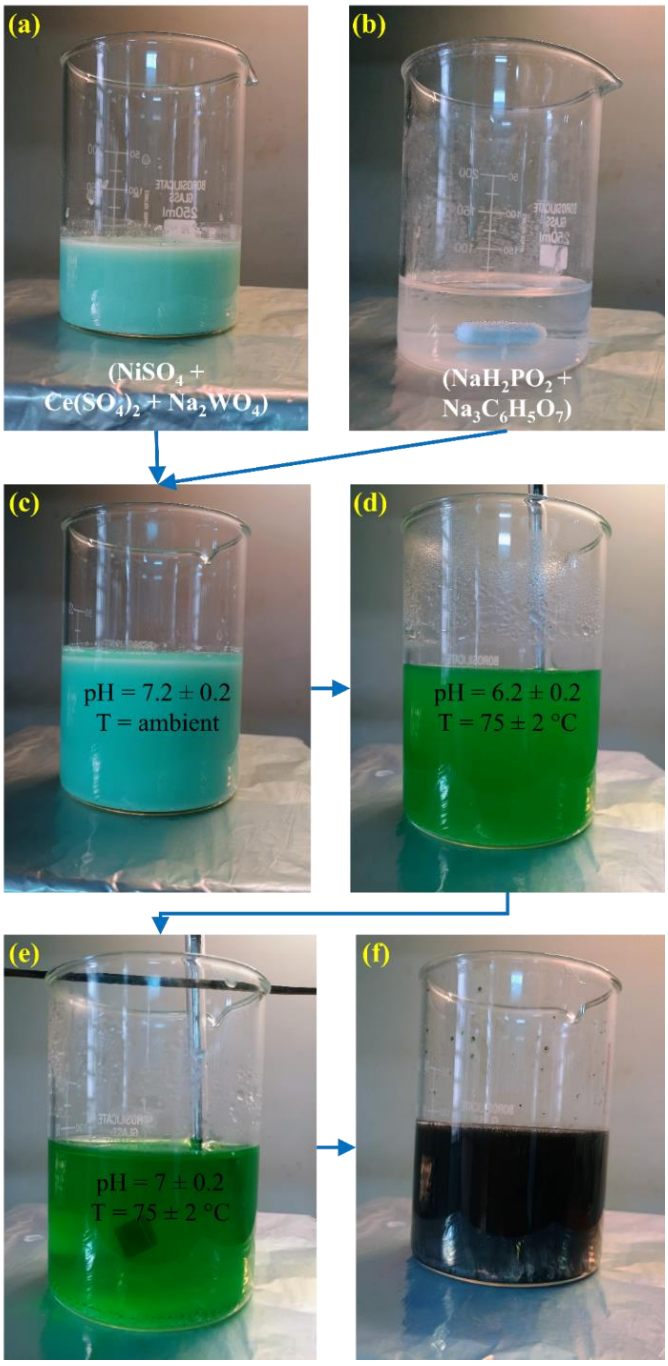

Figure 3.3. Preparation and evolution of Bath N1.

Subsequently, a small amount of ammonia solution was added to the bath, which increased the pH to approximately 7 and further improved the transparency of the solution, as shown in Figure 3.3(e). The addition of ammonia to electroless coating baths serves multiple functions, including the formation of stable metal-ammonia complexes that enhance the solubility of metal ions, facilitating their reduction, and regulating the bath pH, which is crucial for optimizing the deposition conditions. Furthermore, ammonia stabilizes the coating bath, prevents precipitation, and ensures uniform deposition [131]. However, even after this adjustment, the transparency of the bath was not as high as that of Bath A.

The coating process was then performed for one hour, during which the deposition rate was significantly higher than that in Bath A. This aspect is discussed in Section 4.4.2. However, the bath eventually decomposes, as shown in Figure 3.3(f). It appears that tungsten dissolution issues persisted, likely because of its direct mixing with other metal salts under ambient conditions. A white precipitate, most likely tungsten, was observed at the bottom of the beaker, contributing to the decomposition of the bath.

A second neutral bath (Bath N2) was prepared to address the bath decomposition observed in Bath N1. The preparation procedure and chemical composition were identical to those used for Bath N1, as shown in Figure 3.4. The only modification was the dissolution of the sodium tungstate. Sodium tungstate was first dissolved in distilled water in a separate beaker instead of mixing it directly with other metal salts under ambient conditions. It was then introduced into a bath containing all other chemicals once the bath temperature reached 55 °C, as illustrated in Figure 3.4(d). At this stage, pH was maintained at 6.5. Subsequently, ammonia solution was added to the bath, the pH was increased to 7.5, and the final bath temperature was raised to 75 °C. With this modified preparation method, all the chemicals were completely dissolved, resulting in a highly transparent solution, as shown in Figure 3.4(e). The deposition rate was satisfactory. The bath remained stable for up to two hours; however, after this period, it became significantly more viscous, as shown in Figure 3.4(f). The increase in viscosity over time in the electroless coating baths is primarily attributed to the accumulation of salts and byproducts such as sulfates and phosphites, which form during the coating process. This build-up disturbs the chemical equilibrium of the solution, leading to an increased viscosity. These factors ultimately affect the quality and performance of the coatings [132].

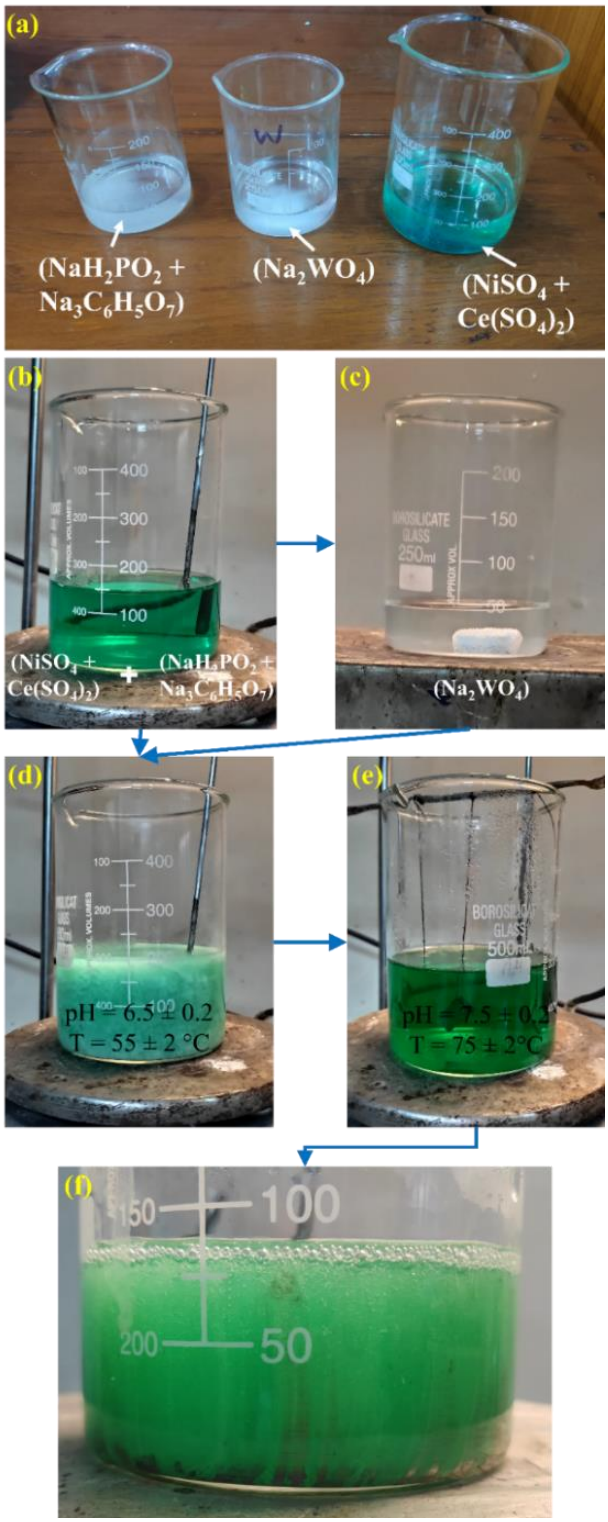

Figure 3.4. Preparation and stability assessment of Bath N2.

3.3.2 Deposition rate

The deposition rates for all the four baths are shown in Figure 3.5. The 1st Bath A, which contained numerous chemicals, exhibited the lowest deposition rate. When the pH is low

(high concentration of H^+ ions), reactions producing nickel from nickel ions (Ni^{2+}) and the reducing agent ($H_2PO_2^-$) are less favorable. Excess H^+ ions drive the reaction backward, resulting in fewer Ni atoms being deposited onto the substrate. Additionally, the slow deposition rate in the acidic medium may be due to the reduced bath stability and formation of insoluble species such as $NiHPO_3$, which precipitates out of the solution and consumes nickel ions, further hindering the deposition process [133]. This bath also had a relatively high phosphorus content, as shown in Table 3.3. A higher phosphorus content typically correlates with a slower deposition rate, regardless of the bath type (acidic or alkaline). This is due to several interrelated factors: the formation of complex species that do not readily participate in the deposition reaction, alteration of the reduction potential of nickel ions, and impeded adsorption of nickel ions on a surface saturated with phosphorus [109,134].

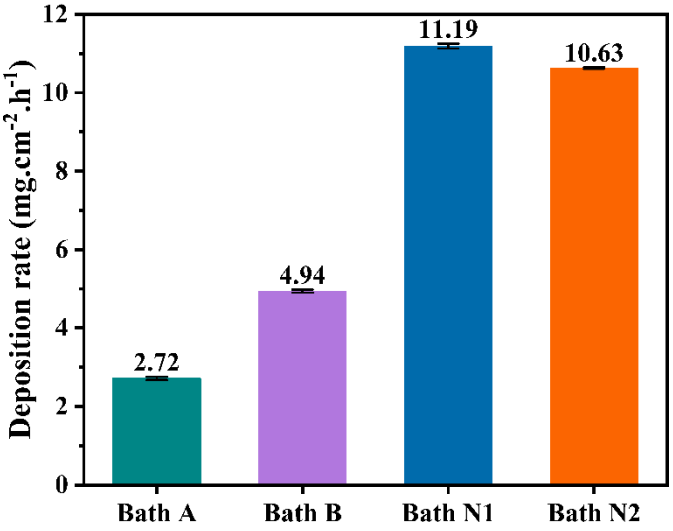

Figure 3.5. Deposition rate of the Ni-W-P-Ce coatings.

Bath B also showed a low deposition rate, primarily because of the absence of a stabilizer and high concentration of cerium. A high Ce ion concentration leads to particle agglomeration, blocking the catalytic active sites on the substrate surface and increasing the surface energy of the coating, which hinders nucleation and growth. Additionally, the presence of excess Ce ions destabilized the coating bath, leading to a decreased deposition efficiency [121].

Bath N1 and N2, which included the stabilizer thiourea, exhibited higher deposition rates, with Bath N1 exhibiting rate of 11.19 $mg.cm^{-2}.h^{-1}$. Thiourea prevents the complexing agent sodium citrate by effectively controlling the release rate of free Ni ions during the reduction reaction, which can increase the deposition rate [135]. In these baths, an optimal

amount of cerium salt is effectively adsorbed onto the substrate surface, reducing the surface energy and facilitating nickel ion reduction, thereby accelerating the coating process [136]. Bath N1, which had a slightly lower pH, decomposed after 1 h of coating, whereas Bath N2, which had a pH of approximately 7.5, remained stable and showed no issues.

3.3.3 Microhardness

The average Vickers microhardness measured at 50 gf for both the substrate and the coated samples is shown in Figure 3.6. The microhardness values of the samples obtained from Bath A and Bath B were more than twice that of the substrate. In contrast, the samples from Bath N1 and Bath N2 demonstrated microhardness values more than four times those of the substrate. The lower microhardness observed in Bath A and Bath B was attributed to the lower deposition rates, as discussed in the deposition rate subsection of the Results and Discussion section. This is corroborated by the SEM images in Figure 3.7, where Bath A shows nonuniform deposition with coating nodules visible only in certain areas of the microstructure. Similarly, the SEM images of Bath B revealed incomplete coverage of the substrate surface by the coating alloys, leading to significant variance and lower microhardness values.

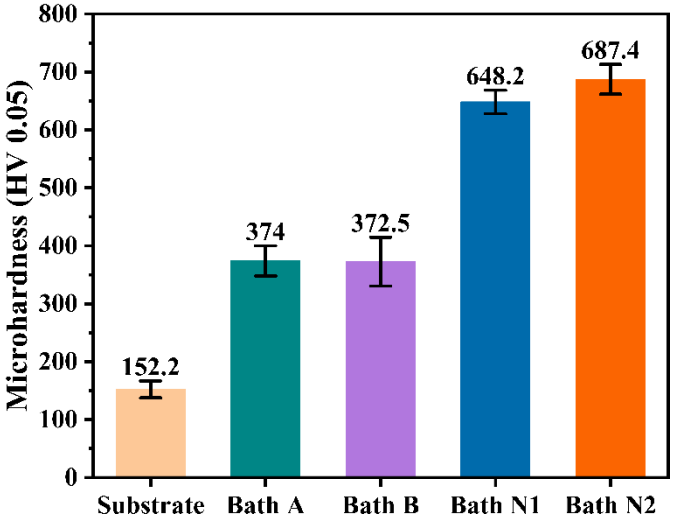

Figure 3.6. Vickers microhardness of the substrate and Ni-W-P-Ce coatings.

However, the coatings produced from Bath N1 and Bath N2 exhibit more compact microstructures. The substantial increase in the microhardness of these samples was primarily due to the presence of small amounts of phosphorus, as indicated by the EDS

results in Table 3.3. A low phosphorus content induces higher internal stresses in the coating, thereby increasing microhardness. Additionally, the formation of a solid solution of tungsten within the nickel matrix contributed to an increase in microhardness. The use of Ce in these baths further refines the microstructure. The hardening effects of Ce as a second phase, enhanced nucleation rates, and stability of the coating under alkaline conditions also play a significant role in increasing microhardness [137,138].

3.3.4 Surface morphology and elemental composition

The surface morphologies of the samples coated with the four baths are shown in Figure 3.7, with each exhibiting distinct characteristics. The surface obtained from Bath A (Figure 3.7(a)) shows a very poor morphology owing to minimal deposition. Coating nodules are sparsely distributed and only visible in a few areas, as indicated by the yellow arrows.

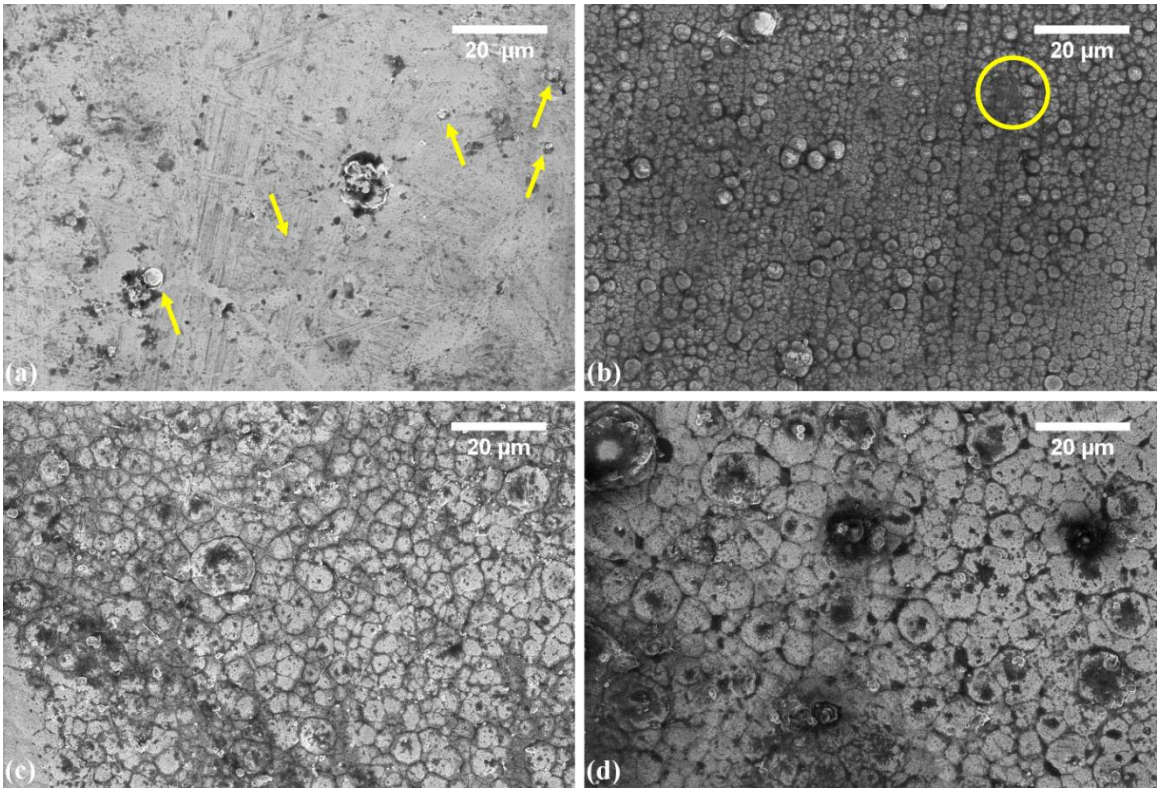

Figure 3.7. Surface morphology of Ni-W-P-Ce coatings: (a) Bath A; (b) Bath B; (c) Bath N1; (d) Bath N2.

In contrast, the surface (Figure 3.7(b)) obtained from Bath B displays visible globular or spherical nodules, which are typical of electroless coatings. This nodule formation results from a rapid nucleation process during electroless deposition, where small clusters

of atoms form quickly, limiting surface diffusion and causing atoms to accumulate into nodules rather than spread evenly. This type of morphology is also influenced by factors such as the bath composition and the condition of the substrate surface [139]. The surfaces obtained from Bath N1 and Bath N2 (Figure 3.7(c) and (d)) exhibited similar spherical or cauliflower-like microstructures. The average nodule sizes for the samples from the Bath B, Bath N1, and Bath N2 were 0.91 μm, 2.05 μm, and 2.07 μm, respectively. The smaller nodule size in Bath B can be attributed to two factors. First, the coating time was brief, preventing the full growth of the nodules, as some regions remained nodule-free, as highlighted by the yellow circle. Second, the high concentration of cerium sulfate in this bath played a significant role. Cerium particles acted as nucleation sites during the coating process, promoting the formation of new grains rather than the enlargement of existing grains, leading to a finer microstructure with smaller nodules [106]. Notably, none of the four coated samples exhibited any cracks, indicating good structural integrity across all coatings.

The weight percentages of the elements present in all the four samples are listed in Table 3.3. Bath A sample, with 8.5 wt.% phosphorus (P), represents a medium phosphorus (6-9 wt.%) electroless coating, which is known for its high corrosion and abrasion resistance. Bath B sample, containing 10.2 wt.% P, falls into the category of high phosphorus (10-15 wt.%) electroless coatings, which are typically associated with good ductility and enhanced corrosion resistance, particularly against chlorides.

Table 3.3. Elemental compositions (wt.%) of coatings deposited from different coatings bath.

Element	Bath A	Bath B	Bath N1	Bath N2
Nickel, Ni (wt.%)	76.2	73.1	78.9	78.8
Tungsten, W (wt.%)	14.5	15.9	16.0	17.6
Phosphorous, P (wt.%)	8.5	10.2	4.0	2.8
Cerium, Ce (wt.%)	0.8	0.9	1.1	0.8

In contrast, the Bath N1 and Bath N2 samples had lower phosphorus contents of 4 wt.% and 2.8 wt.%, respectively. These values represent low phosphorus (3-5 wt.%) electroless coatings, which are generally characterized by superior wear resistance [35,140]. Figures 3.8, 3.9, 3.10, and 3.11 show the elemental mapping for all elements in the four samples, illustrating the uniform distribution of elements across the coated surfaces. The images

clearly demonstrate the dense distribution of phosphorus in the medium- and high-phosphorus coatings, whereas a noticeable decrease in the phosphorus content was observed in the low-phosphorus coatings. Additionally, Ce was uniformly present in all the samples, with the highest content of 1.1 wt.% observed in Bath N1 sample. This confirms the successful integration of Ce into the electroless Ni-W-P coatings. Moreover, the tungsten content was consistently high across all four samples, exceeding 10 wt.%. The presence of tungsten contributes to solid-solution strengthening within the nickel matrix and forms a passivation film of WO_3, which enhances both the hardness and corrosion resistance of the coatings [128].

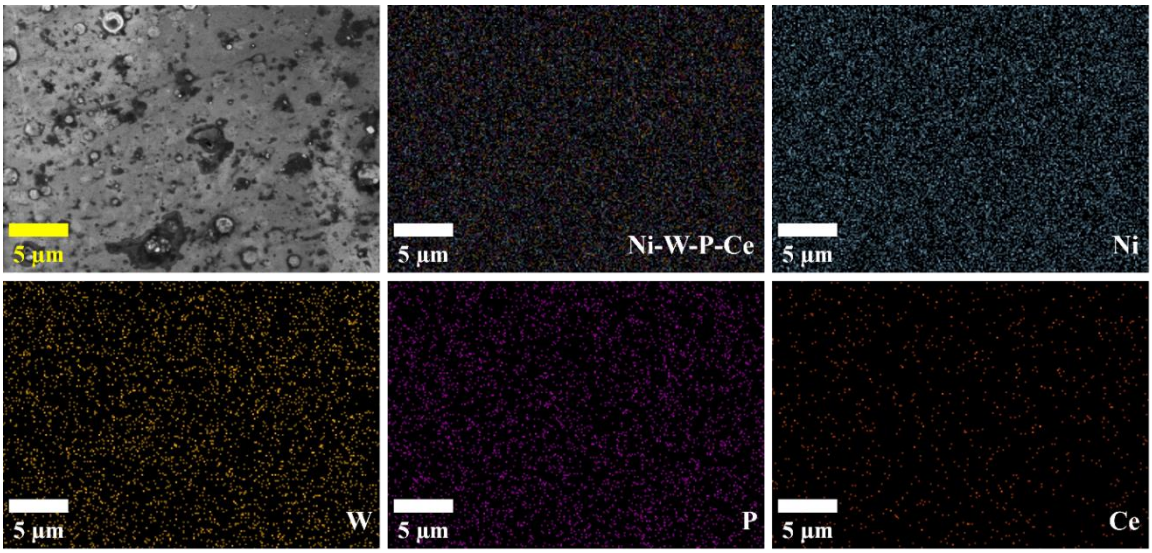

Figure 3.8. EDX mapping images of the coating top surfaces in Bath A.

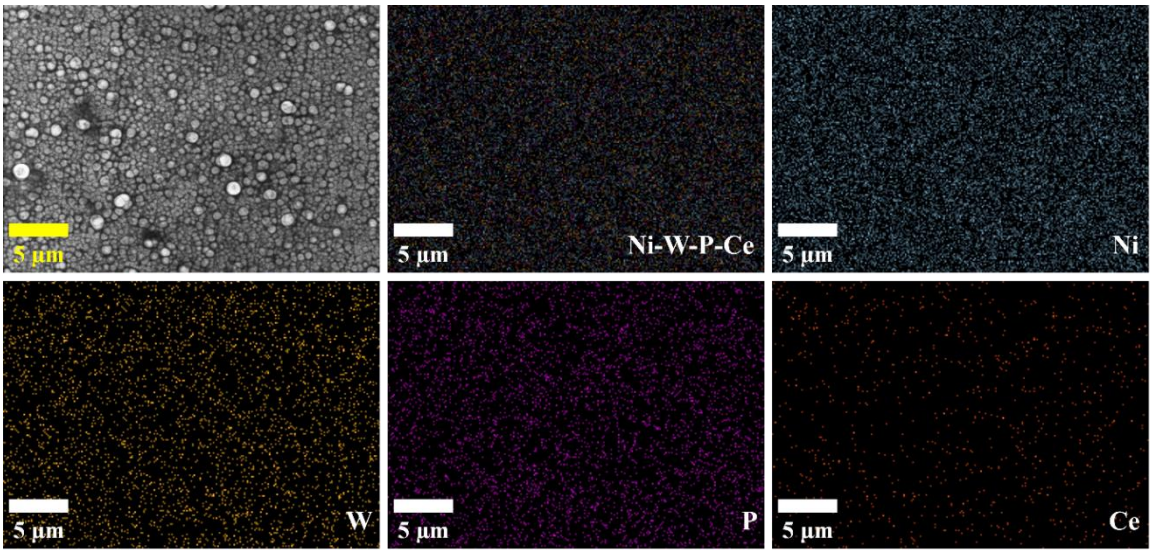

Figure 3.9. EDX mapping images of the top surfaces of the coatings in Bath B.

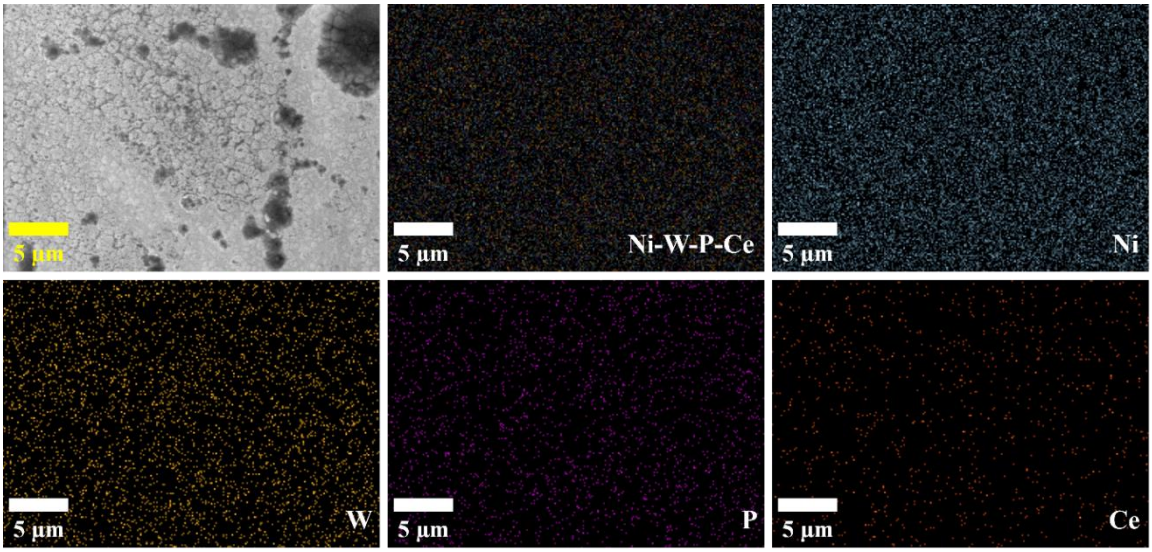

Figure 3.10. EDX mapping images of the coating top surfaces of Bath N1.

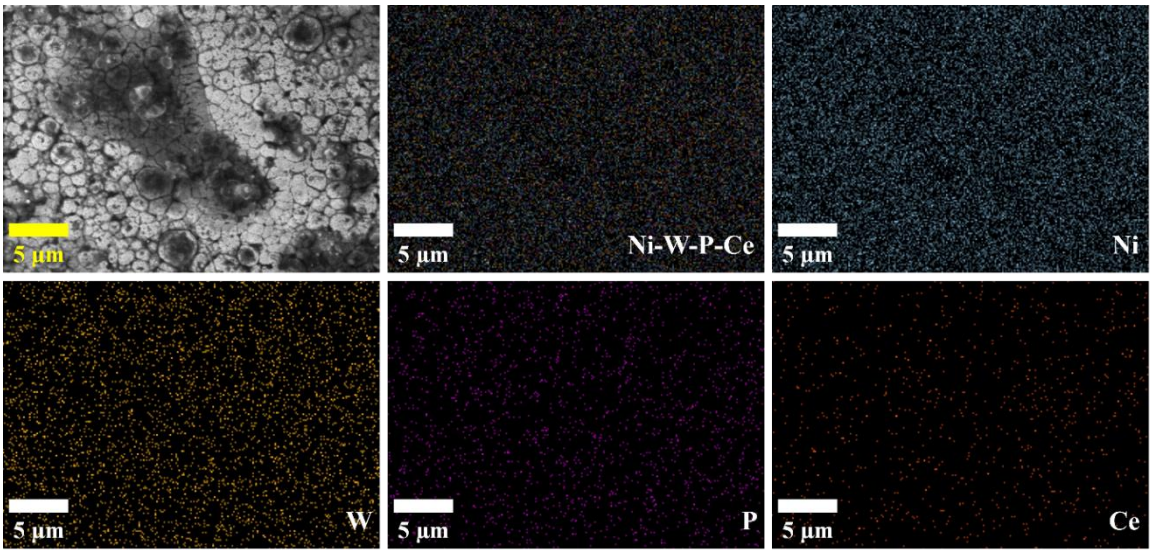

Figure 3.11. EDX mapping images of the coating top surfaces in Bath N2.

3.3.5 Coating structure

Figure 3.12 shows the X-ray diffraction (XRD) patterns of all four samples, revealing similar profiles with variations in peak intensity and broadness. The Ni peak at approximately 44.2° shows a lower intensity and narrower width for the Bath A and Bath B samples than for the Bath N1 and Bath N2 samples, which exhibit a higher peak intensity and broader peaks. The peak intensity is influenced by the atomic positioning within the unit cell, whereas the peak broadness is related to the crystallite size and lattice strain. Crystallites are uniform regions within polycrystalline solids that maintain consistent crystal structures [141]. The higher peak intensity and broader peaks in the Bath N1 and Bath N2 samples suggest a greater degree of crystallinity or a larger amount of the nickel

crystal phase compared to the Bath A and Bath B samples. Additionally, the broader peaks in the Bath N1 and Bath N2 samples indicated smaller crystallite sizes.

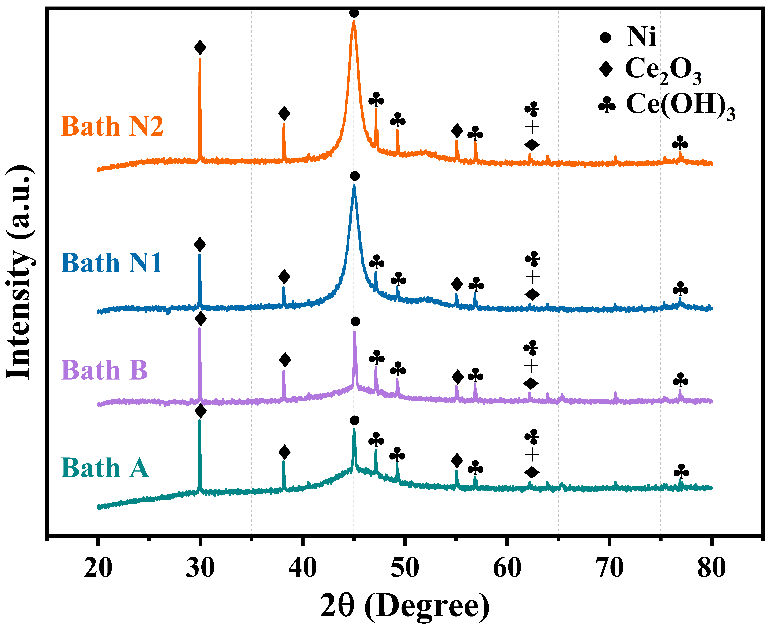

Figure 3.12. XRD patterns of all 4 samples.

In addition to the Ni peaks, the XRD patterns also show peaks corresponding to Ce_2O_3 and $Ce(OH)_3$. These peaks were identified using Match software with entry numbers 96-210-0638 for nickel, 96-153-1456 for cerium oxide, and 96-210-7093 for cerium hydroxide, in agreement with previous studies [54,105,142]. The formation of cerium hydroxide and subsequent cerium oxide during the drying process was observed, with cerium ions initially reacting with hydroxide ions to form cerium hydroxide, which was later converted to cerium oxide [143].

3.4 Closure

This chapter describes the development and evaluation of stable electroless Ni-W-P-Ce coating baths for depositing coatings on low-carbon steel AISI 1010. Four coating baths with different chemical compositions and operating conditions are developed. Bath A and Bath B exhibited low deposition rates and poor coating quality owing to their instability and high Ce content. Bath N1 and Bath N2, which contained thiourea, showed higher deposition rates and better coating quality. Bath N2 with a pH of 7.5 and bath temperature of 75 °C yielded the best results. Microhardness testing revealed that the Bath N1 and Bath N2 samples had hardness values more than four times higher than that of the substrate,

which was attributed to the presence of phosphorus, tungsten, and cerium. The SEM analysis showed distinct surface morphologies for each bath, with the Bath N1 and Bath N2 samples exhibiting compact nodular microstructures. EDS confirmed the uniform distribution of elements including Ce across the coated surfaces. The XRD analysis revealed the presence of nickel, cerium oxide, and cerium hydroxide phases, with the Bath N1 and Bath N2 samples displaying higher crystallinity. Based on mechanical and microstructural characterization, the chemical composition of Bath N2 was found to be the most advantageous for achieving superior coating performance.

Chapter 4 Multi-objective optimization of electroless Ni-W-P-Ce coating bath compositions

This chapter provides a detailed comparison of various optimization techniques for electroless Ni-W-P-Ce coating bath composition, highlighting the integration of artificial neural networks with metaheuristic algorithms to improve prediction accuracy and optimization efficiency.

4.1 Experimental procedure and parameter selection

The chemicals and operating conditions used for the coatings are presented in Table 4.1. The concentration range of the four primary coating element salts was selected based on the data from Chapter 3, while all other operating conditions remained unchanged.

Table 4.1. Chemical composition and operating conditions.

Chemical	Concentration	Conditions
$NiSO_4.6H_2O$	15-40 g/L	Temp.: 75 ± 2 °C
$Na_2WO_4.2H_2O$	15-30 g/L	pH: 7.5 ± 0.2
$Ce(SO_4)_2.4H_2O$	4-12 mg/L	Time: 2 hours
$NaH_2PO_2.H_2O$	25-40 g/L	
$Na_3C_6H_5O_7.2H_2O$	20 g/L	
CH_4N_2S	0.001 g/L	

Electroless Ni-W-P-Ce coating was applied on plain carbon steel following the design created through central composite design of response surface methodology. In this design, the input variables or parameters were the amounts of the four main coating elements: Ni, W, P, and Ce. The pilot experiments showed that the concentration ranges of the chemicals listed in Table 4.2 had the most significant influence on the effectiveness of the coatings. The ±2 coded levels represent the axial (star) points.

After coating, the effects of these variables were measured for five responses: surface roughness, microhardness, fouling weight, surface free energy, and corrosion protection efficiency. A circumscribed central composite design of the response surface methodology with these parameters was constructed using MINITAB 22 software, considering the default distance α of the axial points from the center to be 2. Thirty experimental runs were conducted.

Table 4.2 Input parameters and their levels.

Factors	Units	Code	Levels				
			-2	-1	0	1	2
Nickel sulfate ($NiSO_4.6H_2O$)	g/L	Ni	2.5	15	27.5	40	52.5
Sodium hypophosphite ($NaH_2PO_2.H_2O$)	g/L	P	17.5	25	32.5	40	47.5
Sodium tungstate ($Na_2WO_4.2H_2O$)	g/L	W	7.5	15	22.5	30	37.5
Cerium sulfate ($Ce(SO_4)_2.4H_2O$)	mg/L	Ce	0	4	8	12	16

4.2 Response measurement

The surface roughness of the coated samples was measured by using a Mitutoyo SJ-210 contact-type surface profilometer. The arithmetical mean roughness value (Ra) was recorded with a cutoff length (λc) of 0.8 mm and a measuring speed of 0.5 mm/s, as per ISO 1997 standards. Five measurements were taken at different locations on each sample and the average was calculated as the final Ra value.

The microhardness values of the coatings were measured using a Vickers microhardness tester (UHL VMHT). A load of 50 gf was applied with a dwell time of 12 s and speed of 25 μm/s. Similar to the surface roughness measurements, five readings were obtained for each specimen and the average was used as the final microhardness value.

To evaluate the antifouling performance, the coated samples and substrate were boiled in normal tap water with a total dissolved solids (TDS) value of 2460 ppm for 20 h at the Surface Engineering Laboratory at Jadavpur University, Kolkata, following procedures adopted by previous researchers [118,144]. Samples were collected at 4-hour intervals, dried, and weighed using a precision balance with a resolution of 0.1 mg. The fouling rate was determined based on the weight gain due to the fouling deposits. The surface morphology of the adhered fouling was examined using FESEM in the backscattered imaging mode, and elemental mapping of the deposits was performed using EDS.

The surface free energy of the solid samples was calculated using the Owens and Wendt geometric mean approach, which considers the dispersion and polar components of surface energy. The dispersion energy is associated with Van der Waals forces, whereas the polar energy corresponds to interactions, such as hydrogen bonding. Contact angles of two test liquids, distilled water (y_L=72.8 mN/m, y^d=21.8 mN/m, y^p=51 mN/m) and ethylene glycol (y_L=48 mN/m, y^d=29 mN/m, y^p=19 mN/m), were measured on the coated and substrate

samples using a KYOWA Interface Measurement and Analysis System (FAMAS). The average of three contact angle measurements at room temperature (300 K) was used to calculate the surface free energy using Equations 4.1 and 4.2 [145].

$$y_L(1 + cos\,\theta) = 2(\sqrt{y_S^d y_L^d} + \sqrt{y_S^p y_L^p}) \tag{4.1}$$

$$y_S = y_S^d + y_S^p \tag{4.2}$$

Where y_L and y_S are the surface tension of the test liquid and surface free energy of the solid surface, respectively. y^d and y^p are the dispersion and polar components, respectively. θ is the contact angle between the liquid and solid surfaces.

Electrochemical measurements were conducted using a Metrohm μStat i400 potentiostat in a standard three-electrode setup comprising an Ag/AgCl reference electrode, platinum counter electrode, and electroless Ni-W-P-Ce coated sample as the working electrode. A circular area with a diameter of 10 mm was exposed to a 3.5% NaCl solution as a corrosive medium. Open circuit potential (OCP) measurements were performed for 1 h followed by linear potentiodynamic polarization (LP) tests. LP tests were conducted by polarizing the working electrode in the cathodic and anodic directions within ±250 mV of the OCP, at a scanning rate of 2.5 mV/s. The Dropview software (Metrohm, India) was used for data acquisition and analysis. The protection efficiency (PE) of the deposited coatings was calculated from the Tafel plots by finding the ratio of corrosion current density of the substrate (I_{cor}^s) to that of the coated surface (I_{cor}^c) using the relationship (Equation 4.3) [146]-

$$PE = 1 - \frac{I_{cor}^c}{I_{cor}^s} \tag{4.3}$$

4.3 Optimization using RSM

Response surface methodology (RSM) employs desirability functions [147] to optimize multiple responses by transforming each response into desirability scores ranging from 0 to 1, where 1 indicates an ideal outcome and 0 signifies an unacceptable result (Equation 4.4). These functions are tailored based on objective maximization, minimization, or targeting a specific value. For maximization, the desirability (d_i) increases linearly from a

lower threshold (L) to the target (T) and remains at 1 beyond T, whereas for minimization, the function is inverted.

$$d_i = \begin{Bmatrix} 0 & if\ y_i < L \\ \frac{y_i - L}{T - L} & if\ L \le y_i \le T \\ 1 & if\ y_i > T \end{Bmatrix} \tag{4.4}$$

Where y_i is the response variable of interest for the i-th response. The overall desirability (D) for multiple responses is calculated using the geometric mean of the individual desirability scores (Equation 4.5), ensuring that the overall desirability is zero if any response is undesirable.

$$D = (d_1 . d_2 \ldots . d_m)^{1/m} \tag{4.5}$$

Where 'm' is the number of responses. Optimization involves maximizing D by adjusting the design variables using numerical methods such as gradient-based algorithms or direct search techniques. This approach effectively balances conflicting objectives by assigning weights to prioritize certain responses, enabling a trade-off between competing goals such as maximizing yield while minimizing cost. Visualization tools, such as contour and surface plots, aid in interpreting results, showing how desirability changes across the design space, and highlighting optimal performance regions. This methodology facilitates a systematic and flexible approach for multi-objective optimization.

4.4 Optimization using hybrid ANN-based metaheuristic algorithms

Multi-objective optimization was performed using three hybrid ANN-based metaheuristic algorithms: teaching learning-based optimization (TLBO), whale optimization algorithm (WOA), and red fox optimization (RFO), as illustrated in the flowchart (Figure 4.1). A weighted sum method was used to convert multiple objectives into a single scalar objective, using predetermined weights. This method simplifies the optimization process by combining various objectives into a single-value function, allowing the use of standard optimization techniques. In surface engineering, scalarization aids material selection by balancing properties, such as thickness, adhesion, and cost [148].

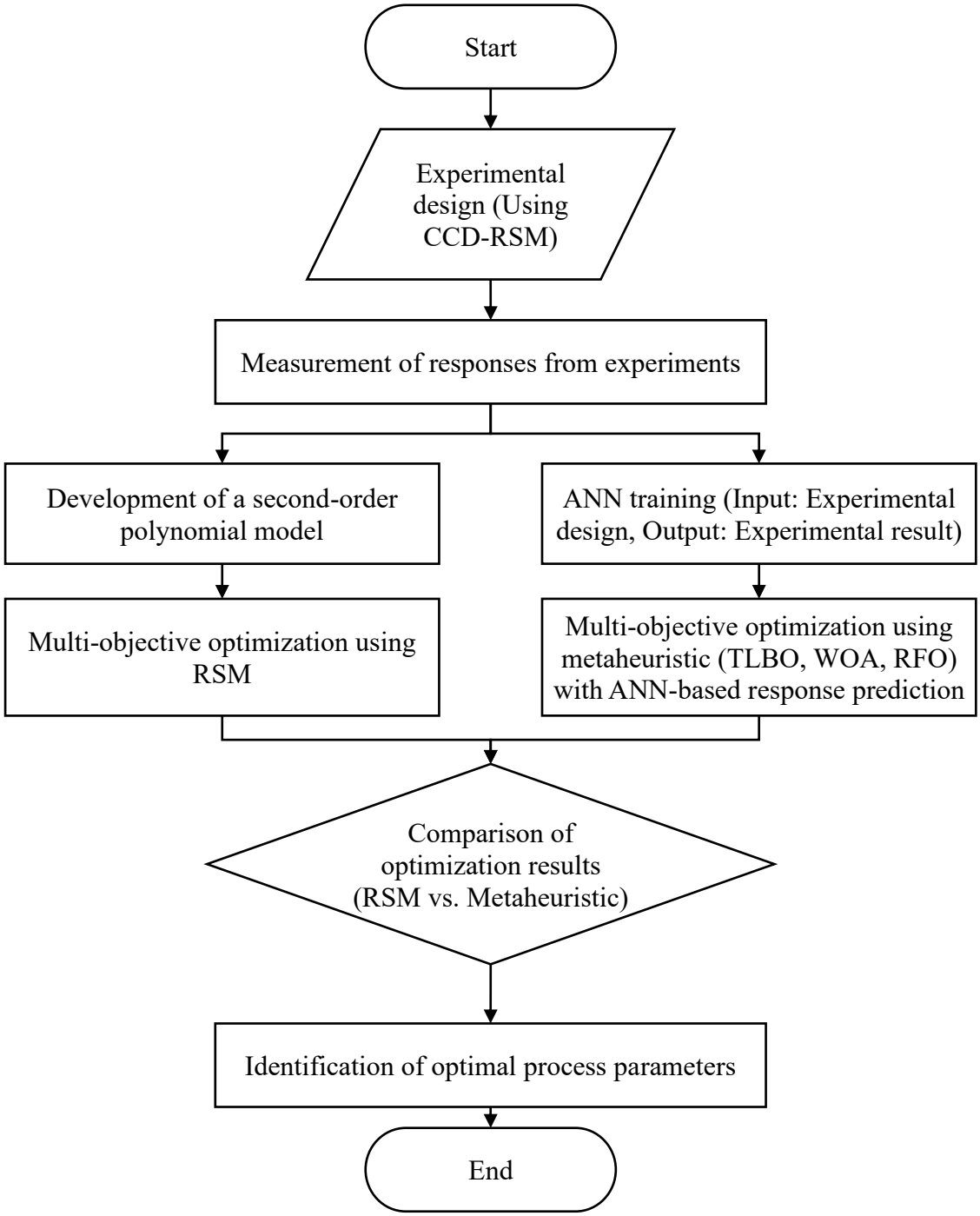

Figure 4.1. Flowchart of the optimization process for the Ni-W-P-Ce coatings.

The problem formulation is as follows:

$$\text{Weights: } w = (w_1, w_2, \ldots . w_m),$$

$$\sum_{i=1}^{m} w_i = 1 \tag{4.6}$$

$$Minimize(or\ Maximize)\ F_{weighted}(X) = \sum_{i=1}^{m} w_i f_i(X) \quad (4.7)$$

where w_i is the weight assigned to the i-th objective function. The weights indicate the relative importance of each objective, which is typically based on the preferences of the decision-maker. These weights dictate the trade-offs between objectives, and varying them can lead to different optimal solutions, thereby facilitating exploration of the Pareto front [149,150].

The ANN trained on the RSM-designed experimental data was integrated into all the three algorithms. Unlike conventional approaches that rely on second-order objective functions to calculate the response values within optimization algorithms, this hybrid implementation utilizes the ANN model to compute the response values. This innovation enhances parameter optimization and response prediction in complex engineering problems where traditional mathematical modeling poses challenges. The hybrid methodologies ANN-TLBO, ANN-WOA, and ANN-RFO were implemented programmatically in MATLAB R2023a. The complete MATLAB script used for conducting the multi-objective optimization is provided in the Appendix. Population sizes of 100 and 50 iterations were chosen to evaluate the consistency of the results across all the three hybrid algorithms.

The ANN employed in this study was a cascade-forward neural network [151], characterized by its feedforward connections and additional direct links between the input and subsequent layers. The architecture of the cascade-forward ANN is shown in Figure 4.2. The network architecture comprises five hidden layers with sizes of 15, 12, 10, 8, and 6 neurons, respectively. The input and output layer sizes were not explicitly specified in the training script because they were determined using the dataset used. The training algorithm utilized is the Levenberg-Marquardt (‘trainlm’) algorithm, which is well-suited for function approximation and regression tasks due to its efficiency and robustness. The activation functions used in the network include the hyperbolic tangent (tansig) function for the hidden layers, which introduces nonlinearity and enables the network to model complex relationships, and the linear (purelin) function for the output layer, which ensures compatibility with regression outputs. Input and output data are preprocessed using the ‘removeconstantrows’ and ‘mapminmax’ functions to enhance training stability and performance.

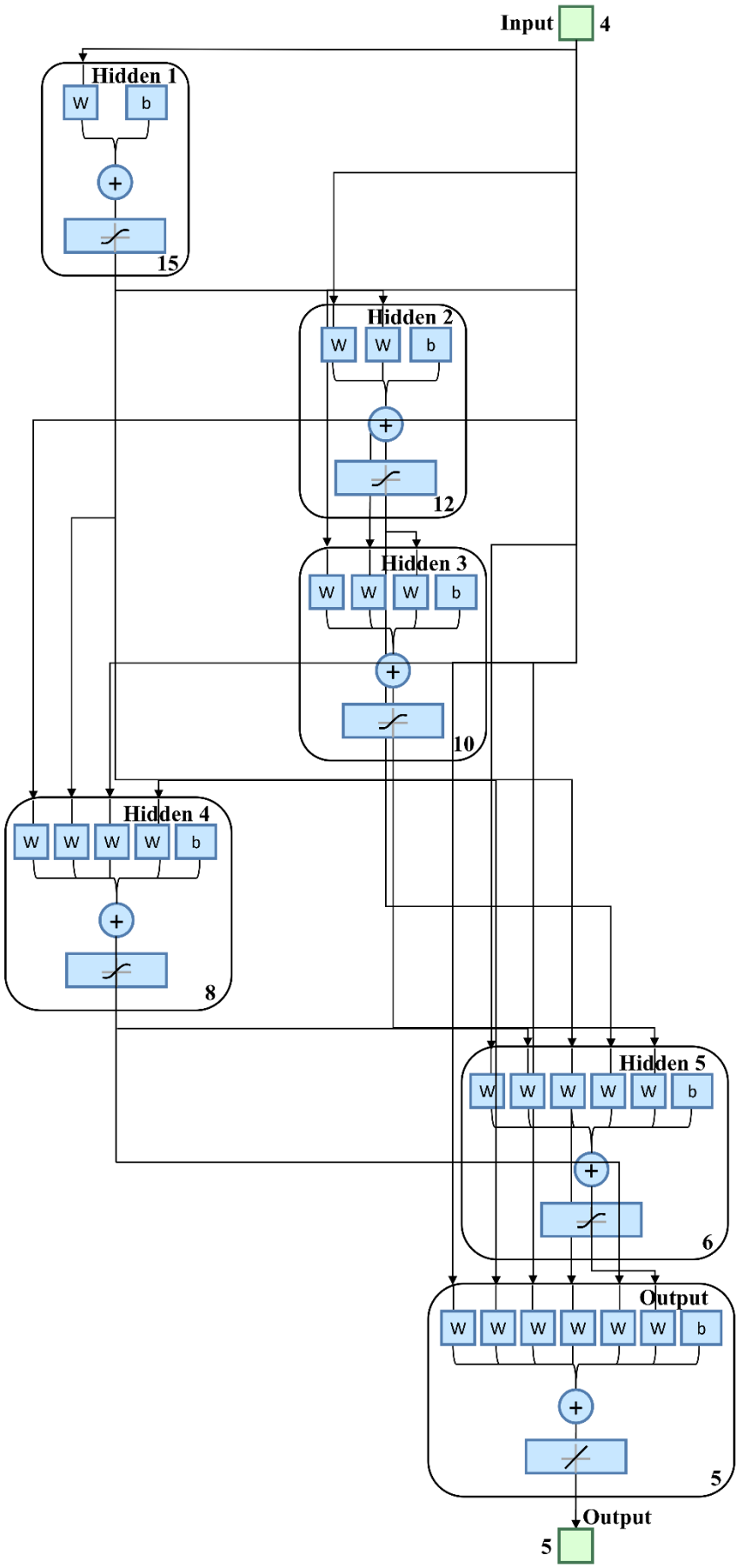

Figure 4.2. Cascade-forward ANN model for response prediction.

The training process was governed by several parameters: a maximum of 1000 epochs, performance goal of 1×10^{-7}, minimum gradient of 1×10^{-9}, and maximum of 40 validation checks. The learning rate was initialized at 0.00005 and dynamically adjusted during training, with a decrease factor of 0.15, increase factor of 1.2, and maximum allowable learning rate of 1×10^{5}. The regularization was incorporated using an L2 regularization parameter of 0.0003 to prevent overfitting. The dataset was divided into training, validation, and test subsets with ratios of 0.75, 0.15, and 0.10. The weights were initialized using an improved weight initialization method to enhance convergence. Additionally, parallel processing is enabled by leveraging the available computational resources to expedite training.

To enhance the performance of the ANN and reduce the best validation performance (mean squared error), all response values were normalized prior to training. This normalization process ensures that each output lies on a consistent numerical scale, thereby preventing any single response from disproportionately influencing the loss function owing to the scale differences. It effectively reduces the high MSE values arising from magnitude mismatches, facilitates faster convergence, and improves the generalization capability of the network. Normalization was performed using the min–max scaling technique, defined as

$$x_{norm} = \frac{x - x_{min}}{x_{max} - x_{min}} \tag{4.8}$$

Where x is the original response value. x_{min}, x_{max} are the minimum and maximum values for each response across the dataset, respectively. x_{norm} is the normalized value in the range [0,1].

Once the ANN model was trained, the predicted outputs (in normalized form) were converted back to their original scale for proper interpretation. This conversion was performed via a denormalization process using Equation 4.9.

$$x = x_{norm} \times (x_{max} - x_{min}) + x_{min} \tag{4.9}$$

The objective function plays a critical role in evaluating ANN performance based on the input and desired output values. It calculates a weighted sum of responses, prioritizing specific objectives through the assigned weights. Positive weights ($w = 0.2$) were used for responses to be minimized, whereas negative weights ($w = -0.2$) were assigned to

responses to be maximized. The objective function normalizes the inputs as required and provides a quantitative metric for the optimization performance, effectively guiding the algorithms toward optimal solutions.

The final optimal solution is determined using the following structured selection process:

Non-dominated solution identification: Non-dominated solutions were identified from the final population using Pareto dominance criteria. A solution was considered non-dominated if no other solution outperformed it across all objectives.

Normalization and scoring: The identified solutions were normalized on a scale of [0, 1] using the following formula:

$$Normalized\ Value = \frac{Value - Min}{Max - Min} \tag{4.10}$$

Compromise solution selection: For each normalized solution, the sum of all normalized objectives was calculated. The solution with the minimum sum is selected as the final optimal solution, ensuring a balanced trade-off across all objectives. This approach ensures that the selected solution is Pareto optimal, unbiased by the original objective scales, and represents the optimal compromise.

The Pareto front, representing non-dominated solutions, was visualized using a modified RadVis technique [152]. The objectives were normalized and the solutions were projected onto a 2D plane using the RadVis projection method. To enhance the interpretability of the visualization, the solutions were color coded based on the first objective value, effectively creating a pseudo-third dimension through color intensity. This 2D projection with color mapping provides an intuitive way to observe the trade-offs among objectives, where the spatial distribution of points represents the relationships between different solutions and the color gradient indicates performance in terms of the first objective. Although this approach simplifies the traditional 3D-RadVis visualization, it maintains essential information about the Pareto front structure and enables an effective analysis of the multi-objective optimization results.

Sensitivity analyses were conducted to assess the influence of input variables on the output responses. Local and global sensitivity analyses were performed using the results of the metaheuristic algorithms.

Local sensitivity analysis (one-at-a-time): This method evaluates the effect of small perturbations in individual input variables on the outputs. For each input, perturbed input vectors were generated with ±1% change, and the local sensitivity index was calculated using the following formula:

$$Local\ SI = \frac{Output_{Plus} - Output_{Minus}}{2 \times \delta \times Nominal\ Value} \tag{4.11}$$

Global sensitivity analysis (Sobol method): This variance-based approach [153] quantifies the contribution of each input variable to output variability across the input space. Using the sampled data, first-order Sobol indices were calculated for each input-output pair as follows:

$$Global\ SI = 1 - \frac{Variance_{Perturbed}}{Variance_{Unperturbed}} \tag{4.12}$$

Heatmaps and bar charts were used to visualize the sensitivity indices, providing insights into the relative significance of the input parameters. These visualizations facilitated comparisons and informed parameter prioritization for optimization.

4.4.1 Teaching-learning-based optimization

The TLBO algorithm, as illustrated in Figure 4.3, was implemented in two main phases: teacher and learner. Initially, a population of candidate solutions (students) was generated and their objective function values were evaluated. In the Teacher Phase, the best-performing individual was considered as the teacher, and the mean of the population was adjusted based on the teacher's influence to guide students toward better solutions. In the subsequent Learner Phase, students interacted with one another to improve their knowledge by comparing their performance and updating their solutions accordingly. This iterative process continues until the convergence criteria are met, thereby optimizing the desired coating parameters [154,155].

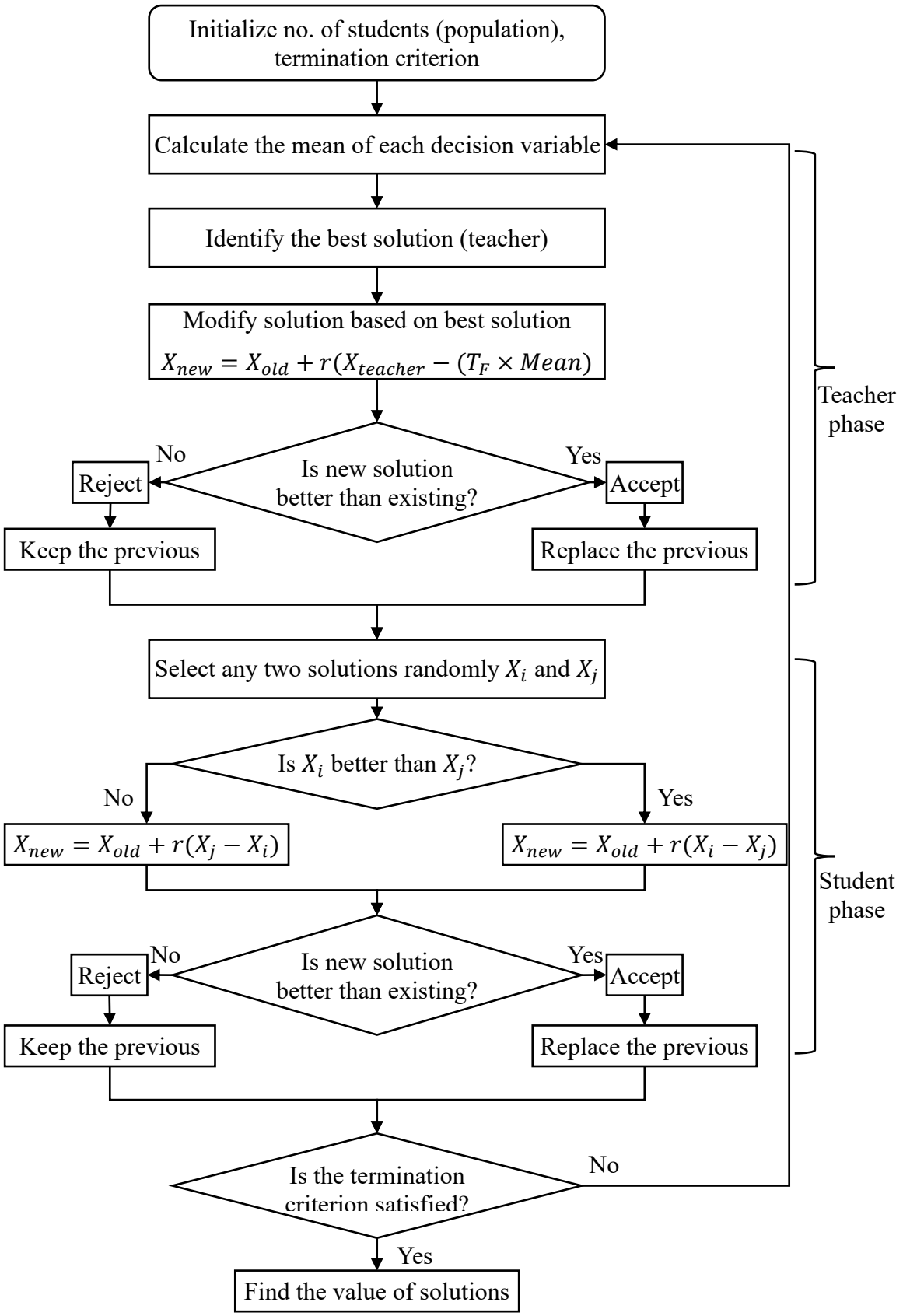

Figure 4.3. Flowchart illustrating the working mechanism of the TLBO algorithm.

4.4.2 Whale optimization

As illustrated in Figure 4.4, the WOA is implemented by initializing a population of whales (candidate solutions) and evaluating their fitness. The best-performing agent is identified, and the control parameters a, A, C, l, and p are updated for each iteration. Depending on the value of p, the whales either engaged in exploitation (using encircling or spiral mechanisms) or exploration (searching for prey). The whale positions were then updated accordingly and their fitness was recalculated. If a better solution is obtained, then the current best solution is replaced. This process continues until the maximum number of iterations is reached, at which point the best solution is returned [156].

4.4.3 Red fox optimization

As shown in Figure 4.5, the RFO algorithm is implemented by initializing a population of red foxes and evaluating their fitness. The best-performing fox was identified, and the positions of other foxes were updated based on natural behaviors such as hunting, hiding, and escaping predators. These behaviors were mathematically modeled to balance exploration and exploitation during the search process. The positions of the foxes were iteratively refined and the fitness was recalculated in each iteration. The algorithm continues until the maximum number of iterations is reached, ultimately yielding the best solution [157].

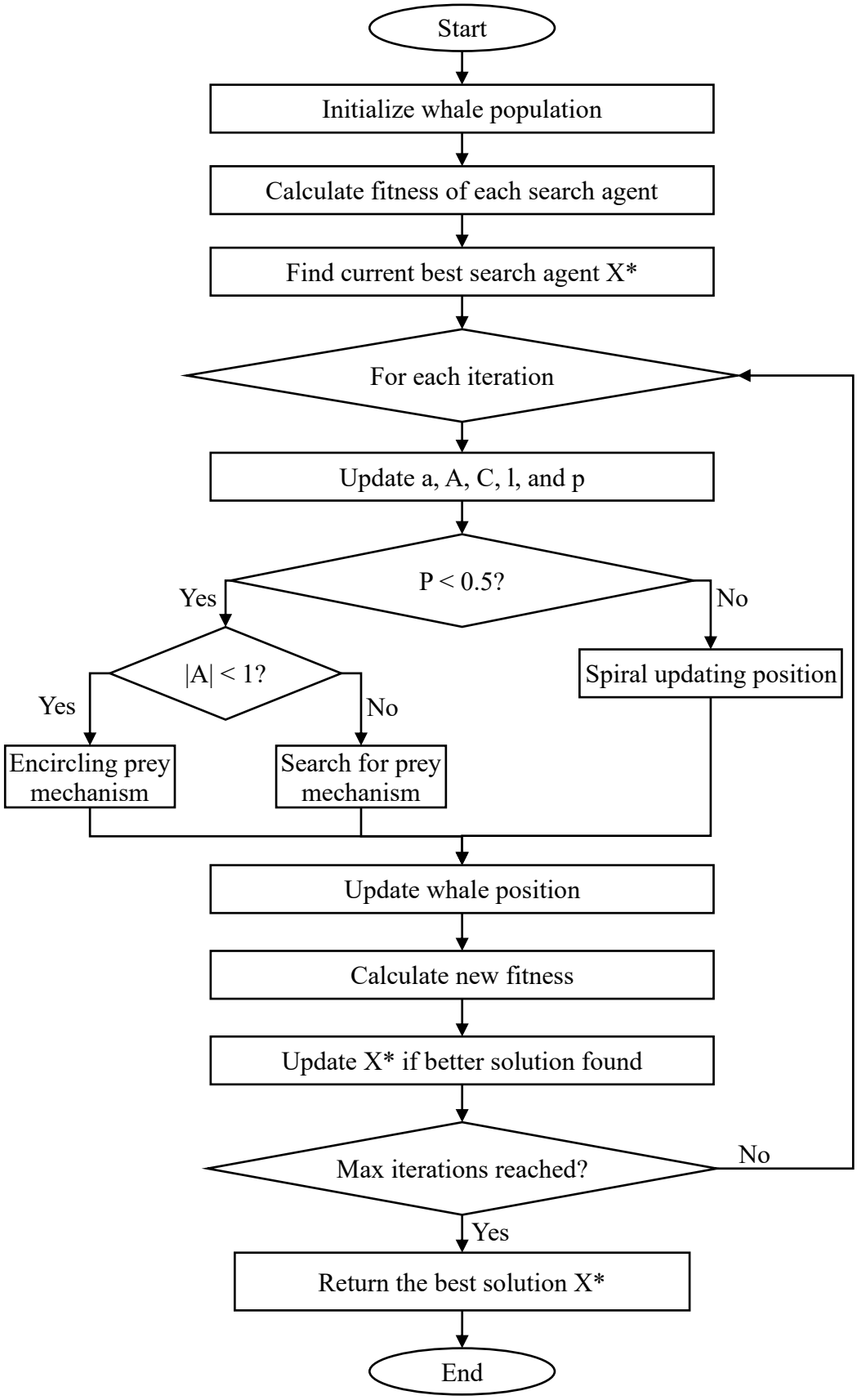

Figure 4.4. Flowchart of the whale optimization algorithm.

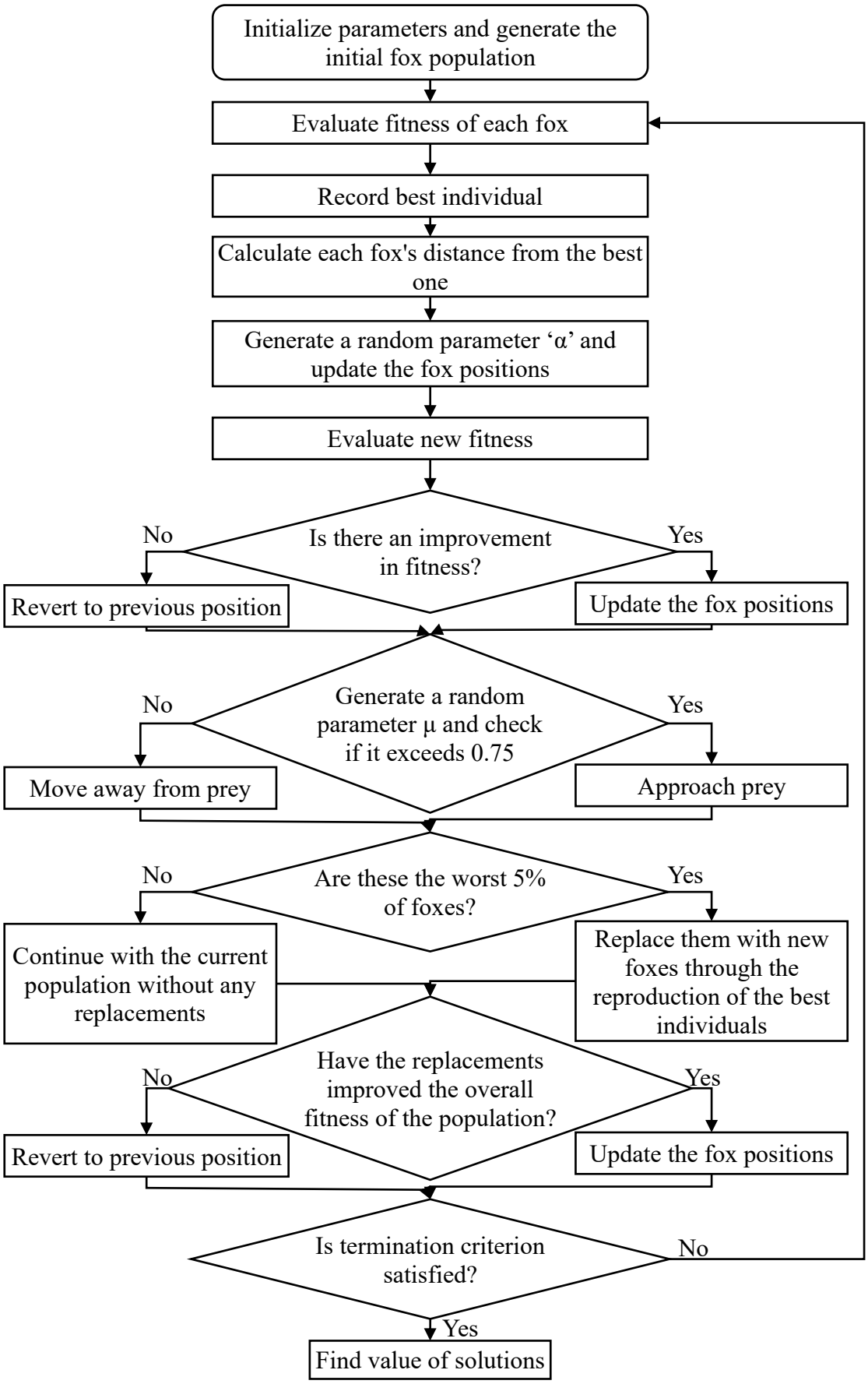

Figure 4.5. Flowchart of the red fox algorithm.

4.5 Results and discussion

The experimental results from all 30 trials, including the influencing factors and their corresponding values for the five key responses (surface roughness, microhardness, fouling weight, surface free energy, and corrosion protection efficiency), are summarized in Table 4.3. Analysis of the data revealed the performance range for each response across different experimental runs.

Surface roughness varied between 0.23 μm in the 22nd run and 1.28 μm in the 19th run, with lower values being preferred for better coating quality. Although the 22nd run achieved the best surface roughness, its performance in other key responses was not as favorable, indicating that an optimal balance was not achieved in that trial. Vickers microhardness ranged from 329.08 HV 0.05 (7th run) to 689.76 HV 0.05 (13th run), with higher values being desirable for enhanced mechanical strength. While the 13th run demonstrated the highest microhardness, it did not perform well in terms of surface roughness, fouling, or corrosion resistance, suggesting that hardness alone does not guarantee the overall coating performance. Fouling weight ranged from a minimum of 59.01 g/m^2 in the 6th run to a maximum of 110.11 g/m^2 in the 19th run. Surface free energy values spanned from 15.02 J/m^2 (6th run) to 34.15 J/m^2 (30th run). The 6th run performed notably well in both fouling resistance and surface free energy, two critical indicators for antifouling and wettability characteristics, although its performance in other responses was moderate. The corrosion protection efficiency ranged from 45.01% in the 7th run to 94.21% in the 15th run, with higher values indicating superior protection. The 15th run demonstrated excellent corrosion resistance, yet its performance in other key parameters, such as surface roughness and microhardness, was less impressive.

These observations indicate that no single run excelled in all five responses simultaneously, underscoring the need for multi-objective optimization to identify process conditions that yield balanced and high-performance coatings across all critical parameters.

Table 4.3. Experimental results for surface roughness, microhardness, fouling weight, surface free energy, and protection efficiency.

	Factors				Responses				
Run no.	Nickel sulfate	Sodium hypophosphite	Sodium tungstate	Cerium sulfate	Surface roughness (μm)	Microhardness (HV 0.05)	Fouling weight (g/m^2)	Surface free energy (J/m^2)	Protection efficiency (%)
1	40.0	40.0	15.0	4	0.40	635.75	69.10	21.35	91.74
2	15.0	25.0	30.0	12	1.06	391.08	101.53	33.05	55.26
3	15.0	25.0	15.0	4	0.67	502.68	83.40	24.35	67.78
4	40.0	25.0	15.0	12	0.31	654.25	59.09	17.06	93.11
5	27.5	32.5	22.5	8	0.25	666.76	67.20	18.28	87.63
6	27.5	32.5	22.5	8	0.28	662.13	59.01	15.02	91.61
7	15.0	40.0	30.0	4	1.18	329.08	108.88	34.00	45.01
8	40.0	25.0	30.0	4	0.72	535.44	85.80	23.74	72.81
9	15.0	40.0	15.0	12	0.73	463.17	93.17	26.35	67.94
10	40.0	40.0	30.0	12	0.88	482.02	88.91	26.64	68.89
11	27.5	32.5	22.5	8	0.28	662.11	67.09	19.10	86.22
12	40.0	40.0	30.0	4	0.68	462.50	88.28	26.54	65.73
13	40.0	25.0	15.0	4	0.30	689.76	61.79	18.33	91.38
14	40.0	40.0	15.0	12	0.42	640.34	70.08	20.23	84.41
15	27.5	32.5	22.5	8	0.31	631.51	68.81	19.27	94.21

16	15.0	25.0	30.0	4	1.11	388.68	107.98	32.06	54.68
17	15.0	40.0	15.0	4	0.89	457.19	91.48	25.02	63.31
18	40.0	25.0	30.0	12	0.66	544.68	81.11	26.69	75.54
19	15.0	40.0	30.0	12	1.28	347.99	110.11	33.90	52.69
20	15.0	25.0	15.0	12	0.64	511.51	86.89	26.44	75.85
21	27.5	32.5	22.5	8	0.37	676.09	66.02	19.26	85.40
22	52.5	32.5	22.5	8	0.23	664.73	65.44	17.73	88.12
23	27.5	32.5	22.5	16	0.78	519.92	89.29	26.01	73.21
24	27.5	32.5	22.5	8	0.34	665.40	66.08	19.85	87.54
25	27.5	47.5	22.5	8	0.83	446.81	93.50	29.21	64.55
26	27.5	17.5	22.5	8	0.67	538.51	83.22	22.99	78.43
27	27.5	32.5	7.5	8	0.31	607.91	65.53	19.51	86.97
28	27.5	32.5	37.5	8	1.08	332.89	105.70	33.15	50.22
29	27.5	32.5	22.5	0	0.83	501.44	83.91	26.04	61.37
30	2.5	32.5	22.5	8	1.14	356.81	106.35	34.15	47.69

4.5.1 Response surface analysis

4.5.1.1 Effect of input parameters on responses

The main effects of the input parameters on the five responses were analyzed to optimize the electroless coating process. Figure 4.6 illustrate these relationships, and the trends are discussed below.

As shown in Figure 4.6(a), the main effects plot highlights the variation in surface roughness with the input parameters. For nickel sulfate, the surface roughness decreased significantly as the concentration increased from 15 to approximately 40 g/L, after which it began to increase. This suggests that a moderate concentration of nickel sulfate achieves the optimal deposition conditions, balancing the nucleation and growth rates to produce a smoother surface. Higher concentrations likely disrupted this balance, resulting in rougher texture. Sodium hypophosphite exhibited a similar trend, where the surface roughness decreased to approximately 32.5 g/L but increased beyond this level. As a reducing agent, sodium hypophosphite enabled uniform deposition at moderate levels. However, excessive amounts may accelerate the nucleation rate, leading to uneven growth and a rougher texture because the grains lack sufficient time to coalesce smoothly [158]. In contrast, sodium tungstate exhibits a different trend. The surface roughness remained low at lower concentrations, but rose sharply beyond approximately 22.5 g/L. This is likely due to the formation of a coarse columnar growth pattern at higher concentrations, which alters the deposition kinetics and introduces internal stresses, resulting in surface irregularities [159]. Cerium sulfate also exhibited a parabolic trend, with surface roughness reaching a minimum of approximately 8 mg/L. Cerium acts as a grain refiner and promotes a uniform coating. However, at higher concentrations, the agglomeration of small CeO_2 and Ce_2O_3 crystallites increases surface roughness [160,161].

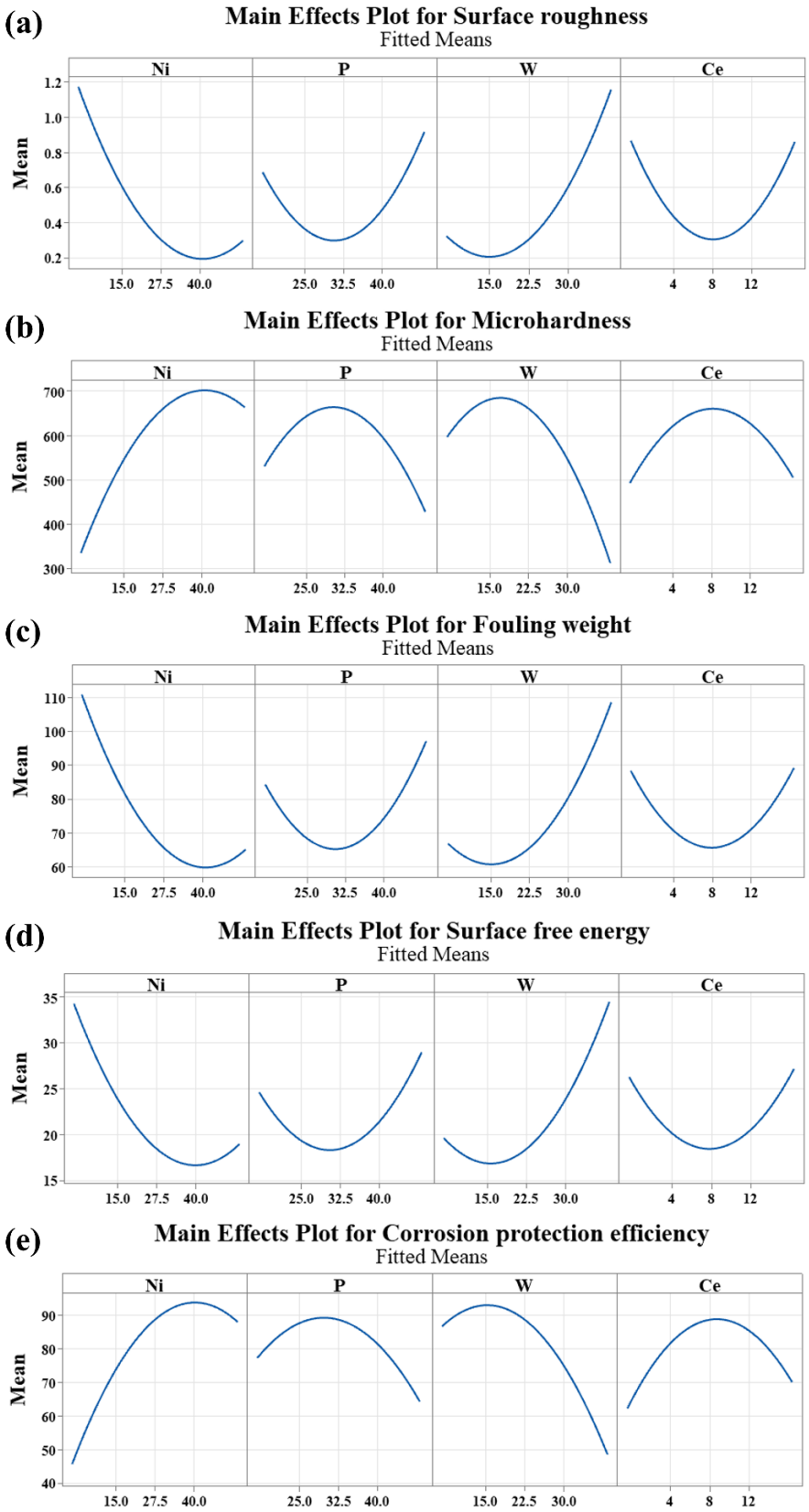

Figure 4.6. Main effect plots of Ni, P, W, and Ce on (a) surface roughness, (b) microhardness, (c) fouling weight, (d) surface free energy, and (e) protection efficiency.

Figure 4.6(b) reveals distinct trends for the input parameters that affect the microhardness. For nickel sulfate, the microhardness increased with the concentration, peaking at approximately 40 g/L before declining. This suggests an optimal Ni concentration for the formation of a dense, hard Ni matrix. Excessive nickel sulfate may lead to rapid deposition, reducing coating uniformity and creating a porous structure associated with lower hardness [162]. Sodium hypophosphite also showed an increasing–decreasing trend, with a peak within the tested range. As a reducing agent, it facilitates nickel deposition and enhances hardness; however, higher concentrations may introduce excessive phosphorus, affecting the structural integrity [158]. Sodium tungstate exhibited a peak at approximately 22.5 g/L, likely owing to the formation of a tungsten-nickel alloy phase. Beyond this concentration, the microhardness decreases as microcracks form, driven by the internal stresses caused by excess tungsten [163]. Cerium sulfate exhibited a moderate peak at approximately 8 mg/L, after which its hardness decreased. Optimal cerium levels refine the microstructure, whereas excessive amounts lead to agglomeration, reducing hardness [160,161].

Optimization of the coating parameters can minimize fouling, as illustrated in Figure 4.6(c). For nickel sulfate, fouling weight decreases steeply from 15.0 to around 27.5 g/L, then stabilizes. A uniform, smooth surface with lower surface energy reduces fouling by minimizing the adhesion of foulants [164]. Sodium hypophosphite followed a similar trend, with a minimum fouling weight of approximately 32.5 g/L. Optimal concentrations promote a compact structure, whereas higher concentrations may result in excessive phosphorus, rougher surfaces, or structural defects, thereby increasing fouling [158]. Conversely, sodium tungstate exhibits an increase in fouling weight with increasing concentration, which is attributed to its reduced thermal conductivity and higher surface energy. These factors enhance adhesion and create an environment conducive to fouling [165]. Cerium sulfate displayed a parabolic trend, with minimum fouling at approximately 8 mg/L. Excessive cerium leads to agglomeration, disruption of deposition, and increasing fouling [121].

Figure 4.6(d) shows that the SFE declined steeply with increasing nickel sulfate concentration, reaching a minimum at 27.5 g/L. This decrease is linked to smoother and denser surfaces with fewer molecular interactions [166]. Sodium hypophosphite exhibited a similar trend, with SFE stabilizing beyond 32.5 g/L. Excess phosphorus increases the SFE owing to changes in surface composition and structure [167]. In contrast, sodium tungstate

increased SFE with increasing concentration. Higher tungsten levels alter the surface morphology and chemical composition by introducing polar functional groups that enhance SFE [168]. Cerium sulfate followed a parabolic trend with a minimum SFE of 8 mg/L. Beyond this level, cerium agglomeration leads to rougher surfaces and higher SFE.

Figure 4.6(e) shows that nickel sulfate increased the efficiency to 40 g/L, after which it declined. Higher nickel sulfate levels enhance the deposition uniformity, but excessive amounts cause spontaneous decomposition and nickel hydroxide formation, compromising the coating quality [73]. Sodium hypophosphite exhibited a similar parabolic trend, with the efficiency peaking at 32.5 g/L. Excessive phosphorus introduces microstructural defects and reduces corrosion resistance [169]. Sodium tungstate exhibited maximum efficiency near 15 g/L. Higher concentrations result in defective passive films, thereby decreasing protection [170]. Cerium sulfate optimized the corrosion resistance to approximately 8 mg/L by enhancing the compactness and thickness of the coating. Excessive cerium introduces structural irregularities and reduces efficiency [143,171].

4.5.1.2 ANOVA and regression analysis

The significance of the input parameters for each response was evaluated using ANOVA considering their linear, quadratic (square terms), and interaction effects. The ANOVA results for the surface roughness, microhardness, fouling weight, surface free energy, and corrosion protection efficiency are listed in Tables 4.4, 4.5, 4.6, 4.7, and 4.8, respectively. Significant factors were identified by p-values less than 0.05, which are marked with an asterisk (*). The four input parameters, nickel sulfate, sodium hypophosphite, sodium tungstate, and cerium sulfate, are denoted in their coded forms as Ni, P, W, and Ce, respectively, in certain paragraphs of this chapter.

The ANOVA for surface roughness indicated that Ni and W were the most influential factors, with their linear and quadratic terms exhibiting high statistical significance ($p = 0.000$). This demonstrates the critical role of these elements in determining the surface roughness. Furthermore, the interaction between Ni and Ce was significant, suggesting a synergistic effect between these factors on surface roughness. The model provided an excellent fit, as evidenced by an R^2 value of 98.64%, indicating its ability to accurately capture the variability in surface roughness. The non-significant lack of fit supports the adequacy of the model in explaining the observed variation.

Table 4.4. ANOVA for surface roughness.

Source	DF	Adjusted SS	Adjusted MS	F-value	P-value
Model	14	3.017	0.215	77.48	0.000*
Linear	4	2.061	0.515	185.29	0.000*
Ni	1	1.043	1.043	375.17	0.000*
P	1	0.071	0.071	25.63	0.000*
W	1	0.946	0.946	340.33	0.000*
Ce	1	0.000	0.000	0.03	0.086
Square	4	0.930	0.233	83.63	0.000*
Ni^2	1	0.262	0.262	94.20	0.000*
P^2	1	0.349	0.349	125.34	0.000*
W^2	1	0.269	0.269	96.63	0.000*
Ce^2	1	0.440	0.440	158.09	0.000*
2-Way Interaction	6	0.025	0.004	1.50	0.243
Ni×P	1	0.003	0.003	1.01	0.331
Ni×W	1	0.003	0.003	0.95	0.344
Ni×Ce	1	0.006	0.006	2.13	0.165
P×W	1	0.000	0.000	0.03	0.859
P×Ce	1	0.005	0.005	1.81	0.198
W×Ce	1	0.009	0.009	3.08	0.100
Error	15	0.042	0.003		
Lack-of-Fit	10	0.033	0.003	1.78	0.272
Pure Error	5	0.009	0.002		
Total	29	3.058			

R^2 = 0.9864, Adjusted R^2 = 0.9736, and Predicted R^2 = 0.9344.

For microhardness, the ANOVA revealed that Ni and W were the most significant factors, with both linear and quadratic terms showing extremely high F-values and p-values of 0.000. P also significantly influenced the microhardness, albeit to a lesser extent. Among the interaction terms, the combination of Ni and W showed statistical significance (p = 0.024), indicating a notable interaction effect on the microhardness. The model demonstrated a robust fit with R^2 = 99.48%, Adjusted R^2 = 99%, and Predicted R^2 = 98.26%, confirming its ability to capture the majority of the variance in microhardness. The

non-significant lack of fit (p = 0.899) further validated the suitability of the model for the data.

Table 4.5. ANOVA for microhardness.

Source	DF	Adjusted SS	Adjusted MS	F-value	P-value
Model	14	397391	28385	205.83	0.000*
Linear	4	269758	67439	489.03	0.000*
Ni	1	145580	145580	1055.65	0.000*
P	1	14183	14183	102.85	0.000*
W	1	109785	109785	796.09	0.000*
Ce	1	210	210	1.52	0.024*
Square	4	125776	31444	228.01	0.000*
Ni^2	1	36447	36447	264.29	0.000*
P^2	1	46062	46062	334.01	0.000*
W^2	1	59422	59422	430.89	0.000*
Ce^2	1	36492	36492	264.61	0.000*
2-Way Interaction	6	1857	310	2.24	0.096
Ni×P	1	3	3	0.02	0.884
Ni×W	1	866	866	6.28	0.024*
Ni×Ce	1	92	92	0.66	0.428
P×W	1	366	366	2.66	0.124
P×Ce	1	256	256	1.86	0.193
W×Ce	1	274	274	1.98	0.179
Error	15	2069	138		
Lack-of-Fit	10	917	92	0.40	0.899
Pure Error	5	1152	230		
Total	29	399460			

R^2 = 0.9948, Adjusted R^2 = 0.99, and Predicted R^2 = 0.9826.

The ANOVA results for fouling weight highlight that Ni and W are the most influential factors, with their linear terms displaying high F-values and p-values of 0.000, thus emphasizing their strong impact. P also exhibited a significant effect, although to a lesser degree. Additionally, the quadratic terms for Ni, P, W, and Ce were statistically significant (p = 0.000), underscoring the importance of the nonlinear effects. However, none of the

interaction terms was significant, indicating minimal synergistic effects among the factors. The model demonstrated excellent predictive capability, with R^2 = 98.71%, Adjusted R^2 = 97.5%, and Predicted R^2 = 95.87%.

Table 4.6. ANOVA for fouling weight.

Source	DF	Adjusted SS	Adjusted MS	F-value	P-value
Model	14	7590.58	542.18	81.90	0.000*
Linear	4	5422.46	1355.62	204.78	0.000*
Ni	1	2840.55	2840.55	429.09	0.000*
P	1	221.92	221.92	33.52	0.000*
W	1	2358.98	2358.98	356.34	0.000*
Ce	1	1.02	1.02	0.15	0.070
Square	4	2123.41	530.85	80.19	0.000*
Ni^2	1	704.01	704.01	106.35	0.000*
P^2	1	885.69	885.69	133.79	0.000*
W^2	1	684.69	684.69	103.43	0.000*
Ce^2	1	753.84	753.84	113.87	0.000*
2-Way Interaction	6	44.71	7.45	1.13	0.394
Ni×P	1	1.40	1.40	0.21	0.652
Ni×W	1	6.86	6.86	1.04	0.325
Ni×Ce	1	2.06	2.06	0.31	0.585
P×W	1	10.40	10.40	1.57	0.229
P×Ce	1	13.84	13.84	2.09	0.169
W×Ce	1	10.14	10.14	1.53	0.235
Error	15	99.30	6.62		
Lack-of-Fit	10	40.44	4.04	0.34	0.929
Pure Error	5	58.86	11.77		
Total	29	7689.88			

R^2 = 0.9871, Adjusted R^2 = 0.975, and Predicted R^2 = 0.9587.

Analysis of the surface free energy revealed that the main effects of Ni, P, W, and Ce, along with their quadratic terms (Ni^2, P^2, W^2, and Ce^2), were highly significant, with low p-values indicating a substantial influence on the surface free energy. However, most interaction terms were not significant, suggesting that the combined effects of these factors

did not contribute significantly to this response. The model achieved a high R^2 value of 96.93%, Adjusted R^2 of 94.06%, and Predicted R^2 of 89.33%, demonstrating its strong ability to explain and predict variations in surface free energy.

Table 4.7. ANOVA for surface free energy.

Source	DF	Adjusted SS	Adjusted MS	F-value	P-value
Model	14	924.69	66.05	33.82	0.000*
Linear	4	644.44	161.11	82.49	0.000*
Ni	1	318.50	318.50	163.08	0.000*
P	1	25.52	25.52	13.07	0.003*
W	1	299.42	299.42	153.31	0.000*
Ce	1	1.01	1.01	0.51	0.048*
Square	4	274.45	68.61	35.13	0.000*
Ni^2	1	93.89	93.89	48.07	0.000*
P^2	1	97.99	97.99	50.17	0.000*
W^2	1	104.04	104.04	53.27	0.000*
Ce^2	1	96.05	96.05	49.18	0.000*
2-Way Interaction	6	5.80	0.97	0.49	0.803
Ni×P	1	1.94	1.94	0.99	0.335
Ni×W	1	1.11	1.11	0.57	0.463
Ni×Ce	1	0.83	0.83	0.43	0.524
P×W	1	0.10	0.10	0.05	0.829
P×Ce	1	1.29	1.29	0.66	0.428
W×Ce	1	0.53	0.53	0.27	0.610
Error	15	29.30	1.95		
Lack-of-Fit	10	13.79	1.38	0.44	0.871
Pure Error	5	15.50	3.10		
Total	29	953.98			

R^2 = 0.9693, Adjusted R^2 = 0.9406, and Predicted R^2 = 0.8933.

The ANOVA for corrosion protection efficiency showed that the main effects and quadratic terms (Ni^2, P^2, W^2, and Ce^2) were highly significant, with p-values below 0.05, highlighting their strong impact on corrosion resistance. Similar to the surface free energy, most two-way interaction terms were insignificant, indicating a limited synergistic effect.

The model exhibited excellent performance, with R^2 = 97.90%, Adjusted R^2 = 95.95%, and Predicted R^2 = 91.7%, confirming its robustness in explaining and predicting corrosion protection efficiency.

Table 4.8. ANOVA for corrosion protection efficiency.

Source	DF	Adjusted SS	Adjusted MS	F-value	P-value
Model	14	6518.58	465.61	50.01	0.000*
Linear	4	4741.84	1185.46	127.34	0.000*
Ni	1	2439.16	2439.16	262.00	0.000*
P	1	230.95	230.95	24.81	0.000*
W	1	1987.62	1987.62	213.50	0.000*
Ce	1	84.11	84.11	9.04	0.009*
Square	4	1736.46	434.11	46.63	0.000*
Ni^2	1	673.51	673.51	72.35	0.000*
P^2	1	451.91	451.91	48.54	0.000*
W^2	1	627.44	627.44	67.40	0.000*
Ce^2	1	715.95	715.95	76.90	0.000*
2-Way Interaction	6	40.28	6.71	0.72	0.639
Ni×P	1	0.41	0.41	0.04	0.837
Ni×W	1	6.80	6.80	0.73	0.406
Ni×Ce	1	26.70	26.70	2.87	0.111
P×W	1	1.72	1.72	0.19	0.673
P×Ce	1	1.54	1.54	0.17	0.690
W×Ce	1	3.11	3.11	0.33	0.572
Error	15	139.64	9.31		
Lack-of-Fit	10	81.31	8.13	0.70	0.707
Pure Error	5	58.33	11.67		
Total	29	6658.23			

R^2 = 0.979, Adjusted R^2 = 0.9595, and Predicted R^2 = 0.917.

The relationships between the input parameters and responses were evaluated using regression equations developed based on quadratic models. These equations provide mathematical representations of the system and facilitate the prediction of responses. The adequacy of the regression models was assessed using statistical parameters such as the

coefficient of determination (R^2), adjusted R^2, and predicted R^2, along with the analysis of residuals. A detailed discussion of each response is provided below. The coefficient of determination (R^2) represents the proportion of variance in the dependent variable explained by the model, with values close to one indicating a strong fit. The adjusted R^2 enhances the R^2 measure by accounting for the number of predictors in the model and mitigates the risk of overfitting by decreasing when unnecessary predictors are included. The predicted R^2, typically calculated through cross-validation, evaluates the ability of the model to generalize new data, making it an essential metric for assessing the performance beyond the training dataset [147].

The regression equation for the surface roughness is given by Equation (4.13). The model exhibited an R^2 value of 0.9864, indicating an excellent fit to the experimental data points that closely aligned with the regression curve. The adjusted R^2 and predicted R^2 values were 0.9736 and 0.9344, respectively, and the difference between these values was less than 0.2, confirming the reliability and accuracy of the model. The normal probability plot of the residuals for the surface roughness, shown in Figure 4.7(a), demonstrates that the residuals follow a near-linear trend, suggesting that they are approximately normally distributed. This observation further validates the adequacy of the model for predicting surface roughness. A high R^2 value indicates that the model explains a significant proportion of the variance in the surface roughness, whereas the adjusted R^2 ensures minimal overfitting by accounting for the number of predictors. The predicted R^2 value highlights the generalization capability of the model for new data.

The regression equation for the microhardness is given in Equation 4.14. The R^2 value for microhardness was 0.9948, confirming the strong fit of the quadratic model to the experimental data. The adjusted R^2 and predicted R^2 values were 0.9900 and 0.9826, respectively, with a difference of less than 0.2, indicating a high model accuracy. The normal probability plot of the microhardness residuals shown in Figure 4.7(b) reveals that most of the residuals aligned closely along a straight line, suggesting a normal distribution. These findings validate the ability of the model to reliably predict microhardness based on the input parameters.

The regression equation for the fouling weight is shown in Equation 4.15. An R^2 value of 0.9871 indicated a robust fit of the quadratic model to the experimental data. The adjusted R^2 and predicted R^2 values were 0.9750 and 0.9587, respectively, with a difference

of less than 0.2, supporting the accuracy and reliability of the model. The normal probability plot of the residuals for the fouling weight, shown in Figure 4.7(c), demonstrates that the residuals closely followed a straight line, indicating an approximately normal distribution. These results confirm the adequacy of the model for predicting the fouling weight.

The regression equation for the surface free energy is given by Equation 4.16. The R^2 value of 0.9693 indicated a strong fit of the quadratic model to the experimental data. The adjusted R^2 and predicted R^2 values were 0.9406 and 0.8933, respectively, with a difference of less than 0.2, which validated the accuracy of the model. The normal probability plot of the residuals for the surface free energy depicted in Figure 4.7(d) shows that the residuals follow a near-linear trend, suggesting a normal distribution. These observations confirm the robustness of the model in capturing the relationship between the input parameters and surface free energy.

$$\begin{aligned} Surface\ roughness \\ &= 4.058 - 0.04648Ni - 0.1229P - 0.0537W - 0.1742Ce \\ &+ 0.000625Ni^2 + 0.002004P^2 + 0.00176W^2 \\ &+ 0.007913Ce^2 - 0.000141NiP - 0.000137NiW \\ &+ 0.000385NiCe - 0.000042PW + 0.000592PCe \\ &+ 0.000771WCe \end{aligned} \tag{4.13}$$

$$\begin{aligned} Microhardness \\ &= -785 + 21.36Ni + 45.09P + 32.04W + 31.09Ce \\ &- 0.2333Ni^2 - 0.7285P^2 - 0.8275W^2 - 2.28Ce^2 \\ &- 0.0047NiP - 0.0785NiW - 0.0479NiCe - 0.085PW \\ &+ 0.1334PCe + 0.1379WCe \end{aligned} \tag{4.14}$$

$$\begin{aligned} Fouling\ weight \\ &= 241.8 - 2.856Ni - 6.173P - 2.189W - 5.4Ce \\ &+ 0.03242Ni^2 + 0.10102P^2 + 0.08882W^2 + 0.3277Ce^2 \\ &+ 0.00316NiP + 0.00699NiW - 0.0072NiCe - 0.0143PW \\ &+ 0.031PCe - 0.0265WCe \end{aligned} \tag{4.15}$$

$$Surface\ free\ energy = 78.67 - 0.964Ni - 2.042P - 1.014W - 1.523Ce + 0.01184Ni^2 + 0.0336P^2 + 0.03462W^2 + 0.117Ce^2 + 0.00371NiP - 0.00281NiW - 0.00456NiCe - 0.00137PW - 0.0095PCe + 0.0061WCe \quad (4.16)$$

$$Protection\ efficiency = -72.9 + 2.859Ni + 4.444P + 2.876W + 6.29Ce - 0.03171Ni^2 - 0.0722P^2 - 0.085W^2 - 0.3193Ce^2 + 0.0017NiP - 0.00695NiW - 0.0258NiCe - 0.0058PW - 0.0104PCe + 0.0147WCe \quad (4.17)$$

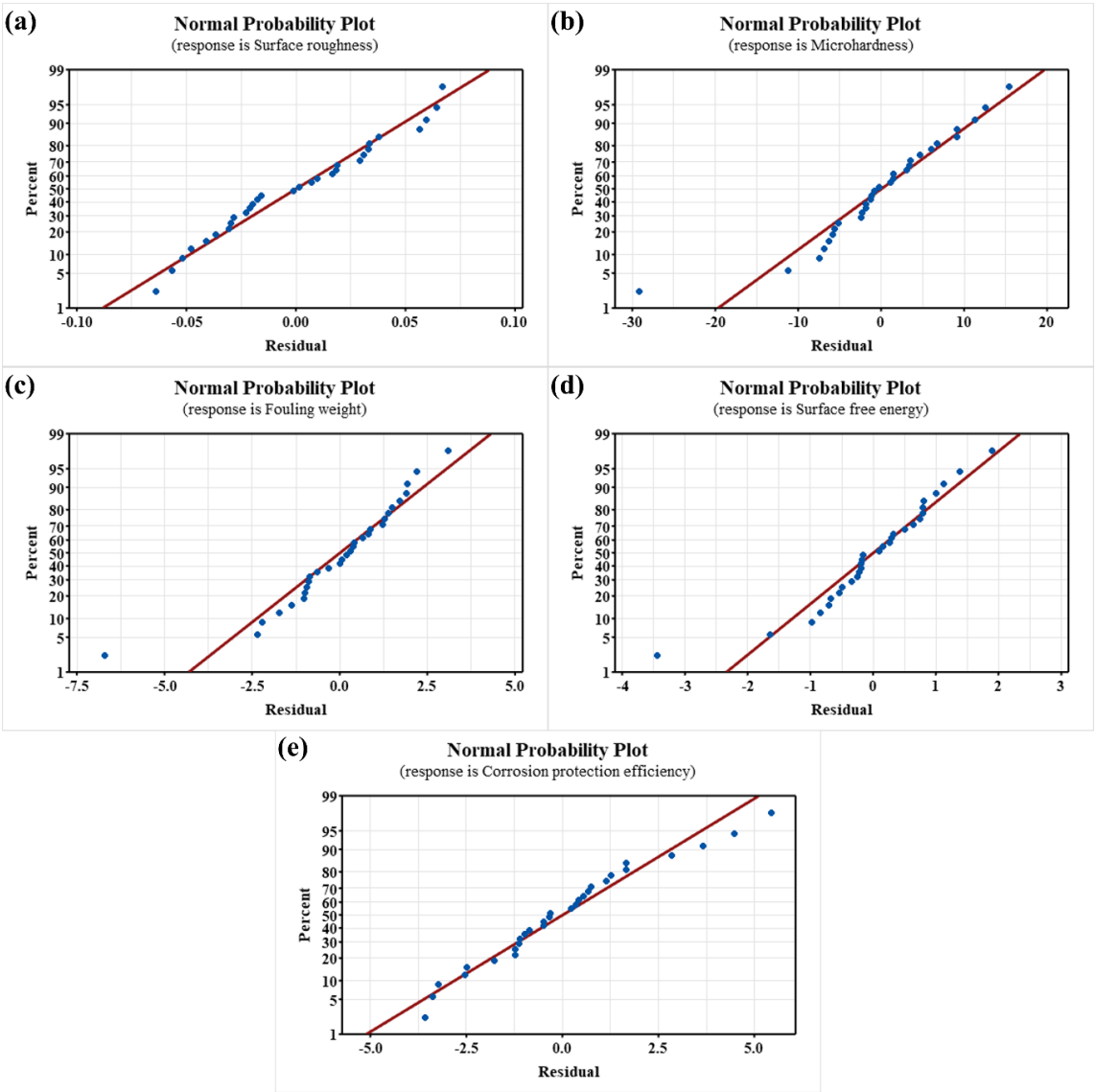

Figure 4.7. Normal probability plots of residuals for (a) surface roughness, (b) microhardness, (c) fouling weight, (d) surface free energy, and (e) protection efficiency.

The regression equation for corrosion protection efficiency is presented in Equation 4.17. An R^2 value of 0.9790 confirmed the strong fit of the quadratic model to the experimental data. The adjusted R^2 and predicted R^2 values were 0.9595 and 0.9170, respectively, with a difference of less than 0.2, indicating high model accuracy and reliability. The normal probability plot of the residuals for corrosion protection efficiency, shown in Figure 4.7(e), reveals that the residuals align closely with the straight line, indicating a normal distribution and further validating the adequacy of the model for prediction.

Across all the responses, the regression equations demonstrated an excellent fit to the experimental data, supported by the high R^2, adjusted R^2, and predicted R^2 values. The minimal differences between the adjusted and predicted R^2 values (less than 0.2) across all models confirmed their reliability and generalization capability. The normal probability plots of the residuals consistently exhibited near-linear trends, validating the assumption of normality and supporting the accuracy of the regression models in capturing the underlying relationships between the input parameters and responses.

4.5.1.3 Interaction effects on responses

In this study, surface plots were generated using Design-Expert 13 software to illustrate the interaction of the two input parameters on the responses while keeping the other parameters fixed at their central values. The response surface plots for surface roughness, microhardness, fouling weight, surface free energy, and corrosion protection efficiency are shown in Figures 4.8, 4.9, 4.10, 4.11, and 4.12, respectively. In these plots, the colored regions represent the response values. In Figures 4.8(a-f), 4.10(a-f), and 4.11(a-f), the blue region indicates the minimum values and the green region indicates the maximum values. In Figures 4.9(a-f) and 4.12(a-f), the green region indicates the minimum values and the red region indicates the maximum values.

The surface plots for the surface roughness (Figure 4.8(a-f)) highlight the conditions required to achieve the minimum roughness. Figure 4.8(a) shows that a nickel sulfate concentration of 40 g/L, combined with a sodium hypophosphite concentration of 30 g/L, yielded the smoothest surface, reflecting an optimal balance between nickel deposition and reducing activity. Similarly, as shown in Figure 4.8(b), the combination of 40 g/L nickel sulfate and 15 g/L sodium tungstate promoted a uniform tungsten distribution and enhanced smoothness. Figure 4.8(c) shows that 8 mg/L cerium sulfate paired with 40 g/L nickel

sulfate contributes to grain refinement, leading to reduced surface roughness. As shown in Figure 4.8(d), sodium hypophosphite (30 g/L) and sodium tungstate (15 g/L) optimized the deposition process to obtain smoother surfaces.

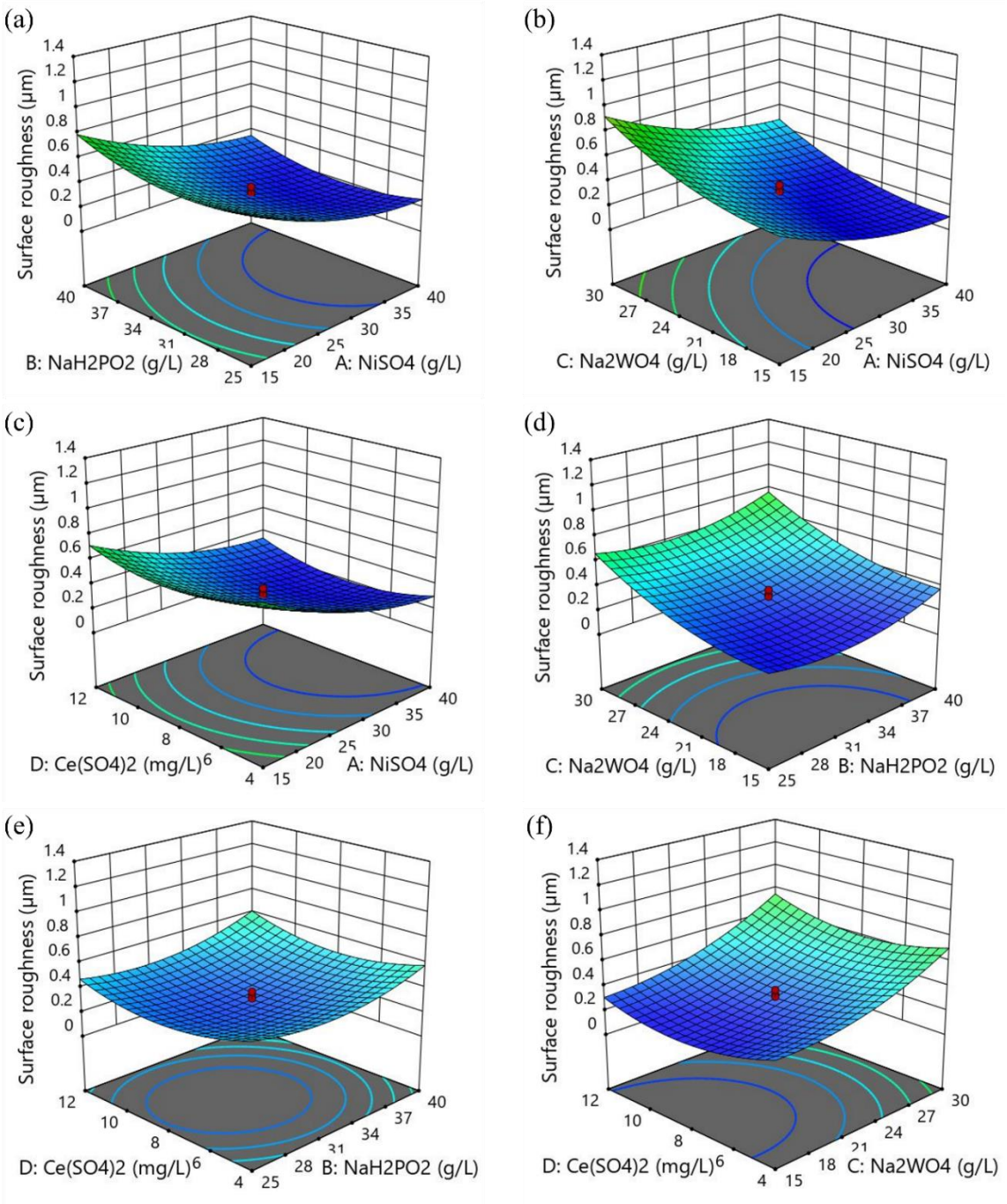

Figure 4.8. Surface plots of the surface roughness with the interaction of (a) nickel sulfate and sodium hypophosphite, (b) nickel sulfate and sodium tungstate, (c) nickel sulfate and cerium sulfate, (d) sodium hypophosphite and sodium tungstate, (e) sodium hypophosphite and cerium sulfate, and (f) sodium tungstate and cerium sulfate.

The synergy between 30 g/L sodium hypophosphite and 8 mg/L cerium sulfate, as shown in Figure 4.8(e), further reduced the roughness through enhanced reducing action. Finally, Figure 4.8(f) shows that the interaction of 15 g/L sodium tungstate and 8 mg/L cerium sulfate effectively minimized the surface roughness through a combined grain-refining effect.

The surface plots for microhardness (Figure 4.9(a-f)) highlight the optimal conditions for maximizing the hardness of the coatings. Figure 4.9(a) shows the highest microhardness at 40 g/L nickel sulfate and 30 g/L sodium hypophosphite resulting from a dense, uniform coating. As shown in Figure 4.9(b), the incorporation of 15 g/L of sodium tungstate and 40 g/L of nickel sulfate strengthened the alloy matrix and enhanced its hardness. The addition of 8 mg/L cerium sulfate, as shown in Figure 4.9(c), further improved the hardness through grain refinement. Figure 4.9(d) shows that the co-deposition of 30 g/L sodium hypophosphite and 15 g/L sodium tungstate increased coating density and hardness. The peak hardness is shown in Figure 4.9(e) for 30 g/L sodium hypophosphite and 8 mg/L cerium sulfate, where cerium contributed to a finer grain structure. Finally, Figure 4.9(f) shows that the interaction of 15 g/L sodium tungstate and 8 mg/L cerium sulfate produces a dense, refined coating that maximizes the hardness.

The surface plots for fouling weight (Figure 4.10(a-f)) illustrate the conditions for minimizing fouling on the coating surface. As shown in Figure 4.10(a), the combination of 40 g/L nickel sulfate and 30 g/L sodium hypophosphite results in a smooth and less porous surface with reduced fouling. Figure 4.10(b) shows that the addition of 15 g/L of sodium tungstate further enhanced the compactness of the coating, thereby lowering the fouling weight. The inclusion of 8 mg/L cerium sulfate and 40 g/L nickel sulfate refined the grain structure and minimized fouling potential, as shown in Figure 4.10(c). Figure 4.10(d) indicates that 30 g/L sodium hypophosphite and 15 g/L sodium tungstate formed a dense, fouling-resistant surface. The combination of 30 g/L sodium hypophosphite and 8 mg/L cerium sulfate, as shown in Figure 4.10(e), further improves the resistance of the surface to fouling. Finally, Figure 4.10(f) highlights the synergistic effect of 15 g/L sodium tungstate and 8 mg/L cerium sulfate in reducing the fouling weight by enhancing surface smoothness.

The surface free energy plots (Figure 4.11(a-f)) depict the conditions required to minimize the surface free energy, which is an essential factor for improving the coating performance. As shown in Figure 4.11(a), the combination of 40 g/L nickel sulfate and 30

g/L sodium hypophosphite produces a smooth, low-energy surface. The addition of 15 g/L of sodium tungstate, as shown in Figure 4.11(b), further reduced the surface energy through enhanced compactness. Figure 4.11(c) shows that the interaction between 40 g/L nickel sulfate and 8 mg/L cerium sulfate refined the surface, thereby minimizing irregularities. Figure 4.11(d) shows that 30 g/L of sodium hypophosphite and 15 g/L of sodium tungstate yielded a dense coating with reduced surface energy. The combination of 30 g/L sodium hypophosphite and 8 mg/L cerium sulfate achieved the lowest surface free energy through the grain refining effect of cerium, as shown in Figure 4.11(e). Finally, Figure 4.11(f) shows that 15 g/L sodium tungstate and 8 mg/L cerium sulfate produced a uniform low-energy surface.

The surface plots for corrosion protection efficiency (Figure 4.12(a-f)) show the conditions for achieving the maximum resistance to corrosion. As shown in Figure 4.12(a), the combination of 40 g/L of nickel sulfate and 30 g/L of sodium hypophosphite formed a dense protective layer. Figure 4.12(b) shows that 15 g/L sodium tungstate with 40 g/L nickel sulfate enhanced corrosion resistance through tungsten incorporation. The addition of 8 mg/L cerium sulfate, as shown in Figure 4.12(c), improves the protection efficiency by refining the microstructure. Figure 4.12(d) indicates that the co-deposition of 30 g/L sodium hypophosphite and 15 g/L sodium tungstate enhances the robustness of the coating. The interaction of 30 g/L sodium hypophosphite and 8 mg/L cerium sulfate, as shown in Figure 4.12(e), achieved the maximum protection efficiency through the grain refining effect of cerium. Finally, Figure 4.12(f) demonstrates that 15 g/L sodium tungstate and 8 mg/L cerium sulfate synergistically enhance surface stability and maximize corrosion protection.

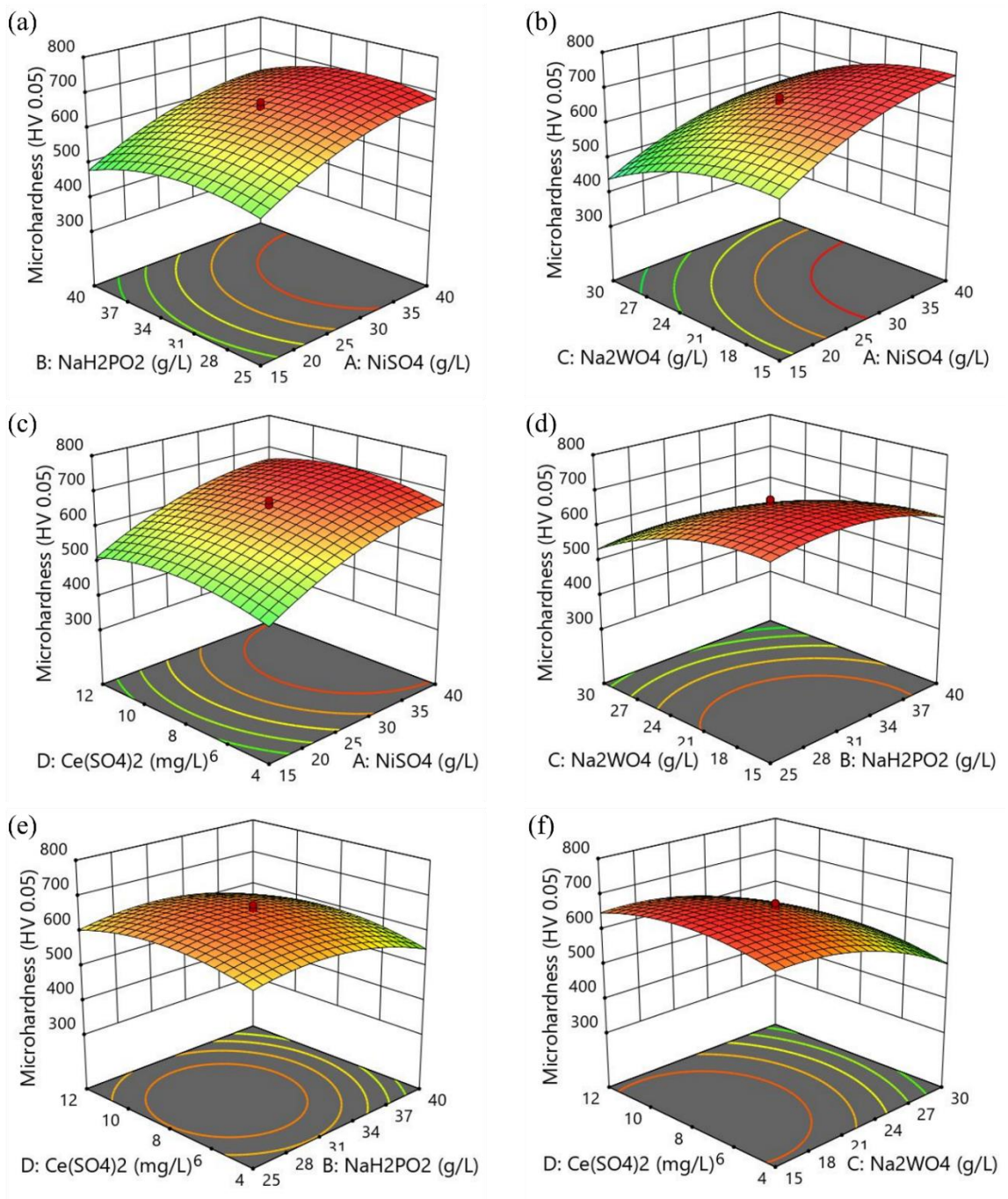

Figure 4.9. Surface plots of microhardness with the interactions of (a) nickel sulfate and sodium hypophosphite, (b) nickel sulfate and sodium tungstate, (c) nickel sulfate and cerium sulfate, (d) sodium hypophosphite and sodium tungstate, (e) sodium hypophosphite and cerium sulfate, and (f) sodium tungstate and cerium sulfate.

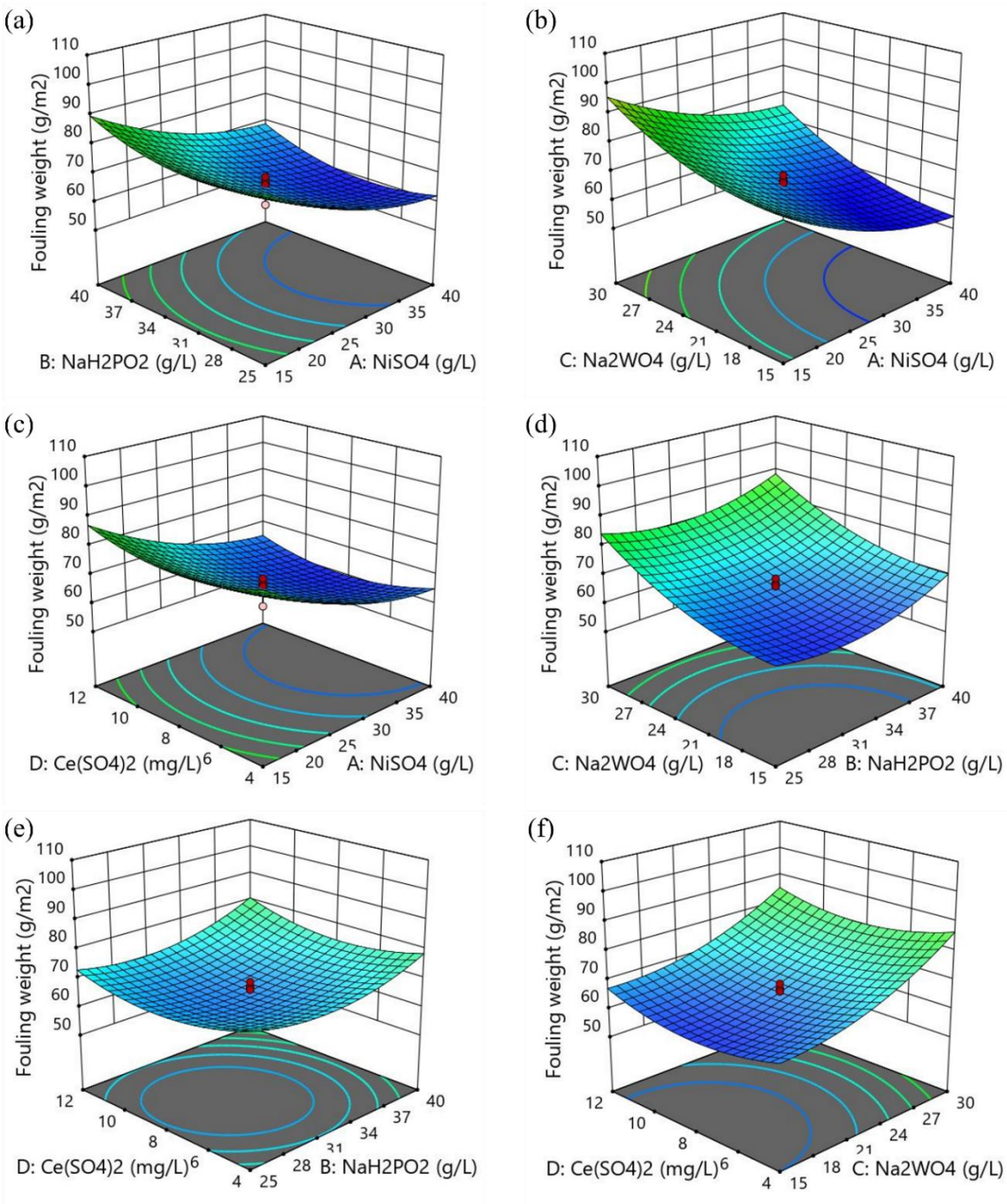

Figure 4.10. Surface plots of fouling weight with the interactions of (a) nickel sulfate and sodium hypophosphite, (b) nickel sulfate and sodium tungstate, (c) nickel sulfate and cerium sulfate, (d) sodium hypophosphite and sodium tungstate, (e) sodium hypophosphite and cerium sulfate, and (f) sodium tungstate and cerium sulfate.

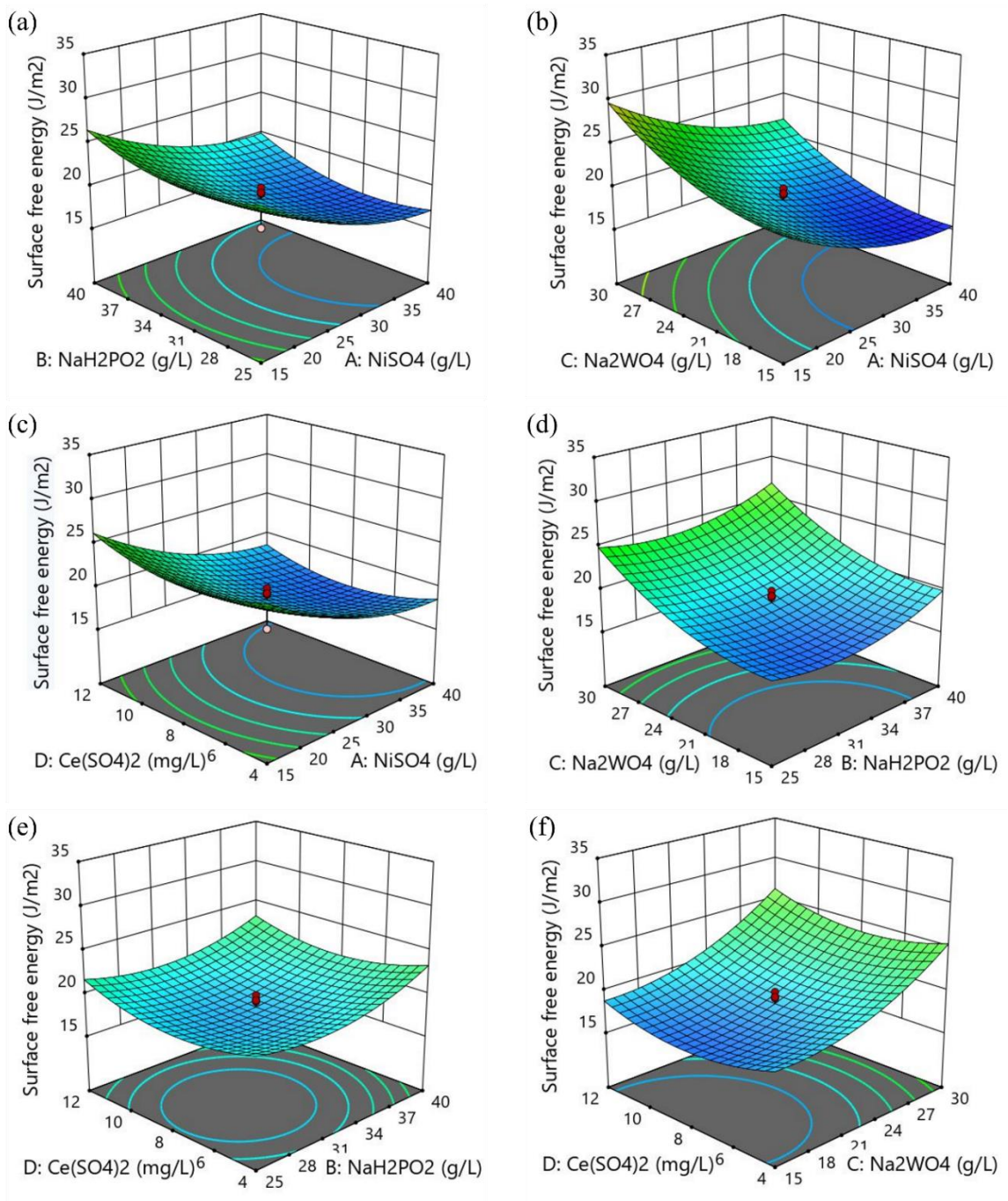

Figure 4.11. Surface plots of surface free energy with the interactions of (a) nickel sulfate and sodium hypophosphite, (b) nickel sulfate and sodium tungstate, (c) nickel sulfate and cerium sulfate, (d) sodium hypophosphite and sodium tungstate, (e) sodium hypophosphite and cerium sulfate, and (f) sodium tungstate and cerium sulfate.

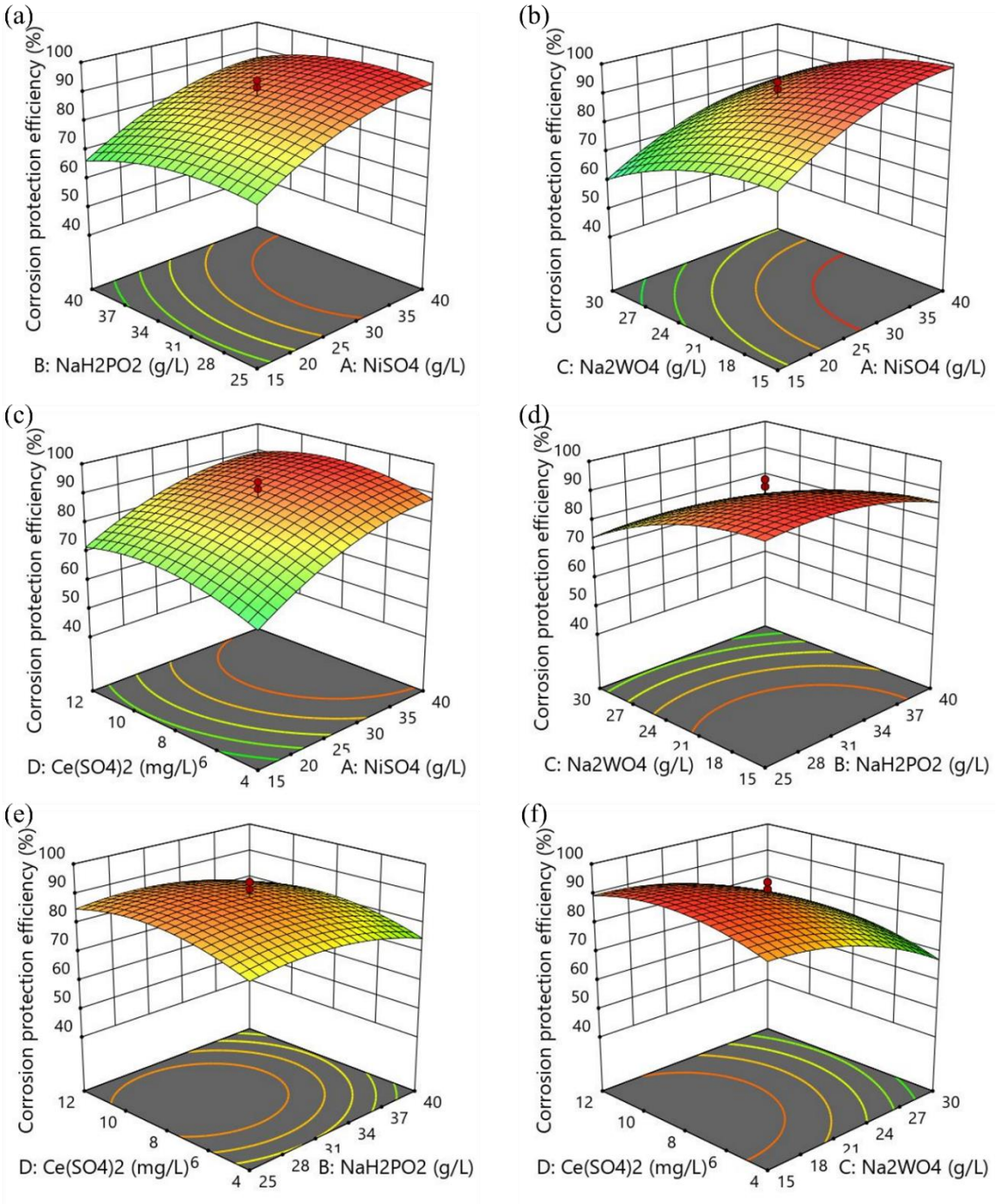

Figure 4.12. Surface plots of corrosion protection efficiency with the interaction of (a) nickel sulfate and sodium hypophosphite, (b) nickel sulfate and sodium tungstate, (c) nickel sulfate and cerium sulfate, (d) sodium hypophosphite and sodium tungstate, (e) sodium hypophosphite and cerium sulfate, and (f) sodium tungstate and cerium sulfate.

4.5.1.4 Multi-objective optimization using RSM

Multi-objective optimization using the desirability function approach in RSM with MINITAB 22 successfully determined an optimal combination of input parameters that enhanced the coating performance across various metrics. The optimized values of the input parameters and the corresponding predicted responses are listed in Table 4.9. These parameters reflect a carefully calibrated combination, enabling the coating to achieve a superior performance across multiple objectives. By addressing conflicting goals with precision, the optimization process delivers a comprehensive solution that balances performance requirements while maintaining essential trade-offs. Notably, the composite desirability value for the optimization was 1, indicating that the process successfully identified a solution that satisfied all objectives simultaneously. This outcome underscores the robustness and efficacy of the proposed optimization methodology.

Table 4.9. Results of multi-objective optimization using RSM.

Optimal setting of input parameters	Predicted responses
Ni = 39.37 g/L	Surface roughness = 0.11 μm
P = 29.62 g/L	Microhardness = 733.21 HV 0.05
W = 15.98 g/L	Fouling weight = 53.86 g/m^2
Ce = 8.08 mg/L	Surface free energy = 15.02 J/m^2
	Corrosion protection efficiency = 99.14%

The optimization ensured that surface roughness remained within acceptable limits, achieving an average value of 0.11 μm with a 95% confidence interval of (0.0558, 0.1589). Maintaining a smooth surface is critical because it prevents surface defects that compromise the functional and aesthetic integrity of coatings.

Improved microhardness, reaching 733.21 HV 0.05 (95% confidence interval: 721.73, 744.68), was another notable achievement. This increase reflects the enhanced resistance of the coating to wear and mechanical damage, which is essential for ensuring its long-term durability in demanding operational environments.

The optimization also achieved a significant reduction in fouling weight, with a mean value of 53.86 g/m^2 and a 95% confidence interval of (51.34, 56.37). A lower fouling weight is crucial for sustaining the coating performance over time by minimizing the accumulation of unwanted deposits, which can hinder its functionality.

A reduction in the surface free energy to an average value of 15.02 J/m^2, with a 95% confidence interval of (13.655 and 16.386), further highlights the effectiveness of the optimization. This decrease was expected to improve the adhesion properties of the coating, contributing to its overall robustness and resistance to environmental factors.

Finally, the optimization process yielded an exceptional corrosion protection efficiency of 99.14%, with a 95% confidence interval of (96.16, 102.12). This result underscores the enhanced ability of the coating to withstand corrosive conditions, demonstrating the success of the optimization in addressing this critical performance parameter.

4.5.2 ANN training performance

Figure 4.13(a) shows the ANN regression results for the training, validation, testing, and combined datasets. The high R-values, close to 1 for all datasets, demonstrate an excellent correlation between the predicted and actual values, confirming the accuracy of the ANN in capturing complex nonlinear relationships in the data. The near-linear alignment of the data points along the diagonal line indicates minimal prediction errors, validating the ANN as a robust predictive model for multi-objective optimization. Figure 4.13(b) illustrates the training performance in terms of mean squared error (MSE) across 16 epochs. The model achieved its best validation performance with an MSE of 0.013233 at epoch 7, demonstrating efficient learning. The subsequent plateauing of the validation and test errors indicates that the model successfully generalized beyond the training data without overfitting. Figure 4.13(c) presents a detailed view of the training dynamics. The gradient steadily declined, reaching a low value of 0.0032 at epoch 16, suggesting a stable convergence. The Mu parameter, indicative of the Levenberg-Marquardt adjustment, remained nearly constant during most epochs but rose sharply toward the final epoch, indicating final optimization refinements. The validation check count reached nine by epoch 16, ensuring that the model performance was carefully monitored to avoid overtraining. Figure 4.13(d) shows an error histogram with 20 bins for the training, validation, and testing datasets. The distribution was sharply centered around zero error, with the highest concentration in the near-zero bin, highlighting the minimal prediction bias. The symmetric and narrow spread of residuals across all datasets further confirmed the high accuracy and consistency of the model. The presence of a few outliers has a negligible influence on the overall predictive capability of the ANN.

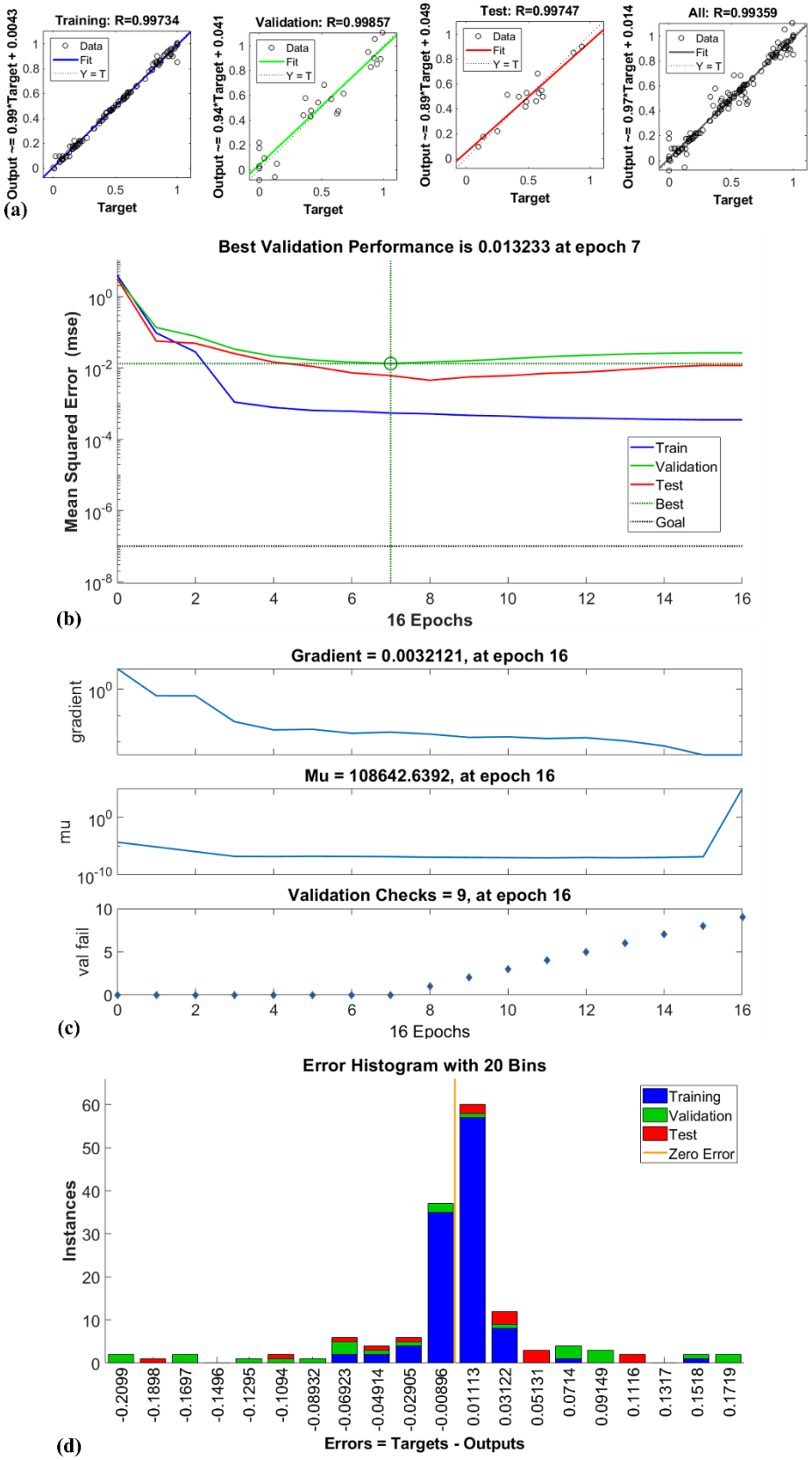

Figure 4.13. ANN analysis plots: (a) regression plot showing R-values for training, validation, testing, and combined datasets; (b) performance plot; (c) training state; and (d) error histogram.

The comparison of the R^2 values from ANOVA and regression analysis with those obtained from the ANN provides insights into the accuracy and robustness of the ANN model in predicting the responses. The R^2 values for the ANOVA and regression analysis ranged between 0.9693 and 0.9948 for all responses, indicating a strong correlation between the predicted and observed values when using a second-order polynomial model. However, the ANN model exhibited even higher R^2 values ($R > 0.999$ for the training, validation, testing, and combined datasets), demonstrating its superior ability to capture the nonlinear and complex relationships between the input parameters and responses. This highlights the effectiveness of ANN in handling intricate data patterns and its potential to replace traditional regression models for optimization purposes. Additionally, the ANN's capacity to generalize across unseen data, as evident from the high R values during validation and testing, further supports its use in multi-objective optimization with metaheuristic algorithms.

4.5.3 Multi-objective optimization using hybrid ANN-based metaheuristic algorithms

4.5.3.1 Convergence behavior analysis

The convergence behavior of the three metaheuristic algorithms (ANN-TLBO, ANN-WOA, and ANN-RFO) was analyzed using convergence plots for all five responses. These plots provide valuable insights into the performance, stability, and adaptability of each algorithm during the optimization process.

The convergence plot of the TLBO algorithm, as shown in Figure 4.14(a), demonstrates rapid convergence within the first 10 generations for all the objectives. The sharp improvement during the early generations is driven by the efficient exploitation of the search space through the teacher phase, whereas the smooth stabilization in later generations reflects the robust fine-tuning capabilities of the learner phase. The minimal oscillations observed after convergence indicate the ability of the TLBO to avoid unnecessary exploration and ensure stable and efficient optimization across all objectives. However, early stabilization suggests a potential risk of premature convergence, which could limit the performance of highly complex or multimodal optimization problems.

The convergence plot of the WOA, as shown in Figure 4.14(b), reveals a dynamic optimization process characterized by oscillations in the objective values during the early and mid-iterations, followed by gradual stabilization in later iterations.

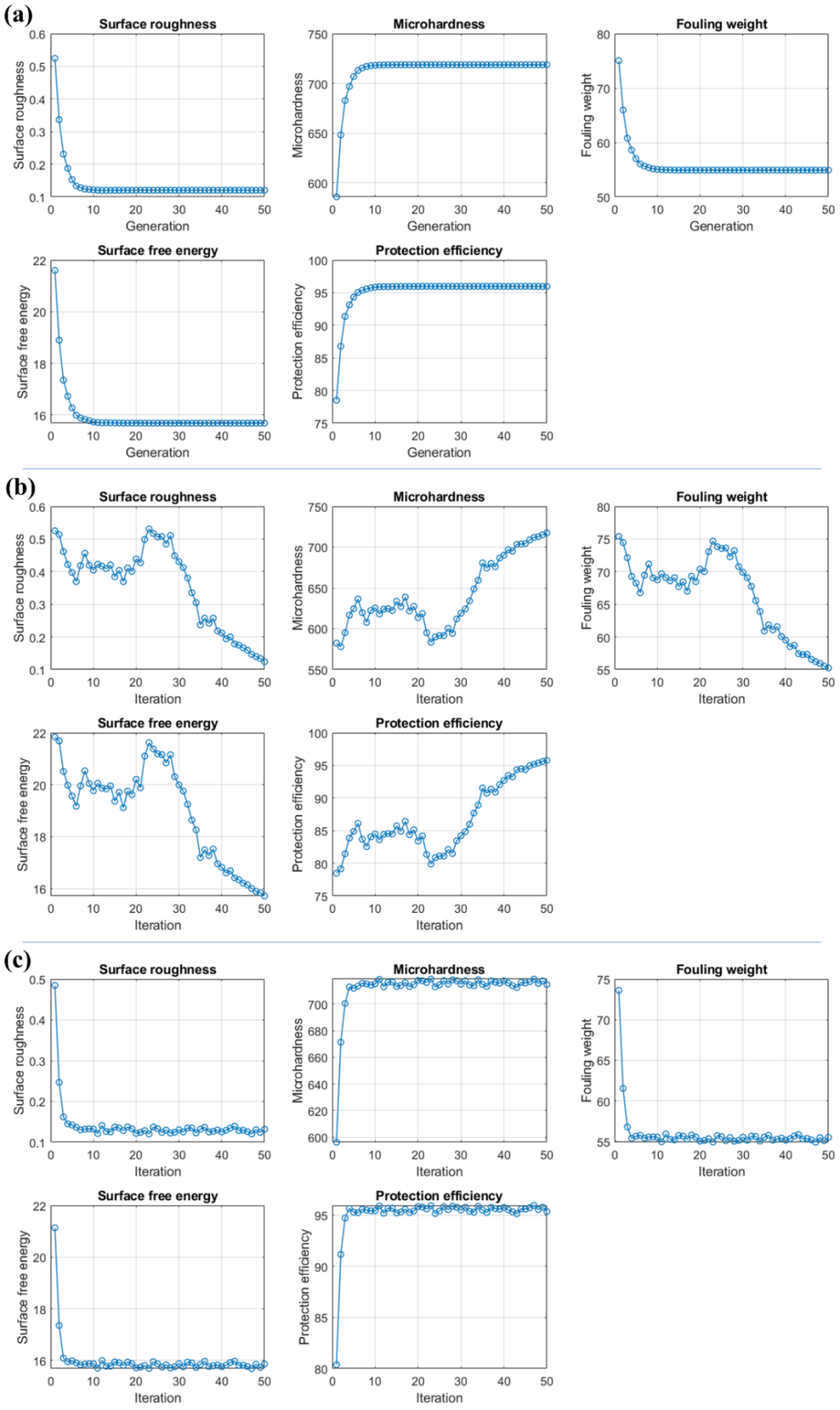

Figure 4.14. Convergence behavior of five responses optimized using hybrid algorithms: (a) ANN-TLBO, (b) ANN-WOA, and (c) ANN-RFO.

Objectives, such as surface roughness, fouling weight, and surface free energy, showed irregular but steady decreases, reflecting the exploratory nature of the WOA during its prey encircling phase. Similarly, the microhardness and protection efficiency exhibited incremental increases, with some fluctuations, before stabilizing near the optimal values after the 40^{th} iteration. These oscillations indicate that the WOA maintains a strong balance between exploration and exploitation, leveraging its bubble-net feeding mechanism to effectively navigate the search space. However, the delayed stabilization compared to TLBO suggests that the WOA requires more iterations to refine the solutions, making it suitable for complex optimization problems where the exploration of multimodal landscapes is critical.

The convergence plot of the RFO algorithm, shown in Figure 4.14(c), demonstrates rapid stabilization across all objectives within the first 5–10 iterations. This behavior highlights the ability of RFO to quickly identify optimal solutions through adaptive exploration and exploitation mechanisms. The objectives exhibited smooth and stable trends after the early iterations, with minimal fluctuations, indicating strong convergence stability. The sharp initial improvements suggest efficient exploration during the early phase, whereas the consistent performance in subsequent iterations reflects robust exploitation. The lack of significant oscillations further demonstrates that RFO effectively balances the search process to avoid premature divergence, while ensuring efficient optimization.

The convergence behaviors of the TLBO, WOA, and RFO algorithms revealed distinct strengths and patterns in their optimization processes. TLBO demonstrates the fastest convergence, with all objectives stabilizing within the first ten generations, reflecting its strong exploitation capabilities through the teacher and learner phases. However, early stabilization in TLBO poses the risk of premature convergence in complex or multimodal landscapes. In contrast, the WOA shows a more dynamic convergence process, characterized by oscillations in the early and mid-iterations, followed by gradual stabilization after the 40th iteration. This behavior highlights the WOA's robust balance between exploration and exploitation, making it suitable for highly complex problems, although its slower convergence compared to TLBO may limit its efficiency in simpler landscapes. RFO, on the other hand, combines rapid convergence and stability, with objectives stabilizing within 5 to 10 iterations. Its smooth and consistent trends after the initial phase reflect a well-balanced approach to exploration and exploitation, making it

ideal for scenarios that require rapid and reliable optimization. Overall, while TLBO excels in speed, WOA offers a thorough exploration of complex problems and RFO provides a balanced and stable solution for both efficiency and reliability.

4.5.3.2 Pareto front and trade-off visualization

The 3D-RadVis visualizations presented in Figures 4.15 (a), (b), (c), (d), and (e) illustrate the evolution of non-dominated solutions at generations 5, 10, 20, 40, and 50, respectively, during multi-objective optimization using the TLBO algorithm. Figure 4.15(f) consolidates all non-dominated solutions across all generations, providing a comprehensive representation of the optimization process. These visualizations highlight the progression, diversity, and trade-offs between the five competing objectives.

In Generation 5, as shown in Figure 4.15(a), the solutions were tightly clustered, indicating the early exploration phase of the algorithm. At this stage, the objective space is not yet well covered, reflecting the limited diversification of non-dominated solutions. By Generation 10, as shown in Figure 4.15(b), the solutions began to spread in different directions toward the anchor points of the individual objectives, demonstrating the algorithm's improved exploration capabilities and an initial representation of the trade-offs. The trend continues until Generation 20, as shown in Figure 4.15(c), where the clustering diminishes and the solutions are better distributed across the objective space. This reflects the ability of the algorithm to simultaneously identify diverse trade-offs and optimize multiple objectives. By generations 40 and 50, as shown in Figures 4.15(d) and (e), the solutions stabilize and exhibit a well-distributed pattern, signifying the algorithm's convergence to the Pareto-optimal region. The stabilization in these later generations indicates that the TLBO algorithm has effectively transitioned from exploration to exploitation, refining the solutions toward optimal trade-offs. The final consolidated visualization, shown in Figure 4.15(f), encompasses all non-dominated solutions identified throughout the optimization process. This comprehensive view highlights the diversity of the Pareto front, with solutions spreading across the objective space and clustering near specific objectives such as microhardness and protection efficiency. The spread of solutions demonstrates the robustness of the TLBO algorithm in maintaining diversity, whereas clustering suggests achievable trade-offs in these areas. In contrast, fewer solutions were observed near the objectives, such as surface free energy, indicating the challenges associated with optimizing these objectives simultaneously.

Overall, these visualizations illustrate the capability of the TLBO algorithm to effectively handle complex multi-objective optimization problems. The progression from clustered solutions in early generations to a well-spread Pareto front in later generations reflects the ability of the algorithm to balance exploration and exploitation. The final consolidated figure underscores the diverse trade-offs available, enabling decision makers to select optimal solutions based on specific application requirements, such as prioritizing microhardness for wear resistance or protection efficiency for corrosion resistance. This dynamic and comprehensive representation validates the robustness and efficiency of the TLBO in generating well-converged Pareto-optimal solutions.

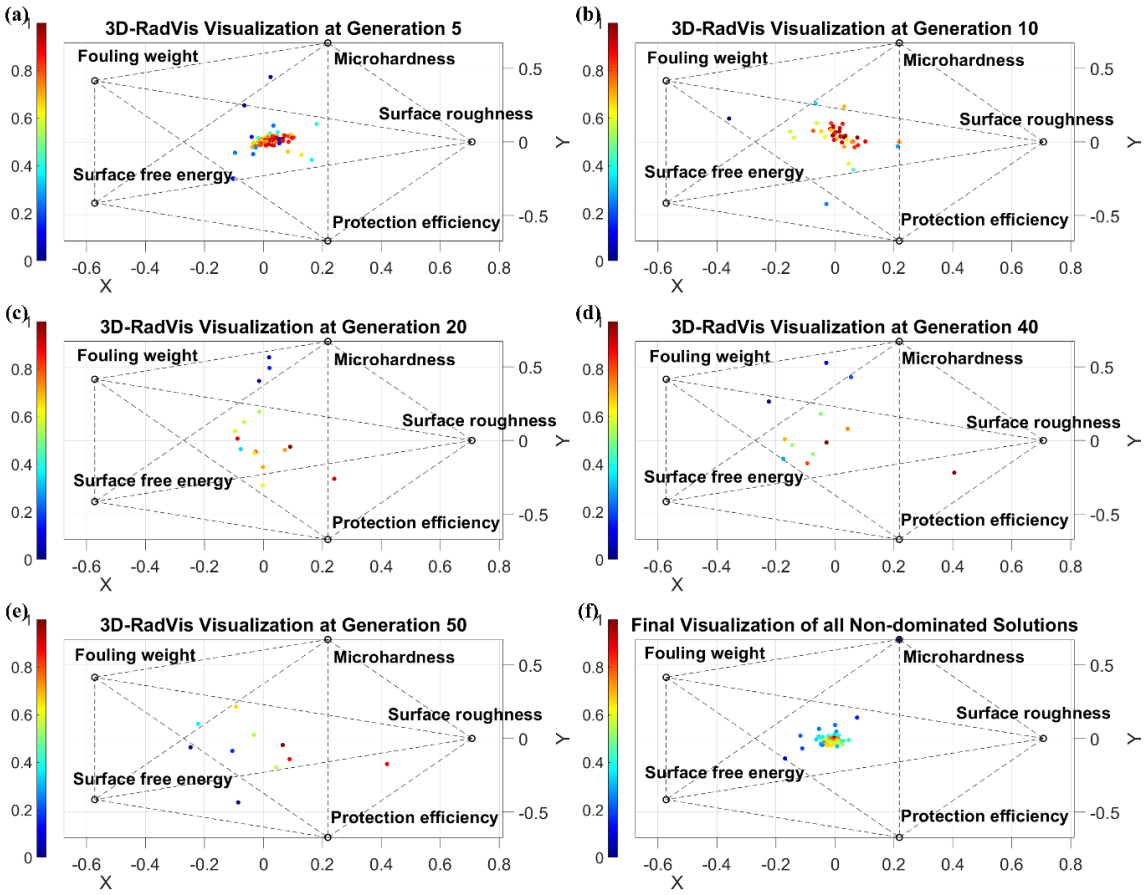

Figure 4.15. 3D-RadVis visualization of non-dominated solutions from the ANN-TLBO algorithm at iterations 5 (a), 10 (b), 20 (c), 40 (d), 50 (e), and all iterations combined (f).

The 3D-RadVis visualizations shown in Figures 4.16 (a), (b), (c), (d), and (e) correspond to iterations 5, 10, 20, 40, and 50, respectively, during the multi-objective optimization process with the WOA. Figure 4.16(f) consolidates all non-dominated solutions across all iterations.

At iteration five, as shown in Figure 4.16(a), the non-dominated solutions were tightly clustered around the central region, indicating a limited exploration of the objective space. This clustering is typical in the early stages of the algorithm, when the search is focused on identifying promising regions.

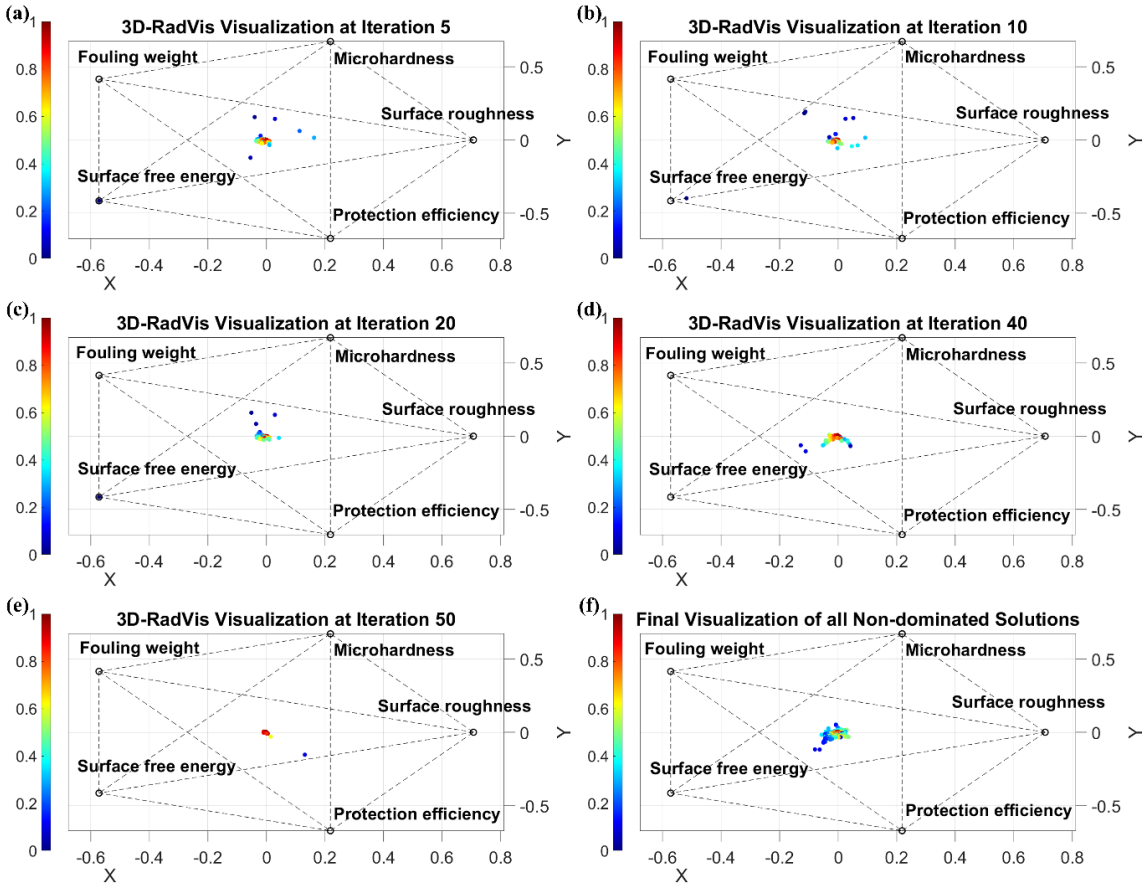

Figure 4.16. 3D-RadVis visualization of non-dominated solutions from the ANN-WOA algorithm at iterations 5 (a), 10 (b), 20 (c), 40 (d), 50 (e), and all iterations combined (f).

By iteration 10, as shown in Figure 4.16(b), the solutions begin to diverge slightly, forming a broader spread that reflects the exploratory capability of the WOA through its encircling prey and spiral update mechanisms. By iteration 20, as shown in Figure 4.16(c), the solutions exhibit further spread, with some moving closer to the individual objective anchor points, indicating progress in achieving diverse trade-offs among objectives. At this stage, the algorithm starts balancing exploration and exploitation more effectively, thereby enabling a better coverage of the Pareto front. At iterations 40 and 50, as shown in Figures 4.16(d) and (e), the solutions stabilize, forming a well-distributed pattern that covers a significant portion of the objective space. This stabilization reflects the convergence phase of the algorithm, in which the search focuses on refining the solutions near the Pareto-

optimal region. The proximity of the solutions to anchor points for specific objectives highlights the trade-offs achieved, such as maximizing microhardness and protection efficiency while minimizing fouling weight and surface roughness. The final consolidated visualization, shown in Figure 4.16(f), provides a comprehensive view of all non-dominated solutions generated during the optimization process. The diversity of the Pareto front is evident, with solutions distributed across the objective space, forming clusters near certain objectives such as microhardness and protection efficiency. This clustering indicates achievable trade-offs, whereas the spread across other areas demonstrates the ability of the algorithm to maintain diversity and explore complex trade-offs between conflicting objectives.

The visualization of non-dominated solutions obtained using the RFO algorithm is depicted in Figures 4.17 (a), (b), (c), (d), and (e) for generations 5, 10, 20, 40, and 50, respectively, and Figure 4.17(f) for all non-dominated solutions. At Generation 5, as shown in Figure 4.17(a), the solutions are sparsely distributed, with some initial clustering toward specific objectives such as surface free energy and protection efficiency. As the algorithm progressed to Generation 10, as shown in Figure 4.17(b), the solutions became slightly more compact, indicating early stage exploration with incremental refinement. By Generation 20, as shown in Figure 4.17(c), clustering became more pronounced and the solutions started to populate a defined region, suggesting a transition toward exploitation. At generations 40 and 50, the solutions exhibited a significant reduction in spread and tighter clustering around the Pareto front, as shown in Figures 4.17(d) and (e), respectively. This behavior suggests a strong convergence and stability in the optimization process of the RFO algorithm. The final visualization of all non-dominated solutions in Figure 4.17(f) demonstrates a well-defined Pareto front with minimal outliers, confirming the ability of the algorithm to effectively balance the trade-offs between competing objectives. The solutions illustrate a good trade-off distribution, emphasizing the competing nature of the objectives, such as the surface roughness and protection efficiency.

Compared with the results obtained using TLBO and WOA, RFO shows distinct advantages. Although TLBO demonstrated rapid convergence within the first few generations and stable clustering, it increased premature convergence with less diversity in the later stages. In contrast, the WOA exhibited significant oscillations and maintained a longer diversity but required more iterations to stabilize. RFO strikes a balance by achieving both rapid convergence and maintaining diversity throughout the optimization

process. The RFO solutions demonstrate tighter clustering and a more distinct Pareto front compared to the WOA, and a more diverse final solution set compared to TLBO, highlighting its superior performance in effectively addressing multi-objective optimization challenges.

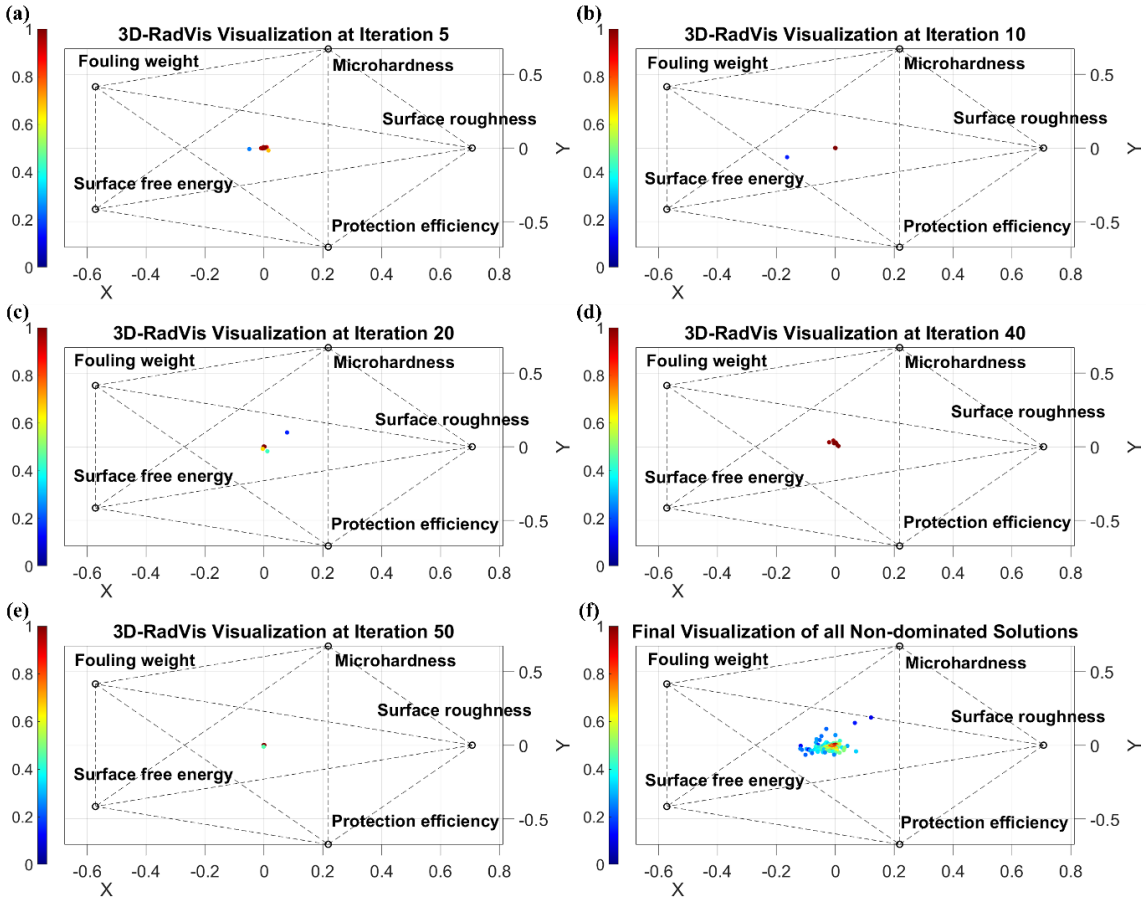

Figure 4.17. 3D-RadVis visualization of non-dominated solutions from the ANN-RFO algorithm at iterations 5 (a), 10 (b), 20 (c), 40 (d), 50 (e), and all iterations combined (f).

4.5.3.3 Sensitivity analysis of parameters

The local sensitivity analysis results, shown in Figure 4.18, quantify the influence of each input parameter (Ni, P, W, Ce) on the five output responses: surface roughness, microhardness, fouling weight, surface free energy, and protection efficiency. The analysis revealed that microhardness is highly sensitive to changes in Ni and W concentrations, as indicated by the large positive and negative sensitivity indices (6.266 for Ni and -7.237 for W, respectively). In contrast, the effects of Ce were generally minor across all the responses. These results suggest that the control of Ni and W concentrations is critical for optimizing surface properties. Notably, the local sensitivity analysis values were identical

for all three optimization algorithms (TLBO, WOA, and RFO) because the local analysis was conducted at a fixed nominal point in the design space, independent of the optimization results.

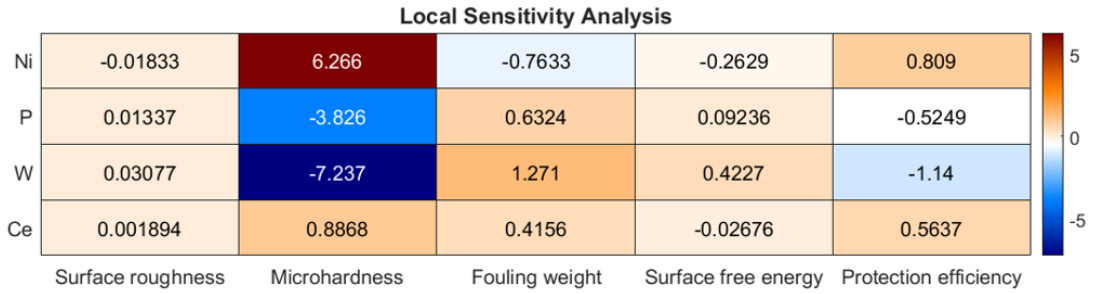

Figure 4.18. Local sensitivity analysis of input parameters on output responses, consistent for all three algorithms.

The global sensitivity analysis of the input parameters of the five output responses for the TLBO algorithm is shown in Figure 4.19(a). The Sobol indices indicate that Ni and W have the strongest influence across most responses, particularly for the surface roughness (0.6494 for Ni) and protection efficiency (0.6564 for Ni). The contribution of Ce is relatively low across all outputs, suggesting that it has a minimal global influence on the system performance when explored within the TLBO-derived solution space. These findings highlight the dominant roles of Ni and W in determining the coating properties when optimized using TLBO.

For the WOA algorithm, illustrated in Figure 4.19(b), the global sensitivity indices were generally lower, with the highest contribution observed for Ce in surface roughness (0.3258) and P for microhardness (0.2476). Unlike TLBO, the WOA search resulted in a more balanced influence among all four input parameters, with no single variable overwhelmingly dominating. This reflects the algorithm's exploration of different regions of the design space, resulting in more moderate and distributed sensitivities across the parameters.

The RFO algorithm results, presented in Figure 4.19(c), show a pattern similar to that of TLBO but with slightly lower peak sensitivities. Ni and W again emerged as the most influential parameters, with Sobol indices of 0.5149 and 0.5233, respectively, for surface roughness. The contribution of Ce remained low and consistent across all algorithms. Overall, the variation in global sensitivity profiles between the algorithms confirms that

each optimizer explores distinct regions of the parameter space, thereby affecting the magnitude of the calculated Sobol indices.

Figure 4.19. Heatmaps of the global sensitivity of the input parameters on multi-objective outputs for different algorithms: (a) ANN-TLBO, (b) ANN-WOA, and (c) ANN-RFO.

4.5.3.4 Parameter interaction and correlation mapping

The parameter interaction map shown in Figure 4.20 provides a visual representation of the interactions among the input variables (Ni, P, W, and Ce) during the multi-objective optimization process using all three algorithms. The values within the map range from -1 to 1, representing the strength and direction of the interactions. Each cell in the matrix quantifies the pairwise correlation or interaction between two variables, highlighting the extent to which they influence each other to obtain optimal solutions. Positive values indicate synergistic relationships, whereas negative values indicate antagonistic relationships.

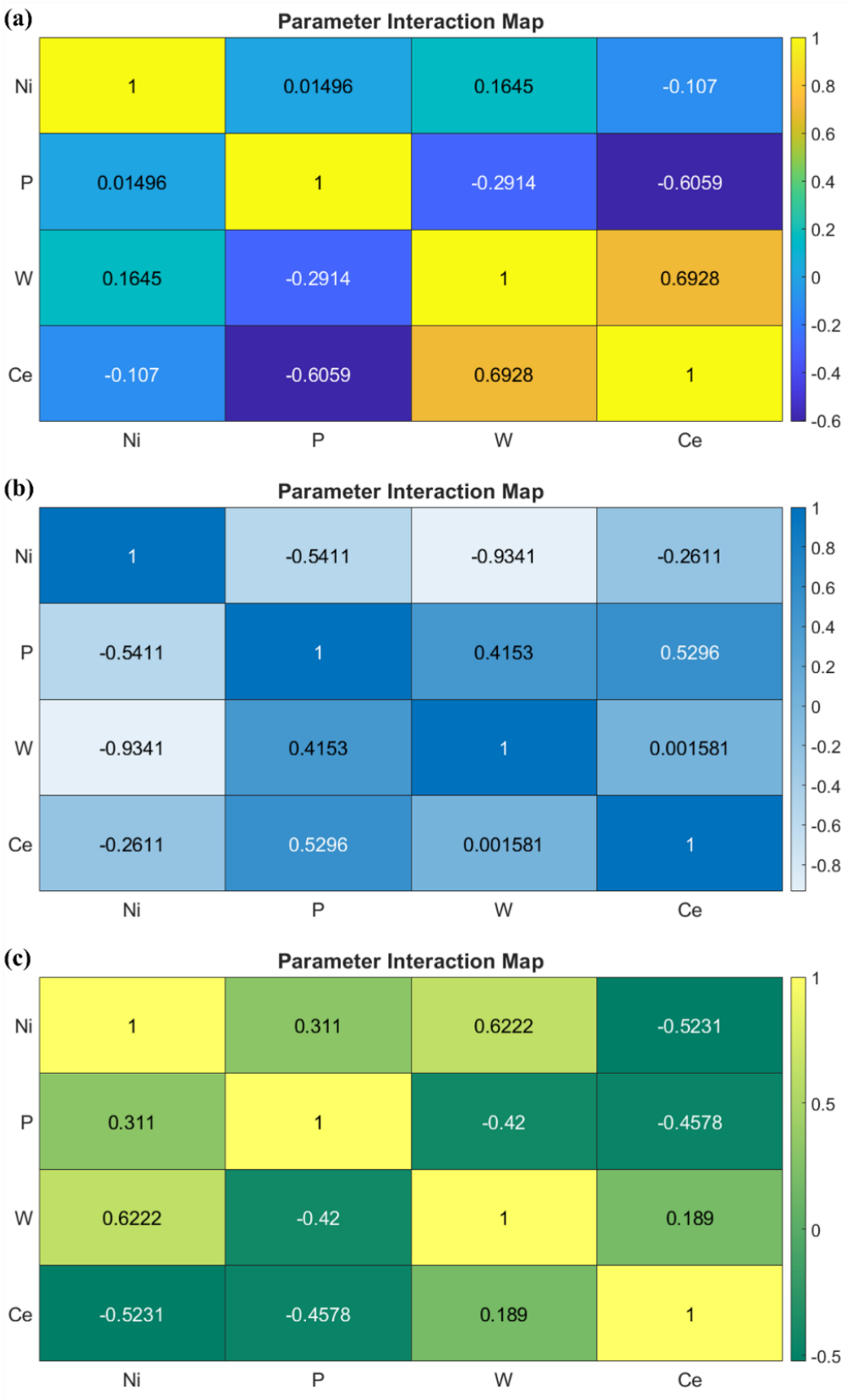

Figure 4.20. Parameter interaction maps using different algorithms: (a) ANN-TLBO, (b) ANN-WOA, and (c) ANN-RFO.

The interaction map for TLBO depicted in Figure 4.20(a) demonstrates a strong positive correlation (0.6928) between W and Ce, indicating a synergistic effect when these parameters were simultaneously varied to optimize the outputs. In contrast, P and Ce exhibited a notable negative correlation (-0.6059), suggesting that increasing one parameter may reduce the effectiveness of the other in achieving the desired optimization outcomes. This antagonistic relationship may imply a trade-off, in which balancing these parameters is critical for optimal performance. The negligible interaction between Ni and P (0.01496) suggests that these variables operate independently, with minimal influence on each other. Similarly, the negative interaction between Ni and Ce (-0.107) indicates a weak but opposing relationship.

The parameter interaction map shown in Figure 4.20(b) illustrates the relationships among the input parameters during the multi-objective optimization process using the WOA. The results show that the interaction between Ni and W (-0.9341) is highly antagonistic, implying that changes in these parameters significantly counteract each other. Conversely, P and Ce exhibited a moderately positive correlation (0.5296), suggesting cooperative behavior when these parameters were adjusted together. The interaction between W and Ce (0.001581) was negligible, indicating that these two parameters were nearly independent in this optimization process.

The parameter interaction map obtained during the optimization process using the RFO algorithm is shown in Figure 4.20(c). The strongest positive interaction was observed between Ni and W (0.6222), indicating that these parameters exhibited a high level of cooperative behavior during the optimization process. Conversely, Ni and Ce demonstrate a strongly negative interaction (-0.5231), indicating that changes in these parameters work against each other. The interaction between P and Ce (-0.4578) also suggests moderate antagonistic effects, whereas W and Ce have a negligible positive interaction (0.189).

In contrast to RFO, the TLBO algorithm displayed a slightly weaker positive interaction between Ni and W (0.1645), and a strong positive correlation between W and Ce (0.6928), which was absent in the RFO map. Additionally, TLBO showed nearly no relationship between P and Ce (0.01496), whereas RFO demonstrated a moderately antagonistic relationship (-0.4578). The TLBO algorithm focuses more on fostering cooperative relationships between parameters, particularly involving Ce, than RFO. WOA showed a strong negative interaction between Ni and W (-0.9341), highlighting the significant

antagonism that is not seen in RFO, where the relationship is positive. Similarly, WOA displays a negligible interaction between W and Ce (0.001581), whereas RFO exhibits a slightly stronger positive interaction (0.189). WOA also revealed a stronger negative interaction between Ni and P (-0.5411) compared to RFO (0.311), where it was weakly positive.

The RFO algorithm appears to balance cooperative and antagonistic relationships more evenly than the TLBO and WOA. The strong positive interaction between Ni and W in RFO suggests that these parameters are critical for obtaining the optimal solutions. Additionally, the moderate antagonistic interactions involving Ce indicate that careful adjustment of this parameter is required to avoid conflict with other variables. Overall, RFO demonstrates a unique pattern of parameter interactions, which sets it apart from the TLBO and WOA algorithms in terms of how it handles multi-objective optimization.

4.5.3.5 Optimized input parameters and predicted responses

Multi-objective optimization was performed using three hybrid ANN-based metaheuristic algorithms: ANN-TLBO, ANN-WOA, and ANN-RFO. The optimized input parameters and corresponding predicted responses, surface roughness (Ra), microhardness (HV), fouling weight (FW), surface free energy (SFE), and protection efficiency (PE) are summarized in Table 4.10.

Table 4.10. Optimized input parameters and predicted responses.

Algorithm	Input parameters				Responses				
	Ni (g/L)	P (g/L)	W (g/L)	Ce (mg/L)	Ra (μm)	HV (0.05)	FW (g/m^2)	SFE (J/m^2)	PE (%)
ANN-TLBO	40	29.32	16.61	7.47	0.120	718.71	54.91	15.69	95.96
ANN-WOA	40	38.39	20.56	9.68	0.115	708.01	57.46	15.45	94.09
ANN-RFO	40	29.33	16.40	7.39	0.117	717.14	54.57	15.49	96.15

4.5.4 Experimental validation of predicted responses and deviation analysis

The predicted input parameters and their corresponding response values for all algorithms are presented in Table 4.11. Coatings were applied using these input parameter settings, and

the coated samples were subsequently characterized to obtain the experimental response values, which are also included in the same table.

Table 4.11. Predicted and experimental values of process responses with corresponding input parameters for different optimization algorithms.

Algorithm			RSM	ANN-TLBO	ANN-WOA	ANN-RFO
Input parameters		Ni	39.37	40	40	40
		P	29.62	29.32	38.39	29.33
		W	15.98	16.61	20.56	16.4
		Ce	8.08	7.47	9.68	7.39
Responses	Surface roughness (μm)	Predicted	0.107	0.12	0.115	0.117
		Experimental	0.128	0.123	0.514	0.118
	Microhardness (HV 0.05)	Predicted	733.21	718.71	708.01	717.14
		Experimental	718.37	729.14	571.35	725.95
	Fouling weight (g/m^2)	Predicted	53.86	54.91	57.46	54.57
		Experimental	56.45	53.18	66.79	52.07
	Surface free energy (J/m^2)	Predicted	15.02	15.69	15.45	15.49
		Experimental	19.43	16.31	21.82	15.97
	Protection efficiency (%)	Predicted	99.14	95.96	94.09	96.15
		Experimental	95.81	97.86	78.12	98.73

To facilitate the error comparison across the four algorithms (RSM desirability function, ANN-TLBO, ANN-WOA, and ANN-RFO), the percentage deviation for each response was calculated by comparing the predicted and experimental values using the Equation 4.18:

$$Deviation\ (\%) = \frac{|Predicted\ Value - Experimental\ Value|}{Experimental\ Value} \times 100 \qquad (4.18)$$

Table 4.12 summarizes the percentage deviation results. To visually assess the accuracy of each optimization algorithm in predicting the response values, scatter plots were created, as shown in Figure 4.21. The proximity of the data points to the $y = x$ line indicates the accuracy of the predictions, with points closer to the line reflecting better agreement

between the predicted and experimental values. The analysis combining the input parameters and response values, percentage deviations, and scatter plots provides a comprehensive comparison of the performances of the four optimization algorithms.

Table 4.12. Percentage deviation between predicted and experimental response values.

Response	RSM	TLBO	WOA	RFO
Surface roughness (μm)	16.41	2.44	77.63	0.85
Microhardness (HV 0.05)	2.07	1.43	23.92	1.21
Fouling weight (g/m^2)	4.59	3.25	13.97	4.8
Surface free energy (J/m^2)	22.70	3.8	29.19	3.01
Protection efficiency (%)	3.48	1.94	20.44	2.61
Mean % Deviation	9.85	2.57	33.03	2.5

The percentage deviation of the surface roughness highlights the superiority of RFO, which achieved the lowest deviation (0.85%) and was closely aligned with the experimental values. The scatter plot further supports this, as the data point for RFO lies closest to the $y = x$ line. In contrast, the WOA demonstrated a significant deviation of 77.63%, indicating notable overestimation. The RSM desirability function and TLBO perform moderately, with deviations of 16.41% and 2.44%, respectively, but fall short of the precision of RFO.

In terms of microhardness, RFO outperformed the other algorithms with a minimal deviation of 1.21%, underscoring its accuracy in maximizing this response. TLBO also shows strong performance, with a deviation of 1.43%, making it a close second. The RSM desirability function achieved reasonable accuracy (2.07%), whereas the WOA prediction was considerably off, with a deviation of 23.92%. This discrepancy is visually evident in the scatter plot, where the WOA data point is far from the $y = x$ line.

The RSM desirability function also performed well in terms of fouling weight, with a deviation of 4.59%. However, the WOA again underperforms, with a deviation of 13.97%, highlighting its limitation in accurately predicting this parameter.

To minimize the surface free energy, RFO achieved a deviation of 3.01%, followed by TLBO at 3.80%. The RSM desirability function demonstrated a much larger deviation of 22.70%, indicating relatively poor prediction accuracy. The WOA, with the highest deviation of 29.19%, further emphasized its lack of reliability in this response.

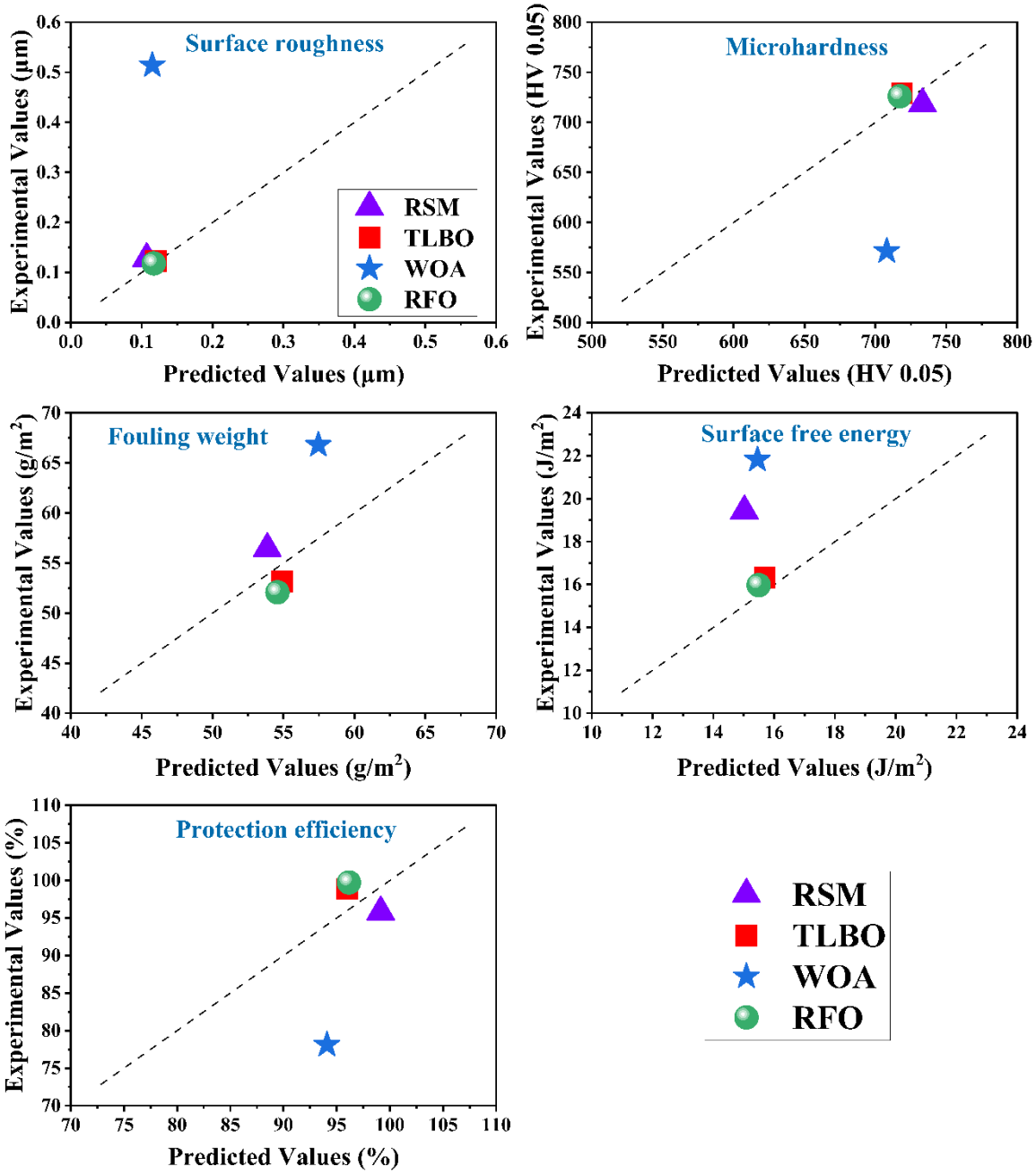

Figure 4.21. Scatter plots comparing predicted and experimental response values.

To maximize the protection efficiency, TLBO achieved the best result, with a deviation of 2.93%, followed closely by RFO at 3.59%. The RSM desirability function exhibits a deviation of 3.48%, reflecting a competitive but slightly less accurate prediction. However, the WOA again struggles with a significant deviation of 20.44%.

The overall performance of the algorithms was summarized by their mean percentage deviations. RFO achieved the lowest mean deviation of 2.69%, followed closely by TLBO, at 2.77%. The RSM desirability function, with a mean deviation of 9.85%, demonstrated a

moderate performance, whereas the WOA exhibited the highest deviation of 33.03%, underscoring its weaker predictive accuracy across all responses.

The combined analysis of the tables and scatter plots unequivocally established RFO as the most effective optimization algorithm, delivering consistently accurate predictions with the lowest percentage deviations across most responses. Its performance is particularly suitable for surface roughness and microhardness, and its predictions closely align with experimental values. TLBO has emerged as a strong competitor, particularly in terms of the fouling weight and protection efficiency. Although the RSM desirability function provides reasonable accuracy for certain responses, its overall performance is less consistent than those of RFO and TLBO. By contrast, the WOA demonstrated significant predictive inaccuracies across all responses, as evidenced by its high deviations and scatter plot outliers. This comprehensive evaluation highlights RFO as the preferred algorithm for multi-objective optimization, with TLBO being a reliable alternative for specific responses.

4.5.5 Analysis of optimized coating

This study compares the best coating surface obtained from CCD experiments with that achieved through optimization. The optimal coating surface was identified using the ANN-RFO algorithm, which is referred to as the optimized coating in this subsection. The surface morphology of the coating from the CCD experiment with the lowest surface roughness (22^{nd} run) and the optimized coating are shown in Figure 4.22(a) and (b), respectively. Both surfaces are free of defects, such as pores, cracks, or pinholes, and exhibit a compact structure with a distinct nodular microstructure.

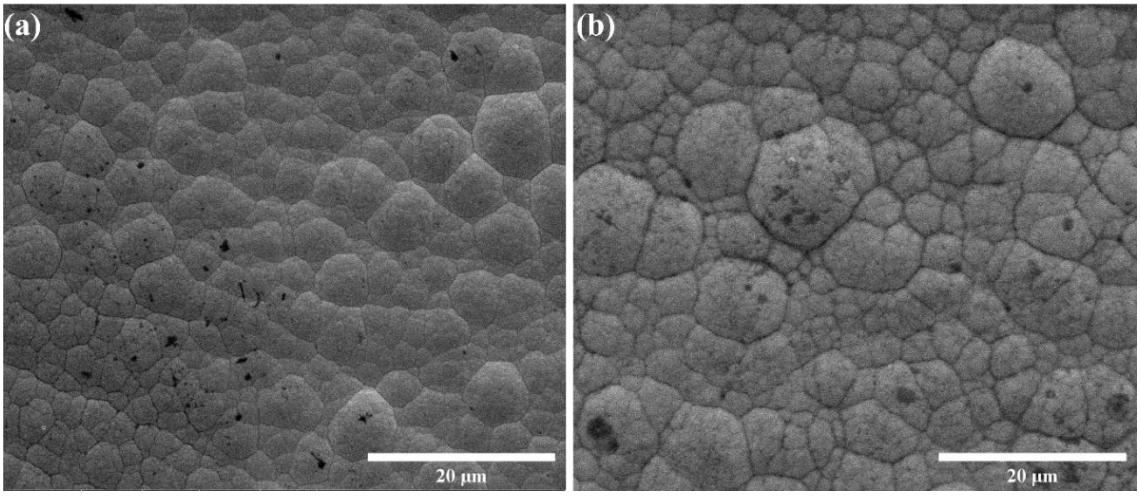

Figure 4.22. Surface morphologies of coatings from (a) CCD and (b) RFO optimizations.

The experimental surface roughness values obtained from the CCD experiments ranged from 0.23 µm to 1.28 µm. Subsequent optimization using the RSM reduced the surface roughness to 0.13 µm. Further improvements were achieved with metaheuristic algorithms: TLBO and RFO optimization both produced a minimum roughness of 0.12 µm, while WOA achieved a roughness of 0.51 µm. Figure 4.23 illustrates the 3D surface profiles of the coating before and after optimization. The surface obtained from the CCD experiment at 0.23 µm (Figure 4.23a) exhibits more pronounced surface irregularities compared to the smoother surface of the best optimized coating (0.12 µm, Figure 4.23b).

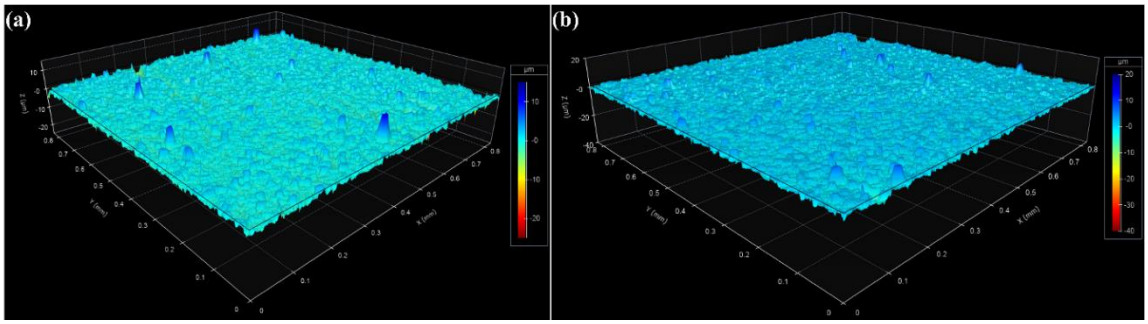

Figure 4.23. 3D surface profiles of coating samples: (a) as-deposited coating from the CCD experiment and (b) optimized coating after RFO optimization.

Figure 4.24 illustrates the difference in Vickers microhardness between the coating obtained from the best CCD experimental run and the coating optimized using the ANN-RFO algorithm. The CCD-based coating exhibited a microhardness of 689.8 HV 0.05, whereas the optimized coating achieved a higher value of 726 HV 0.05. The improvement in hardness suggests that the ANN-RFO approach successfully identified the process parameters that enhanced the mechanical strength of the coating.

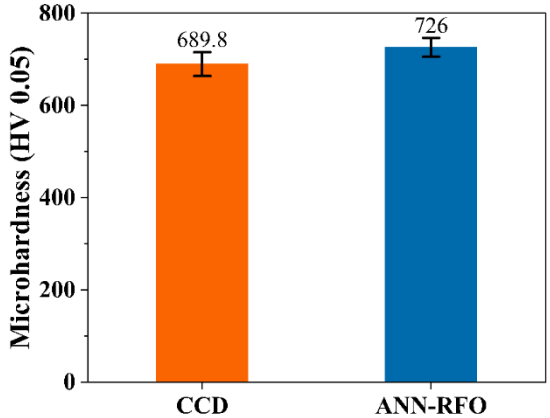

Figure 4.24. Comparison of microhardness (HV 0.05) between the best CCD experimental coating and optimized coating.

The fouling weight from the CCD experiments varied between 59.01 and 110.11 g/m^2. Post-optimization, RFO achieved the lowest experimental fouling weight of 52.07 g/m^2, followed by TLBO with 53.18 g/m^2, both outperforming the CCD minimum. The RSM desirability function also reduced the fouling weight to 56.45 g/m^2, which was slightly lower than the CCD minimum, indicating a moderate improvement. In contrast, the WOA failed to achieve a significant reduction, with a fouling weight of 66.79 g/m^2, which was within the CCD range but higher than the CCD minimum. The fouling weight per unit area for the uncoated low-carbon steel substrate was measured at 145.43 g/m^2, whereas the optimized coated sample exhibited a significantly lower fouling weight, highlighting the enhanced antifouling performance of the coated surface.

The fouling behavior also showed distinct differences in surface morphology. As shown in Figure 4.25, the surface morphology of fouling on both the uncoated substrate and the optimized coated sample was examined after 20 h of fouling adhesion in boiling water. On both surfaces, fouling was uniformly distributed, with microstructures primarily composed of needle-shaped aragonite-phase calcium carbonate [172]. No other calcium carbonate phases, such as calcite, were observed. However, the uncoated substrate exhibited quadrangular and spherical ferric oxides, which are corrosion products clustered into spherical shapes. These corrosion products exacerbate fouling deposition on the uncoated substrate by creating a severely corroded surface, further promoting fouling accumulation [173].

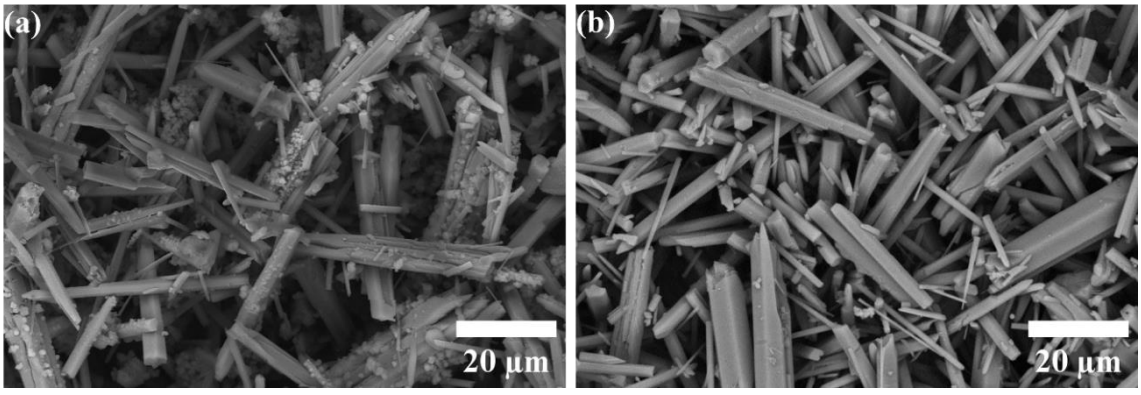

Figure 4.25. Surface morphology of the fouling surface: (a) substrate and (b) optimized coated sample.

In contrast, the optimized Ni-W-P-Ce coating lacks these corrosion products, resulting in improved antifouling performance. The looser structure of aragonite on the coated surface facilitates easier removal compared with the denser fouling scales on the uncoated

substrate [174]. This finding is consistent with prior studies, such as Ren et al. [165], who observed that electroless Ni-W-P coatings reduce fouling adhesion in solar collectors (mild steel, 1015) by lowering the surface free energy. Specifically, the presence of tungsten in the coating significantly reduces the surface free energy, thereby inhibiting the adhesion of fouling materials, such as calcium carbonate ($CaCO_3$). The surface free energy (SFE) observations presented in Table 4.3 further corroborate these findings. The SFE of the uncoated substrate was measured at 31.97 J/m^2, indicating a higher tendency for fouling adhesion. The lower SFE of the Ni-W-P-Ce coating contributes to its superior antifouling properties by reducing the adhesive forces between the fouling materials and the surface. Overall, the combination of reduced corrosion products, lower surface free energy, and easier removal of aragonite scales underscores the effectiveness of the Ni-W-P-Ce coating in mitigating fouling adhesion compared to uncoated low-carbon steel.

The elemental composition of the resulting fouling was analyzed using EDS. The obtained results, summarized in Table 4.13, reveal distinct differences in the elemental composition of fouling between the two samples, which is indicative of the impact of the coating on fouling behavior. Fouling on an uncoated low-carbon steel substrate shows a predominance of calcium and iron. This indicates significant scaling caused by calcium-based compounds, such as calcium carbonate or calcium sulfate, which are commonly found in tap water during boiling. The presence of oxygen further supports the formation of oxides and hydroxides. Trace amounts of chlorine and sulfur suggest the potential inclusion of chloride or sulfate salts in the fouling layer.

Table 4.13. Elemental composition of fouling (wt.%).

Elements	O	S	Cl	Ca	Ni	W	P	Ce	Fe
Substrate	16.34	1.85	2.05	48.52	-	-	-	-	31.24
Coating (RFO)	16.76	1.57	0.29	70.25	5.27	3.62	1.63	0.61	-

The fouling on the electroless Ni-W-P-Ce coated sample demonstrates a markedly different composition. Ca remained the predominant element, indicating that scaling was a significant phenomenon. However, the absence of iron (Fe) in the fouling layer highlights the protective role of the coating, which effectively prevents substrate exposure and the subsequent Fe oxidation or dissolution. Coating elements, such as nickel (5.27 wt.%), tungsten (3.62 wt.%), phosphorus (1.63 wt.%), and cerium (0.61 wt.%), are also detected in the fouling layer. This indicated that the coating remained intact and interacted with the

fouling environment. The presence of Ni and W contributes to the anti-corrosive and antifouling properties of the coating, whereas Ce, a rare earth element, enhances scaling resistance through its catalytic effect on surface passivation [99]. Furthermore, the reduced chlorine and sulfur contents in the fouling on the coated sample indicate a lower tendency for chloride or sulfate salt deposition. The elemental mapping of the fouling layer on the RFO-optimized electroless Ni-W-P-Ce coated sample is also shown in Figure 4.26, which provides a spatial distribution of the elements deposited during fouling. The mapping revealed the uniform dispersion of key coating elements, such as Ni, W, P, and Ce, confirming the integrity and consistency of the coating, even in a fouling environment.

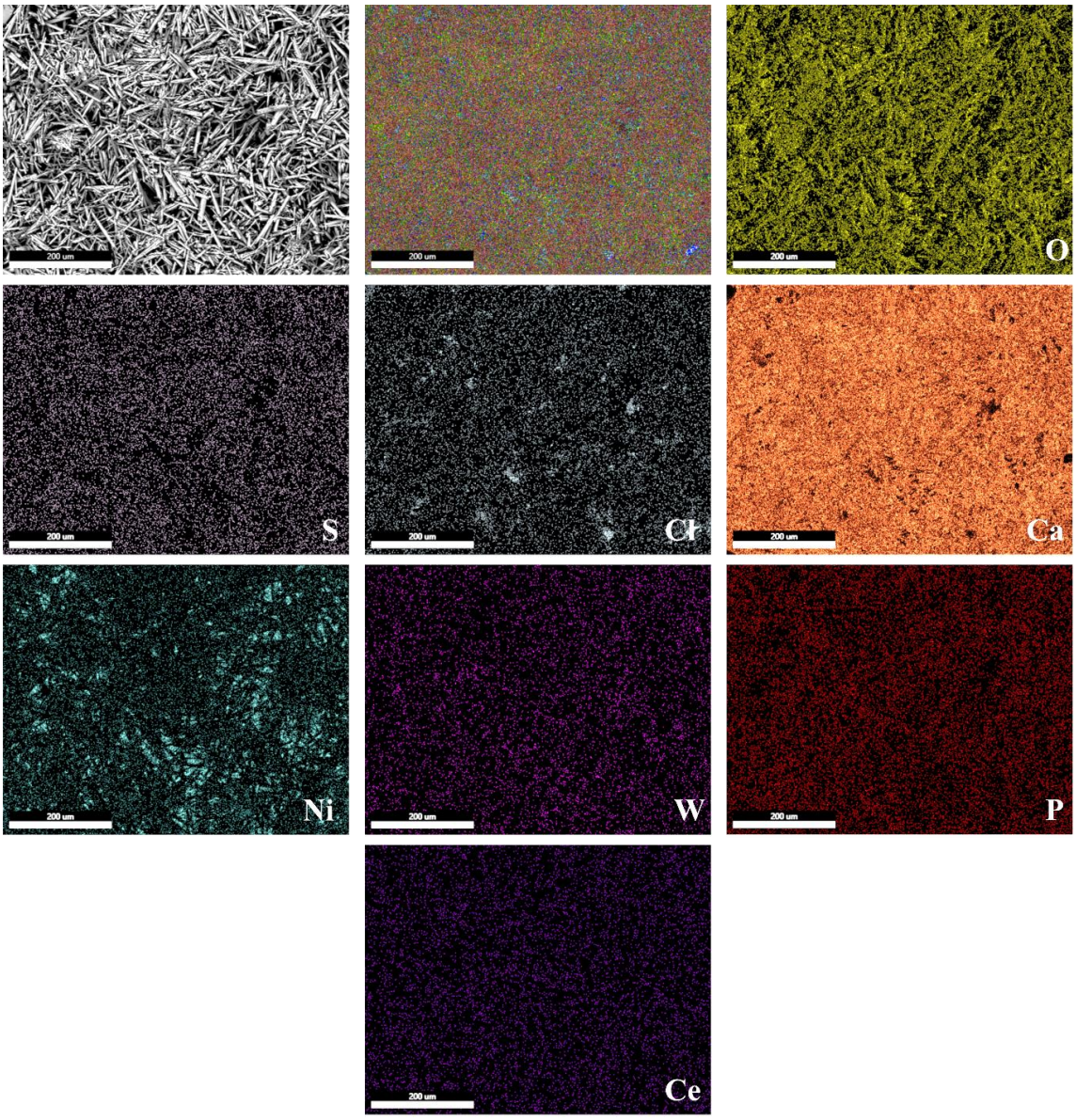

Figure 4.26. EDX mapping images of the fouling surface of the optimized coating sample.

The XRD patterns of the fouling scales deposited on the substrate and optimized Ni-W-P-Ce coating are shown in Figure 4.27. The analysis revealed that the majority of peaks, which are not explicitly marked in the graph, correspond to the aragonite phases of calcium carbonate. In addition, a few peaks representing the calcite phase and one peak corresponding to the nickel-iron phase were identified, which are denoted by specific symbols. All peak positions are listed in Table 4.14.

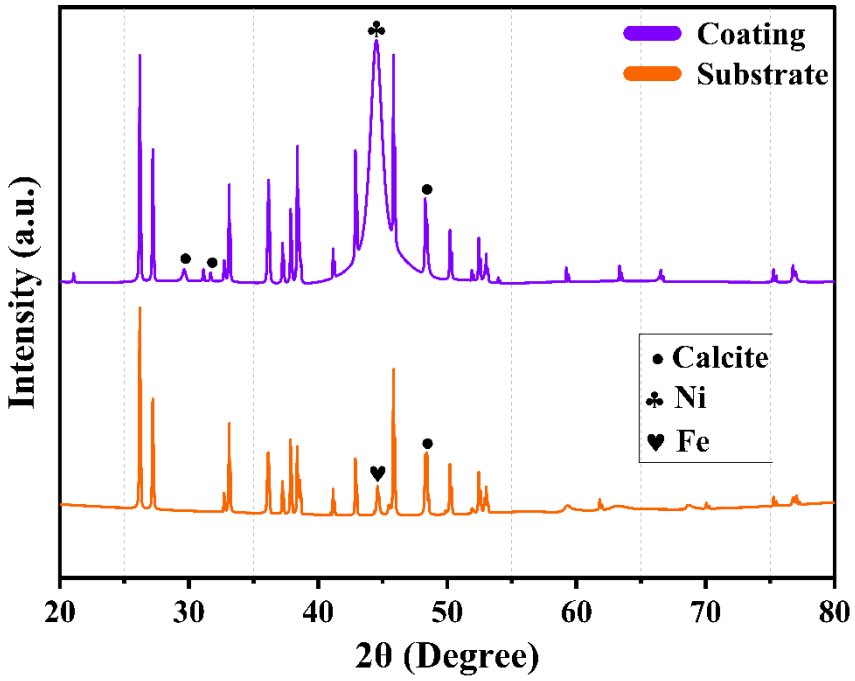

Figure 4.27. X-ray diffraction patterns of fouling.

Table 4.14. Analysis of the XRD spectra of fouling.

		XRD peaks, 2θ (°)
Aragonite	Substrate	26.19, 27.19, 32.73, 33.12, 36.14, 37.86, 38.39, 42.88, 45.82, 48.29, 50.2, 52.44, 52.87, 61.96
	Coating	26.19, 27.19, 31.11, 32.73, 33.12, 36.16, 37.86, 38.39, 42.89, 45.84, 48.29, 50.21, 52.44, 63.5
Calcite	Substrate	48.42
	Coating	29.62, 31.66, 48.42

The presence of both the aragonite and calcite phases in the fouling layer confirms that calcium carbonate scaling occurred during the boiling process, a well-documented phenomenon commonly observed in water heaters and boilers. These results are consistent with previous literature [175–177]. A highly intense Ni peak was observed in the fouling

layer of the Ni-W-P-Ce-coated sample, indicating that the fouling layer on the coated surface was relatively thin. Conversely, a very low intensity Fe peak was detected on the substrate, suggesting significant fouling deposition. The dominance of the aragonite polymorph of calcium carbonate on the fouling scale was further corroborated by SEM imaging, which provided a clear visual confirmation of its morphology. This comparative analysis highlights the improved fouling resistance of the Ni-W-P-Ce coating owing to its ability to minimize scale deposition.

The CCD experiments recorded surface free energy values ranging from a minimum of 15.02 J/m^2 to a maximum of 34.15 J/m^2. Among the optimized results, RFO achieved a surface free energy of 15.97 J/m^2, which was closest to the CCD minimum, showing a considerable reduction. TLBO, followed by a surface free energy of 16.31 J/m^2, indicating moderate improvement. The RSM desirability function resulted in a surface free energy of 19.43 J/m^2, whereas WOA performed the worst at 21.82 J/m^2, which was far from the minimum within the CCD range. These results underline the effectiveness of RFO in minimizing the surface free energy, with TLBO performing reasonably well.

The corrosion protection efficiency in the CCD experiments varied from 45.01% to 94.21%. After optimization, all algorithms, except the WOA, achieved significant improvements. RFO recorded the highest experimental protection efficiency of 98.73%, followed closely by TLBO with 97.86% and the RSM desirability function with 95.81%, all exceeding the CCD maximum. However, the WOA managed only 78.12%, which was within the CCD range but was substantially lower than the CCD maximum. The results indicate that RFO and TLBO are exceptionally effective in enhancing corrosion protection efficiency.

A comparison of the responses highlights the significant benefits of using ANN-trained metaheuristic algorithms for optimization. Both RFO and TLBO consistently outperformed the baseline CCD results for all the responses. RFO has emerged as the most effective algorithm, achieving superior performance in minimizing fouling weight and surface free energy, while maximizing microhardness and protection efficiency. TLBO followed closely, excelling in microhardness and protection efficiency optimization. The RSM desirability function provided balanced but slightly lower improvements compared to the metaheuristic algorithms. WOA, on the other hand, showed limited success and failed to

outperform the CCD baseline for certain responses, such as microhardness and protection efficiency.

4.6 Closure

This study investigated the optimization of the electroless Ni-W-P-Ce coating parameters using various multi-objective optimization techniques. The research employed the response surface methodology with a central composite design along with three metaheuristic algorithms: teaching-learning-based optimization, whale optimization algorithm, and red fox optimization. Artificial neural networks were integrated with metaheuristic algorithms to enhance the prediction accuracy and optimization efficiency of the coating process. This combination leveraged the learning capabilities of ANNs to model the complex relationships between the input parameters and coating properties, whereas metaheuristic algorithms efficiently explored the solution space.

Among all the optimization methods employed, the hybrid ANN-RFO algorithm delivered the most effective coating results, exhibiting a minimal deviation between the predicted and experimental values. The RFO algorithm stood out for its superior convergence speed, prediction accuracy, and capability to optimize multiple objectives. It consistently outperformed both the TLBO and WOA across various performance metrics. Additionally, RFO showed marked improvements over the baseline CCD results for all measured responses, underscoring the advantages of integrating machine learning with optimization techniques. Sensitivity analysis identified nickel sulfate and sodium tungstate concentrations as the most influential parameters affecting the coating characteristics, offering valuable insights for process control and optimization. Similarly, the RSM approach confirmed that these two components are key factors impacting the coating properties. Through the desirability function approach within RSM, optimal parameter settings were determined, achieving a composite desirability score of 1, indicating successful simultaneous optimization of all targeted responses. The optimized Ni-W-P-Ce coating demonstrated significantly enhanced antifouling performance compared to the uncoated substrate, with a 64% reduction in fouling weight and improved surface morphology. Other key properties, including the surface roughness, microhardness, surface free energy, and corrosion resistance, also showed notable improvements following optimization.

Chapter 5 Influence of cerium concentration and heat treatment on functional properties of Ni-W-P-Ce coatings

This chapter provides a comprehensive analysis of how cerium incorporation and heat treatment can be used to tailor the functional properties of Ni-W-P electroless coatings to improve their performance in applications requiring wear, corrosion, and microbial resistance.

5.1 Experimental details

5.1.1 Coating bath preparation

Six distinct coatings were prepared by varying the concentration of ceric sulfate, while keeping all other chemical concentrations constant. The bath compositions and operating conditions are listed in Table 5.1. The electroless Ni-W-P-Ce coatings derived from baths containing 0, 2, 5, 8, 11, and 14 mg/L of cerium salt are referred to as Ce0, Ce2, Ce5, Ce8, Ce11, and Ce14, respectively.

Table 5.1. Chemical composition, functions, and operating conditions.

Chemical	Function	Concentration	Conditions
$NiSO_4.6H_2O$	Metal salt	40 g/L	Temp.: 75 ± 2 °C
$Na_2WO_4.2H_2O$	Metal salt	15 g/L	pH: 7.5 ± 0.2
$Ce(SO_4)_2.4H_2O$	Metal salt	0, 2, 5, 8, 11, and 14 mg/L	Time: 2 hours
$NaH_2PO_2.H_2O$	Reducing agent	30 g/L	
$Na_3C_6H_5O_7.2H_2O$	Complexing agent	20 g/L	
CH_4N_2S	Stabilizer	0.001 g/L	

5.1.2 Coating characterization

Deposition rates were calculated for all samples by measuring the weight difference before and after coating, using Equation 3.1 provided on page 37, and the coating thickness was estimated using the weight gain method given in Equation 5.1, as well as the metallographic method according to the EN ISO 1463:2021 standard [178,179].

$$t = \frac{100.(G2 - G1)}{\rho.F} \tag{5.1}$$

In this equation, t is the coating thickness in μm, G1 and G2 are the weights of the sample before and after coating, respectively, in grams, ρ is the density of the deposited coating in g/cm^3, and F is the total surface area of the substrate in dm^2. The deposition density was calculated using the formula given in Equation 5.2.

$$Deposition\ density = \sum_{1^{st}element}^{n^{th}\ element} (elemental\ density \times weight\ percent) \quad (5.2)$$

The elemental densities (in g/cc at standard temperature and pressure) of Ni, P, W, Ce, and O are 8.9, 1.823, 19.3, 6.77, and 0.001308, respectively [180]. The weight percentages were calculated by EDS, as reported later. An optical microscope (BX53M, Olympus) was used to measure the thickness of the coating.

Field-emission scanning electron microscopy was used to analyze the microstructural morphology. Elemental mapping was performed using EDX coupled with FESEM.

Structure and phase analyses of the samples were performed in the scan range of 10-80° using an X-ray diffractometer (XRD, Bruker D8 Advance) equipped with a 0.15418 nm X-ray. Using the Debye-Scherrer equation (Equation 5.3), the crystallite size was determined from the XRD data with the peaks assumed to be of Gaussian shape-

$$Crystallite\ size, D = \frac{K\lambda}{\beta\ cos\ \theta} \quad (5.3)$$

Where K is the Scherrer constant (0.98), λ is the wavelength, and β is the full width at half maximum (FWHM) of the detected peaks. The surface chemical compositions of the samples were analyzed using PS (FEI PHI 5000 Versa Probe II). The acquisitions consisted of wide scans in the binding energy range of 1200-0 eV. High-resolution core line spectra were obtained by setting the analyzer pass energy at 23.5 eV and the energy step at 0.025 eV/0.05 eV, 50 ms time per step, and 10 cycles. The radiation source was Al Kα (1486 eV). All binding energies were normalized to the reference C1s core level (binding energy of 284.79 eV).

The topographical characteristics of the coated surfaces were measured using an optical profilometer (Zygo Newview9000), and the data were analyzed using Mx. For surface energy estimation, the Owens and Wendt geometric mean approach [145] was adopted, in which the surface free energy is given by (Equations. 5.4-5.5)-

$$y_L(1 + cos\,\theta) = 2(\sqrt{y_S^d y_L^d} + \sqrt{y_S^p y_L^p}) \quad (5.4)$$

$$y_S = y_S^d + y_S^p \quad (5.5)$$

Where $y_L, y_S, y^d, y^p,$ and θ are the surface tension of the test liquid, surface free energy of the solid surface, dispersion component, polar components, and surface contact angle, respectively. Contact angles of the surfaces with two test liquids, namely, distilled water (y_L=0.0728 J/m^2, y^d=0.0218 J/m^2, y^p=0.051 J/m^2) and ethylene glycol (y_L=0.048 J/m^2, y^d=0.029 J/m^2, y^p=0.019 J/m^2) were measured with the help of a goniometer (KYOWA FAMAS), and the average of three measurements on each sample was used to determine the surface free energy.

5.1.3 Microhardness and scratch resistance

The Vickers microhardness of the coating at five different locations was measured with an indentation load of 100 gf and dwell time of 10 s.

A scratch test was performed on a universal tribometer (MFT 5000, Rtec Instruments, USA) using a diamond indenter with a tip radius (R) of 0.2 mm and apex angle (2θ) of 120° as the counter body to determine the adhesion strength between the coating and substrate layer. The indenter was made to slide on the coated surface under a constant load of 3 N, scratch velocity of 0.2 mm/s, run time of 20 s, and a scratch length of 5 mm. The average scratched areas were calculated using OmniSurf3D software by analyzing the 3D surface texture collected with an optical profilometer, and the scratch volume loss was estimated by multiplying the average scratched area by the total scratch length. The scratch hardness (H_S), an indicator of the coating's capacity to withstand plastic deformation or scratching, was determined from the scratch testing results using the following relationship (Equation 5.6)-

$$H_S = \frac{8F}{\pi W^2} \quad (5.6)$$

where F is the magnitude of the applied load and W is the width of the scratch [181].

Furthermore, the fracture toughness (K_C) of the coating was assessed by analyzing the scratch data using Equation 5.7, derived from linear elastic fracture mechanics [182]. This

equation was employed to estimate the fracture toughness when dealing with very small penetration depths, as was the case in this study.

$$K_C = \frac{F_X}{4d\sqrt{\frac{2}{3}R}} \quad if\ d \ll R \tag{5.7}$$

Here, F_X represents the average tangential or lateral force recorded during scratching, and d is the depth of penetration from the sample surface. Because the sphere-to-cone transition depth (= R(1-Sinθ) for the indenter tip radius R and apex angle 2θ) was approximately 26.8 μm, the penetration depths remained smaller than the sphere-to-cone transition depth across all the samples in our study, indicating that only the spherical region made contact with the sample in all scratch tests, and the cone region of the indenter did not contribute to deformation, aligned with the conditions under which this fracture toughness formula operates.

5.1.4 Wear resistance

A ball-on-flat linear reciprocating tribological test was performed using a universal tribometer under unlubricated conditions using a 5 mm diameter 316 stainless steel ball as the counter body. All wear experiments were performed at a normal load of 5 N, frequency of 3 Hz, and stroke length of 5 mm under ambient conditions (300 K). The coefficient of friction was recorded for a total time of 300 s (total sliding distance of 9 m). In addition, the wear volume and morphology of the worn surfaces were investigated using a non-contact 3D optical profilometer and scanning electron microscope, respectively. The average of the three cross-sectional worn areas was multiplied by the stroke length to calculate wear volume.

5.1.5 Corrosion resistance

The ability of the deposited coatings to resist electrochemical corrosion was evaluated using an electrochemical workstation as discussed in last chapter. For electrochemical impedance spectroscopy (EIS) analysis, a sinusoidal signal of ±10 mV was applied in the frequency range 10^{-2}-10^{5} Hz.

5.1.6 Biofilm formation

The extent of biofilm formation on different coated surfaces provides an estimate of their ability to protect components from microbial corrosion. The marine bacterial strain *P.* aeruginosa PFL-P1 was used for this purpose following the protocol described in a previous study [183]. The protocol involved growing Pseudomonas aeruginosa PFL-P1 biofilms on various samples by incubating bacterial cultures with the surfaces under controlled conditions. In brief, the surfaces were cleaned with 70% ethanol and inoculated in a six-well plate with 4 ml of 1:100 diluted bacterial strain maintained in Luria Bertani (LB) broth medium (Himedia, India). The samples were incubated at 37 °C for 48 h under static conditions, washed with PBS, and stained with 5 µmol/L Syto9 (Invitrogen, USA). The stained biofilms were imaged using a TCS SP8 confocal system (Leica Microsystems, Germany). The integrated intensity of the images, calculated using the FIJI software tool, was used as a semi-quantitative measure of biofilm growth.

5.1.7 Annealing of the depositions and subsequent property assessment

A tube furnace was used to heat treat the sample with 8 mg/L Ce content for an hour at three different temperatures: 200, 400, and 600 °C. These samples are referred to as Ce8/200, Ce8/400, and Ce8/600, respectively, in the remainder of the manuscript. In all cases, the time from room temperature to the annealing temperature was set to one hour using a proportional-integral-derivative (PID) controller attached to the furnace, and the samples were kept at a constant temperature for the next hour. The samples were then cooled to room temperature in the same furnace.

Microhardness, roughness, wettability, FESEM, XRD, corrosion, scratch, and wear tests were performed on the heat-treated samples. A ferroxyl reagent test (ASTM B689-97), which detects the presence of iron ions (Fe^{2+} and Fe^{3+}), was conducted to determine the porosity and pinholes in the heat-treated coatings [39][184]. Filter papers soaked in ferroxyl indicator solution (25 g/L potassium ferrocyanide + 15 g/L sodium chloride) were placed on the heat-treated samples, and any resulting color change was monitored. In the presence of cracks or holes, the solution can penetrate the coating to reach the base material, and a blue color emerges.

5.2 Results and discussion

5.2.1 Appearance of the as deposited and annealed coatings

A digital image of the substrate, coated samples, and heat-treated samples is shown in Figure 5.1, to visualize the surface appearance just before and after coating, as well as after heat treatment. In contrast to the shiny reflective surface of the polished substrate, all the as-coated samples exhibited a silver-grey appearance, typical of Ni. The appearance did not vary with different cerium concentrations; however, annealing resulted in a noticeable change. The color did not change noticeably after annealing at 200 °C (Ce8/200); however, the Ce8/400 coating had yellow-blue tinges, whereas the Ce8/600 coating was dark green and almost black. This change in color can be ascribed to the change in the thickness of the nickel oxide film [185]. At lower annealing temperatures, the oxide film was relatively thinner; however, higher temperatures led to thicker oxide films, thus affecting their appearance. These findings are consistent with the EDX results (Table 5.12), which revealed an increase in oxygen content with increasing heat-treatment temperature.

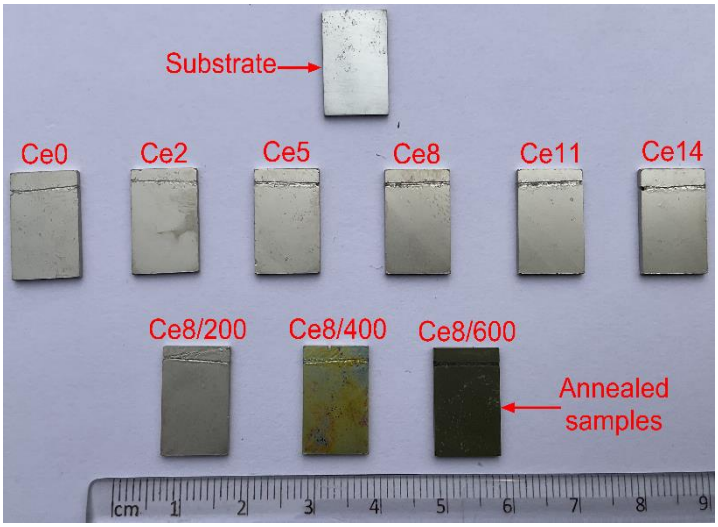

Figure 5.1. Digital images of the samples.

The driving force of the spontaneous electroless deposition process is the potential difference between the anodic and cathodic reactions, which proceeds under mixed-potential control. The possible cathodic half-cell reactions involved in the coating along with their standard electrode potentials (E°, in volts at standard temperature and pressure) are described below [180]. Accordingly, the dehydrogenation of hypophosphite ions occurs, resulting in the formation of metaphosphate ions, and the adsorbed active hydrogen reduces nickel on the steel surface. Simultaneously, some of the absorbed hydrogen atoms

reduce a small amount of hypophosphite to water, hydroxyl ions, and phosphorus (Equations 5.8-5.10) [186].

$$H_2PO_2^- + 3OH^- = HPO_3^{2-} + 2H_2O + 2e \quad (E° = -1.65) \quad (5.8)$$

$$Ni^{2+} + 2e = Ni \quad (E° = -0.257) \quad (5.9)$$

$$H_2PO_2^- + 2H^+ + e = P + 2H_2O \quad (E° = -0.508) \quad (5.10)$$

$$WO_4^{2-} + 6e + 4H_2O = W + 8OH^- \quad (E° = -1.06) \quad (5.11)$$

$$4Ce^{4+} + 2H_2O = 4Ce^{3+} + 4H^+ + O_2 \quad (E° = 1.715) \quad (5.12)$$

The reduction of tungsten occurs via the nickel catalytic surface (Equation 5.11), with sodium hypophosphite serving solely as the electron source, and the inclusion of tungsten in the Ni-P electroless deposition system does not directly affect the redox reaction between the nickel and hypophosphite ions [187]. The reduction of Ce^{4+} ions to Ce^{3+} ions by the freely available hydrogen atoms following the reaction given in Equation 5.12 leads to the accommodation of these ions in the coating [188]. Because the difference between the electrode potentials of $Ce(SO_4)_2$ and the reducing agent is too large, it is difficult for a redox reaction to occur between the ceric ions and the reducing agent; therefore, the addition of Ce ions is not expected to influence the deposition characteristics of the Ni-W-P coating [186].

5.2.2 Deposition rate

No discontinuities, cavities, porosity, or cracks were visible at the interface between the coating and substrate, as shown in the optical micrographs (Figure 5.2(a-b)) and scanning electron micrographs (Figure 5.2(c-d)) of the cross-sections of the coatings prepared with or without Ce. The thickness values estimated from the weight difference and measured from the optical images are shown in Figure 5.2(e). Figure 5.2(f) shows the calculated deposition rates.

The agreement between the estimated and measured thickness values indicated the uniformity of the deposited coatings. Both the coating thickness and the deposition rate displayed a similar increasing-decreasing trend with increasing Ce concentration in the bath, and both the thickness and deposition rate were the highest for Ce8.

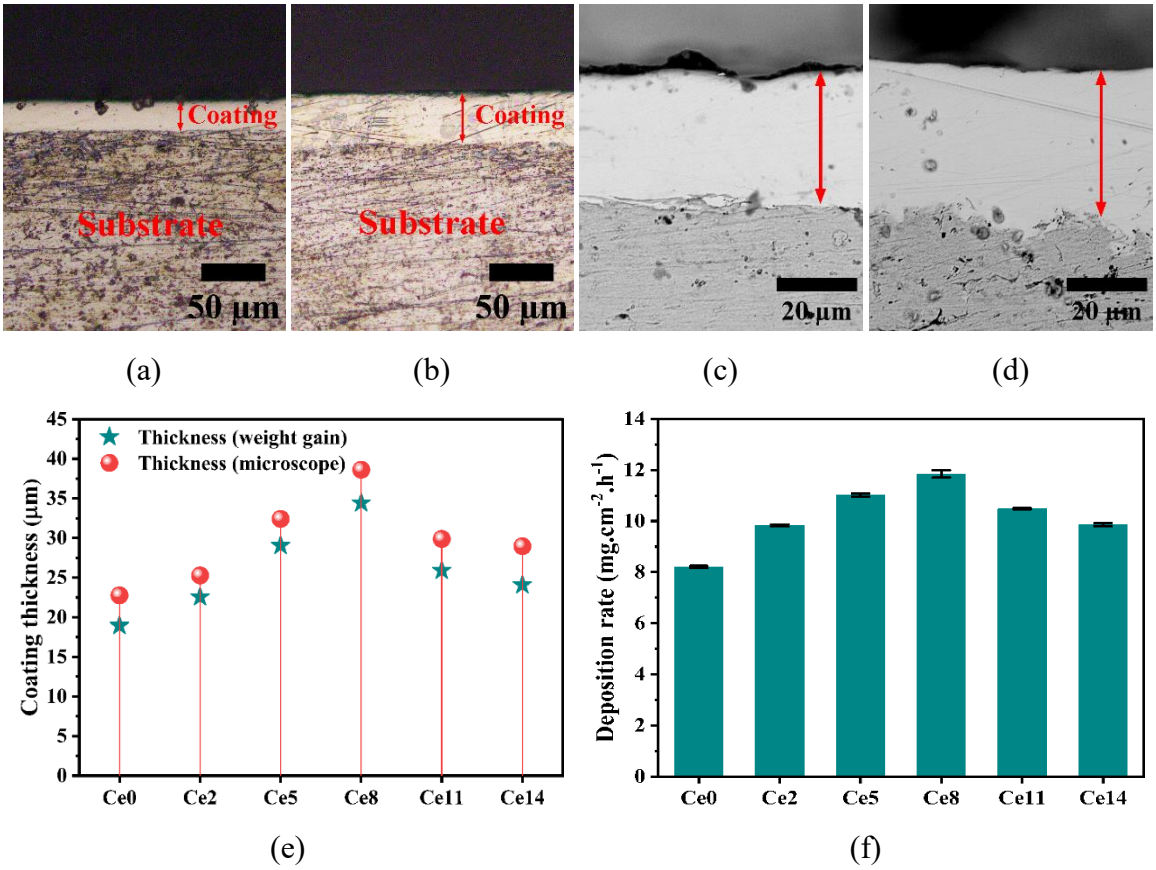

Figure 5.2. (a-b) Cross-sectional optical micrographs of Ce0 and Ce8 coatings, respectively; (c-d) Cross-sectional SEM micrographs of Ce0 and Ce8 coatings, respectively; (e-f) Effect of Ce concentration on the coating thickness and deposition rate.

The development of a dense coating, characterized by the absence of cracks, as observed in the cross-sectional images, results from a progressive stepwise process, as presented schematically in Figure 5.3. Initially, the Ni, W, P, and Ce ions must undergo nucleation on the substrate surface via the redox reactions mentioned in Equations (5.8)–(5.12). Ni^{2+} and WO_4^{2-} form stable complexes ($(Ni^{2+})_x(WO_4^{2-})_y.L_z$) with the complexing agent in the coating solution. These complexes then diffuse from the solution to the outer Helmholtz layer (OHL) as two different complexes, $(Ni^{2+}).L_m$ and $(WO_4^{2-}).L_n$. Gradually, these complexes dissociate into free Ni^{2+} and WO_4^{2-}, which then diffuse towards the inner Helmholtz layer (IHL). Free Ni^{2+} ions reach the IHL first and undergo reduction on the substrate surface, preceding the co-deposition of the Ni-W alloy coatings. Simultaneously, $H_2PO_2^-$ undergoes redox reactions for P deposition in the coating, facilitated or catalyzed by the presence of the Ni catalyst. Ce^{4+} ions are adsorbed

onto the substrate surface in their native form or after being reduced by free electrons to Ce^{3+}, which may act as active sites for further nucleation or deposition [105].

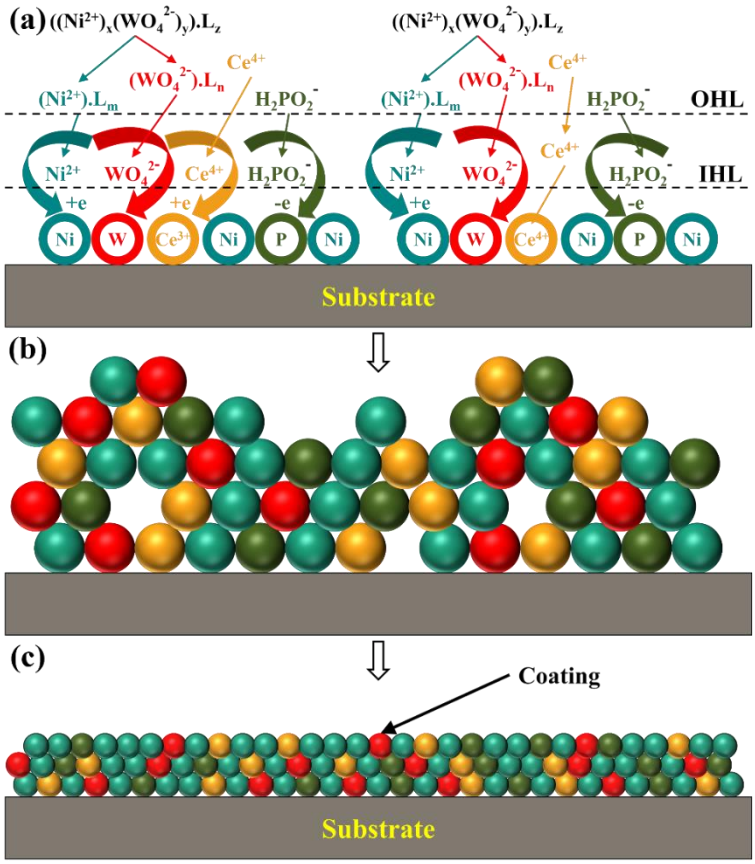

Figure 5.3. Schematic representation of the coating growth.

This nucleation step initiated the formation of primary cores or clusters (represented by hollow circles in Figure 5.3(a)) via electrochemical crystallization. Under the influence of interatomic forces, these clusters may gradually accumulate, increase in size, and align with the substrate surface. Subsequently, during the cluster growth and crystal regularity phases (Figure 5.3(b)), these clusters expanded following the typical growth patterns observed in metal crystals, resulting in the development of irregularly shaped nodules within the coating morphology. These clusters exhibited non-uniform growth perpendicular to the surface, displaying preferential growth patterns and aggregation. Finally, the process transitions into a macroscopic coating formation, and multiple clusters converge to form a macroscopic coating with a crystal lattice structure [128,189], as shown schematically in Figure 5.3(c).

As observed from the experimental results, the concentration of Ce ions can significantly alter the rate of coating deposition, and the influence of Ce on the deposition rate stems from multiple factors. It can be observed from the electrochemical reactions

mentioned earlier (Equations 5.8-5.12) that hydrogen is a by-product of the deposition process, and the adsorption of the gas onto the surface hinders the reduction reactions induced by the steel substrate, as well as the autocatalytic activities of the deposited Ni. Ce ions have high adsorption capabilities on metal surfaces [190–192] and, as surface-active elements, they can lower the surface energy of the substrate. This helps the H_2 gas bubbles escape from the surface [84] so that the reactant species present in the bath can come into contact with the deposited metal, and the autocatalytic reaction can proceed forward. The removal of hydrogen from the system also shifts the reaction kinetics towards the reduction of metal ions, accelerating the deposition rate. The lower surface energy in the presence of Ce ions can also facilitate the initial deposition of a thin Ni layer onto the substrate in the primary stage of coating deposition [193], which accelerates the later stages of the autocatalytic reaction. Furthermore, Ce ions adsorbed on the surface can act as nucleation sites for deposition to take place. An increased number of nucleation sites reduced the mean free path of the ions to collide with the formed nuclei, thereby increasing the probability of the ions to coalesce. Some researchers have also suggested that the 4f configuration of Ce promotes electron transfer between the metal ions and reducing agent, thereby promoting the rate of reduction reactions. These mechanisms enhance process efficiency and fast-track the deposition rate, as observed for Ce-containing coatings [96,194]. However, excessive accumulation of Ce on the surface limits the active surface area for reduction reactions to occur and can also consume more electrons for its own oxidation, resulting in a reduced deposition rate. A very high amount of surface-adsorbed Ce can also significantly reduce the surface energy and inhibit further nucleation on the surface. Additionally, at elevated concentrations, Ce may combine with hypophosphite ions to form neutral molecules, further impeding oxidation of the reducing agent and effectively poisoning the overall reaction [195]. Therefore, excess Ce can limit the deposition rate.

5.2.3 Microstructure of the deposition

No discernible defects such as cracks, pores, or cavities were observed on any of the surfaces, indicating the high integrity of the coatings. FESEM micrographs revealed the morphology of the deposition (Figure 5.4(a-f)), characterized by its resemblance to that of a cauliflower composed of a large central mass with many smaller floret-like nodules attached to it.

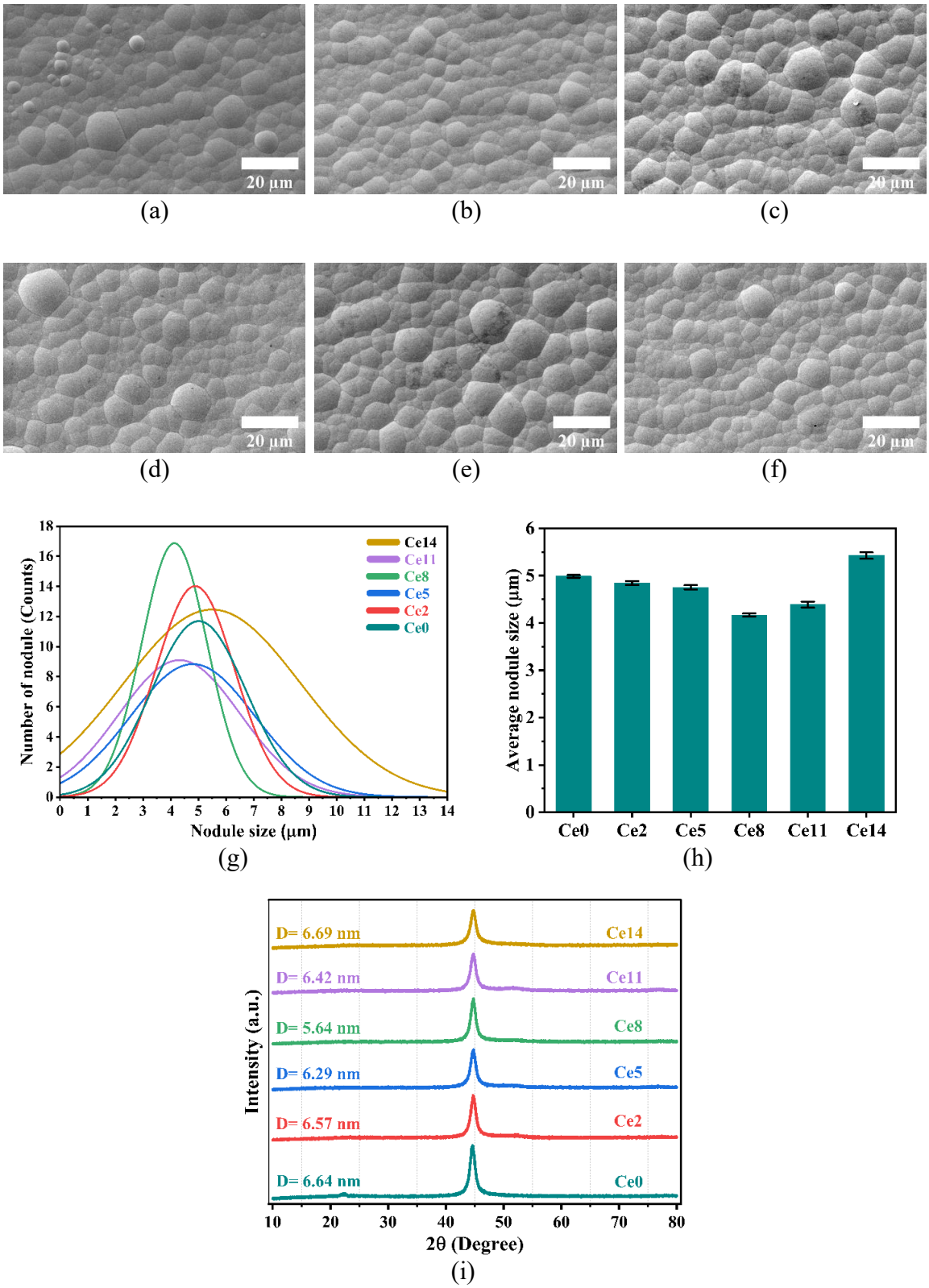

Figure 5.4. Microstructure of Ni-W-P-Ce coatings with different Ce contents: (a-f) Surface morphology of Ce0, Ce2, Ce5, Ce8, Ce11, and Ce14, respectively; (g) nodule size distribution; (h) average nodule size; and (i) XRD patterns of as-coated surfaces (D = Crystallite size).

Analysis of nodule sizes from the SEM images revealed that the size distribution of the nodules gradually shifted to lower values, and the peaks became sharper with increasing Ce content in the coating bath, indicating greater uniformity of the nodule sizes and smaller modal size. However, the trend was reversed as the Ce concentration increased beyond 8 mg/L (Figure 5.4(g)). This was also evident in the average nodule size (Figure 5.4(h)). A similar trend was observed for the crystallite size (calculated from the XRD spectra) (Figure 5.4(i)).

Because both the Ce-free (Ce0) coating and the Ce-containing (Ce2-Ce14) coatings had structurally similar morphologies, it can be assumed that the addition of Ce did not fundamentally alter the growth mechanism of the Ni-W-P coating. As experimentally observed by Vitry et al., the development of coatings is a sequential process [193,196] initiated by the oxidation of the reducing agent (phosphate salt in this case) induced by the steel substrate and the subsequent reduction of the Ni salt, creating a very thin continuous layer on the substrate. This initial layer drives autocatalytic reactions forward, and as a result, three-dimensional nucleation starts to occur in a cluster or island form (Volmer-Weber mode of growth), as mentioned earlier, where surface scratches and defects act as preferential sites for nucleation. Subsequently, the reduced metal ions from the bath accumulate around these nuclei, forming balloon-like nodules. As the process continued, the surface was packed with such nodules, and their lateral growth was restricted. This results in the formation of a dense coating that grows vertically. Secondary germination is also possible at this stage, causing branching and refinement of growing columns. Therefore, the close packing of such balloon-like nodules results in a cauliflower-like appearance on the top surface.

Therefore, a reduction in the average nodule size was directly correlated with an increase in the number of active sites on the substrate surface. Because the nodule formation process begins with surface roughness features, defects, or discontinuities, and all the surfaces received similar pre-treatment, the variation in the quantity of Ce was the only differentiator between them. Surface-adsorbed Ce can provide additional nucleation sites, and the dense distribution of such sites shortens the period of lateral nodule growth, thereby reducing the average nodule size [105,138]. The heterogeneity in nodule size indicates a non-uniform distribution of active sites as well as non-simultaneous nodule formation, where larger nodules are the result of sparsely spaced nucleation sites and early nucleation [197]. Such spatial and temporal variations in nodule formation are reduced in the presence

of surface-adsorbed Ce, which acts as an active site for deposition [96]. However, a very high quantity of Ce impedes the nucleation process as discussed earlier, resulting in larger and non-uniform nodules. Such a V-shaped trend in the influence of rare-earth element content on nodule size has been observed by previous researchers [138,198,199].

In the XRD spectra for all the depositions, a solitary peak was positioned in the range 44.6-44.8°, representing the (111) plane of the face-centered cubic structure of Ni (Figure 5.4(i)). The peaks for the Ce-containing coatings were slightly broader and had diminished intensity compared to the peak for the Ce0 coating, and this microstructural change serves as evidence of the successful integration of Ce into the Ni-W-P coating. As the P and W contents in the coating, as determined by EDX (Table 5.2), were within their solubility limits in Ni, they were incorporated as a solid solution within the Ni lattice, preventing the formation of distinct phases and the introduction of discernible diffraction peaks in the XRD pattern [200].

Table 5.2. Elemental composition of the coatings (wt.%).

$Ce(SO_4)_2$, mg/L	Ce	Ni	P	W	O
0 (Ce0)	0	91.3	5.6	2.5	0.6
2 (Ce2)	1.1	91.2	4.7	2.4	0.6
5 (Ce5)	1.3	90.6	4.8	2.6	0.7
8 (Ce8)	1.5	91	3.8	2.7	1.0
11 (Ce11)	1.8	90.3	4.5	2.7	0.7
14 (Ce14)	2.1	88.9	5.8	2.6	0.6

The calculated crystallite size (D) for all samples is presented in the same XRD Figure 5.4(i), with Ce8 exhibiting the smallest crystallite size of 5.64 nm. Here, crystallite size refers to the size of the individual crystalline regions or coherent scattering domains. Therefore, the presence of small diffraction coherent domains, that is, crystallites smaller than 10 nm, suggests that the coatings fall into the ultrafine/nanocrystalline regime [89]. Detailed X-ray diffraction (XRD) results, including the FWHM and corresponding d-spacing values for the peaks in all six samples, are provided in Table 5.3.

Considering the P content across all samples, it is apparent that the coatings were in the low-P category, and the quantity of P alone was not sufficient to induce significant distortion of the Ni lattice structure, resulting in a nanocrystalline structure. However, the

roles of the W and Ce atoms are also crucial. It is known that W acts in tandem with P in influencing the microstructural characteristics of electroless Ni-W-P coatings, and up to approximately 2% W can be positioned inside the Ni lattice for this purpose [201]. The incorporation of Ce, which has a significantly larger atomic radius of 0.1824 nm than those of Ni, W, and P (0.1246, 0.139, and 0.106 nm, respectively), can also cause lattice expansion, disturbing the long-range order and inducing some degree of amorphousness [109,136,138,202].

Table 5.3. Analysis of the XRD spectra.

Coating	Peak position, 2θ (°)	FWHM, β (°)	d-spacing (Å)	Crystallite size (nm)
Ce0	44.619	1.35075	2.0308	6.64
Ce2	44.748	1.36612	2.0252	6.57
Ce5	44.728	1.42661	2.0261	6.29
Ce8	44.75	1.59057	2.0251	5.64
Ce11	44.735	1.39754	2.0258	6.42
Ce14	44.736	1.34166	2.0257	6.69

5.2.4 Chemical composition of the deposition

EDX analysis and elemental mapping of the coating top surface indicated the well-distributed presence of Ni, W, P, and Ce in the coating (Figure 5.5), and elemental mapping of the coating cross-section (Figure 5.6) indicated the same.

Quantitatively, the amount of Ce in the coating exhibited a monotonically increasing relationship with Ce concentration in the bath (Table 5.2). The P content of all the coatings ranged from 3.8 to 5.8 wt.%, categorizing them as low-to-medium phosphorus electroless coatings. Interestingly, the quantity of P decreased with increasing Ce up to 8 mg/L, and both trends reversed after that threshold. A minute quantity of oxygen was detected in the samples, with Ce8 exhibiting the highest oxygen weight percentage of 1%. From the relevant literature on the electroless preparation of quaternary alloys, where a fourth element was introduced to the Ni-W-P system, it can be seen that such alloys typically have low quantities of P and W as compared to the ternary Ni-W-P. For example, the Ni-W-P-Cu coatings developed by Balaraju et al. [203] had 4.5-6.0% P, but the W content was higher than that in this study at 3.5-6.0% W, and the proportion of the fourth element (Cu) was also higher at 1.4-6.4%.

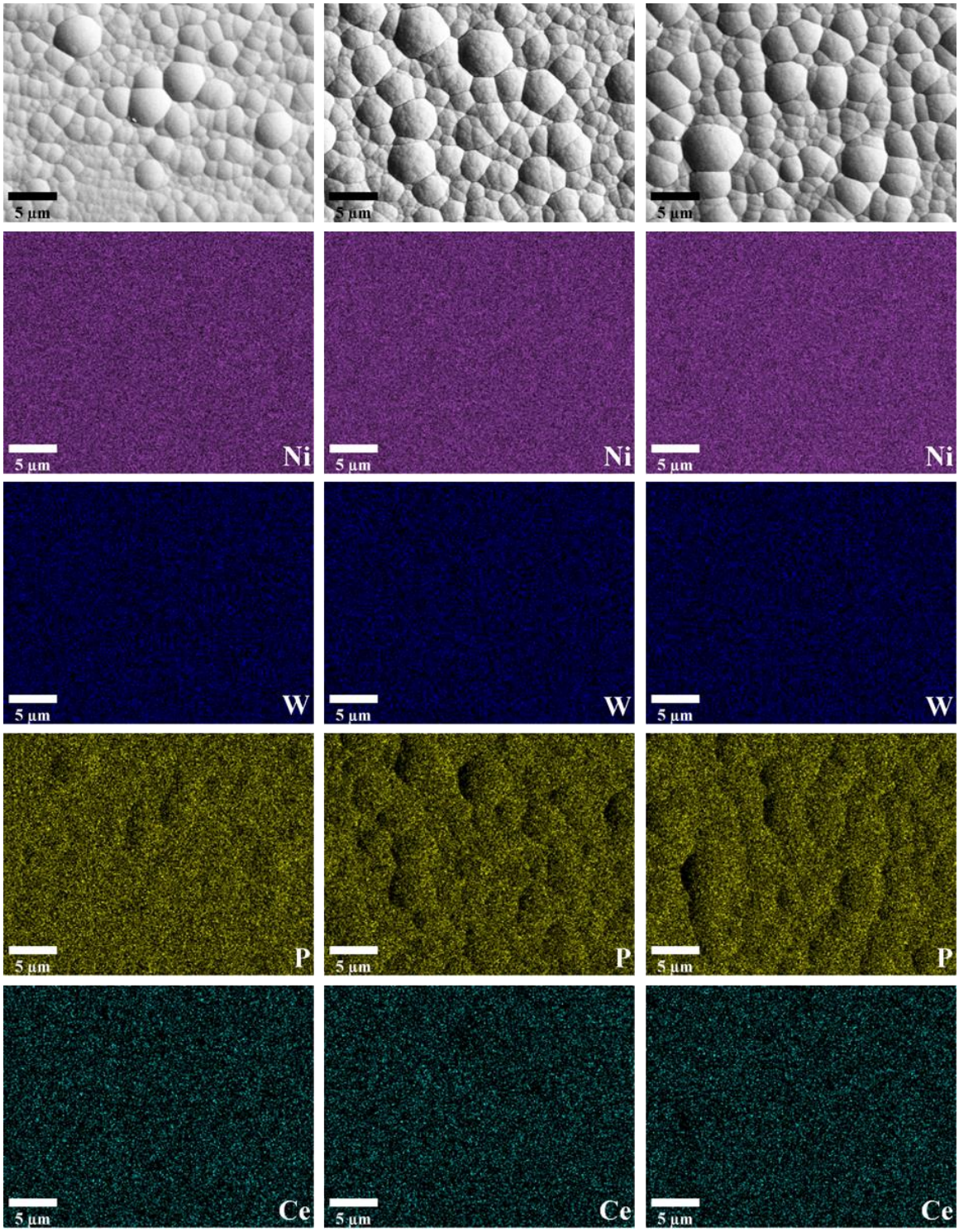

Figure 5.5. EDX mapping images of the coating top surfaces with varying Ce salt concentrations: (a) Ce5, (b) Ce8, and (c) Ce11.

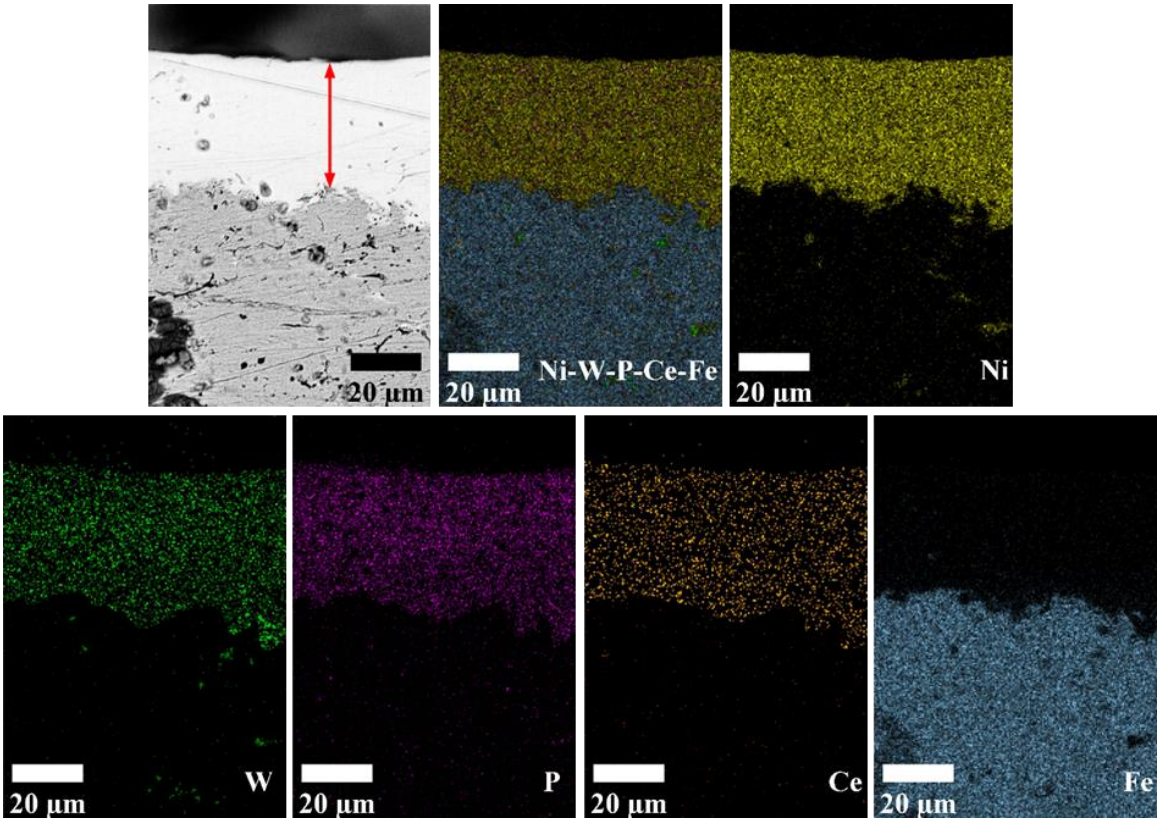

Figure 5.6. EDX mapping analysis of the cross-section of Ce8.

For the Ni-W-P-Co and Ni-W-P-Mo coatings, the P quantities were much lower (2.1-2.2%), with a relatively higher W (3.9-7.1%) and a larger share of the fourth element (5.1-5.9%) [94]. Similarly, the addition of Cr resulted in alloys with 5.6% P, 5.3% W, and 3.0% Cr [204]. In contrast, in Ce-containing quaternary Ni-P coatings, the P content is similarly low at 4.5-6.5% with Ce being undetectably low to a maximum of 1.3% [84,199]. In the current study, the P range was similar, although higher quantities of Ce were present, resulting in reduced W. It should be noted that because the solubility of W in the Ni matrix is low at only approximately 2% and any added W is typically precipitated at the grain boundaries, the changes in the lattice structure due to the presence of P and W in our study are expected to be in line with previously reported results, and any changes can be attributed to the higher share of Ce present in the coatings.

Because the reaction order of hydrogen atoms or electron adsorption in the Ni^{2+} reduction reaction (Equation 5.9) is twice that of the H_2PO_2- reduction reaction (Equation 5.10), the reduction rate of Ni^{2+} ions is significantly higher than that of H_2PO_2- ions. Therefore, although the deposition rates of both Ni and P increased with the addition of Ce, as mentioned earlier, the increase in the Ni deposition rate exceeded the increase in the P

deposition rate, leading to a relatively lower P content in the coatings with increasing Ce concentration in the coating baths [171]. Earlier studies have also reported prioritized Ni deposition and reduced P content with the addition of Ce in the electroless Ni-P [109], Ni-Co-P [84], and Ni-Cu-P [199] systems. Furthermore, when the addition of Ce started to limit the coating deposition rate, it affected Ni deposition to a relatively higher extent, and the proportion of P increased.

An XPS analysis was conducted to determine the chemical states of the coating constituents. Representative XPS spectra for the Ni 2p, W 4f, Ce 3d, and P 2p orbitals are shown in Figure 5.7, for three different coatings, namely Ce5, Ce8, and Ce11, and the detected peaks along with the areas under the curve are presented in Table 5.4. The analysis for Ce is provided separately in Tables 5.5-5.6 because of the larger number of peaks detected. The area under the peaks can provide insight into the relative proportions of the constituents in their different chemical states.

The Ni 2p spectrum was composed of $2p_{3/2}$ and $2p_{1/2}$ doublets, as shown in Figure 5.7(a). In the Ce5 coating, the peak at 851.5 eV can be attributed to the elemental Ni [100,138,205–207], whereas the peaks at 855.9 and 860.7 eV are assigned to $2p_{3/2}$ and the peaks at 874.1 and 880.1 eV are assigned to $2p_{1/2}$, which are related to the chemical state of either Ni^{2+} or Ni^{3+} and their respective shake-up satellite peaks [94,138,205–208] originating from valence electron transitions toward discrete and/or non-discrete energy levels in proximity to the Fermi edge [209]. The chemical compounds formed by Ni^{2+} and Ni^{3+} ions are NiO, $Ni(OH)_2$ and Ni_2O_3, respectively [138,206,207,210]. Nonetheless, the presence of two satellite peaks and an energy separation value of 18.2 eV between the two $2p_{3/2}$ and $2p_{1/2}$ peaks indicate that Ni was primarily present in the hydroxide form [211]. In chemical processes, the reduction of H^+ ions to H_2 occurs exclusively at the surface, resulting in the oxidation of only the surface-bound P. This redox reaction induces an increase in pH, which facilitates the formation of $Ni(OH)_2$ [212]. Similar peaks were observed for the Ce8 and Ce11 coatings, although elemental Ni was not detected in the Ce8 coating. An examination of the XPS spectra of the other constituent elements revealed that the coating surfaces that did not contain elemental Ni were devoid of elemental P, as discussed in the next few pages of this subsection. Therefore, the reasons for the absence of elemental Ni and P were interdependent. It has been observed that if P in the coating is readily oxidized, it will likely form PO_4^{3-} ions, necessitating cations (such as Ni^{2+}) to maintain electrical neutrality.

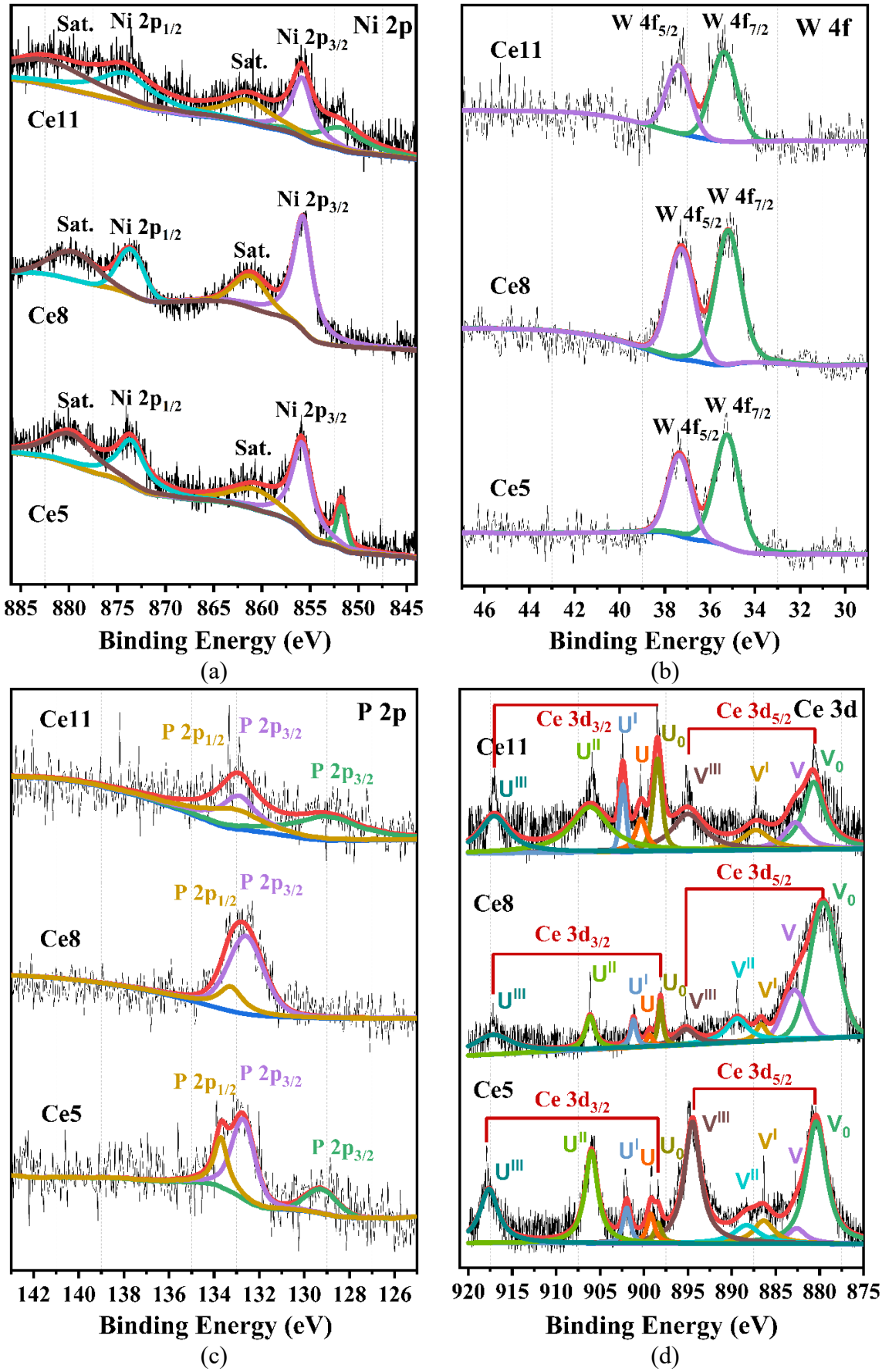

Figure 5.7. High-resolution XPS spectra of (a) Ni 2p, (b) W 4f, (c) P 2p, and (d) Ce 3d.

Table 5.4. Peaks for Ni, W, and P were detected from the XPS spectra, and the area under these peaks.

Element		Ce5	Ce8	Ce11
Ni	Ni $2p_{1/2}$	425.26	477.74	402.17
	Ni $2p_{3/2}$	670.84	958.13	583.71
W	W $4f_{5/2}$	49.36	66.91	19.98
	W $4f_{7/2}$	77.92	85.19	28.64
P	P $2p_{1/2}$	22.54	23.33	30.11
	P $2p_{3/2}$ (BE 129)	19.26	-	42.46
	P $2p_{3/2}$ (BE 133)	52.37	91.89	36.76

With abundant Ni^{2+} ions, phosphate, hydroxide, or oxide may have formed as a consequence of this interaction [213]. This conclusion is further supported by the presence of a high-intensity Ni^{2+} peak at approximately 855.9 eV.

The high-resolution XPS spectra of W 4f, consisting of W $4f_{7/2}$ and W $4f_{5/2}$ core levels, are shown in Figure 5.7(b). The two peaks for the Ce5 coating were at binding energies of 35.25 and 37.4 eV, indicating the presence of W in the chemical state of W^{6+} [205,208], corresponding to $NiWO_4$ and WO_3, respectively [206,207]. The Ce8 and Ce11 depositions exhibit similar spectra, indicating a similar chemical composition of W in all three coatings, marked by the absence of elemental W.

The P 2p spectra were deconvoluted into three peaks consisting of two doublets: P $2p_{3/2}$ and P $2p_{1/2}$ (Figure 5.7(c)). In the Ce5 coating, the 129.25 eV peak corresponds to elemental P [214], and the 132.8 and 133.64 eV peaks correspond to $2p_{3/2}$ and $2p_{1/2}$ orbitals, respectively, indicating presence of P^{5+} ions in the form of NaH_2PO_2 or $CePO_4$ [138,206]. A similar peak distribution was observed for the Ce11 coating, and no elemental P could be detected in the Ce8 coating. By observing the lowest P content in Ce8 through EDX analysis coupled with the alkaline nature of the coating bath, it can be suggested that the forward reaction converting $H_2PO_2^-$ into P (Equation 5.10) is likely inhibited under these conditions. This suppression of the forward reaction in Ce8 may account for the absence of elemental P in the coating [138], which in turn results in the absence of elemental Ni, as explained earlier.

For Ce, a total of 10 fitted peaks in the form of spin-orbit multiplets in the entire range of 880-918 eV were observed (Figure 5.7(d)). The doublets Ce $3d_{5/2}$ and Ce $3d_{3/2}$ can

correspond to Ce^{3+} and Ce^{4+} ions formed under different chemical reactions in the bath (Equations 5.13-5.15).

$$Ce^{3+} + 3OH^{-} = Ce(OH)_3 \quad (5.13)$$

$$Ce(OH)_3 = CeO_2 + H_3O^{+} + e^{-} \quad (5.14)$$

$$2Ce(OH)_3 = Ce_2O_3 + 3H_2O \quad (5.15)$$

During the deposition process, the initial formation of $Ce(OH)_3$ occurs, and subsequently, during a process akin to drying (the elimination of water or moisture from the system), this hydroxide undergoes transformation into multiple compounds including Ce_2O_3, CeO_2, and $CeO_2.xH_2O$, as observed by Wang et al. [143]. The possible Ce cations present in the coating and their corresponding binding energies are listed in Table 5.5 [138,143,215–218], and the calculated areas under these peaks are listed in Table 5.6. In the Ce $3d_{5/2}$ region, the peaks associated with Ce^{3+} are V_0 and V^{I}, whereas the peaks associated with Ce^{4+} are V, V^{II} and V^{III}. Similarly, the peaks in the Ce $3d_{3/2}$ region feature the letter U and a similar indexing. Ce_2O_3, $Ce(OH)_3$, and CeO_2 are the possible compounds responsible for Ce^{3+} and Ce^{4+}, respectively [109,218,219]. The inter-component energy separation i.e., ΔE (V, U) is 16.5 eV, 16.47 eV, and 17.55 eV for the Ce5, C8, and Ce11 coating, respectively. Ce^{4+} ion having $3d^{10}4f^{0}$ electronic state dominates Ce^{3+} with $3d^{10}4f^{1}$ electronic state, although Ce^{3+} ion concentration was also significant in all the three coatings, as evidenced by the high-intensity peaks of V_0, V^{I}, U_0, and U^{I}. Notably, as the Ce concentration in the coating increased, the reduction of Ce^{4+} to Ce^{3+} increased. Ce^{3+}, which has a lower oxidation state than Ce^{4+}, can participate more effectively in redox reactions with reactants [215]. Furthermore, Ce^{3+} is thermodynamically more stable, due of the more negative value of the standard molar Gibbs free energy of the formation of Ce_2O_3 than that of CeO_2 [138]. There is a slight shift towards lower or higher binding energies for all peaks with increasing concentrations of Ce in the bath. This may be due to the different surface chemical compositions and altered electron density resulting from the interactions of Ce with Ni, W, and P. Ce_2O_3 was dominant in the Ce8 sample, as indicated by the high-intensity peak at 880.18 eV. The resolved peaks in our study did not match the binding energy of Ce in the elemental state, implying that Ce is only available in the oxidized state [109].

Table 5.5. Binding energies (eV) of Ce 3d XPS spectra for different Ni-W-P-Ce coatings.

Coating	Spin-orbit doublets	Ce cations				
		Ce^{3+}	Ce^{4+}	Ce^{3+}	Ce^{4+}	Ce^{4+}
Ce5	Ce $3d_{5/2}$	880.87 eV, V_0	882.62 eV, V	886.37 eV, V^{I}	888.32 eV, V^{II}	894.92 eV, V^{III}
	Ce $3d_{3/2}$	898.40 eV, U_0	899.12 eV, U	902.07 eV, U^{I}	905.97 eV, U^{II}	917.92 eV, U^{III}
Ce8	Ce $3d_{5/2}$	880.18 eV, V_0	882.88 eV, V	886.65 eV, V^{I}	889.41 eV, V^{II}	895.23 eV, V^{III}
	Ce $3d_{3/2}$	898.13 eV, U_0	899.35 eV, U	901.2 eV, U^{I}	906.13 eV, U^{II}	917.2 eV, U^{III}
Ce11	Ce $3d_{5/2}$	880.68 eV, V_0	882.78 eV, V	887.27 eV, V^{I}	-	895.23 eV, V^{III}
	Ce $3d_{3/2}$	898.51 eV, U_0	900.33 eV, U	902.46eV, U^{I}	905.91 eV, U^{II}	917.05 eV, U^{III}

Table 5.6. Area under different peaks for Ce as detected from the XPS spectra.

	V_0	V	V^{I}	V^{II}	V^{III}	U_0	U	U^{I}	U^{II}	U^{III}
Ce5	106.12	11.25	19.91	19.31	91.92	6.44	10.14	11.31	56.12	41.09
Ce8	171.76	51.39	10.07	28.51	15.89	12.02	4.24	9.25	18.08	33.63
Ce11	49.85	20.77	18.31	-	40.66	26.38	12.67	12.88	48.99	32.83

Thus, the XPS results show that as the Ce content increased, the proportions of Ni^{2+} [NiO or $Ni(OH)_2$], W^{6+} [WO_3], P^{5+}, and Ce^{3+} compounds initially increased until Ce8, after which they were all reduced. Conversely, the opposite trend was observed for WO_4 and Ce^{4+}. Furthermore, in the Ce8 coating, all constituents, namely Ni, W, Ce, and P, were completely in their oxidized states, whereas the other two coatings had Ni and P in their elemental states. A summary of all the peaks found in the XPS data for the four elements and their corresponding possible compounds is provided in Table 5.7. In standard low-P electroless Ni-P coatings, elemental and oxide forms of Ni and P can be observed, with a strong dominance of elemental forms [220]. For low-P Ni-W-P coatings, the surface oxidation levels are highly dependent on the coating composition, as Ni-W-P with smaller

quantities of W ions of W, having a crystalline microstructure, has been found to have stronger oxide peaks than the higher W, amorphous Ni-W-P coatings.

Table 5.7. Possible existence of compounds, as detected in the XPS spectra.

Element		Binding energy (eV) with its corresponding compound.	
Ni	Ni $2p_{1/2}$	869.5 eV: Ni_2P Ref. [210] 872.4 eV: NiO Ref. [210] 873.8 eV: $Ni(OH)_2$ Ref. [221]	
	Ni $2p_{3/2}$	856.4 eV, 855.8 eV: Ni_2O_3 Ref. [138], [207] 855.8 eV: $Ni(OH)_2$ Ref. [206], [207] 852.3 eV: Ni_2P Ref. [210] 855.3 eV: NiO Ref. [210] 856.1 eV: $Ni(OH)_2$ Ref. [221]	
W	W $4f_{5/2}$	37.4 eV: WO_3 Ref. [206] 37.5 eV: WO_3 Ref. [208]	
	W $4f_{7/2}$	35.5 eV: $NiWO_4$ Ref. [206] 35.4 eV: WO_3 Ref. [208]	
P	P $2p_{1/2}$	133.5 eV: NaH_2PO_2 Ref. [138] 133.8 eV: $CePO_4$ Ref. [214]	
	P $2p_{3/2}$	132.7 eV: NaH_2PO_2 Ref. [138] 132.5 eV: NaH_2PO_2 Ref. [206]	
		Ce^{3+} (Ce_2O_3)	Ce^{4+} (CeO_2)
Ce	Ce 3d5/2	(884.9 eV, Ref. [214]) (880.6, 885.3, 880.2, 879.7 and 886.1 eV, Ref. [218])	(884.9 eV, Ref. [214]) (882, 888.1, 897.4, 882.1, 888, 897.7, 882.6, 888.9 and 895.9 eV, Ref. [218]) (890.02 eV, Ref. [219])
	Ce 3d3/2	(902.8 eV, Ref. [214]) (899, 903.8, 898, 903.9, 898.2 and 904.4 eV, Ref. [218]) (901.6 eV, $Ce(OH)_3$ Ref. [219])	(902.8 eV, 917.5 eV, Ref. [214]) (900.7, 906.8, 916.1, 900.9, 916.2, 901.1, 907.3 and 916.5 eV, Ref. [218]) (907.36 eV, 907.93 eV, Ref. [219])

The easy diffusion path of oxygen via the grain boundaries in crystalline structures has been proposed as a possible reason for these observations [201]. In this study, the dominance of oxide or hydroxide peaks over the elemental peaks was observed, but this

depended on the quantity of Ce, as elemental Ni and P were present in very low or very high Ce coatings and not in the Ce8 coatings, as explained previously. The presence of these oxides or hydroxides on the coating surface may act as a protective layer to improve the anti-corrosion performance of coatings. Furthermore, because nickel oxides have lubricant properties, a higher proportion of the oxides may also help to reduce friction and augment wear resistance. Finally, surface oxides can effectively inhibit biofilm formation in various working environments. As a result, the Ni-W-P coating with an optimized quantity of Ce may be a better alternative to Ni-W-P coatings in expected applications such as valves, impellers, pumps, mixer shafts, heat exchangers in marine water, cooling towers, mines, oil and hydrocarbon wells, wastewater ponds, and oil tanks.

5.2.5 Coating roughness and surface energy

The 3D surface profiles and calculated roughness parameters for the substrate and coated surfaces are shown in Figure 5.8. It should be noted that the profile shown in Figure 5.8(a) is for a polished substrate without any chemical treatment, because chemical treatments are necessary for coating only. Scratch marks resulting from polishing are observable for the substrate as well as for Ce0 (Figure 5.8(a–b)), but are not noticeable for Ce-containing coatings (Figure 5.8(c-d), presumably due to the higher coating thickness. The latter coatings appear rougher with peaks compared to the former ones, which is also reflected in the high average roughness, quadratic (root mean square, RMS) roughness, skewness, and kurtosis (S_a, S_q, S_{sk}, and S_{ku}) values of the Ce-containing coatings (Figure 5.8(e-f)).

Among the measured roughness parameters, S_a is the measure of the average absolute deviation of the peaks and valleys from the mean line, S_q measures the RMS deviation, S_{sk} represents asymmetry in height distribution with positive values associated with peak-dominated surfaces, and S_{ku} can be described as the extent of sharpness of the peaks. The formulas used for calculating these four surface roughness parameters according to the ISO 25178-2 standard are provided below- (Equations (5.16)-(5.19)). In these equations '*A*' represents the area over which integration is performed, $Z(x, y)$ is the height of the surface at coordinates (x, y), and $dx\,dy$ represents the differential area element in the x-y plane.

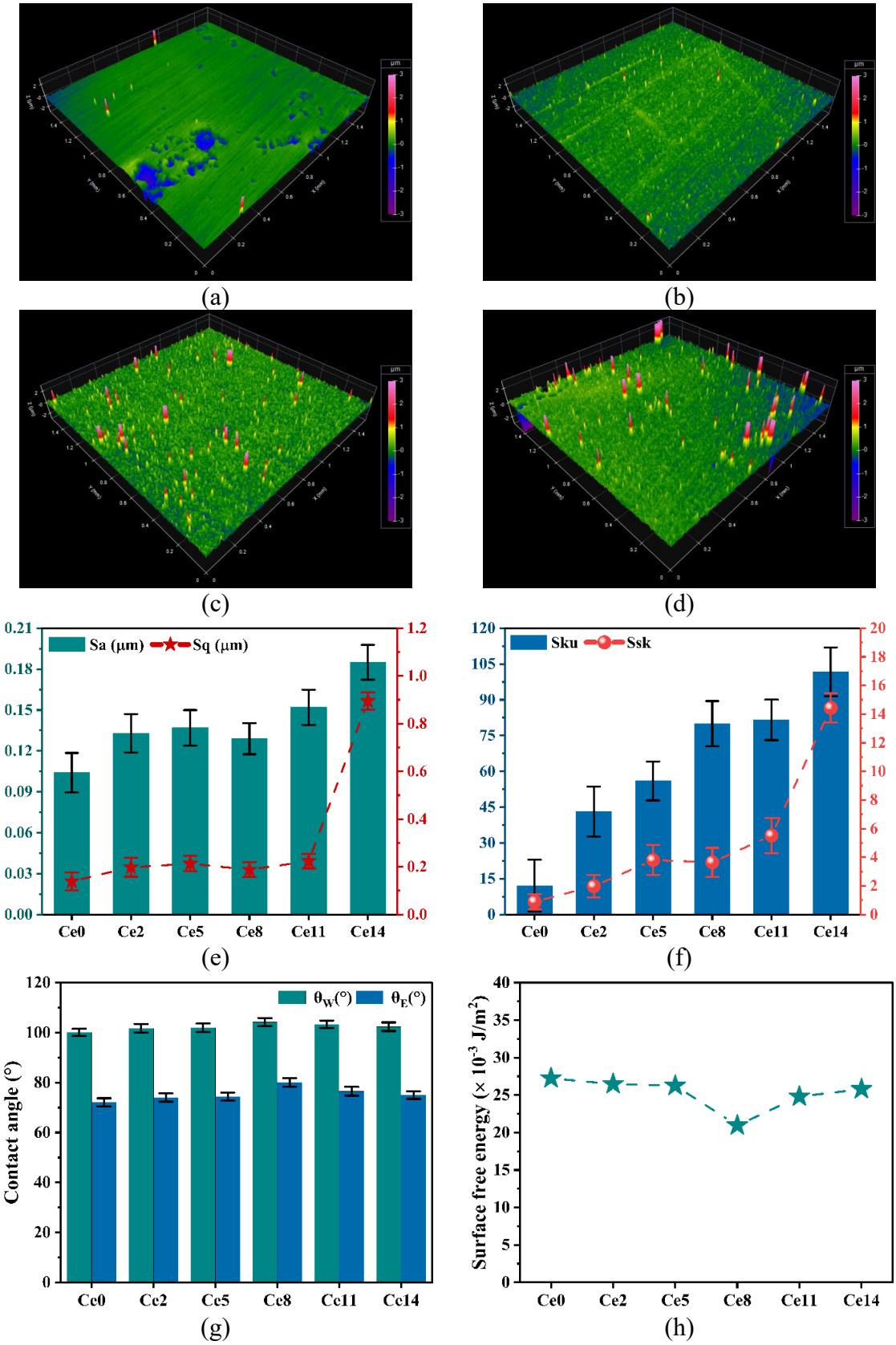

Figure 5.8. (a-d) 3D surface topography of the substrate, Ce0, Ce8, and Ce14, respectively; (e-f) surface roughness of the coatings; (g) measured contact angles with water and ethylene glycol; (h) surface energy of the coatings.

$$S_a = \frac{1}{A}\iint_A |Z(x,y)|\,dx\,dy \tag{5.16}$$

$$S_q = \sqrt{\frac{1}{A}\iint_A Z^2(x,y)\,dx\,dy} \tag{5.17}$$

$$S_{sk} = \frac{1}{{S_q}^3}\left(\frac{1}{A}\iint_A Z^3(x,y)\,dx\,dy\right) \tag{5.18}$$

$$S_{ku} = \frac{1}{{S_q}^4}\left(\frac{1}{A}\iint_A Z^4(x,y)\,dx\,dy\right) \tag{5.19}$$

All the coated surfaces had higher roughness than the polished substrate, which can be attributed to the combined effect of the chemical etching/activation-induced roughening of the substrate underneath the coating, as well as the inherent roughness of the nodular coating morphology because higher substrate roughness leads to increased nodule density [196,222]. Increasing S_a and S_q indicates that the undulations on the coating topographies became larger with increasing Ce, whereas the large values of S_{sk} and S_{ku} signify that the coating topographies were dominated by sharper peaks. Such peaks can be attributed to the uneven formation of nodules arising from the cluster-based growth mechanism of electroless coatings. As Ce ions adsorbed onto the substrate surface facilitated nucleation during the coating growth, they also introduced heterogeneity into the cluster formation process, thereby inducing localized variations in nodule formation [223]. Such localized variations in nodule morphologies are reflected in the form of randomly distributed sharp peaks in the coating topographies. This effect becomes stronger for high-Ce coatings. Furthermore, when excess Ce tends to obstruct the catalytic sites for reduction reactions, the local variations in the coating growth become more pronounced, and the roughness increases significantly.

The variations in the surface contact angles of the different coatings with two different test liquids, namely, water and ethylene glycol (EG), are presented in Figure 5.8(g), and the surface energies of the coatings are shown in Figure 5.8(h). All the coated surfaces were hydrophobic in nature, with water contact angles greater than 90°, in contrast to the native

substrate surface, which had contact angles of 76.45° and 74.65° with water and EG, respectively. Interestingly, the contact angle with water was similar for all coatings, but that with EG showed some variation, with the contact angle being the maximum for Ce8. The corresponding surface energy also showed a dip in the case of the Ce8 coating.

The surface energy (SE) is intrinsically dependent on the surface composition, whereas the contact angle is a function of a multitude of factors, including SE and surface roughness. From the chemical analysis, we concluded that all coating surfaces were predominantly composed of Ni and its compounds, with some P, W, and Ce compounds. $Ni(OH)_2$ has a very low SE (0.07 J/m^2), but the presence of other compounds increased the effective SE of the coated surfaces, as shown in Figure 5.8(h). Presence of elemental Ni can significantly impact the SE of the coating since the SE of Ni is very high at 2.34 J/m^2 [224–226]. Furthermore, the higher Ce concentration in the bath resulted in coatings with relatively higher amounts of Ce_2O_3 and lower quantities of CeO_2, with this ratio being the highest for Ce8. From the literature, the measured SE of CeO_2 is 1.2 ±0.2 J/m^2 [227], and its stable form has the Miller indices of (111), which, when converted to Ce_2O_3, has Miller indices of (0001) with SE 0.7 J/m^2 [228]. As the Ce8 coating had no elemental Ni, and relatively higher quantities of $Ni(OH)_2$ and Ce_2O_3 compared to the other coatings containing Ni in its elemental form and low quantities of hydroxide and Ce_2O_3, the distinctive chemical composition of the Ce8 coating can be a potential reason for the low surface energy and relatively high contact angle with EG.

5.2.6 Coating microhardness and scratch resistance

From the microhardness and scratch testing results, both of these characteristics had a very clear dependence on the Ce content of the coating, with the Ce8 coating having the highest microhardness (Figure 5.9(a)), resulting in the lowest scratch friction coefficient (SFC) and scratch volume (SV) (Figure 5.9(b)).

Compared to the microhardness of the bare substrate (132 ± 4.7 $HV_{0.1}$), that of the Ce8 coating was almost 500% higher. Similarly, the coating reduced the average SFC and scratch volume of the bare substrate by approximately 50 and 75%, respectively. Furthermore, compared to the standard coating without Ce (Ce0), the Ce8 coating had almost 18% higher microhardness, almost 50% lower SFC, and almost 75% lower scratch volume.

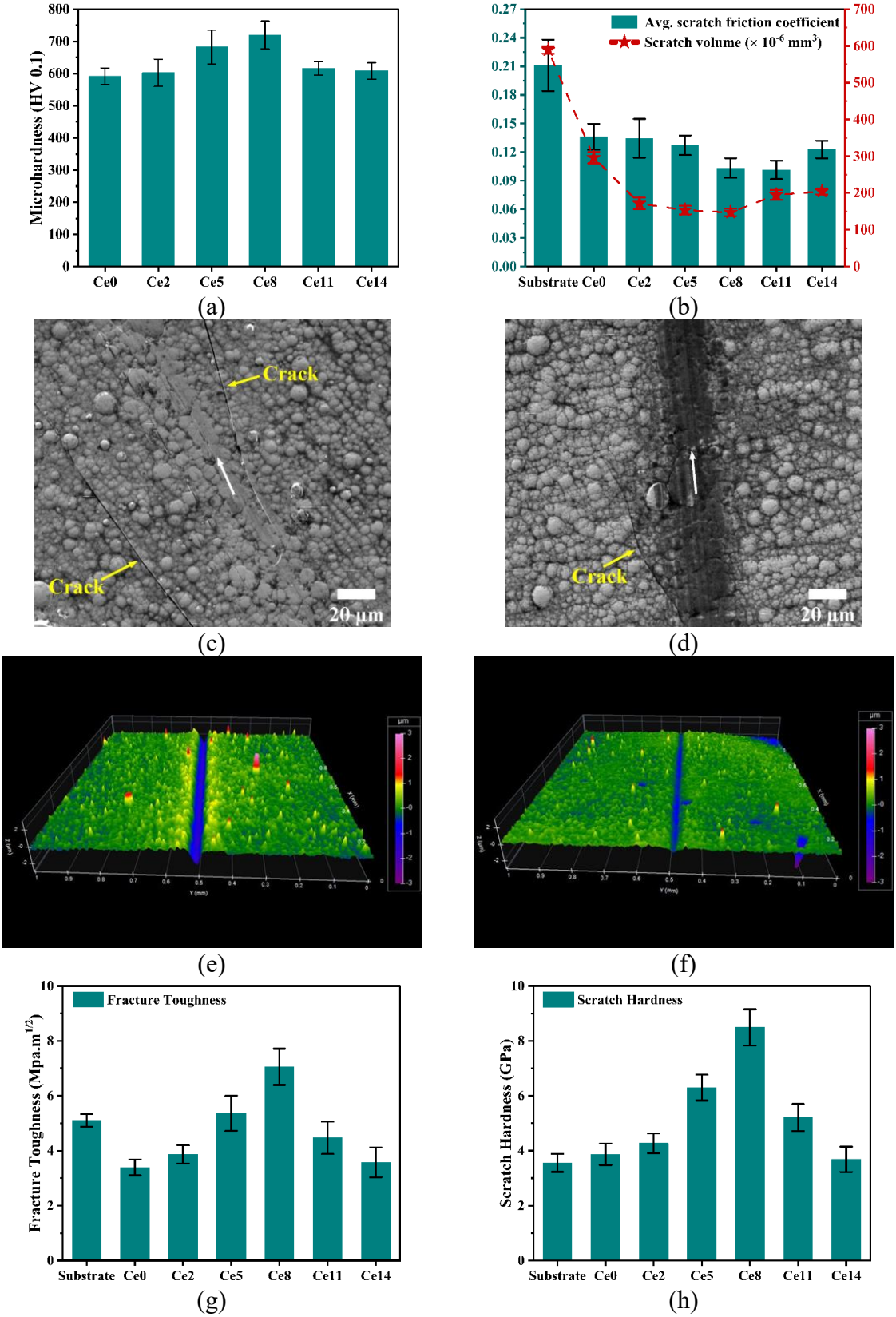

Figure 5.9. (a-b) Effect of different concentrations of Ce on microhardness, scratch friction coefficient, and scratched volume, (c-d) SEM micrographs of scratch tracks on Ce0 and Ce8, respectively, (e-f) Surface topography of scratch tracks on Ce0 and Ce8, (g-h) Fracture toughness and scratch hardness of coatings.

In the FESEM images (Figure 5.9(c-d)), it is evident that the scratched tracks show no significant deformation or damage, such as spallation or peeling, indicating strong adherence of the coatings to the substrate. However, cohesive failure, characterized by the presence of cracks, was observed across all the coatings, and no fundamental difference in the cracking behavior was observed based on the coating compositions. The optical profilometer results depicted in Figure 5.9(e-f) reveal significant differences between the coated surfaces with and without Ce. Specifically, the Ce0 coating exhibited deeper and wider scratches, along with a more pronounced material pile-up along the sides of the scratch tracks, suggesting increased material deformation and potential weaknesses in scratch resistance. In contrast, all Ce-containing coatings displayed smaller scratch dimensions than Ce0, indicating an enhanced resistance to plastic deformation and damage. Both the fracture toughness and scratch hardness (Figure 5.9(g-h)) followed a trend similar to that of microhardness, with the values gradually increasing up to Ce8 and then receding.

In these coatings, the enhancement in microhardness arises from the combined effects of W and Ce incorporation into the Ni-P matrix. W atoms impede dislocation motion within the Ni lattice, boosting both the hardness and strength of the coating, while the formation of $NiWO_4$ and the conversion of metallic Ni to its oxide, as evidenced by XPS analysis, also contribute to the increased microhardness [159,229]. In addition, W reinforces hardness by forming a solid solution with Ni via solid-solution strengthening mechanisms [122]. In addition, because their crystallite sizes are less than 10 nm, they can be dispersed within an amorphous metal matrix, which acts as an obstacle to dislocation movement and further increases the hardness of the material [195]. With the introduction of Ce into the coating bath, the added Ce occupied the dislocations and empty the space in the coating to refine the grains, and the higher density of grain boundaries further increased the resistance to dislocations [108]. As a result, refined microstructures tend to have high microhardness and typically follow the Hall-Petch relationship, according to which the microhardness is inversely proportional to the square root of the average crystallite size of a material. Such a correlation between the crystallite sizes (from XRD) and microhardness values was also noticeable in our results. It should also be noted that the microhardness of the coatings was inversely related to the amount of P, as the coatings with lower P content exhibited higher hardness. Because the P content can affect the degree of crystallinity in electroless Ni coatings and higher P compositions have a lower degree of crystallinity, it is possible that in our study, the relatively higher crystallinity of lower P-containing coatings also

contributed to the higher microhardness values [230–232]. While comparing the Ce5 and Ce11 coatings, it can be observed that the Ce5 had a relatively greater quantity of P in it (4.8% vs 4.5%) while having smaller crystallites (6.29 nm vs 6.42 nm), and the microhardness is also higher. Therefore, the influence of crystallite size according to the Hall-Petch relationship appears to be the driving reason for the trends observed in the microhardness data. However, at high concentrations of rare earth metals, a decrease in the redox reaction results in a decrease in the coating quality as well as a decrease in mechanical properties [199].

The low scratch volume suggests that the coatings are relatively strong and resistant to plastic deformation, have good adherence to the substrate material, and are wear-resistant. The interaction between the three key elements–plowing, adhesion, and internal stress–plays a crucial role in shaping the evolution of the scratch friction coefficient under various scratch conditions. In the case of the Ce0 coating, which is characterized by lower hardness, the indenter displaces more material and induces greater deformation while traversing the surface. This heightened plowing, evident in the optical profilometer image (Figure 5.9(e-f)), contributes to an increased frictional resistance, thus yielding higher scratch friction coefficient values [233]. The SFC and SV decreased with increasing Ce content up to the Ce8 coating, and any higher Ce deteriorated the scratch resistance. This improvement in scratch resistance generally matches the trend in microhardness properties. Notably, the Ce5 coating, with a higher microhardness and scratch hardness than Ce11, showed a higher SFC with a lower SV than Ce11. Usually, a higher microhardness is associated with a reduction in surface friction, as the indenter cannot dig deeper into the material; however, the reversal of the relationship may occur based on the deformation behavior of the coating. A tougher coating with better surface adhesion may offer higher frictional resistance to the indenter, even with a lower degree of indentation, whereas brittleness, lack of internal cohesion, and poor adhesion may lead to the formation of microcracks on the coating, leading to a lower frictional resistance. The presence of cracks on scratched surfaces indicates a brittle nature supplemented by a lack of internal cohesiveness of the coatings, which depends on internal stress, among other factors [234–236]. From the fracture toughness and scratch hardness values (Figure 5.9(g-h)), Ce5 had better surface integrity than Ce11 because resistance to plastic deformation under indentation or abrasion (as measured from microhardness and scratch hardness), as well as the ability to absorb energy before fracturing and resistance to crack propagation (indicated by fracture toughness), was

higher for Ce5. The presence of Ce, which has a significantly larger atomic radius than the other constituents, results in dissimilar coherence strains, lattice distortions, and dislocation loops, which increase the internal stress and reduce the cohesive strength of the coating [233–235]. Therefore, Ce5 may have a higher internal cohesion because of its relatively lower Ce content compared to Ce11, resulting in a higher SFC.

5.2.7 Tribological performance of the coating

The tribological performance of the coatings was evaluated based on the coefficient of friction (CoF) and the specific wear rate (SWR). The CoF of the bare substrate increased to a very high value at the initiation of tribo-testing, whereas that of the coated surfaces increased with a relatively low slope (Figure 5.10(a)). However, after 175 s (5250 mm) of sliding, the coatings with little or no Ce (Ce0 and Ce2) began to deteriorate, and the CoF gradually increased to match that of the substrate after 200 s (6000 mm) of sliding. Ce5 also exhibits signs of deterioration, albeit to a lesser degree. In comparison, the Ce8 and Ce11 coatings produced low and very stable CoFs throughout the tests. Apart from a sudden spike, plausibly due to the detachment of the transfer layer followed by gradual regrowth of the layer [237], Ce14 also caused a low CoF. The formation and detachment of the transfer layer are typical characteristics associated with the 'stick-slip' mode of wear, which has been observed for Ni-based coatings in earlier studies.

The SWR of the coatings exhibited a similar trend, with the lowest wear occurring for the Ce8 and Ce11 coatings (Figure 5.10(b)). It should be noted that the SWR of the bare substrate and the coating without Ce (Ce0) were approximately 1400% and 300% higher, respectively, than those of the Ce8 and Ce11 coatings.

From the FESEM micrographs and 3D profilometry data (Figure 5.10(c-f)), the wear track of the coating without Ce is wider and deeper than that of the Ce-containing coating. Cracks developed on both types of coatings owing to the high loads applied during tribo-testing, indicating the relatively brittle nature of the depositions. The scratches and grooves formed after microcutting and microplowing in the middle of the wear track represent the material loss from the coating surface and are indicative of an abrasive wear mechanism. The presence of oxides and small pits, as observed on the wear track (Figure 5.10(d)), can also promote adhesion, thereby promoting adhesive wear [207,238,239]. The decrease in the CoF with increasing Ce can be attributed to the development of a hard surface facilitated by the dispersion of Ce within the coating, along with the presence of elements in their

oxidized state, as identified in the XPS results. However, Ce8 and Ce11 exhibited similar wear performances in terms of both the CoF and SWR.

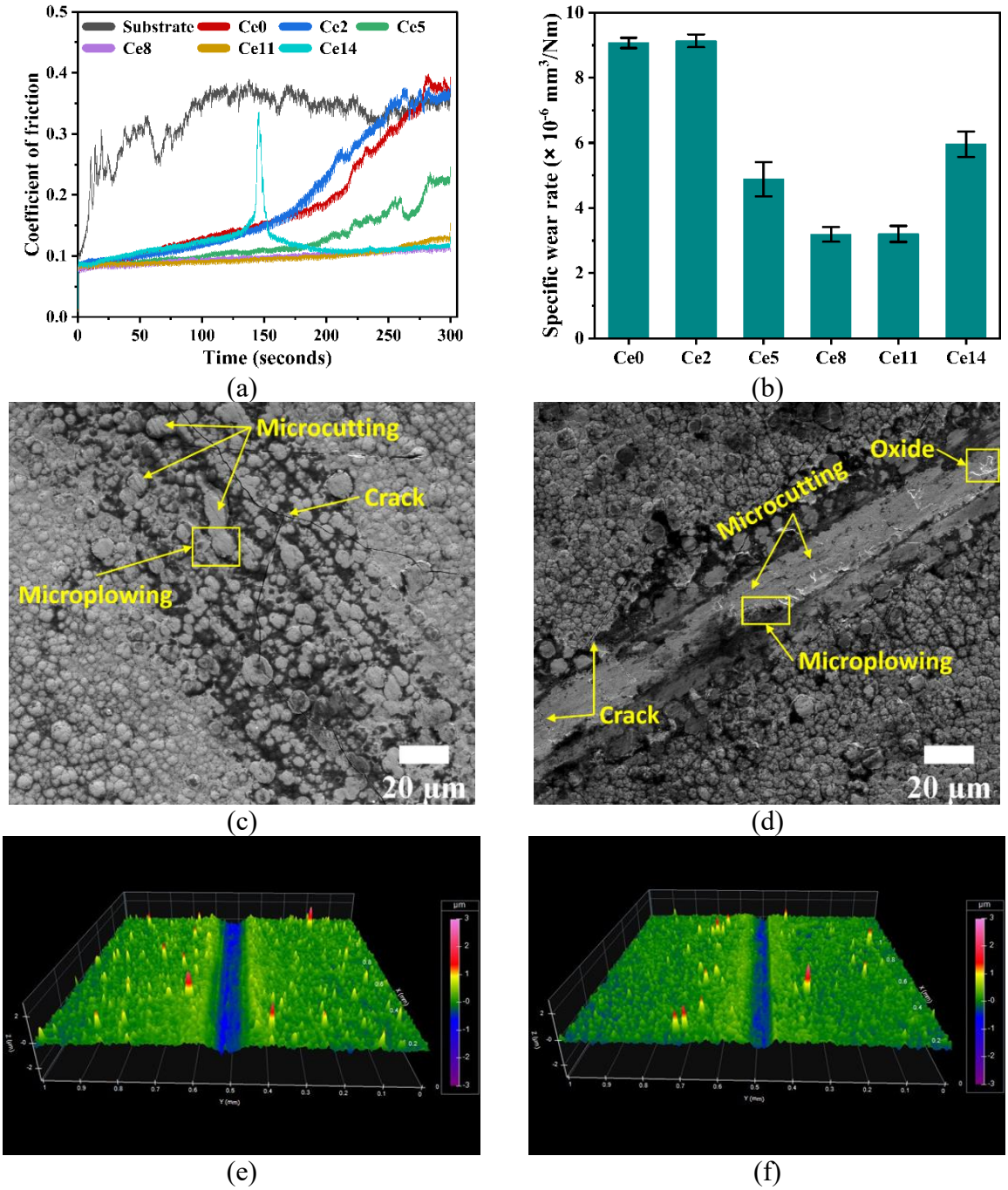

Figure 5.10. Influence of Ce content on wear behavior: (a) Variation in CoF, (b) specific wear rate, (c-d) SEM micrographs of wear tracks on Ce0 and Ce8, and (e-f) surface topography of wear tracks on Ce0 and Ce8.

Interestingly, the Ce14 coating, apart from the sudden spike, also showed very similar CoF values, indicating similar wear mechanisms. The spike in the CoF in Ce14 points to the stick-slip phenomenon, and the wear track morphologies also indicate adhesive wear,

which was not detected on the Ce0 or low-Ce surfaces. It is possible that the wear mechanisms changed according to the nature of the coatings. The wear resistance of protective coatings can originate from different factors, including microhardness, toughness, and self-lubricating properties. In the abrasive mode of wear between the hard counter-body and the coating, marked by the presence of micro-cutting and micro-plowing, the ability of the coating to resist indentation and plastic deformation from scratch is the most crucial aspect, and the wear performance of the coating depends on its microhardness and scratch hardness. However, for hard and brittle coatings, some parts of the hard coating may become dislodged, resulting in three-body wear that aggravates the wear rate. Therefore, high fracture toughness of the coating is necessary to mitigate such situations. Therefore, the increase in microhardness, scratch hardness, and fracture toughness associated with increasing Ce content in the coating led to improved wear performance, as evidenced by the lowering of CoF and SWR. However, the associated low internal cohesion of the coating arising from the highly stressed lattice structures in the presence of a relatively large quantity of Ce may also cause the detachment of some materials, and the affinity and solubility of Ni and P in the coating on the steel ball may give rise to adhesive wear [240–242], as observed in the wear tracks of Ce8. Notably, the no-or-low-Ce coatings did not show any evidence of adhesive wear, which became prominent at higher Ce contents. If the adhesion mode of wear dominates the wear mechanism, instead of a deteriorating situation, the wear performance may improve in some cases if the coating exhibits lubrication properties. Therefore, the self-lubricating properties of Ni and W oxides, with W oxides particularly offering effective lubrication at elevated temperatures, can contribute to lower the CoF and the wear rate [243–245]. The presence of such oxides was confirmed by EDX analysis of the wear tracks and counter-body (Table 5.8).

Table 5.8. Elemental composition of the as-coated surface after the scratch and wear tests.

Elements (wt.%)	Ni	W	Ce	P	O	Fe
Scratch test						
Ni-W-P	75.18	0.19	–	1.85	22.71	0.07
Ni-W-P-Ce8	75.38	0.33	–	1.55	22.59	0.14
Wear test						
Ni-W-P	74.71	0.2	–	2.09	22.9	0.1
Ni-W-P-Ce8	74.94	0.54	0.13	1.63	22.6	0.15

5.2.8 Corrosion resistance

All coated surfaces displayed a fairly stable OCP compared to that of the uncoated surface, for which the OCP gradually shifted to a relatively cathodic value (Figure 5.11(a)). In addition, the final OCP values of all coatings were higher than those of the bare substrate.

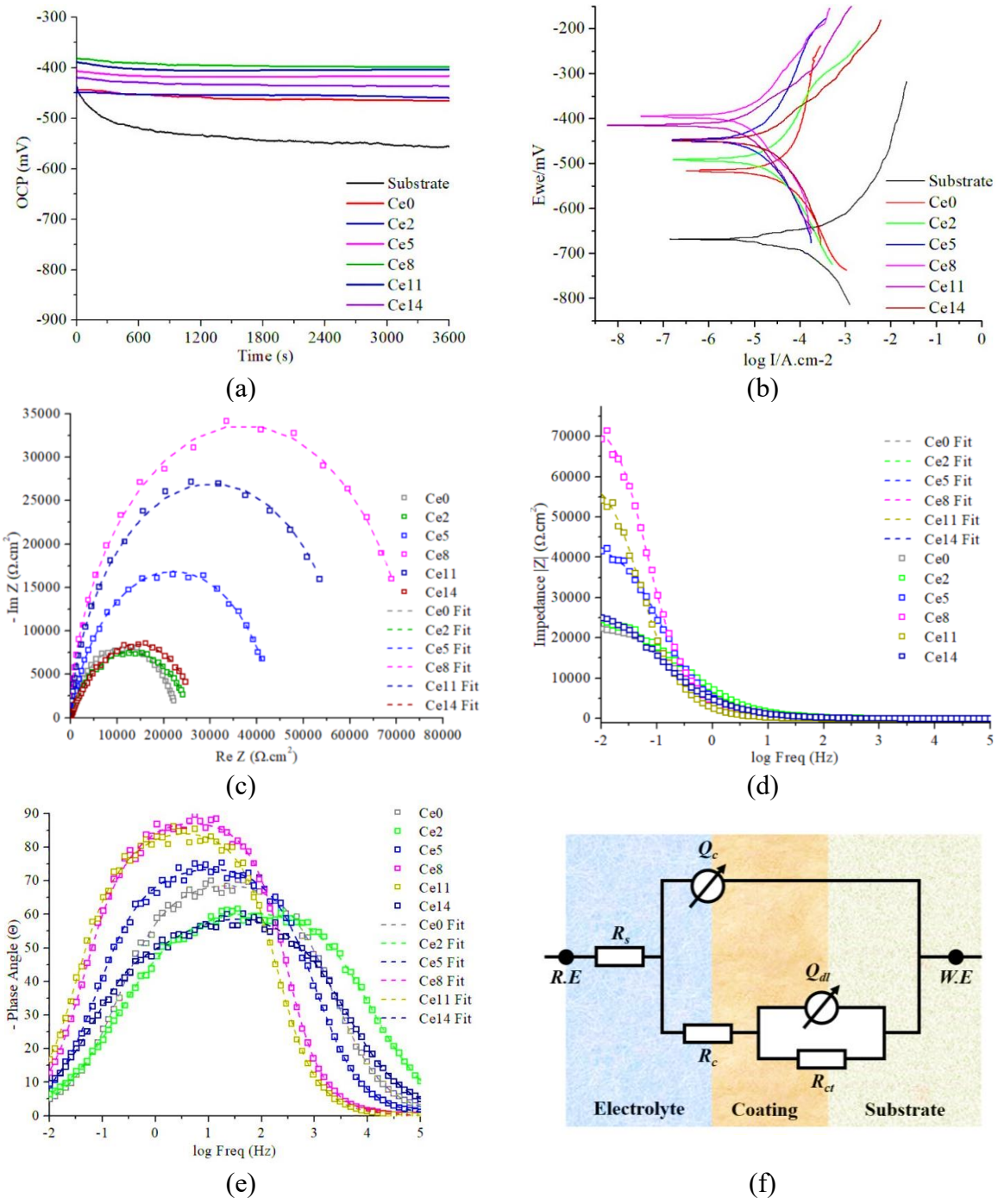

Figure 5.11. Corrosion resistance of the surfaces: (a) OCP, (b) Tafel plot, (c) Nyquist plot, (d) Bode impedance plot, (e) Bode phase plot, and (f) Proposed equivalent circuit.

Among the coated surfaces, the OCP tended to increase with increasing Ce content, because Ce8 exhibited the highest OCP values, and a decrease in the OCP value was observed. A similar trend was further validated by the LP results (Figure 5.11(b)), as the corrosion potential (E_{cor}), corrosion current density (I_{cor}), and calculated protection efficiency (PE) were lowest for the uncoated substrate and highest for the Ce8 and Ce11 surfaces (Table 5.9). The polarization resistance (R_P) was calculated from the corrosion current (I_{cor}) and the anodic and cathodic Tafel slopes (β_a, β_c) using the Stern-Geary equation (Equation 5.20) [246].

$$R_P = \frac{1}{2.303} \cdot \frac{\beta_a \beta_c}{(\beta_a + \beta_c) I_{cor}} \tag{5.20}$$

Table 5.9. Electrochemical corrosion resistance from Linear Polarization testing.

Sample	Substrate	Ce0	Ce2	Ce5	Ce8	Ce11	Ce14
OCP (mV)	-564.26	-465.574	-460.13	-415.96	-398.15	-403.77	-436.23
E_{cor} (mV)	-666.94	-514.85	-492.70	-447.87	-395.86	-414.56	-449.41
I_{cor} (μA/cm^2)	108.626	59.266	28.245	20.962	6.346	8.679	35.961
R_P (kΩ.cm^2)	3.99	30.71	46.02	57.44	69.96	62.03	32.39
PE (%)	-	45.44	73.99	80.70	94.16	92.01	66.89

The E_{cor}values were relatively lower than the OCP values for all the surfaces because during the potential sweep, the cathodic reactions damaged the protective oxide films present on the surface.

The Ni present in the Ni-P coating may be preferentially dissolved in the solution, resulting in P enrichment. P interacts with the electrolyte to form a hypophosphate layer, which prevents further hydration of Ni [247]. The initial drop in the OCP before stabilization, as can be observed in the Ce0 surface, can be correlated to the initial dissolution followed by corrosion protection. Multiple plausible reasons for the corrosion inhibition effect of RE elements or their oxides in coatings have been suggested by earlier researchers. One model proposes that the nodule boundaries and defects in Ni-P coatings act as the major paths for corrosion. In coatings where nucleation occurs on the substrate surface during the initiation of the coating, the grain boundaries continue from the substrate surface to the coating surface, providing a direct pathway for chemical attack on the substrate surface via the continuous grain boundaries. However, rare-earth oxides or ions,

when incorporated into the coating system, can act as additional nucleation sites. Therefore, the occurrence of nucleation is not limited to the initiation phase of the coating but can occur throughout the coating deposition duration. Therefore, new grains can start forming at any level of the coating cross section, creating grain boundaries that do not extend to the substrate surface. Hence, such discontinuities in the grain boundaries essentially prevent corrosive agents from reaching the substrate surface [248]. This secondary germination and the resulting refinement of the coating also make the coating denser, blocking voids, porosities, and other defects. Second, the presence of Ce oxides on the coating surface with resistivity (~10^9 Ω.cm) as compared to that of Ni oxides (~10^3 Ω.cm) can act as a passive layer, limiting the active area for corrosion [249–251]. The formation of a Ce-hydroxide layer at the coating-aqueous electrolyte interface is also possible, creating a barrier layer [252]. However, the deterioration of the coating quality at high Ce concentrations started to negate the beneficial effects, and the corrosion resistance degraded.

In the Nyquist plots (Figure 5.11(c)), the arc radius is indicative of the corrosion resistance capability, and the Ce8 coating has the largest characteristic arc radius, followed by the Ce11, Ce5, and Ce14 coatings, all of which are larger than the arc radius of the Ce0 coating. The impedance magnitude at low frequencies was the highest for Ce8, and Ce11 also exhibited an impedance higher than that of the Ce0 coating, as observed in the Bode impedance plots (Figure 5.11(d)). From the Bode phase plots (Figure 5.11(e)), all the coatings were found to have high phase angles for a wide range of frequencies, which is indicative of the presence of multiple time constants. Because the capacitive reactance is expected to be high at low frequencies, the current in the low-frequency signals is due to the resistive part of the circuit. Therefore, the low phase angle at low frequencies is indicative of ionic permeability or current leakage for all coatings. The peak shifted to higher frequencies for very low or very high concentrations of Ce, and for the optimal amount of Ce in the Ce8 and Ce11 coatings, the peaks shifted to lower frequencies compared to the Ce0 coating.

The EIS results were modeled using an equivalent circuit $R_s(Q_c(R_c(Q_{dl}R_{ct})))$ with two time constants (Figure 5.11(f)). The circuit consists of two Randles cells in parallel, representing the substrate-coating interface and the coating-electrolyte interface. The substrate-coating interface has a characteristic charge transfer resistance (R_{ct}) and constant phase element (Q_{dl}) akin to double-layer capacitance, whereas the coating electrolyte interface is represented by the coating resistance (R_c) and constant phase element (Q_c). The

electrolyte resistance is denoted by R_s. The impedance of the coating interfaces was modeled as a 'constant phase element' (CPE) whose impedance is (Equation 5.21).

$$Z_{CPE} = Q^{-1}(j\omega)^{-\alpha} \quad (5.21)$$

Where the exponent α approaches the value of unity as the interface characteristics near an ideal capacitive nature. Because the coating is not expected to act as a perfect capacitor to block any kind of ion transfer through it, it is necessary to model its behavior with such CPEs. In the equivalent circuit, R_s depends on the type of ions and their concentrations in the electrolyte. The rationale behind such a circuit is that the ion-conduction behavior and mechanism at the coating-electrolyte interface are different from those at the substrate-coating interfaces, and both of these interfaces contribute to the final characteristic current flow. Therefore, the equivalent circuit should have components representing both interfaces, and the circuit considered here is commonly used to model the corrosion properties of coatings on metals, including electroless Ni coatings [2,253].

Considering a non-ideal coating, there may be ion-conducting paths between the electrolyte and the substrate via defects in the coating, and R_c and Q_c are associated with this phenomenon. Therefore, they described the resistance and capacitive nature of the coating, respectively. However, if an electrolyte finds its way into the cracks to reach the substrate-coating interface, it will corrode ions from the substrate and coating in it, and its behavior will be different from that of the bulk electrolyte in the bath. This situation is modeled using Q_{dl} and R_{ct}, where the double-layer capacitance represents the capacitive characteristics arising out of the two layers, one of metal ions and the other of ions in the electrolyte, separated by a layer of water (Helmholtz Plane), and the kinetically controlled charge-transfer reactions are responsible for the R_{ct}. The polarization resistance (R_P) was calculated as the sum of R_c and R_{ct}, because the value of R_s was very low compared to them.

From the equivalent circuits (Table 5.10), it can be observed that the introduction of Ce improved the capacitive nature of the coating, as reflected by the high α values. In addition, both the coating resistance and the charge transfer resistance increased. It is noteworthy that for Ce0, R_c was almost four times R_{ct}, but the ratio significantly changed for the Ce-containing coatings, indicating a changed corrosion mechanism. For Ni-P coatings, the coating-electrolyte interface is expected to have a thin porous layer of corrosion products

and hypophosphate, as discussed earlier. The presence of Ce can affect the composition and integrity of the layer, and factors like surface roughness, non-uniform current distribution, "leaky" capacitor, the mixed occurrence of diffusion/kinetic-controlled adsorption of ions, etc. can also induce changes in the corrosion kinetics [254]. The coating resistance (R_c) showed a trend similar to that of the coating thickness, and it can be expected that a thicker coating provides more resistance to ion conduction, thereby increasing the R_c value. The R_P values calculated from the EIS analysis were in a similar range to those calculated from the linear polarization sweep (Table 5.9) for most samples, and they followed similar trends, that is, the polarization resistance increased with increasing Ce up to the Ce8 sample, after which it deteriorated. Because it denotes the tendency of the coating to resist any deviation from the OCP, a higher R_P essentially implies a higher ability of the coating to protect the substrate underneath.

Table 5.10. Fitted circuit components from the Electrochemical Impedance testing results.

	Substrate	Ce0	Ce2	Ce5	Ce8	Ce11	Ce14
R_s ($\Omega.cm^2$)	11.7	13.8	12.7	15.9	14.49	16.35	20.4
Q_c ($F.s^{(\alpha-1)}.cm^{-2}$)	1.82×10^{-5}	3.60×10^{-5}	3.06×10^{-5}	3.78×10^{-5}	4.00×10^{-5}	6.31×10^{-5}	4.54×10^{-5}
α_c	0.84	0.79	0.69	0.84	0.99	0.96	0.69
R_c ($k\Omega.cm^2$)	1.62	18.18	16.10	26.81	44.67	36.13	14.43
Q_{dl} ($F.s^{(\alpha-1)}.cm^{-2}$)	0.65×10^{-5}	2.15×10^{-5}	3.49×10^{-5}	1.48×10^{-5}	3.97×10^{-5}	4.60×10^{-5}	4.02×10^{-5}
α_{dl}	0.77	0.46	0.51	0.71	0.78	0.81	0.84
R_{ct} ($k\Omega.cm^2$)	1.09	4.91	10.10	17.26	29.84	24.28	13.35
R_P ($k\Omega.cm^2$)	2.71	23.09	26.20	44.07	74.51	60.41	27.78

Although the grains were smaller for the high-Ce-content coatings, resulting in a higher density of grain boundaries, the corrosion resistance was not adversely affected, as evident from the EIS results. This observation also indicated the blocking of grain boundaries by Ce-induced nucleation and grain formation, as mentioned earlier. For the coating capacitance, the presence of highly inert Ce-oxides on the surface, acting as dielectric, imparts a shielding effect on the exchange of ions and transfer of electrical charges, thus limiting the diffusion kinetics of Cl^- ions at the surface [251]. The roughness of the coating is also important because the effective surface area of the coating increases with increasing roughness; however, the leakage current also increases [255]. Therefore, the increase in the coating roughness with increasing Ce initially induced a more capacitive characteristic of

the coating; however, with highly rough surfaces at higher Ce concentrations (Ce14), the capacitive behavior deteriorated.

5.3 Biofilm formation

Fluorescence microscopic images of the biofilms formed on the substrate and the coated surfaces showed the presence of biofilms on all surfaces under observation (Figure 5.12(a-e)). From the integrated intensity of the images, it was possible to estimate the total amount of irradiance from the absorbed stain, which in turn was an indicator of the quantity of the developed biofilm. Therefore, low intensity implies a low degree of biofilm formation. For each sample type, an average of five images was considered. From this measurement (Figure 5.12(f)), all the Ce-containing coatings fared better than the Ni-W-P coating in resisting biofilm formation, and the biofilm was significantly reduced with increasing Ce in the coating up to the concentration of Ce8, after which the biofilm inhibition ability of Ce tapered down, although there was no statistical difference between the integrated intensities of Ce11 and Ce14, pointing towards a plateau of the protection capabilities.

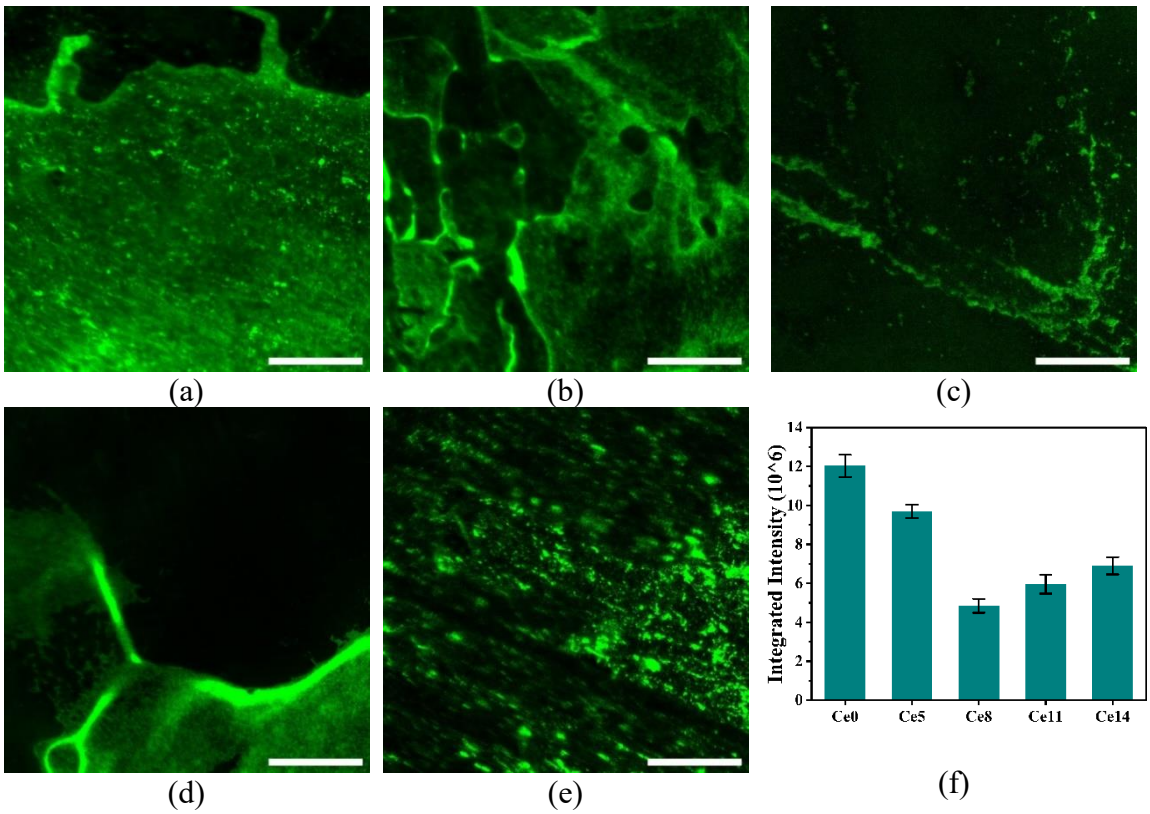

Figure 5.12. (a-e) Fluorescence micrographs of biofilms formed on Ce0, Ce5, Ce8, Ce11, and Ce14 surfaces, respectively (scale bar: 100 μm), and (f) integrated intensities of the images for semi-quantitative estimation of the degree of biofilm formation.

CeO_2 nanocrystals have been shown to inhibit biofilm formation via a quorum quenching mechanism, which essentially interferes with quorum sensing or intercellular communication among bacteria [256]. The results of this study indicate that rare-earth oxides can maintain these properties even when they are part of a polyalloy coating. Increasing the amount of Ce in the coating helped to cover the surface with a higher amount of CeO_2, leading to a reduction in biofilm formation. However, there was a limit to this effect, as no performance improvement was observed with increasing Ce content when the threshold was reached. It is possible that the clustering of CeO_2 at higher Ce concentrations limits the area of influence of the oxide. In addition, the very low surface energy of the Ce8 coating can also contribute to this effect, as a low surface energy tends to limit the initial bacterial adhesion [257].

5.4 Influence of annealing

5.4.1 Microstructural characteristics

Because the Ce8 coating was found to provide better functional performance in comparison with the other coatings, it was selected for further evaluation, and post-coating annealing treatment was carried out at three different temperatures to identify the best post-processing conditions. The annealing temperature had a significant influence on the microstructural characteristics of the deposition, as shown in Figure 5.13(a-i). No apparent changes in the appearance of the coatings were observed up to an annealing temperature of 200 °C. However, larger nodules were observed, accompanied by a nanoporous appearance of the coating surface, for coatings treated at 400 °C or above. This nodule growth and nanopore formation further intensified at 600 °C (Figure 5.13(d-i)). The nanoporous morphology of the coatings suggests that NiO begins to form after annealing [68]. Defects such as holes also emerged at an elevated temperature of 600 °C (Figure 5.13(g)). However, no cracks were observed on any of the surfaces. To determine whether these pores or voids extend through the coating thickness, a ferroxyl reagent test was conducted. The results, shown in Figure 5.13(j), revealed Prussian blue coloration only at the lower-right edge where the substrate was exposed prior to the test. This indicated that the ferroxyl reagent could not penetrate any of the heat-treated coatings to reach the substrate and react with the Fe ions present therein, signifying that there were no defects extending through the coating thickness in any of the heat-treated samples.

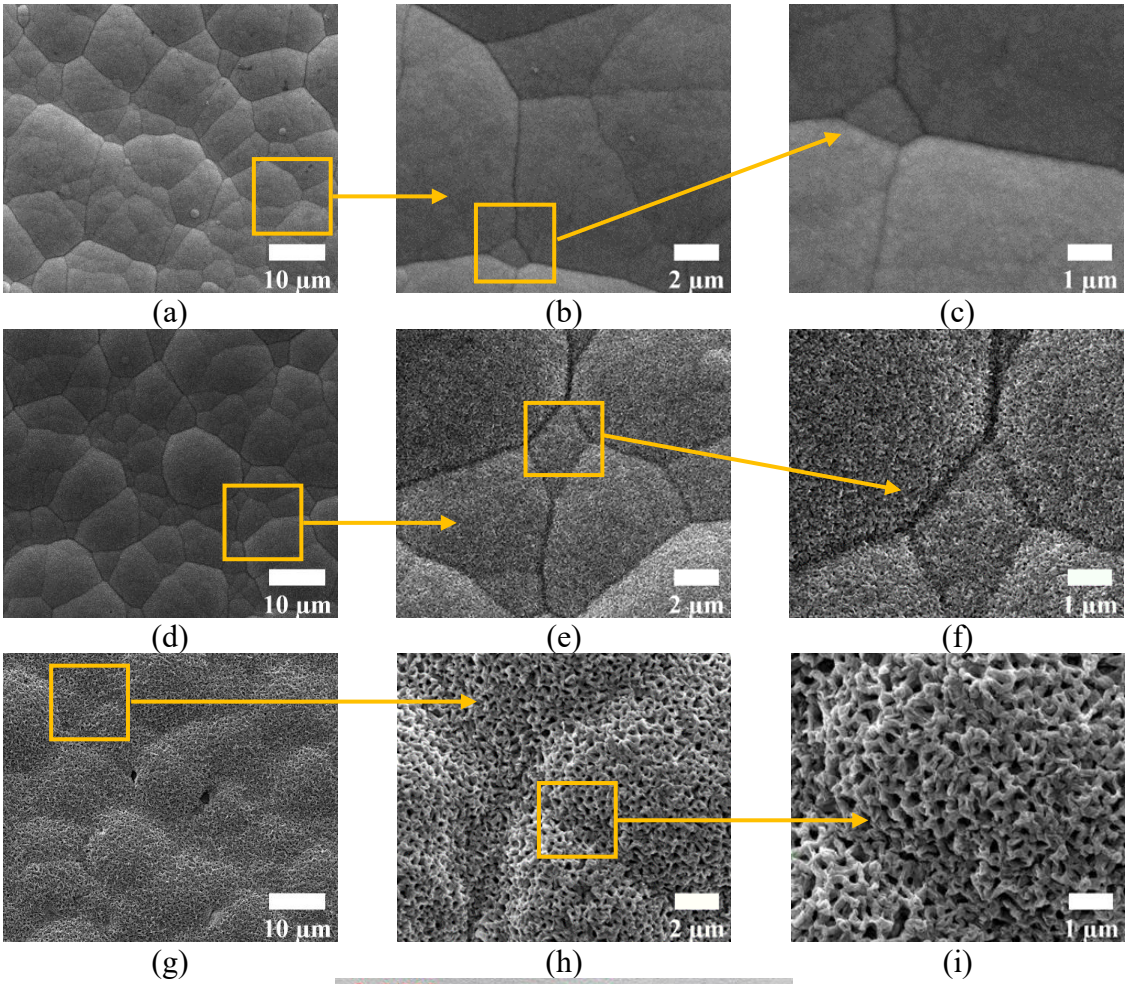

Figure 5.13. (a-c) FESEM images of the coating heat-treated at 200 °C, (d-f) FESEM images of the coating heat-treated at 400 °C, (g-i) FESEM images of the coating heat-treated at 600 °C, (j) outcome of the ferroxyl reagent test, (k) nodule size distribution of the heat-treated coatings, and (l) X-ray diffraction patterns of the heat-treated coatings.

The grain size distribution shifted to higher values as the temperature increased (Figure 5.13(k)), and both the modal grain size and the number of larger grains increased at high annealing temperatures.

The XRD spectrum of Ce8/200 is similar to that of the as-deposited Ce8 coating, with a singular peak of face-centered cubic Ni at 44.63° (Figure 5.13(l)), indicating the nanocrystalline/amorphous nature of the coating. The calculated crystallite was 6.32 nm, which was similar to that of the as-deposited Ce8 coating. The peak became sharper after annealing at 400 °C, and characteristic peaks of Ni_3P appeared. The crystallite size for the Ni peak was found to be 25.94 nm. Upon further heating, the main Ni peak became taller and sharper, and more Ni and Ni_3P peaks became prominent. In addition, new NiO peaks were observed. The calculated crystallite size was high at 42.61 nm. The results suggest that a higher annealing temperature leads to higher crystallinity but also induces oxidation. Details of the characteristic peaks identified in the XRD spectra of the annealed samples are listed in Table 5.11.

Table 5.11. Analysis of the XRD spectra of annealed coatings.

Coating	Peak position, 2θ (°)	FWHM, β (°)	d-spacing (Å)	Crystallite size (nm)
Ce8/200	44.630	1.41903	2.0303	6.32
Ce8/400	44.626	0.34596	2.0305	25.94
Ce8/600	44.603	0.21062	2.0315	42.61

Annealing results in the reorganization of atoms in the lattice, leading to a reduced strain in the lattice and grain growth. However, heat induces oxidation and generates a porous oxide layer. Increasing the annealing temperature increased the oxide content in the deposition, as revealed by the elemental composition data provided in Table 5.12, from the EDX analysis of the annealed samples.

Table 5.12. Elemental compositions of the annealed coatings (wt.%).

Elements	Ce	Ni	P	W	O
Ce8/200	1.8	91	4.4	2.5	0.5
Ce8/400	1.7	82	4.4	2.6	9.3
Ce8/600	1.7	77.1	0.3	1.4	19.7

5.4.2 Surface roughness and surface free energy

The coatings became smoother after annealing, as revealed by the measured surface roughness parameters, S_a and S_q (Figure 5.14(a)). The Ce8/400 sample displayed slightly higher roughness than that of the sample treated at 200 °C. Despite the inferior surface morphology observed in the FESEM images of Ce8/600, it exhibited lower roughness than Ce8/400. This reduction in roughness at 600 °C can be attributed to the extensive nodule growth and crystallization within the material, resulting in a smoother surface. The other two roughness metrics, skewness and kurtosis, showed an inverse relationship with the annealing temperature in Ce8/200 and Ce8/400 (Figure 5.14(b)). However, S_{sk} and S_{ku} were the lowest in Ce8/600 among all the annealed samples. Notably, the kurtosis values in Ce8/200 and Ce8/400 exceeded three, indicating noticeable peaks and valleys on the surfaces and suggesting a more repeated and textured surface profile.

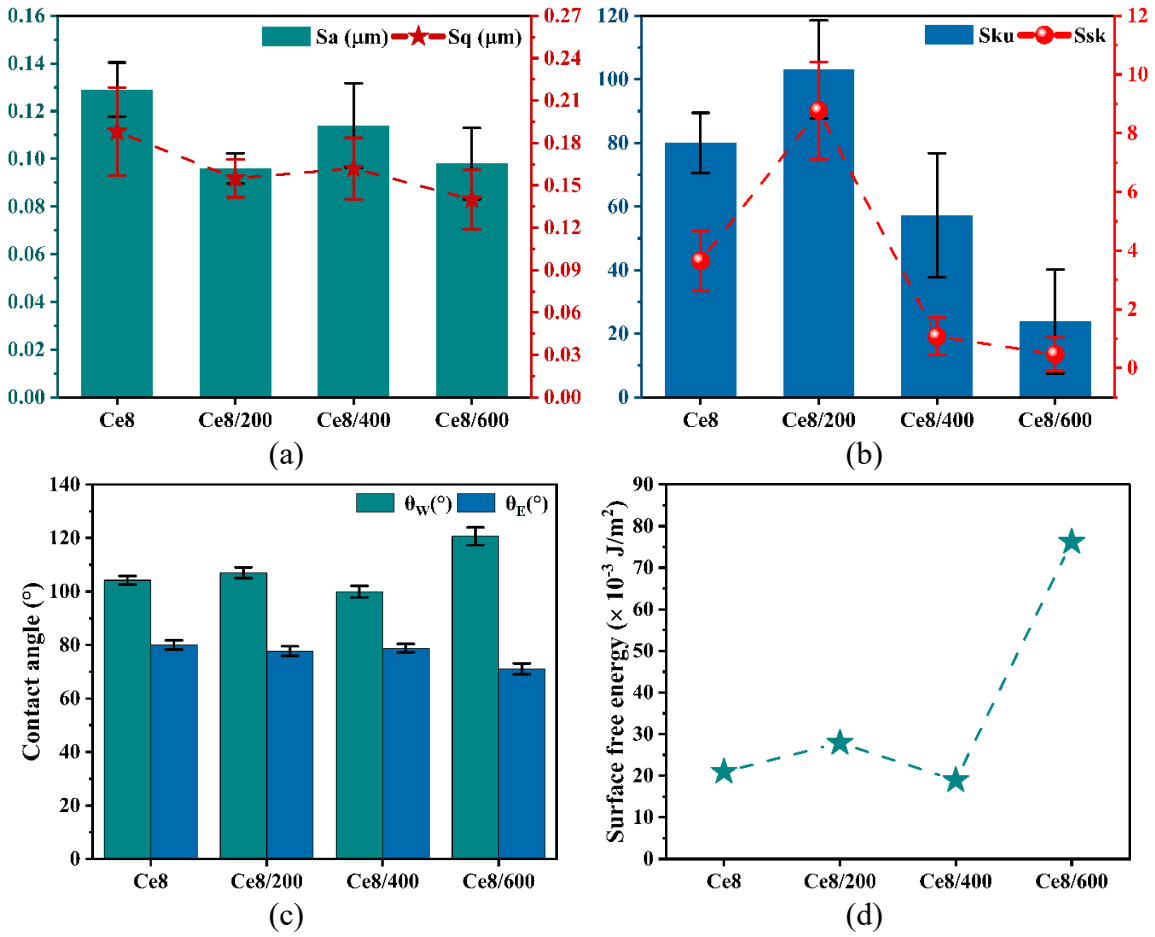

Figure 5.14. (a-b) 3D surface roughness parameters for heat-treated coatings and (c-d) contact angles and surface free energies for heat-treated samples.

At the highest annealing temperature of 600 °C, S_{sk} decreased to nearly zero, implying that the surface exhibited a symmetrical distribution of heights or valleys across its profile, without any prominent inclination towards higher or lower values. In summary, heat treatment has emerged as an effective method to enhance the smoothness of electroless-coated surfaces.

Figure 5.14(c) shows the recorded contact angles observed for water and ethylene glycol in the heat-treated samples. The surface energy of the coating increased at an annealing temperature of 200 °C, and further increased to a very high level when the coating was annealed at 600 °C; however, the surface energy of Ce8/400 was lower than that of the as-deposited coating (Figure 5.14(d)).

Recrystallization and grain growth during the heat treatment process, leading to the elimination of small grains, may reduce surface irregularities, thus reducing the surface roughness. The conversion of $Ni(OH)_2$ (surface free energy of 0.070 J/m^2) to NiO (surface free energy of 0.015 J/m^2) and formation of Ni_3P (surface free energy of 1.63 J/m^2) during the heat treatment process combined with the change in surface roughness can be a potential reason for the changes in surface energy. The reduced roughness can initially reduce the surface energy and improve wettability, and the conversion of $Ni(OH)_2$ to NiO also helps to reduce the surface energy; however, the formation of Ni_3P has a significantly negative influence on it. Because Ni_3P formation occurs at temperatures above 400 °C, the surface energy increases dramatically for the coatings annealed at that temperature.

5.4.3 Surface microhardness, scratch resistance, and wear resistance

In terms of microhardness, an initial improvement followed by degradation of the properties was observed as the heat treatment temperature increased (Figure 5.15(a)). The Ce8/400 coating had the highest microhardness of 1076 ± 40.63 $HV_{0.1}$, almost 40% higher than that of the as-deposited Ce8 coating, whereas the Ce8/600 coating had a microhardness of 611.4 ± 107.57 $HV_{0.1}$, which is less than that of the as-deposited Ce8 coating. The microhardness of the high-temperature annealed coating was not uniform, as evidenced by the high standard deviation. The presence of nickel phosphide combined with higher crystallinity in the heat-treated coatings could be a factor behind the increased hardness, but the formation of a nanoporous NiO layer at elevated temperatures could also deteriorate the properties when the annealing temperature exceeds 600 °C [121,258,259].

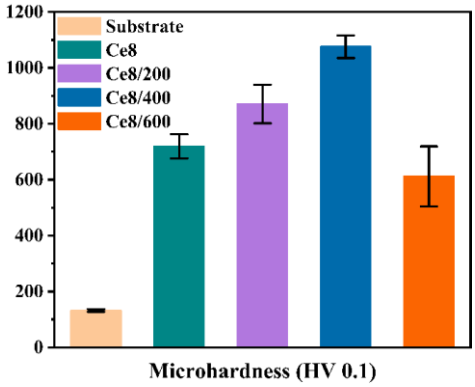

(a)

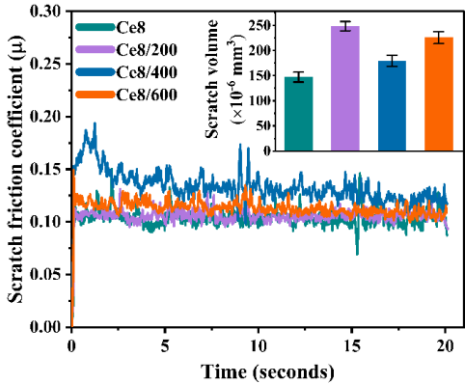

(b)

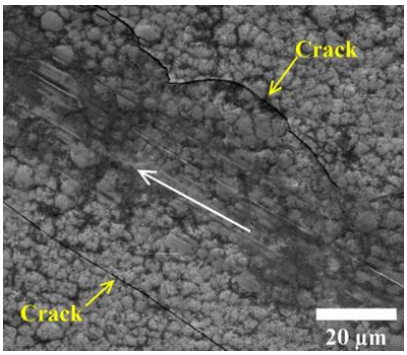

(c)

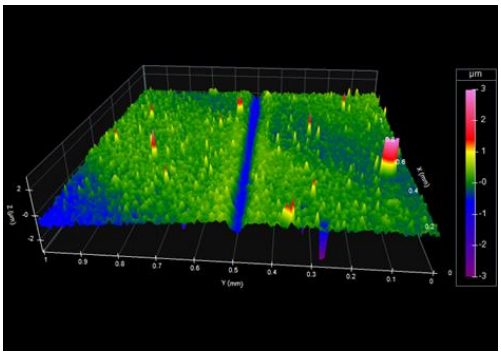

(d)

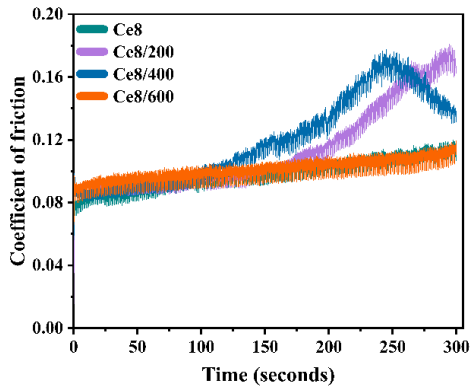

(e)

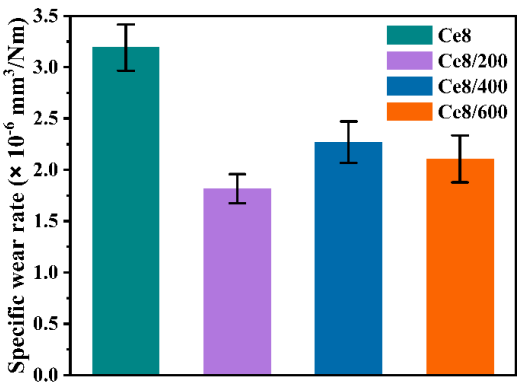

(f)

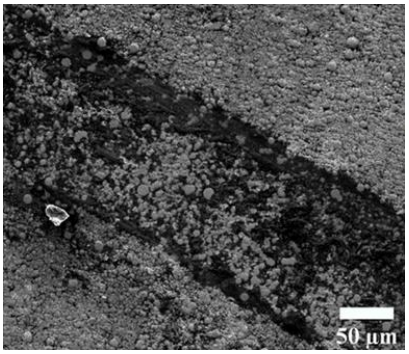

(g)

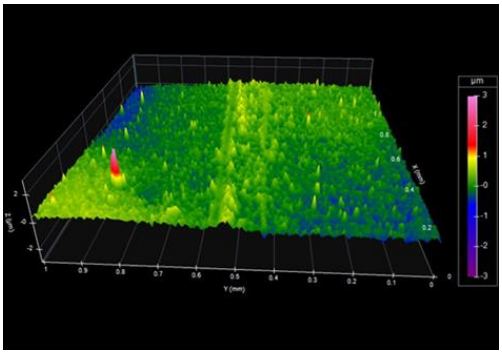

(h)

Figure 5.15. (a-b) Microhardness and scratch resistance of the surfaces, (c-d) scratch track on Ce8/400 coating captured by FESEM and optical profilometer, (e-f) wear resistance of the surfaces, and (g-h) wear track on Ce8/400 coating captured by FESEM and optical profilometer.

The scratch test results exhibited a pattern similar to that of the microhardness values, with the Ce8/400 coating experiencing the least scratch volume loss. Although no significant difference between the as-deposited Ce8 and Ce8/400 coatings could be observed in terms of the scratch volume loss, the other two annealed coatings showed degraded scratch resistance compared to the as-deposited coating (Figure 5.15(b)). Variations in the thermal expansion between the substrate and coating material cause mechanical stresses at the interface, resulting in a loss of adhesion or bonding between the coating and substrate [260].

In terms of the frictional coefficients, the scratch friction coefficient (SFC) of the coatings deteriorated after annealing; among the annealed surfaces, Ce8/400 had the highest SFC. The Ce8/400 coating also exhibited the highest CoF during wear with transfer layer build-up and detachment, as indicated by the gradual rise and fall in the coefficient (Figure 5.15(e)). Although the specific wear rate (SWR) of the annealed coatings was relatively smaller than that of the Ce8 as-deposited coating, annealing at higher temperatures led to a higher SWR as the degree of mismatch in the thermal expansion of the coating and the substrate increased with temperature (Figure 5.15(f)). Indentation and sliding also led to the formation of cracks in the coating (Figure 5.15(c) and (g)) because of the brittle nature of the deposit, as discussed earlier. The depths of the scratch track (Figure 5.15(d)) and wear track (Figure 5.15(h)) were within 5 μm, indicating that the damage was limited to the coating itself, and the substrate surface was not exposed.

5.4.4 Surface corrosion resistance

The microstructural changes induced by heat treatment also affected the corrosion resistance properties of the surfaces, as evident from the OCP, linear polarization, and EIS results (Figure 5.16(a-d), Tables 5.13-5.14).

An improvement in the anti-corrosion properties was observed for the coating annealed at lower temperatures; however, the performance deteriorated for the coatings annealed at 400 °C and 600 °C. The grain growth associated with annealing leads to a reduction in the grain boundary density; thus, the number of attack sites decreases, making the coating more resistant to corrosion. In addition, the electroless deposition of Ni involves the evolution of hydrogen, and the occluded hydrogen atoms induce a tensile stress inside the coating. The heat treatment cycle leads to the expulsion of hydrogen and stress relief, all of which contribute to the augmentation of the corrosion resistance properties. However, when

heated at 400 °C or above, the formation of Ni_3P may introduce micro-galvanic cells between the nanocrystalline Ni_3P precipitate and the matrix, which could be the reason for the increase in the corrosion current density. The cracks and defects that appeared in the coating after annealing at 600 °C could also be detrimental to corrosion resistance.

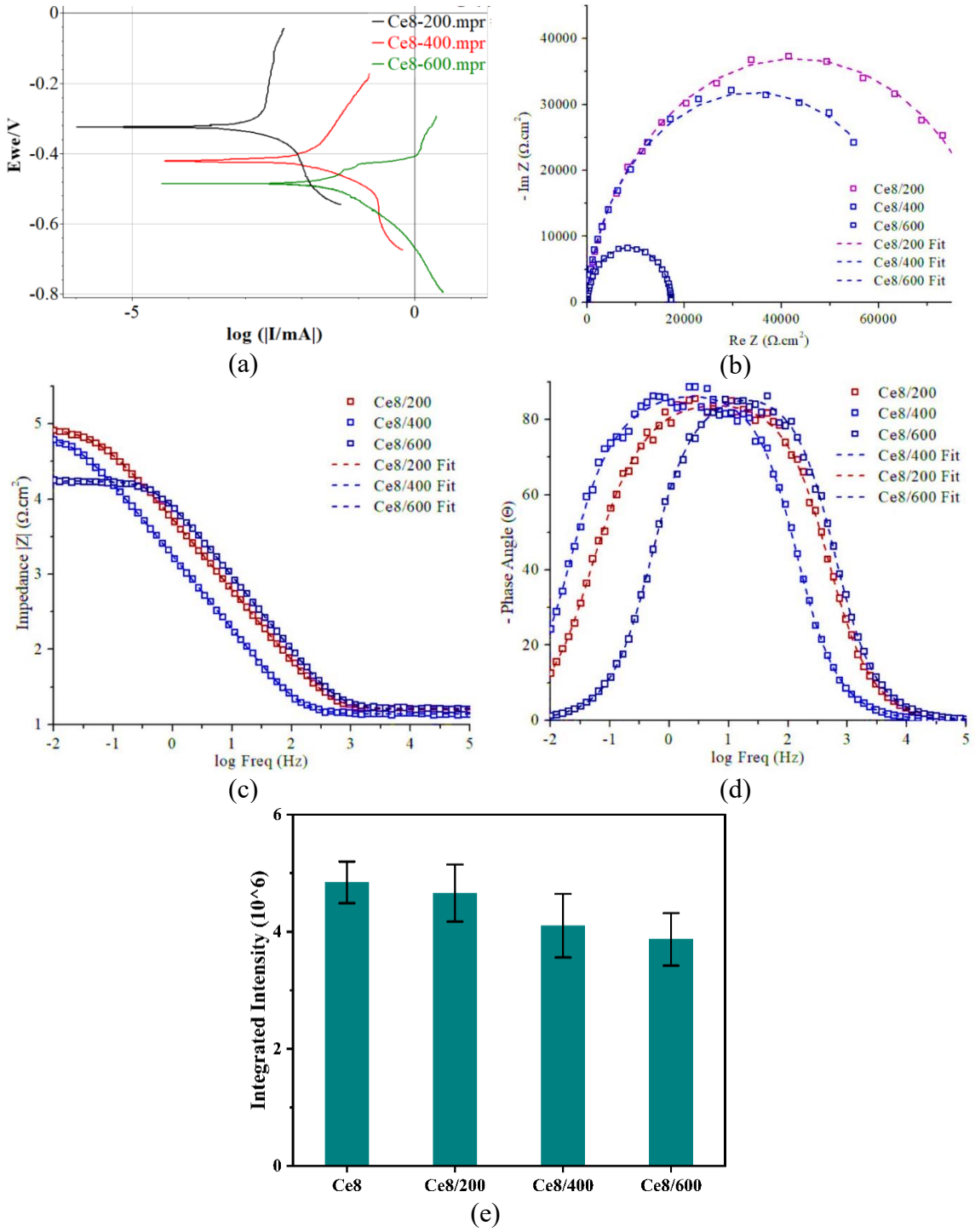

Figure 5.16. Corrosion resistance of the surfaces: (a) Tafel Plot, (b) Nyquist plot, (c) Bode impedance plot, (d) Bode phase plot, and (e) semi-quantitative estimation of the degree of biofilm formation.

Table 5.13. Electrochemical corrosion resistance from Linear Polarization testing of annealed coatings.

Sample	Ce8/200	Ce8/400	Ce8/600
OCP (mV)	-293.69	-424.04	-544.39
E_{cor} (mV)	-323.16	-420.49	-484.42
I_{cor} (μA/cm^2)	1.54	13.389	36.61
R_P (kΩ.cm^2)	98.77	75.97	32.42
PE (%)	98.56	87.67	66.29

The EIS spectra revealed that the Nyquist arc radius of Ce8/200 was the largest and the impedance at low frequencies was the highest, indicating improved corrosion resistance. As indicated by the fitted circuits, the coatings retained their capacitive nature after annealing (Table 5.14) and the coating resistance deteriorated at higher annealing temperatures.

Table 5.14. Fitted circuit components from Electrochemical Impedance testing results of annealed coatings.

Coating	R_s (Ω.cm^2)	Q_c (F.s$^{(\alpha-1)}$.cm^{-2})	α_c	R_c (kΩ.cm^2)	Q_{dl} (F.s$^{(\alpha-1)}$.cm^{-2})	α_{dl}	R_{ct} (kΩ.cm^2)	R_P (kΩ.cm^2)
Ce8/200	15.77	3.17E-05	0.95	59.68	4.53E-05	0.76	26.13	85.81
Ce8/400	13.99	9.24E-05	0.98	40.32	4.77E-05	0.82	28.10	68.42
Ce8/600	16.35	1.74E-05	0.99	12.93	1.95E-05	0.85	4.35	17.28

From the results of the biofilm formation study (Figure 5.16(e)), it is interesting to note that the extent of biofilm formation on the coating surfaces exhibited a gradually decreasing trend, signifying a marked improvement in the ability of the coating to withstand microbial-induced corrosion. The higher amount of oxides formed on the surfaces coupled with the increased surface energy could be responsible for such interesting trends, and further in-depth studies are required to properly analyze the driving factors.

5.5 Closure

This study highlights that controlled addition of the rare earth element Ce in the electroless deposition of Ni-W-P coatings can result in a higher deposition rate with smaller grains, and the Ce-containing coatings exhibited higher resistance to scratch, wear, and corrosion,

as well as biofilm formation. The surfaces also became rougher with a lower surface free energy. The changes in the properties were not monotonically related to the quantity of Ce ions in the coating. The added Ce also helped augment the tendency for biofilm formation on the surfaces, thus acting as a deterrent against microbiologically induced corrosion of components exposed to marine environments. The results indicated that the addition of up to 8 mg/L $CeSO_4$ to the deposition bath improved the coating properties; however, higher concentrations led to gradual deterioration. Therefore, the concentration of 8 mg/L $CeSO_4$ in the bath was selected as the optimum concentration for the development of high-performance coatings.

Furthermore, annealing the coating by heating it to a high temperature followed by furnace cooling greatly augmented the coating properties. In addition, the performance of the annealed coating depended on the annealing temperature, and the coating annealed at 400 °C had a lower surface roughness and surface free energy with lower resistance to surface scratches and wear, albeit with a diminished resistance to surface corrosion. From these observations, we can understand that a wide spectrum of combinations of different properties can be obtained by controlling the deposition and post-processing parameters of electroless deposited Ni-W-P-Ce coatings, making the process suitable for adaptation in many industrial applications.

Chapter 6 Effects of activator, bath loading and substrate roughness on deposition and properties of Ni-W-P-Ce coatings

This chapter investigates the influence of key process variables, such as activator type, bath loading, and substrate roughness, on the deposition, growth, and properties of electroless Ni-W-P-Ce coatings. Through systematic experimentation and advanced characterization techniques, suitable coating parameters were identified.

6.1 Experimental details

To investigate the effect of activators on coating quality, two types of coatings were produced by activating a low-carbon steel substrate using palladium chloride ($PdCl_2$) or hydrochloric acid (HCl) solutions. The substrate was activated in $PdCl_2$ solution (55 °C) for 10 s and in 30% diluted HCl for 30 s. To prepare the $PdCl_2$ solution, 1 liter of distilled water was mixed with 9.5 ml of concentrated HCl (specific gravity of 1.18) and stirred for 10 min, followed by addition of 450 mg of $PdCl_2$ and further stirring for 20 min. The solution was prepared at ambient temperature in a clean dry beaker.

To examine the impact of bath loading on coating quality and bath conditions, coatings were applied to substrates of various sizes using uniform 200 ml baths. A total of six coatings were produced, each in a separate 200 ml bath, as shown in Figure 6.1. Substrates with different dimensions were coated individually.

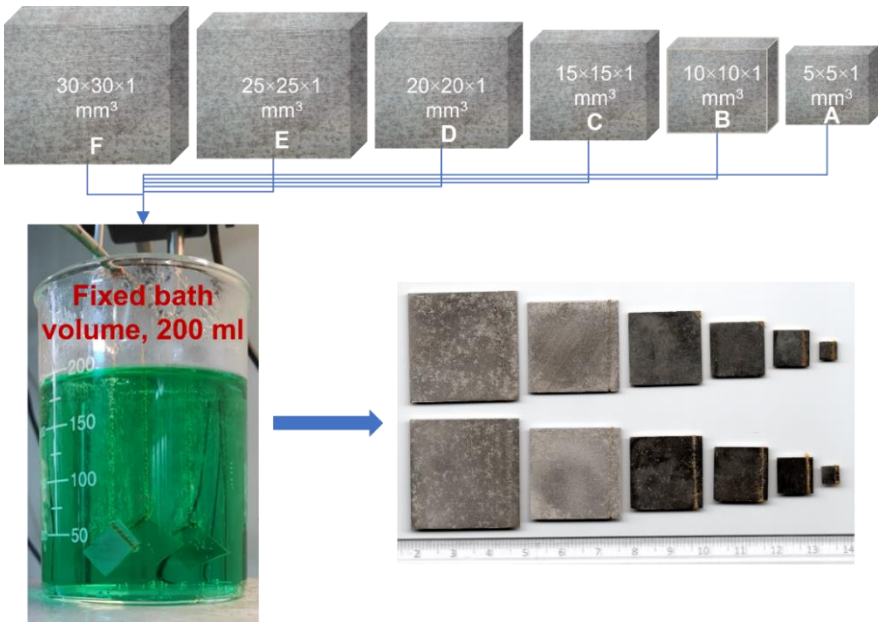

Figure 6.1. Electroless coating at different bath loading levels.

The bath loading [261] is defined as the ratio of the total surface area of the substrate to the bath volume, as shown in Equation 6.1.

$$Bath\ loading = \frac{Total\ substrate\ surface\ area}{Total\ bath\ volume}\ (dm^2.L^{-1}) \quad (6.1)$$

The deposition rate was measured to assess the effect of bath loading, and the coated samples were examined using FESEM and EDS to analyze surface morphology and elemental composition. The influence of bath loading on the chemical composition of the coating baths was evaluated using micro-energy dispersive X-ray fluorescence (micro-EDXRF) with a HORIBA Scientific XGT-7200 instrument. The analysis was performed using an X-ray tube voltage of 30 kV, a preset acquisition time of 900 s, automatic current mode, a 1.2 mm XGT beam, and no X-ray filter. The bath composition was monitored at four stages: before substrate immersion (initial) and after 40, 80, and 120 min of coating.

To investigate the effect of substrate roughness on coating initiation, growth, evolution, and adhesion strength, coatings were applied to substrates with varying surface roughness under optimal bath loading conditions for durations ranging from 10 s to 2 h (10, 20, 30, 60, 120, 240, 480, 960 s, and 2 h). Four distinct levels of substrate surface roughness were achieved by polishing with sandpapers of different grit sizes: 400, 800, 1200, and 1500. The polishing process for each sample began with coarse 400-grit sandpaper, followed by finer grades as needed. The corresponding sample codes are listed in Table 6.1.

Table 6.1. Samples and their corresponding codes.

Activator study		Bath loading study		Surface roughness study	
Activator	Sample code	Substrate dimension (mm^3)	Bath loading ($dm^2.L^{-1}$)	Coating surfaces on polished substrates with sandpapers up to	Code
$PdCl_2$	PA	5 × 5 × 1	0.07	400	S400
HCl	HA	10 × 10 × 1	0.24	800	S800
		15 × 15 × 1	0.51	1200	S1200
		20 × 20 × 1	0.88	1500	S1500
		25 × 25 × 1	1.35		
		30 × 30 × 1	1.92		

The surface roughness was measured using an optical profilometer. The morphological evolution of the coatings was examined using FESEM, and EDS was employed to identify the deposited elements. To evaluate the influence of substrate roughness on the adhesion strength, constant-load scratch tests were performed at 3 N and 6 N using a universal tribometer. These tests were conducted on four coated samples and one uncoated substrate polished with 400-grit sandpaper. The scratch hardness and fracture toughness were derived from the scratch test data.

The sample exhibiting the highest adhesion strength was further characterized using XRD, Fourier transform infrared spectroscopy (FTIR), and corrosion testing to assess its performance. All the experiments described in this chapter were carried out under the same chemical concentrations and coating conditions outlined in Chapter 5, including a cerium sulfate concentration of 8 mg/L.

6.2 Results and discussion

6.2.1 Effect of activator solution on coating deposition

The adhesion and quality of the Ni-W-P-Ce coatings developed on low-carbon steel were found to be significantly influenced by the choice of activator solution ($PdCl_2$ or HCl) used during the substrate preparation. The obtained coatings are shown in Figure 6.2.

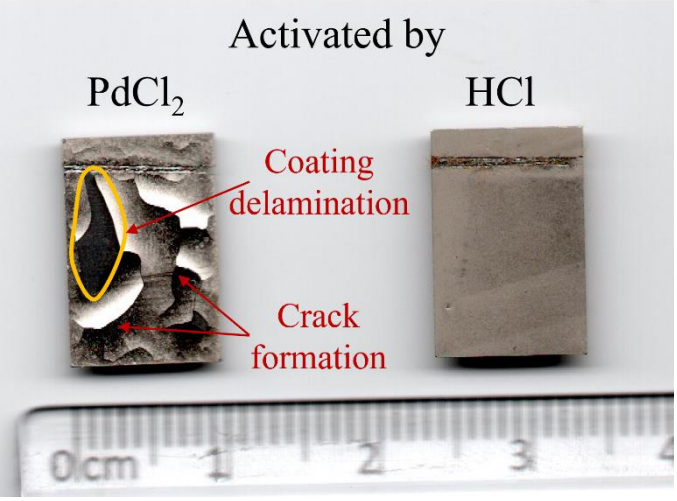

Figure 6.2. Comparison of Ni-W-P-Ce coatings developed on low-carbon steel substrates activated using $PdCl_2$ and HCl solutions.

The coating applied to the $PdCl_2$ activated substrate exhibited poor adhesion, as indicated by the visible delamination and cracking. The coatings flaked off with a minimal

applied force, suggesting brittleness and a weak bond between the substrate and coating. Activation with $PdCl_2$ likely results in the deposition of a thin palladium layer, which may act as an intermediate layer between the substrate and coating. While this Pd layer offers catalytic activity, provides nucleation sites, and aids in the reduction of metal ions from the coating bath, it does not form strong mechanical bonds with the coating. The primary adhesive forces at the interface van der Waals forces [262] were inadequate because of the smoothness of the Pd layer, ultimately leading to weak adhesion. Another factor contributing to the poor adhesion observed in the PA sample was the extended coating duration (2 h) used in this study. Prolonged coating times typically lead to the growth of larger crystallites. These structural changes can introduce internal stresses within the coating, further compromising the adhesion and increasing the likelihood of delamination [263,264].

In contrast, the sample activated by HCl solution exhibited defect-free coatings with no observable cracks or pinholes. Adhesion was significantly improved, which can be attributed to the etching effect of HCl. This etching creates micro-roughening on the steel substrate, enhancing the mechanical interlocking between the coating and substrate. The roughened surface not only increased the contact area, but also strengthened the van der Waals forces, leading to better adhesive strength. Unlike $PdCl_2$ activation, HCl did not deposit an intermediary layer on the substrate, allowing the reduced metal ions to bond directly with the etched steel surface.

As a result, the subsequent two studies employed HCl as the activator because of its effectiveness in promoting strong adhesion between the substrate and coating.

6.2.2 Effect of bath loadings

6.2.2.1 Influence of bath loading on deposition rate

The relationship between bath loading and deposition rate, as illustrated in Figure 6.3, demonstrates the critical dependence of the electroless deposition process on the substrate-to-bath volume ratio. At the lowest bath loading of 0.07 $dm^2.L^{-1}$, the deposition rate was the highest, achieving 18.5 $mg.cm^{-2}.h^{-1}$. However, as the bath loading increased, the deposition rate progressively declined, reaching its lowest value of 5.37 $mg.cm^{-2}.h^{-1}$ at the highest bath loading of 1.92 $dm^2.L^{-1}$.

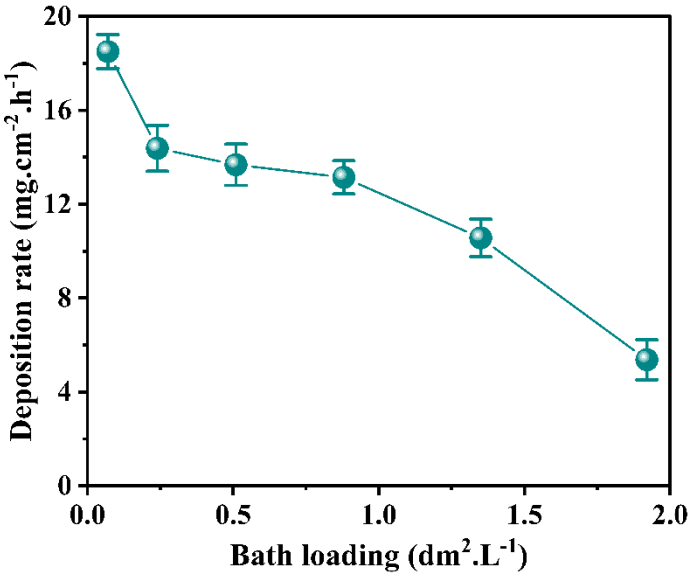

Figure 6.3. Influence of bath loading on the deposition rate of Ni-W-P-Ce coatings.

The results showed that the deposition rate remained relatively high until a bath loading of 0.88 $dm^2.L^{-1}$. Beyond this threshold, the deposition rate begins to decrease significantly. For example, at bath loadings of 1.35 $dm^2.L^{-1}$ and 1.92 $dm^2.L^{-1}$, the rates dropped to 10.56 $mg.cm^{-2}.h^{-1}$ and 5.37 $mg.cm^{-2}.h^{-1}$, respectively. This decrease coincided with an increase in bath viscosity and reactant depletion, as discussed in Subsection 6.2.2.3.

The decrease in deposition rate with increasing bath loading can be attributed to several interconnected factors. A higher bath loading corresponds to a larger substrate surface area relative to the fixed bath volume, leading to a faster consumption of metal ions (e.g., Ni and W) from the solution. This rapid reduction causes the dilution of the concentration of available metal ions, which slows the reduction reactions essential for deposition. Furthermore, at higher bath loadings, the increased generation of hydrogen gas during the electroless coating process creates shear forces that can dislodge the loosely deposited metal from the substrate. This phenomenon further reduces the efficiency of the deposition process. Additionally, a higher bath loading limits the movement of ions within the bath, reducing their accessibility to active sites on the substrate surface. This restriction in ion mobility exacerbates the inefficiency of the deposition process as the autocatalytic nature of the electroless coating becomes less effective. A significant proportion of metal ions may fail to deposit on the substrate, forming byproducts that reduce the overall deposition rate. These combined effects lead to a substantial reduction in deposition efficiency at higher bath loadings [117,265].

6.2.2.2 Effect of bath loading on coating morphology and composition

The surface morphologies of the samples coated for a duration of 2 hours at different bath loadings (0.07, 0.24, 0.51, 0.88, 1.35, and 1.92 $dm^2.L^{-1}$) are shown in Figure 6.4(a-f), corresponding to each loading, respectively. All the surfaces were free from defects and showed no pores or cracks. Although the bath exhibited increased viscosity under higher bath loading conditions, as discussed in Subsection 6.2.2.3, it had no adverse effect on the surface morphology.

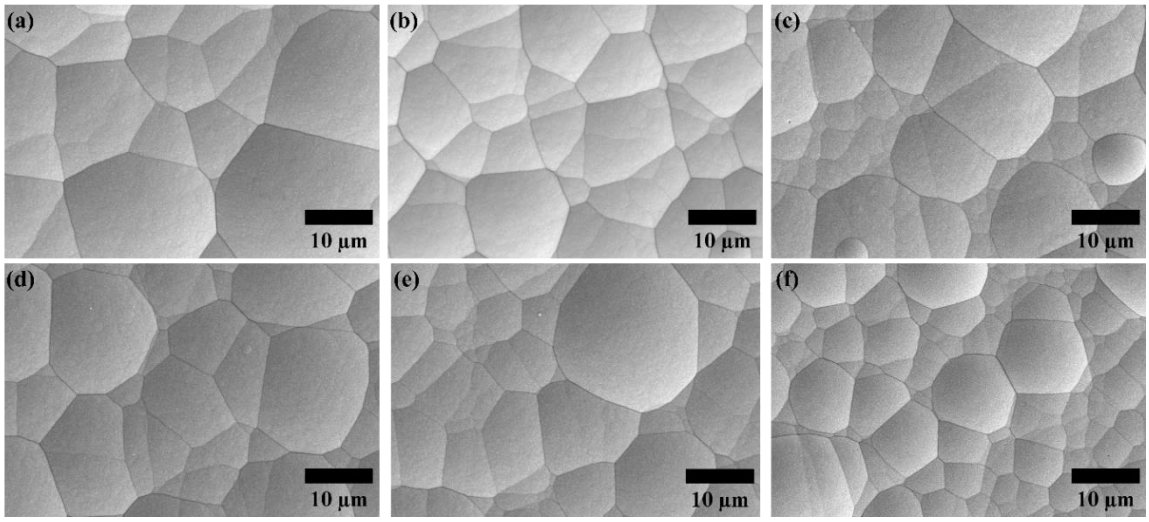

Figure 6.4. Surface morphology of the samples coated for 2 h at different bath loadings.

The elemental weight percentages of the coating samples with different bath loadings are presented in Table 6.2.

Table 6.2. Elemental weight percentages of the coating samples at different bath loadings.

Bath loading ($dm^2.L^{-1}$)	Elements (wt.%)			
	Ni	P	W	Ce
0.07	91.66	5.43	2.27	0.64
0.24	88.73	7.09	3.4	0.79
0.51	89.52	6.64	3.09	0.75
0.88	86.58	7.41	5.16	0.86
1.35	87.01	7.25	4.65	1.09
1.92	92.11	2.95	4.17	0.77

Interestingly, the coatings produced at varying bath loadings resulted in two distinct types of coatings: low-phosphorus (<5 wt.%) Ni-W-P-Ce coatings and medium phosphorus

(6-9 wt.%) Ni-W-P-Ce coatings. Furthermore, as discussed in Subsection 6.3.2.1, a significant increase in the tungsten percentage was observed after a bath loading of 0.88 $dm^2.L^{-1}$. This observation is supported by the EDS results, which showed a decrease in the tungsten percentage for the sample with bath loading exceeding 0.88 $dm^2.L^{-1}$.

To observe the trend in elemental composition variation, a graph was plotted, as shown in Figure 6.5.

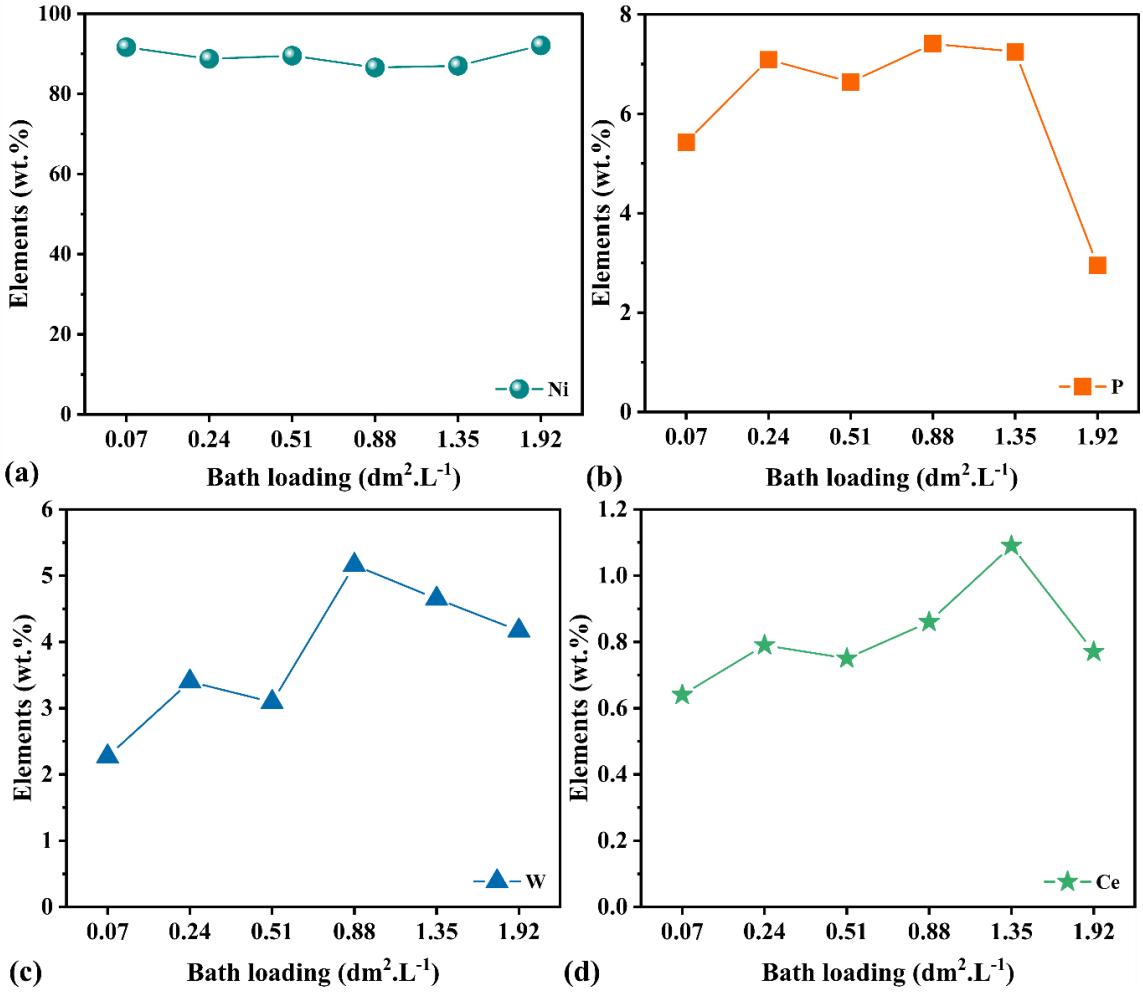

Figure 6.5. Variation in elemental composition of the coating samples with respect to bath loading.

Ni remained the predominant element across all the samples, consistently exceeding 85 wt.%. Its concentration exhibited minor fluctuations, with a slight dip at intermediate bath loadings (0.51-0.88 $dm^2.L^{-1}$), and a notable increase at 1.92 $dm^2.L^{-1}$, suggesting enhanced deposition efficiency at higher loadings. The P content shows a gradual increase and stabilizes over the mid-range bath loadings (0.24-1.35 $dm^2.L^{-1}$), followed by a significant

decline at 1.92 $dm^2.L^{-1}$. The W content increased steadily increases from 0.51 to 1.92 $dm^2.L^{-1}$, indicating more favorable conditions for incorporation at higher loadings. Although Ce was present at the lowest concentration, it remained relatively stable with minor variations throughout.

6.2.2.3 Effect of bath loading on bath conditions

The study of bath loading on coating deposition revealed crucial insights into the impact of substrate dimensions on the bath stability and coating quality. As the substrate area increased, the reduction of metal ions from the coating bath accelerated, leading to the faster depletion of metal salts and reducing agents. For bath loadings of 1.35 $dm^2.L^{-1}$ and 1.92 $dm^2.L^{-1}$, the bath became significantly viscous after approximately 70 and 55 min, respectively, indicating a sharp decline in bath stability as the substrate-to-bath volume ratio increased. Figure 6.6 illustrates the bath conditions in these scenarios.

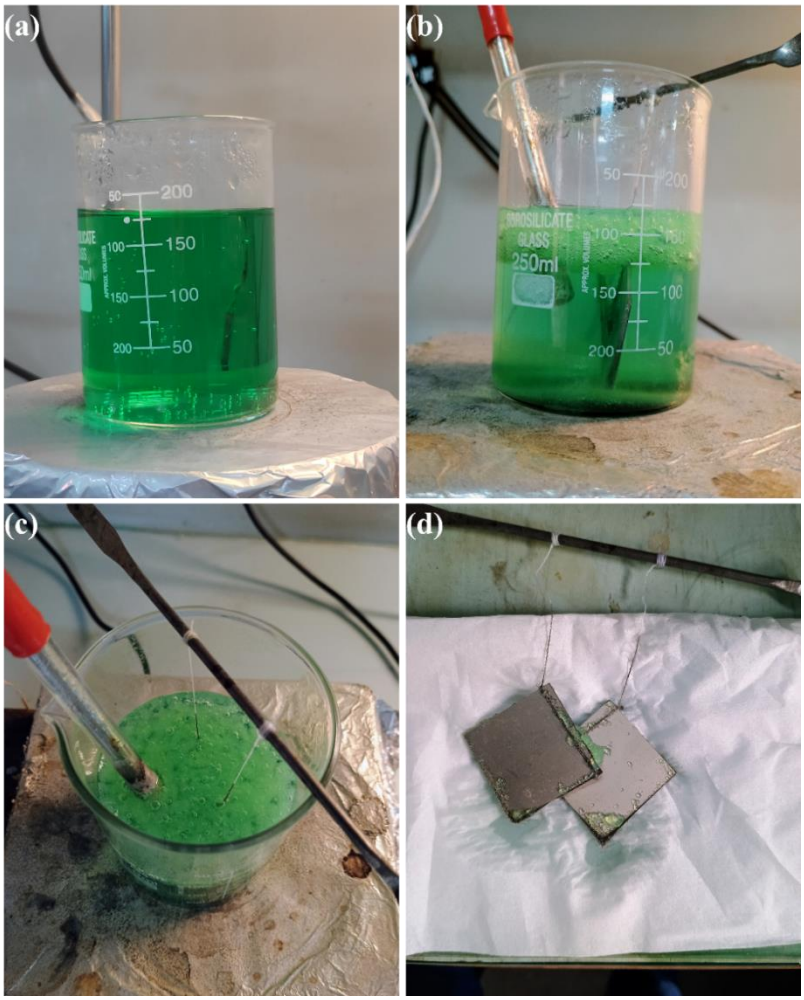

Figure 6.6. Coating bath conditions for 1.35 $dm^2.L^{-1}$ bath loading: (a) unused bath, (b) (c) bath after 70 min, and (d) coated sample at 1.35 $dm^2.L^{-1}$ bath loading.

The as-prepared coating bath, depicted in Figure 6.6(a), was characterized by its transparent appearance and low viscosity. However, as the coating process progressed, the bath became progressively viscous and less transparent, as shown in Figures 6.6(b) and 6.6(c), which represent the front and top views of the bath at 1.35 $dm^2.L^{-1}$ bath loading. The increased viscosity is primarily attributed to the accelerated reduction of metal ions and subsequent accumulation of reaction byproducts, including hydrogen gas and precipitated hydroxides, which are inherent to electroless coating reactions [266]. The high substrate area associated with the increased bath loading amplified the formation of byproducts, leading to particle agglomeration and further thickening of the bath. This accumulation of byproducts disrupts the bath composition, reducing its stability and eventually causing gelation or thickening of the solution [267].

Additionally, the depletion of critical reactants, such as nickel ions, creates an imbalance in bath chemistry, which further destabilizes the coating environment. As shown in Figure 6.6(d), the viscous bath chemicals adhered to the coated sample upon removal, highlighting the severity of viscosity changes at higher bath loadings. The adherence of these viscous byproducts not only interfered with the surface quality of the coating but also indicated the diminished efficiency of the deposition process under such conditions. These findings emphasize the importance of optimizing the bath loading to maintain bath stability and ensure high-quality coatings. Larger substrate areas result in faster reactant depletion and accelerated byproduct accumulation, necessitating careful control of the bath composition and substrate dimensions to prevent imbalanced conditions and bath thickening. Notably, the results from Section 6.2.2.4 support these observations, showing a significant depletion of metal ions and an increase in byproduct formation at higher bath loadings.

Based on the overall analysis, it is evident that bath loadings beyond 0.88 $dm^2.L^{-1}$ resulted in compromised bath conditions, making this the optimal loading for stable bath chemistry and uniform coating deposition. At this bath loading, the deposition rate remained sufficiently high, and no significant issues related to the bath viscosity, thickening, or instability were observed. This bath loading allowed for the adequate availability of reactants and stable bath chemistry, ensuring efficient deposition and uniform coating quality.

6.2.2.4 Elemental analysis of coating bath composition at different bath loadings

Changes in the elemental composition of the coating bath during electroless deposition were analyzed using EDXRF, as illustrated in Figure 6.7. This figure presents the variations in elemental mass percentages over time for each bath loading, highlighting the trends in metal ion consumption and deposition behavior. The corresponding numerical values are summarized in Table 6.3. A bath loading of zero represented the initial condition, in which no substrate was dipped inside the coating bath. As the coating duration and bath loading increased, the Ni concentration in the bath decreased progressively. For example, at the highest bath loading of 1.92 $dm^2.L^{-1}$, the Ni concentration drastically decreased from 33.66% (initial) to 9.06% after 120 min. This depletion was expected because Ni ions were consumed during the reduction process to form a coating. Conversely, the phosphorus concentration exhibited the opposite trend, increasing with both coating duration and bath loading.

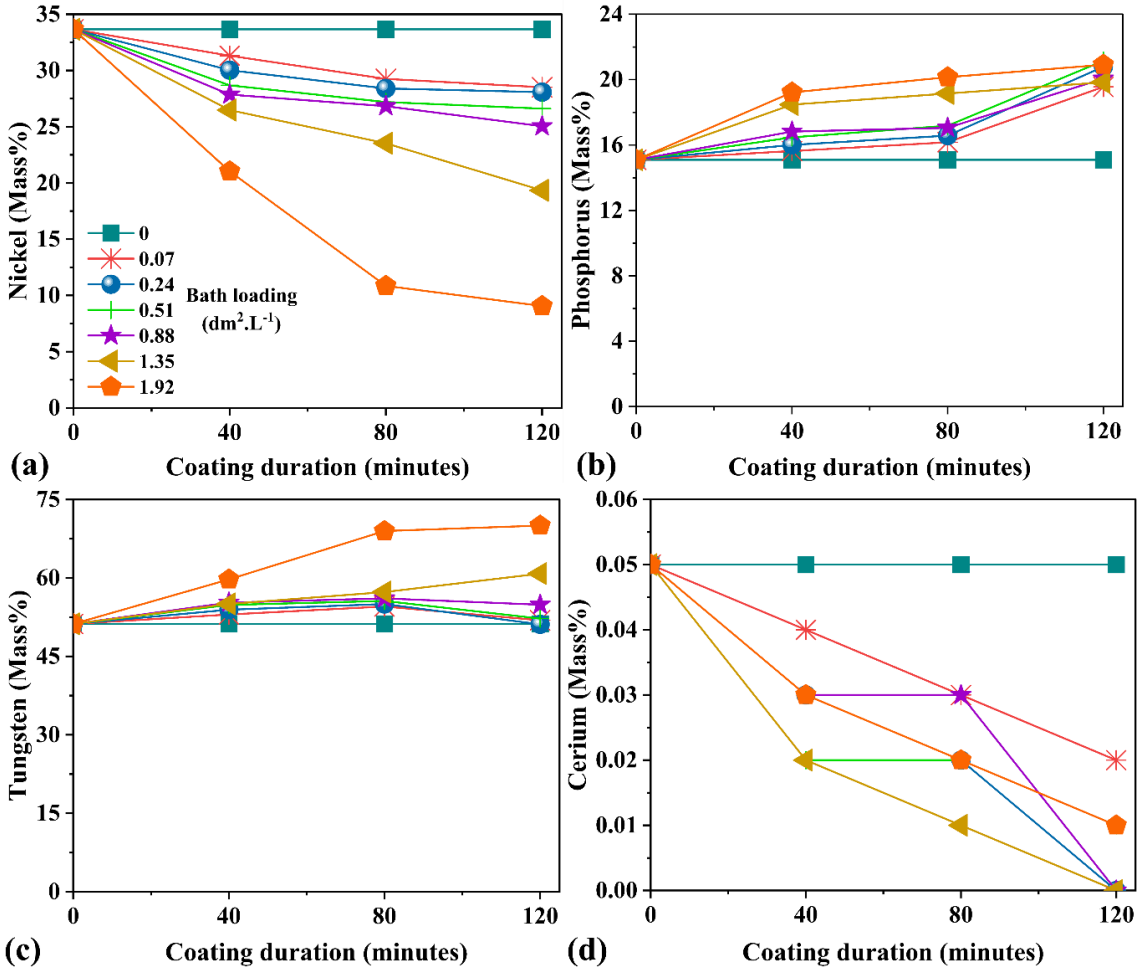

Figure 6.7. EDXRF analysis showing the variation in (a) Ni, (b) P, (c) W, and (d) Ce concentration in the coating bath with time at different bath loadings.

This is likely due to the accumulation of phosphorus byproducts such as hypophosphite-derived compounds during the reduction process [213]. The variation in tungsten concentration followed a different pattern. For bath loadings up to 0.88 $dm^2.L^{-1}$, the tungsten concentration initially increased during the first 80 min of coating but began to decrease thereafter. Beyond this bath loading, however, the tungsten concentration continuously increased with the coating time, reaching 70.02% after 120 minutes at 1.92 $dm^2.L^{-1}$. This trend can be attributed to the tungsten ions not forming strong complexes with the complexing agent (trisodium citrate) as nickel ions, resulting in a higher free ion concentration of tungsten in the bath [268].

Table 6.3. Elemental composition analysis of the electroless coating bath using EDXRF.

Bath loading ($dm^2.L^{-1}$)	Coating duration (minutes)	Elements (Mass%)			
		Ni	P	W	Ce
0	0	33.66	15.1	51.2	0.05
0.07	40	31.32	15.63	53.02	0.04
	80	29.26	16.17	54.54	0.03
	120	28.51	19.56	51.91	0.02
0.24	40	30.03	16.01	53.93	0.03
	80	28.4	16.58	55	0.02
	120	28.08	20.79	51.13	0
0.51	40	28.68	16.47	54.83	0.02
	80	27.2	17.18	55.6	0.02
	120	26.61	21.15	52.23	0.01
0.88	40	27.86	16.82	55.29	0.03
	80	26.83	17.05	56.09	0.03
	120	25.05	20.06	54.89	0
1.35	40	26.48	18.47	55.03	0.02
	80	23.53	19.15	57.31	0.01
	120	19.34	19.84	60.82	0
1.92	40	21.04	19.22	59.72	0.03
	80	10.85	20.15	68.98	0.02
	120	9.06	20.91	70.02	0.01

The Ce concentration, on the other hand, consistently decreased with both the coating time and increasing bath loading. For instance, at a bath loading of 1.92 $dm^2 \cdot L^{-1}$ after 120 min, Ce ions were completely depleted, indicating their rapid consumption during the deposition process. This observation aligns with the relatively low initial concentration of cerium sulfate (8 mg/L) in the bath. Interestingly, despite the higher initial concentration of nickel sulfate (40 g/L) compared to that of tungsten ions, the EDXRF analysis showed a higher mass percentage of tungsten than nickel in the bath. This discrepancy can be attributed to two factors. First, the higher atomic number of tungsten results in a stronger X-ray fluorescence yield, exaggerating its apparent concentration in the analysis [269]. Second, tungsten ions remain more free in the bath, as they do not form stable complexes and are deposited only after interaction with the nickel catalytic surface through induced co-deposition, rather than direct autocatalytic deposition such as nickel ions, as detailed in Chapter 5. The overall analysis indicates that the bath composition became increasingly imbalanced at higher bath loadings, particularly above 0.88 $dm^2.L^{-1}$, where a drastic nickel depletion and excessive tungsten accumulation were observed. These changes negatively impact the bath stability and coating quality. Therefore, 0.88 $dm^2.L^{-1}$ emerged as the optimal bath loading condition, providing a balance between adequate metal ion availability and stable bath chemistry, and ensuring high-quality and uniform coatings.

6.2.3 Impact of substrate roughness on electroless Ni-W-P-Ce coatings

6.2.3.1 Surface roughness analysis of substrates and coatings

The roughness parameters S_a, S_q, S_{ku} and S_{sk} for both the substrates and coatings (after 2 h) were analyzed to understand the relationship between the substrate surface features and the final coating morphology. The results are summarized in Table 6.4. To visualize this trend, bar plots were generated, as shown in Figure 6.8. The substrate roughness decreased with finer sandpaper grades, as evidenced by the reductions in the S_a and S_q values. The substrates polished with 400 grit sandpaper had S_a = 0.19 µm and S_q = 0.25 µm, whereas those polished with 1500 grit sandpaper exhibited much smoother surfaces with S_a = 0.03 µm and S_q = 0.04 µm. The skewness (S_{sk}) values for all the substrates were negative, indicating a negatively skewed surface. These surfaces are characterized by the presence of concave valleys. They exhibit a downward distribution of surface heights relative to the mean plane [270].

Table 6.4. Surface roughness parameters of the substrates and coatings.

Sandpaper	Sample	Roughness parameters			
		S_a (µm)	S_q (µm)	S_{ku}	S_{sk}
400	Substrate	0.19	0.25	8.25	-0.52
	Coating	0.77	1.01	15.11	0.48
800	Substrate	0.17	0.24	11.91	-0.99
	Coating	0.94	1.26	10.06	1.31
1200	Substrate	0.03	0.05	24.37	-1.26
	Coating	1.20	1.76	11.66	2.23
1500	Substrate	0.03	0.04	12.73	-0.71
	Coating	0.85	1.07	28.99	-1.70

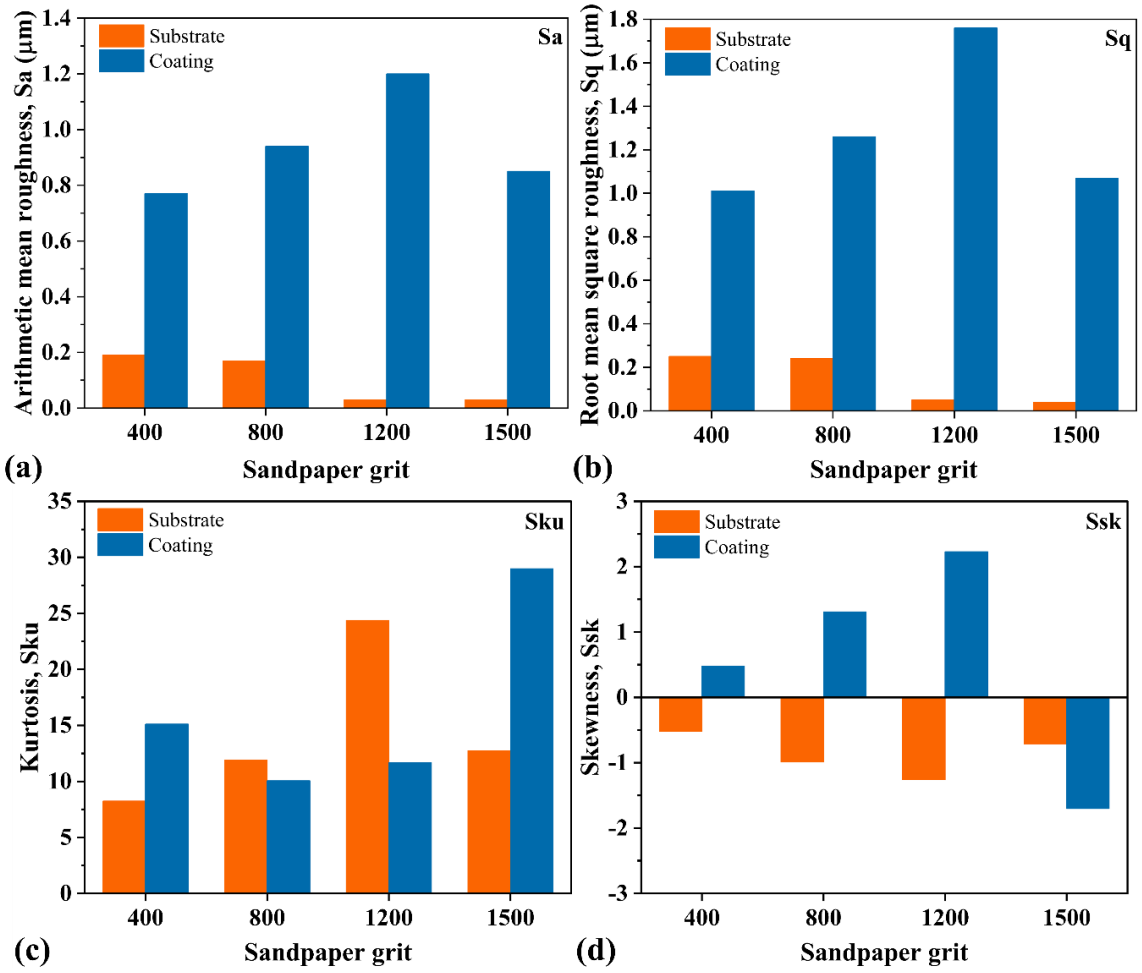

Figure 6.8. Roughness parameters of substrates and coatings for different sandpaper grits.

Coarser sandpaper grades (400 and 800 grit) exhibited S_{sk} values of -0.524 and -0.988, respectively, suggesting the presence of shallow valleys. Substrates prepared with finer sandpapers (1200 and 1500 grit) displayed more negative S_{sk} values (-1.259 and -1.698), indicating deeper valleys. The kurtosis (S_{ku}) values increased with finer sandpaper, indicating higher sharpness of the surface profile. When finer sandpapers were used, they tended to create surfaces with more pronounced peaks and sharper edges, resulting in increased kurtosis values [271].

After 2 h of coating, all the coated surfaces showed a significant increase in the roughness parameters S_a and S_q. All the coated surfaces had higher roughness than the polished substrate, which can be attributed to the combined effect of chemical etching/activation-induced roughening of the substrate underneath the coating as well as the inherent roughness of the nodular coating morphology [139,222]. Coatings on substrates prepared with 400 and 800 grit sandpaper exhibited moderate roughness values (S_a = 0.77 µm, S_q = 1.01 µm for 400 grit, and S_a = 0.94 µm, S_q = 1.26 µm for 800 grit). The coatings on substrates polished with 1200 grit displayed the highest roughness values (S_a = 1.2 µm, S_q = 1.76 µm, S_{sk} = 2.23), suggesting enhanced nodule formation. In contrast, coatings on 1500 grit substrates showed relatively smoother profiles (S_a = 0.85 µm, S_q = 1.07 µm) compared to 1200 grit coatings.

The S_{sk} values of the coatings transitioned from negative (valley-dominated substrate surfaces) to positive (peak-dominated coating surfaces) for substrates polished to 1200 grit. This indicates that the valleys of the substrates were initially filled with the coating material, and the subsequent nodule formation, a characteristic feature of electroless coatings [139], led to the development of peak-dominated surfaces. However, for the 1500 grit substrates, the S_{sk} values for both the substrate and coating remained negative, suggesting that chemical treatment (etching) after polishing further enhanced the roughness, resulting in valley-dominated surfaces even after coating. This effect of the chemical treatment on skewness was less evident in coarser substrates (400, 800, and 1200 grit) because of their higher initial roughness. The kurtosis (S_{ku}) values increased significantly after coating all substrates, particularly for finer substrates. This increase indicated the formation of sharp, well-defined peaks on the coating surfaces, with the highest kurtosis observed for coatings on 1500 grit substrates (S_{ku} = 28.991). The comparatively lower S_a values observed for the 400 grit coating surface indicate minimal

surface roughness; however, the implications of this characteristic can only be determined through further studies, as discussed in the subsequent paragraphs.

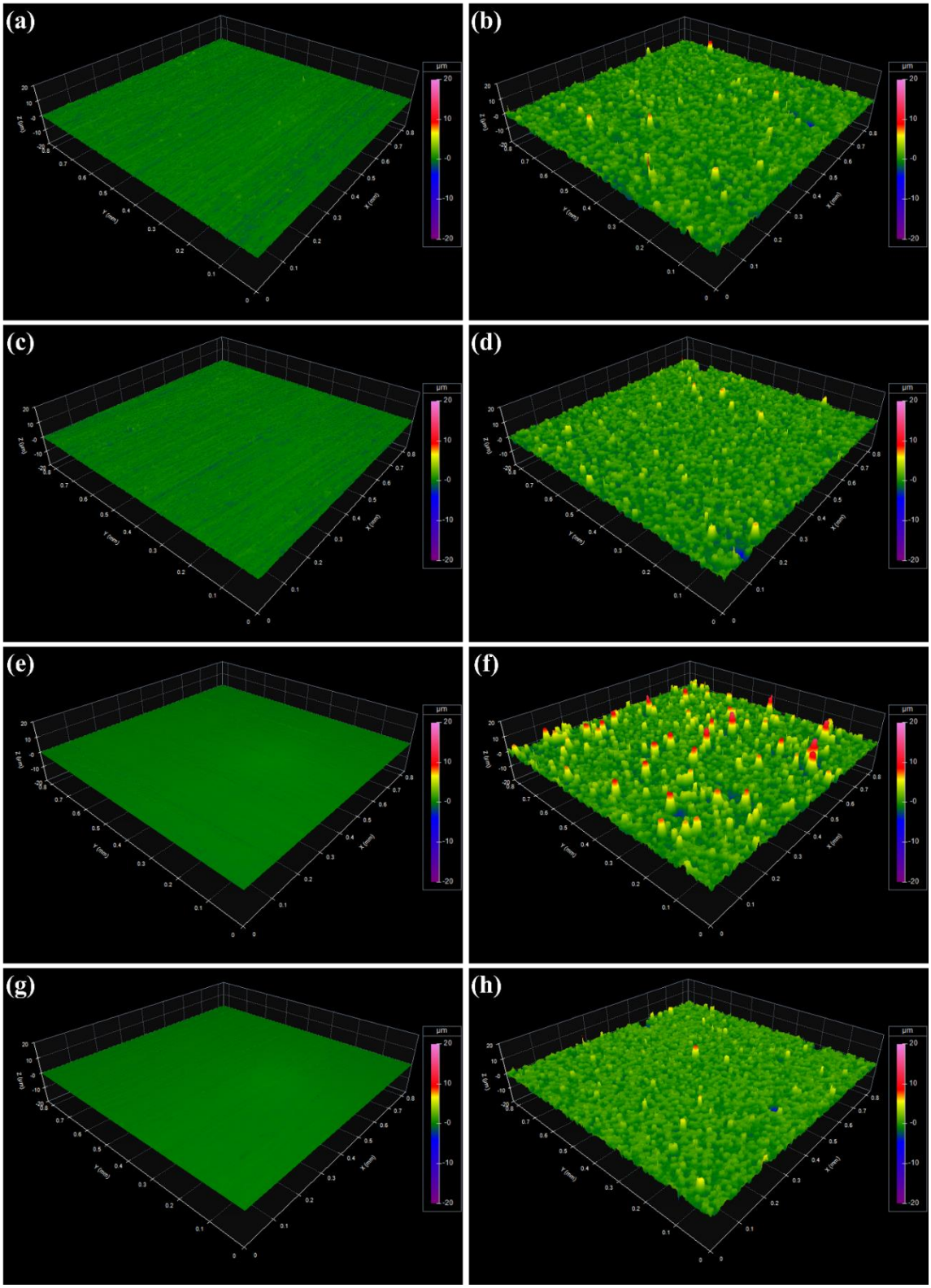

Figure 6.9. 3D optical profilometer images of the substrates and coatings for different sandpaper grits: (a, b) 400, (c, d) 800, (e, f) 1200, and (g, h) 1500 grit.

The 3D optical profilometer images of the four substrates and their respective coatings shown in Figure 6.9, provide a visual representation of the surface topography before and after coating. Figures 6.9(a) and 6.9(b) highlight the relatively rough texture of the 400 grit substrate and its coated surface, respectively, with noticeable valleys in the substrate being partially filled and transformed into a nodule-like morphology after coating. Similarly, Figures 6.9(c) and 6.9(d) for the 800 grit substrate and coating, respectively, reveal a smoother initial texture compared to the 400 grit substrate, with the coated surface showing well-distributed peaks indicative of uniform growth. For the 1200 grit substrate (Figure 6.9(e)), the 3D images revealed a smoother and more refined substrate surface, whereas the coating (Figure 6.9(f)) exhibited the most prominent nodule formation, consistent with the high roughness values observed. In contrast, the 1500 grit substrate (Figure 6.9(g)) and its coating (Figure 6.9(h)) displayed a highly smooth initial surface that transitioned to a moderately roughened coating surface, reflecting the interplay between the chemical treatment and nodule growth. These images visually corroborate the roughness parameter data and further illustrate the critical role of the substrate roughness in determining the morphology and growth characteristics of the coatings.

6.2.3.2 Effect of substrate roughness on deposition rate

As shown in Figure 6.10, the deposition rates for substrates prepared with different sandpaper grits show only minor variations, suggesting that the substrate surface roughness has a limited effect on the deposition efficiency.

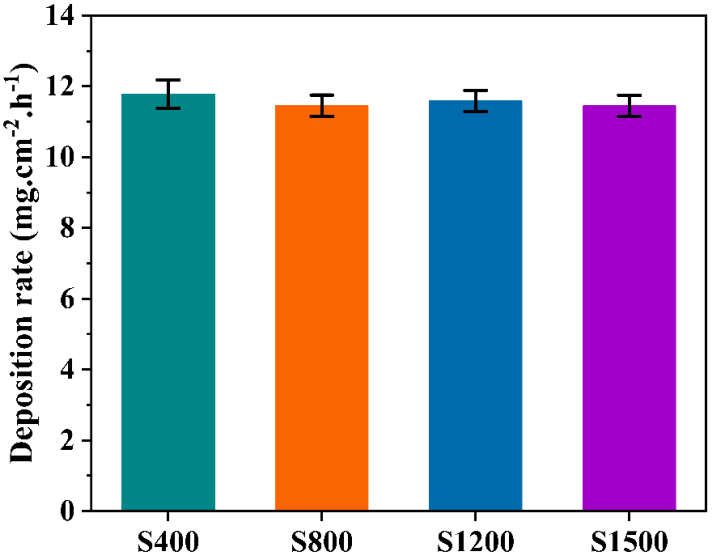

Figure 6.10. Deposition rates of coatings on substrates prepared with various sandpaper grit.

While the 400 grit substrate exhibited the highest deposition rate (11.78 $mg.cm^{-2}.h^{-1}$), and 1500 grit was the lowest (11.45 $mg.cm^{-2}.h^{-1}$), the overall differences were small. This indicates that although rougher surfaces may slightly enhance deposition owing to increased nucleation sites and better mechanical interlocking [272], electroless deposition remains largely consistent across the studied roughness range.

6.2.3.3 Coating characteristics on substrate polished with 400 grit sandpaper

The surface morphology of the Ni-W-P-Ce coatings deposited on substrates polished with 400 grit sandpaper was studied using FESEM at various coating durations, as shown in Figure 6.11. At an early deposition time of 10 s (Figure 6.11(a)), a few randomly distributed white dots, representing nickel deposits approximately 0.12 µm in size, were observed primarily along the corners of the surface scratches and defects. These locations served as preferential sites for nucleation, providing a foundation for further deposition. As the coating duration increased to 20 seconds (Figure 6.11(b)), the average nodule size grew to 0.19 µm, with deposition still occurring predominantly on the rough regions of the substrate, while smoother areas remained largely uncoated.

A similar trend was observed after 30 s (Figure 6.11(c)), when the nodule size increased to 0.25 µm. The rough texture of the substrate provided more irregularities, which facilitated additional nucleation and growth, whereas smoother regions exhibited minimal deposition. At 60 seconds (Figure 6.11(d)), larger nodules with an average size of 0.43 µm were observed, and coalescence of individual nodules into small columnar structures began. However, some areas of the substrate surface were still devoid of coatings, indicating an incomplete coverage. After 120 s of coating (Figure 6.11(e)), a complex structure of nodule columns was evident because of the selective nucleation at different sites on the rough substrate. Despite the increased coverage, some deep grooves or valleys remained uncoated, with an average nodule size of 0.64 µm. At 240 s (Figure 6.11(f)), the nodule size further increased to 1.44 µm, and the coating appeared to cover the entire substrate surface with a plateau-like morphology. However, despite significant coverage, the coating was neither compact nor homogeneous, and voids and interstices were still present. The presence of these voids suggests that substrates with higher roughness experience slower densification owing to the increased surface area that requires filling.

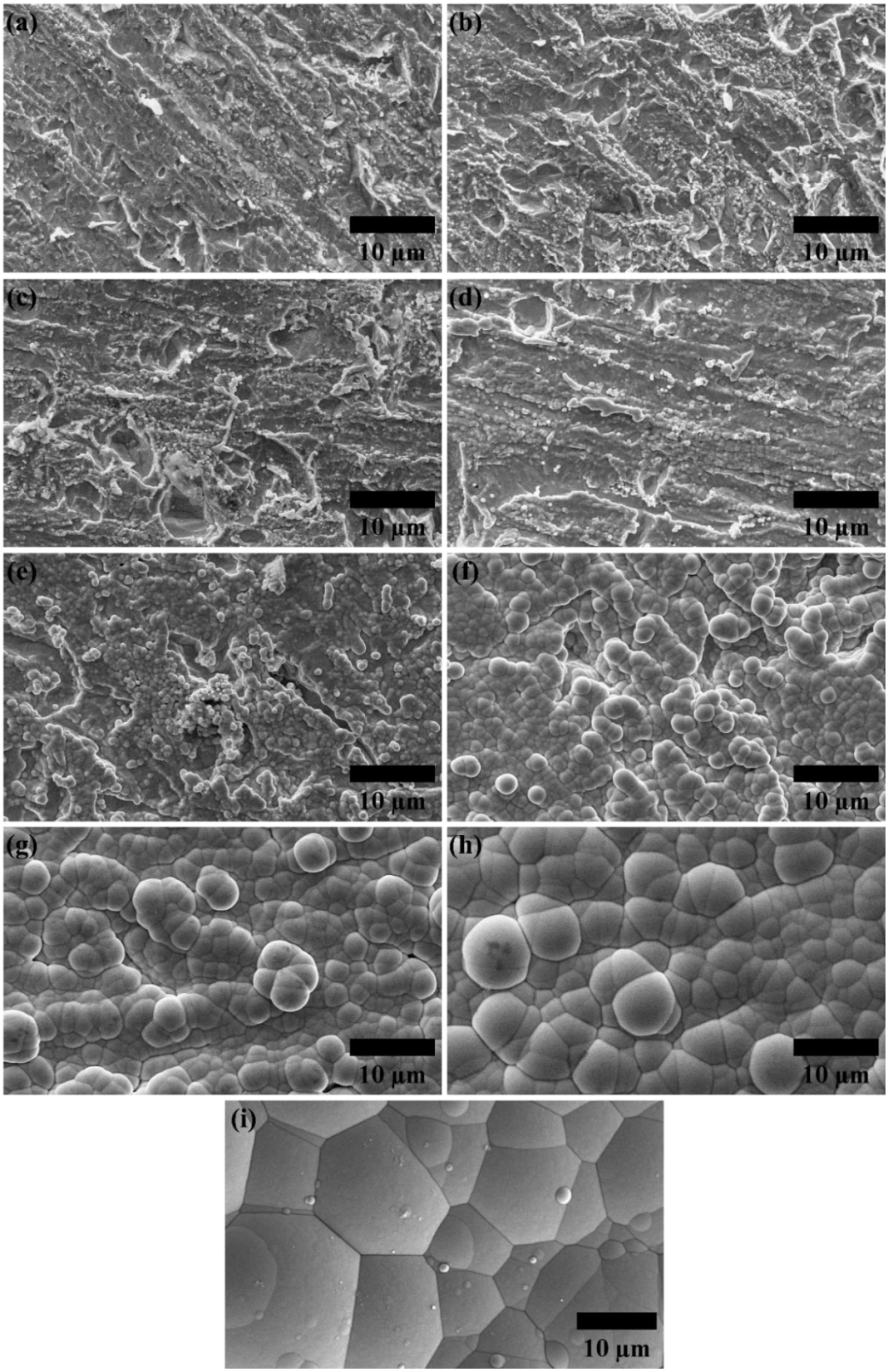

Figure 6.11. SEM images of Ni-W-P-Ce coatings on 400 grit polished substrates for different durations: (a) 10s, (b) 20s, (c) 30s, (d) 60s, (e) 120s, (f) 240s, (g) 480s, (h) 960s, and (i) 2h.

As the coating duration increased to 480 s (Figure 6.11(g)), the nodule size further increased to an average diameter of 2.94 μm, and the coating structure appeared more compact with significantly fewer voids and a more uniform morphology. After 960 s (Figure 6.11(h)), the coating exhibited a homogeneous structure, with a slightly larger average nodule size of 3.73 μm. The morphology transitioned into a well-defined cauliflower-like structure, which is a characteristic of fully developed electroless coatings. Finally, after 2 h of coating (Figure 6.11(i)), the surface was entirely free of defects, with a fully developed structure and an average nodule size of 9.92 μm. The absence of visible defects and consistent growth observed over time indicate that prolonged deposition leads to a dense, uniform coating with enhanced surface coverage. The observed trends suggest that rougher surfaces, such as those polished with 400 grit sandpaper, promote nucleation at higher rates because of the availability of numerous surface irregularities and defects, which act as favorable sites for initial deposition. The increased roughness facilitates mechanical interlocking between the coating and the substrate, enhancing adhesion. However, as the coating growth progressed, the densification phase slowed because of the need to fill the voids and interstices created during the early stages of deposition.

The elemental compositions of the coatings on the polished substrate with 400 grit sandpaper at different deposition times, as obtained by energy dispersive spectroscopy (EDS), are presented in Table 6.5.

Table 6.5. Elemental contents of coatings at different time durations on substrates polished with 400 grit sandpaper.

Coating duration (sec)	Elements (wt.%)				
	Ni	W	P	Ce	Fe
10	8.8	1.4	0.5	1.9	86.5
20	32.6	1.9	1.3	1.9	61.8
30	53.3	2.1	2.3	1.8	40
60	75.9	2.1	3	1.7	17.3
120	82.8	2.2	3.1	1.6	10
240	87.8	2.3	3.3	1.6	6.3
480	87	2.4	4.3	1.5	4.7
960	89.7	3	4.5	1.4	2.4
7200	90	3.4	4.8	1.4	0.3

The data show progressive changes in the weight percentages of Ni, W, P, Ce, and Fe as the deposition time increases, which correlates well with the previously discussed morphological evolution observed in the SEM analysis.

Figure 6.12 graphically illustrates the variation in Ni, W, P, Ce, and Fe content with increasing deposition time on substrates polished with 400 grit sandpaper. In the initial stages of deposition (10 s), the coating consisted primarily of 8.8 wt.% Ni, with a substantial presence of Fe (86.5 wt.%), indicating incomplete coverage of the substrate surface.

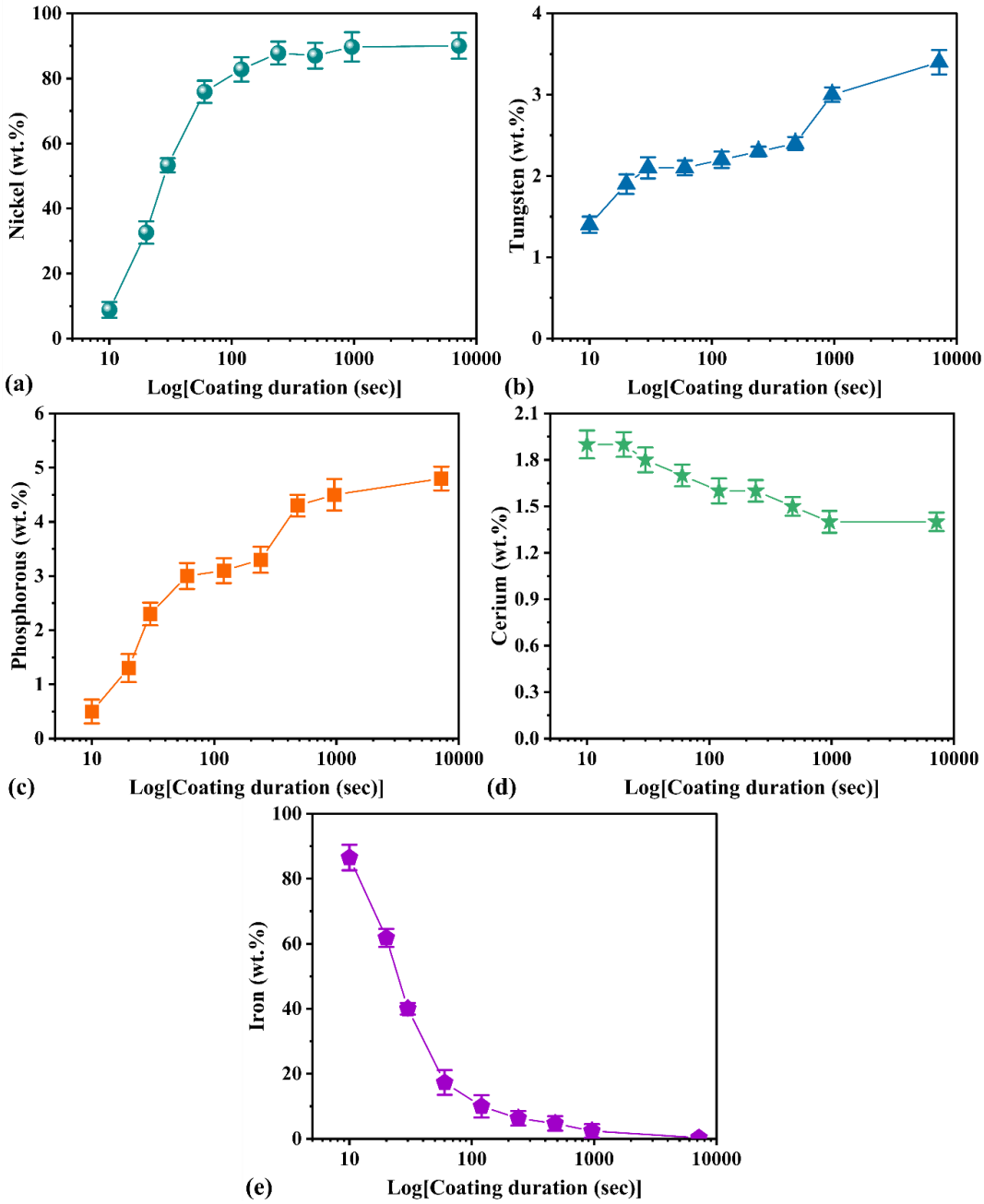

Figure 6.12. Elemental composition (wt.%) of coatings at different durations on 400 grit polished substrates: (a) Ni, (b) W, (c) P, (d) Ce, (e) Fe.

The presence of Fe suggests that at this stage, the coating only begins to nucleate, primarily at high-energy sites, such as surface defects and rough regions, as observed in the SEM images. A gradual increase in the Ni content to 32.6 wt.% at 20 seconds and 53.3 wt.% at 30 seconds signifies the expansion of nucleation sites and the initial coalescence of nodules over the rough surface, while the Fe content decreases correspondingly, confirming the progressive coverage of the substrate. By 60 seconds, the Ni content reaches 75.9 wt.%, marking a significant transition where the coating becomes more continuous, covering a larger portion of the substrate. The reduction in the Fe content to 17.3 wt.% at this stage aligns with SEM observations, where the formation of larger nodules and coalescence into columns was seen. As the deposition continued beyond 120 s, the Ni content further increased to 82.8 wt.%, while Fe content declines to 10 wt.%, indicating a more uniform and extensive coating coverage with minimal substrate exposure. The W and P content remained relatively stable at approximately 2.1-3.3 wt.%, suggesting consistent incorporation of alloying elements during the growth process. At 240 seconds, the Ni content reaches 87.8 wt.%, with Fe reducing to 6.3 wt.%, signifying near-complete surface coverage. The phosphorus (P) and cerium (Ce) contents remained relatively steady, contributing to the formation of the plateau-like structure observed in the SEM images. This phase marks the densification period where voids and interstices begin to fill, although some non-uniformity in the coating morphology remains. After 480 s, the Ni content increased further to 87 wt.%, and Fe is reduced to 4.7 wt.%, indicating the formation of a compact coating. The phosphorus content increases to 4.5 wt.%, which contributes to the observed improved densification and reduced voids. During the final stages of deposition (960 s to 2 h), the Ni content stabilized at approximately 89.7-90 wt.%, with Fe content reaching a minimal 0.3 wt.%, confirming complete coverage of the substrate. The increase in W and P content to 3.4 wt.% and 4.8 wt.%, respectively, indicates the formation of a well-alloyed coating, improving properties such as hardness and corrosion resistance. At 7200 s (2 h), the coating achieved its final structure with a highly uniform composition, characterized by a significant reduction of Fe to nearly negligible levels, confirming full substrate coverage. The increase in W content suggests further densification and refinement of the coating structure, as shown in the SEM images, where a cauliflower-like morphology was observed.

The progressive increase in the Ni content and simultaneous reduction in the Fe content with increasing deposition time confirmed the gradual and continuous growth of the

coating. The early stages are characterized by nucleation and partial coverage, whereas the intermediate stages focus on growth and densification. The final stage yielded a highly uniform defect-free coating with an optimal Ni, W, P, and Ce composition. These findings correlate well with the SEM observations and emphasize the crucial role of substrate roughness in influencing deposition kinetics and coating quality.

6.2.3.4 Coating characteristics on substrate polished with 800 grit sandpaper

The SEM images of the evolution of the electroless Ni-W-P-Ce coatings on the 800 grit polished substrate are presented in Figure 6.13. The coating behavior on this substrate showed significant differences compared to the 400 grit polished substrate, highlighting the impact of substrate roughness and surface preparation on the initiation and growth of coatings. After 10 seconds of deposition (Figure 6.13(a)), the surface exhibited a greater density of small white deposits compared to the 400 grit substrate, with an approximate nodule size of 0.14 μm, which is larger than the nodules density observed on the 400 grit substrate. This increase in the deposition rate was further confirmed by EDS analysis (Table 6.6), which showed a 27.4 wt.% nickel content at this stage, more than three times higher than that observed on the 400 grit polished substrate. The increased nucleation density can be attributed to the combined effects of the surface roughness and etching process applied before deposition.

Each substrate was etched in a 30% dilute HCl solution prior to coating, which influenced the surface chemistry and morphology differently depending on the polishing grade. The 800 grit polished substrate may have experienced a more uniform and finer etching effect, creating an ideal surface for electroless deposition by exposing a higher density of active sites. In contrast, the 400 grit substrate, owing to its coarser texture, may have developed larger voids and irregularities during etching, which hindered uniform nucleation. The finer and more uniform surface features of the 800 grit substrate, enhanced by etching, provided a better anchoring environment for nickel deposition, contributing to the observed increase in early stage deposition. At 20 seconds (Figure 6.13(b)), the nodules increased in size to 0.2 μm, with uniform and widespread coverage across the surface. The fine surface features created by polishing and etching continued to support the deposition process, ensuring that the coating was spread more evenly than on the 400 grit substrate.

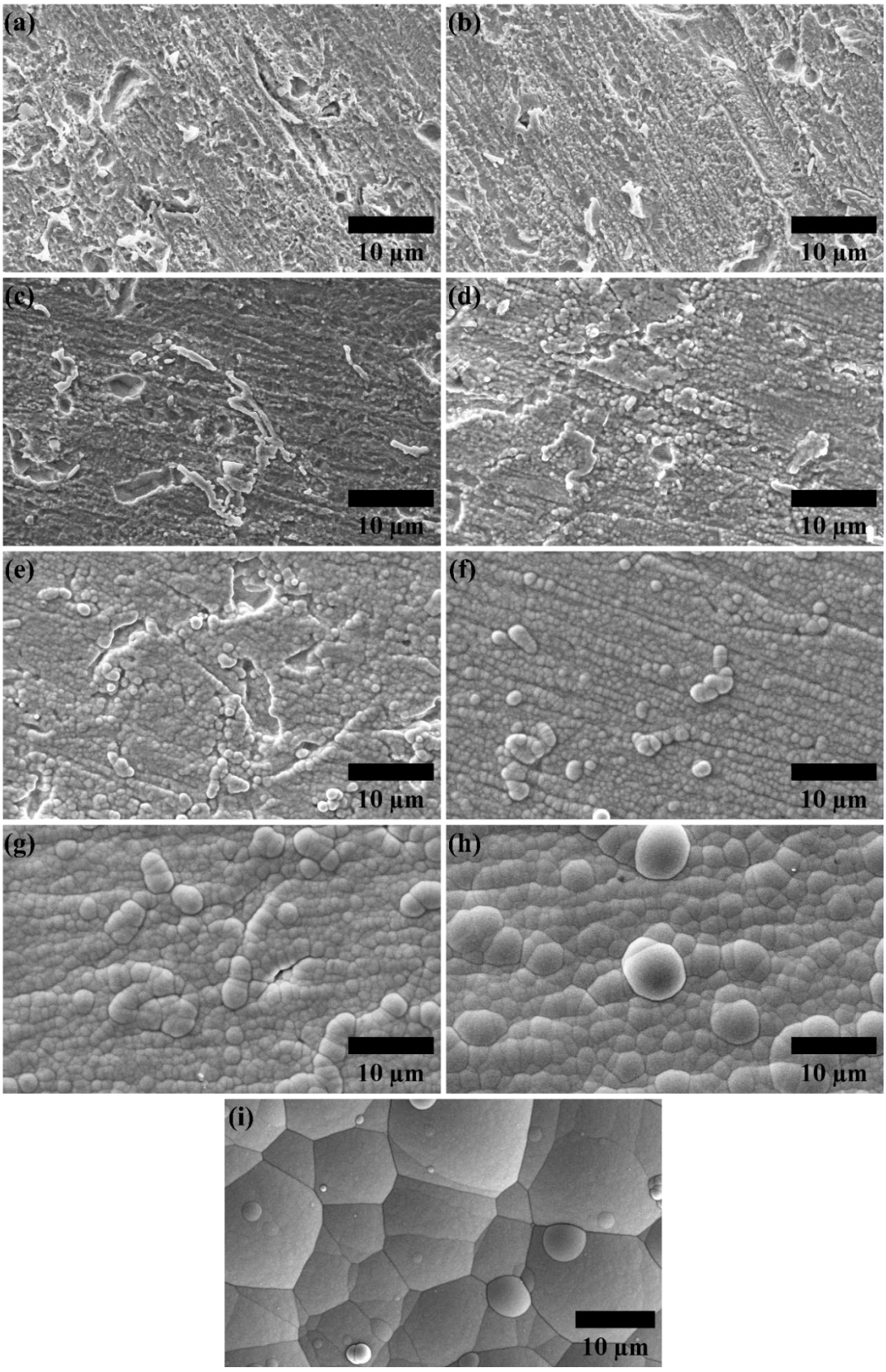

Figure 6.13. SEM images of Ni-W-P-Ce coatings on 800 grit polished substrates for different durations: (a) 10s, (b) 20s, (c) 30s, (d) 60s, (e) 120s, (f) 240s, (g) 480s, (h) 960s, and (i) 2h.

After 30 s (Figure 6.13(c)), the nodule size increased to 0.29 μm, and the deposits began to coalesce, forming columnar structures, an effect that was observed at a later stage (60 s) for the 400 grit substrate. This accelerated growth confirms that the etching of the 800 grit substrate created a more favorable condition for coating adhesion and growth by exposing more uniform nucleation sites compared to the rougher 400 grit substrate. After 60 seconds of coating (Figure 6.13(d)), a steady-state growth phase was observed, with an increased nodule size of 0.46 μm and enhanced densification. At 120 s (Figure 6.13(e)), the nodules grew to an average size of 0.83 μm, and the coating exhibited improved densification, although some voids were still visible. By 240 s (Figure 6.13(f)), the coating surface was almost fully covered with nodules averaging 1.28 μm in size. Minimal voids were observed, suggesting that the uniform etching pattern contributed to well-distributed coating growth. The coating morphology continues to evolve with increasing deposition time. After 480 s (Figure 6.13(g)), the nodules reached an average size of 2.2 μm, and the coating became denser, more compact, more uniform in size, and more tightly bonded. At 960 s (Figure 6.13(h)), the nodule size further increased to 3.3 μm, and the coating exhibited a highly uniform and defect-free appearance. After 2 h of deposition (Figure 6.13(i)), the coating achieved a final nodule size of 9.47 μm, forming a compact and homogeneous structure.

The 800 grit substrate facilitated larger nodule sizes during the early stages (up to 120 s) compared to the 400 grit substrate, indicating that the finer surface features and uniform etching enhanced nucleation. However, beyond 120 s, the growth rate slowed, and the final nodule size became smaller than that observed for the 400 grit substrate. This difference was attributed to the presence of larger voids and irregularities in the 400 grit substrate, which provided additional space for densification and resulted in larger nodules in the long term.

The elemental compositions of the Ni-W-P-Ce coatings deposited on the 800 grit polished substrate for various durations, as obtained from the EDS analysis, are presented in Table 6.6. Figure 6.14 graphically illustrates the variation in Ni, W, P, Ce, and Fe content with increasing deposition time on substrates polished with 800 grit sandpaper. In the early stage of deposition, the Ni content increased rapidly, reaching 27.4 wt.% at 10 seconds, significantly higher than that observed for the 400 grit substrate. This indicates that the finer and more uniform surface of the 800 grit substrate provided more nucleation sites, facilitating greater nickel uptake. The Fe content, initially at 65.7 wt.%, highlights incomplete coverage, but the faster deposition rate compared to the 400 grit substrate

suggests improved adhesion and surface compatibility. After 20 s, the Ni content increased to 48.3 wt.%, with a further decline in Fe content, demonstrating progressive coverage. After 30 s, the coating grew substantially with a Ni content of 53.8 wt.%, and Fe reduced to 37.9 wt.%, reflecting rapid surface coverage and early-stage densification. After 60 s, the Ni content reached 78.8 wt.%, with Fe content reducing to 13.5 wt.%, indicating substantial substrate coverage and coalescence of nodules. After 120 s, the Ni content further increased to 84 wt.%, with Fe at 8.3 wt.%, signifying near-complete coverage and the onset of densification. Phosphorus and tungsten contents showed consistent incorporation, contributing to the coating's stability.

Table 6.6. Elemental contents of coatings at different time durations on substrates polished with 800 grit sandpaper.

Coating duration (sec)	Elements (wt.%)				
	Ni	W	P	Ce	Fe
10	27.4	2.1	1.3	2	65.7
20	48.3	2.2	2.3	1.9	45.5
30	53.8	2.3	3.1	1.8	37.9
60	78.8	2.8	3.4	1.7	13.5
120	84	2.8	3.8	1.7	8.3
240	85.4	3	4.1	1.7	7.2
480	85.6	3.4	4.5	1.6	4.7
960	87.8	3.5	4.8	1.6	2.4
7200	89.7	3.9	4.9	1.4	0.2

At 240 s, the Ni content stabilized at 85.4 wt.%, indicating uniform deposition with minimal remaining substrate exposure. As deposition continued, the coating became more compact and uniform. At 480 s, the Ni content reached 85.6 wt.%, while Fe decreased to 4.7 wt.%, showing further densification. After 960 s, the coating composition reached 87.8 wt.% Ni, confirming the near-complete coverage with minimal Fe at 2.4 wt.%. By the end of 2 h, the coating was fully developed with 89.7 wt.% Ni, and Fe content was reduced to a negligible 0.2 wt.%, reflecting a fully formed and compact coating. EDS analysis confirmed that the finer surface of the 800 grit polished substrate resulted in faster nickel deposition, higher early stage coverage, and a more uniform final coating. The gradual

decline in Fe content and steady incorporation of W, P, and Ce indicate a well-structured coating with enhanced adhesion and uniformity.

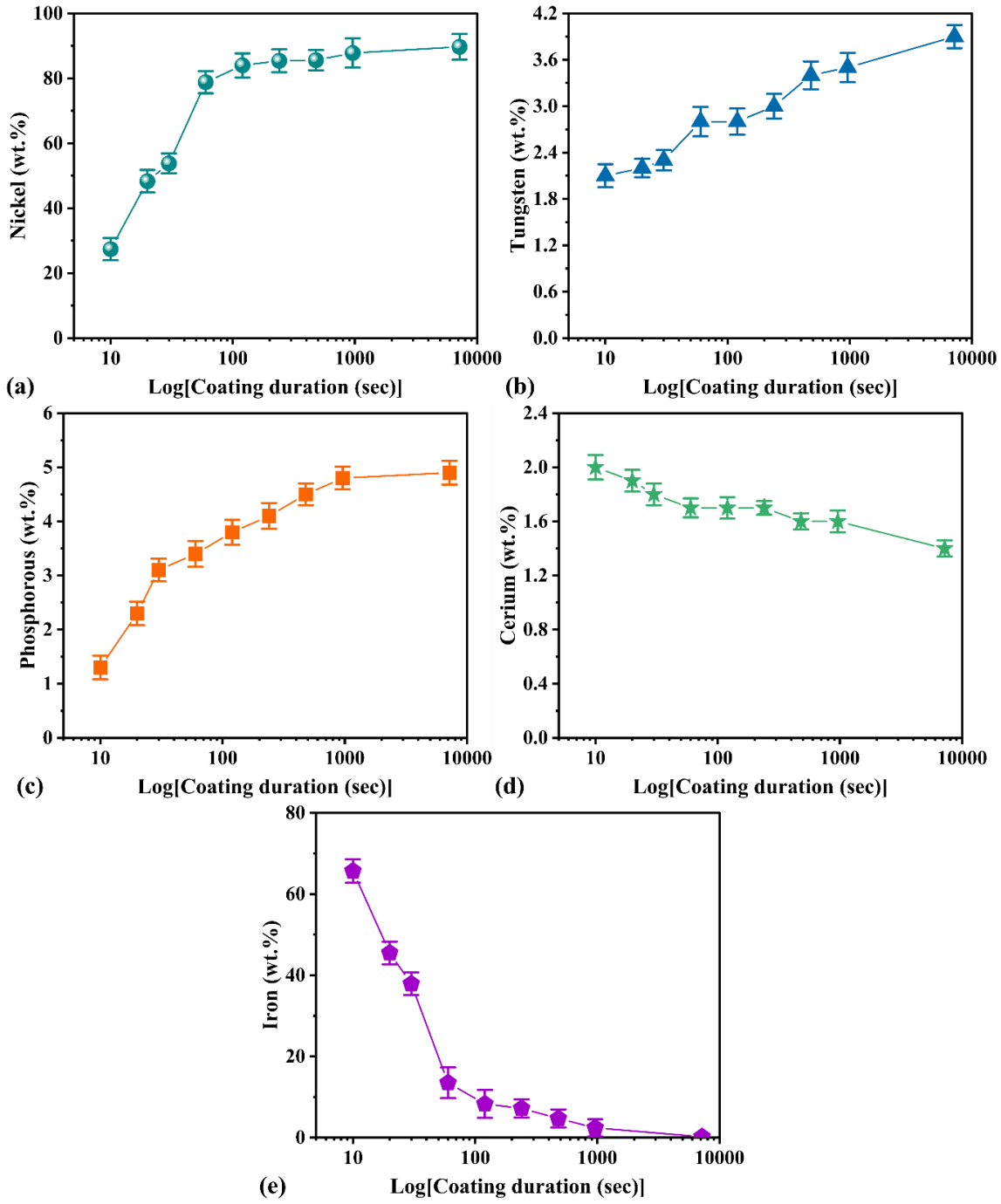

Figure 6.14. Elemental composition (wt.%) of coatings at different durations on 800 grit polished substrates: (a) Ni, (b) W, (c) P, (d) Ce, (e) Fe.

6.2.3.5 Coating characteristics on substrate polished with 1200 grit sandpaper

The coating evolution on the substrate polished with 1200 grit sandpaper was analyzed at various deposition times, and the corresponding SEM images are presented in Figure 6.15. The deposition behavior on this substrate exhibited distinct characteristics compared to the 400 and 800 grit polished substrates, emphasizing the critical role of finer surface roughness in influencing the initiation and growth of electroless coatings.

After 10 s of coating (Figure 6.15(a)), the substrate surface appeared relatively rough and was characterized by scratches, grooves, and valleys. Unlike the 400 and 800 grit substrates, no visible coating deposits in the form of small white dots are observed at this stage. However, the elemental analysis confirmed the presence of 19.3 wt.% nickel along with other elements, indicating that deposition had indeed begun, albeit at a much slower and more uniform rate. The absence of visible deposits at this stage suggests that the smoother surface of the 1200 grit substrate delayed the appearance of nucleation sites, likely because of the reduced surface defects and available anchoring points compared to coarser substrates. By 20 seconds of coating duration (Figure 6.15(b)), the formation of very small nodules with an average size of 0.15 μm was observed, primarily concentrated in surface scratches and defects. This indicates that the initial deposition was guided by the surface imperfections of the substrate, where nucleation was more likely to occur because of the localized surface energy variations. The slower initiation of visible deposition compared to coarser substrates suggests that finer surface roughness results in a more uniform nucleation process, with fewer preferential sites. At 30 seconds (Figure 6.15(c)), nodules with an average size of 0.21 μm were seen spreading uniformly across the surface. The improved dispersion of the coating material suggests that the finer surface roughness facilitated better lateral growth and even coverage compared to the 400 and 800 grit substrates, where deposition was more localized in the early stages. After 60 s (Figure 6.15(d)), uniformly sized nodules with average dimension of 0.35 μm were observed. The coating morphology revealed the growth of nodules into small columnar structures that gradually covered more of the substrate surface. The uniformity of the nodules at this stage highlights the effect of the finer roughness of the 1200 grit substrate, which promotes consistent nucleation and growth across the entire surface. By 120 seconds (Figure 6.15(e)), the nodule size increased to 0.66 μm, and the coating appeared dense, with minimal voids.

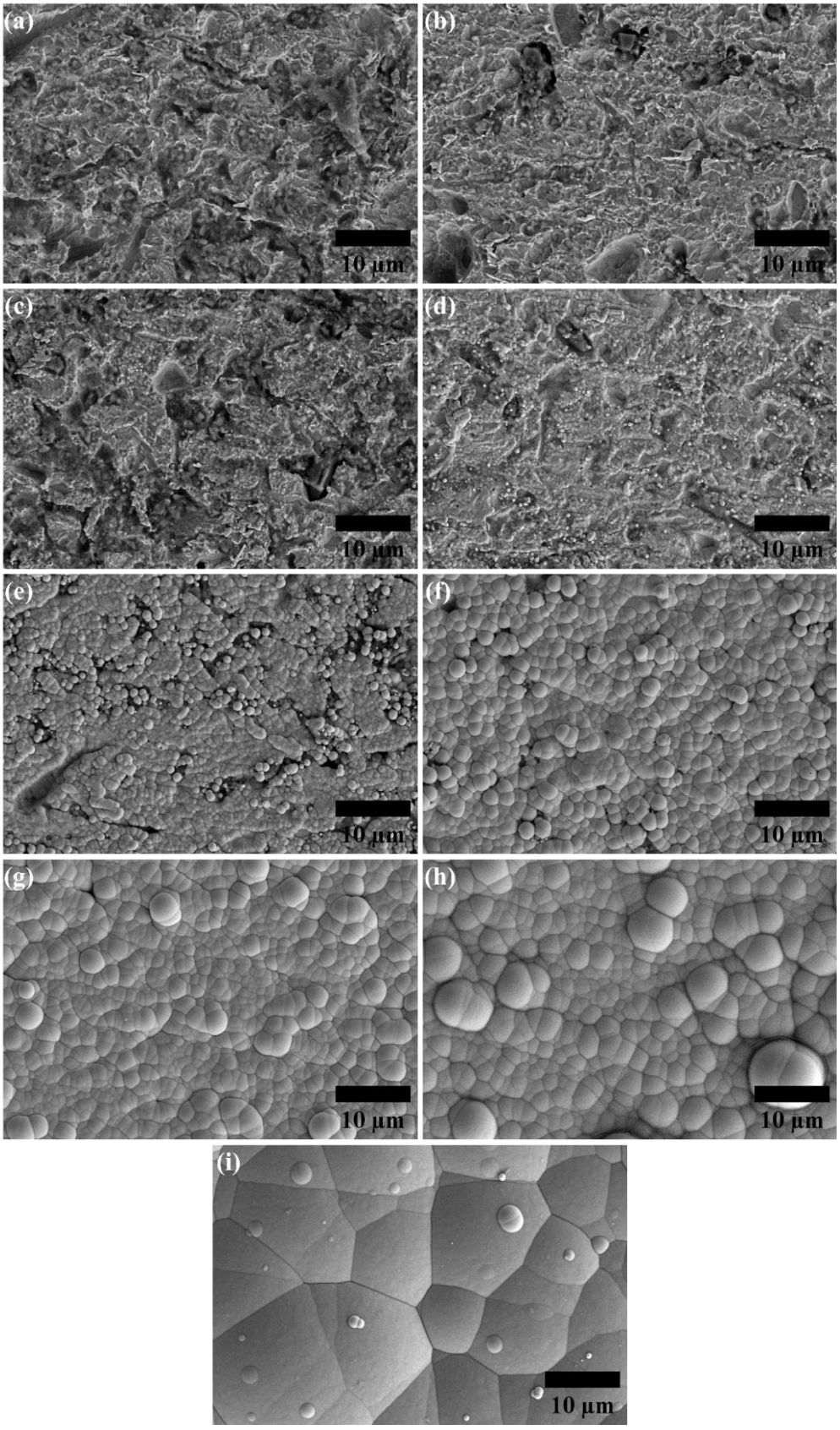

Figure 6.15. SEM images of coatings on 1200 grit polished substrates for different durations: (a) 10s, (b) 20s, (c) 30s, (d) 60s, (e) 120s, (f) 240s, (g) 480s, (h) 960s, and (i) 2h.

This stage marked a critical transition, where the coating began to exhibit significant densification, leading to improved structural integrity and uniformity. The finer texture of the 1200 grit substrate provided a stable platform for controlled growth, resulting in a well-defined coating layer. At 240 s (Figure 6.15(f)), the coating showed very dense deposition, with uniformly sized nodules averaging 1.43 μm, and the substrate was almost fully covered. Only a few voids are present, indicating that the coating is fully developed. Compared to coarser substrates, the 1200 grit substrate facilitated earlier coverage completion, reducing the presence of voids and ensuring a more compact coating. After further deposition, at 480 s (Figure 6.15(g)), the nodule size increased to 2.15 μm, and the coating was completely defect-free. The uniform distribution of the nodules suggests that the coating process reached a stable growth phase, where deposition continued to occur evenly across the substrate surface without significant structural irregularities. By 960 s (Figure 6.15(h)), the nodule size further increased to 3.16 μm, and the coating morphology remained consistent, showing continued growth with no observable defects. After 2 h of deposition (Figure 6.15(i)), the final coating exhibited an average nodule size of 9.46 μm, with a completely defect-free and compact structure. The uniformity of the final coating confirmed that the 1200 grit substrate provided an optimal balance between the surface roughness and coating growth dynamics, leading to an even and well-structured coating layer.

The evolution of coatings on the 1200 grit polished substrate demonstrated a more controlled and uniform growth process compared to coarser substrates. The finer surface roughness provided fewer but more evenly distributed nucleation sites, resulting in a delay in visible deposition but a more consistent and uniform coating formation in the later stages. Unlike the 400 and 800 grit substrates, where early stage deposition was concentrated on surface defects, the 1200 grit substrate allowed for a gradual and controlled growth that ultimately resulted in a denser and more uniform coating.

The elemental compositions of the Ni-W-P-Ce coatings deposited on the 1200 grit polished substrate at different time intervals, as obtained from EDS analysis, are presented in Table 6.7. Figure 6.16 graphically illustrates the variation in Ni, W, P, Ce, and Fe content with increasing deposition time on substrates polished with 1200 grit sandpaper.

In the early stage of deposition, the Ni content was 19.3 wt. % after 10 seconds, indicating the onset of the coating process. However, large amounts of Fe (75.6 wt.%)

suggests that significant portions of the substrate were still exposed. Compared with coarser substrates, the delayed visible coating formation aligns with earlier SEM observations, where no apparent deposition was observed at this stage. The tungsten (W), phosphorus (P), and cerium (Ce) contents were relatively low, indicating a slow and steady nucleation process. After 20 s, the Ni content increased to 40.7 wt.%, with Fe decreasing to 54.1 wt.%, confirming progressive coverage of the substrate. The phosphorus content also increased to 1.8 wt.%, indicating enhanced coating integrity.

Table 6.7. Elemental contents of coatings at different time durations on substrates polished with 1200 grit sandpaper.

Coating duration (sec)	Elements (wt.%)				
	Ni	W	P	Ce	Fe
10	19.3	2	0.8	1.9	75.6
20	40.7	2.1	1.8	1.7	54.1
30	60.5	2.3	2.5	1.6	33.3
60	67.7	2.4	3.7	1.5	23.6
120	77.9	2.5	3.7	1.4	14.6
240	85.4	2.6	4.3	1.4	5.8
480	86.7	2.8	4.5	1.4	4.7
960	88.3	3.1	4.6	1.3	3.1
7200	91.4	3.2	4.9	1.1	0.2

At 30 s, the Ni content further increased to 60.5 wt.%, and Fe content reduced to 33.3 wt.%, demonstrating substantial coverage, correlating well with the appearance of small, well-distributed nodules in the SEM analysis. The increase in the W and P contents suggests improved alloying of the coating as the deposition continues. After 60 s, the Ni content increased to 67.7 wt.%, while Fe content further decreased to 23.6 wt.%, signifying significant surface coverage and nodule coalescence. Phosphorus content reached 3.7 wt.%, enhancing the structural stability of the coating. An increase in the Ce content to 1.9 wt.% indicates its incorporation into the coating, contributing to the refinement of grain structure and overall coating properties. After 120 s, the Ni content increased to 77.9 wt.%, with Fe content decreasing to 14.6 wt.%, suggesting near-complete surface coverage. The uniformity and densification observed in the SEM images at this stage are consistent with the EDS results, highlighting that the finer 1200 grit substrate allowed for a more controlled

and homogeneous coating growth process. The increase in phosphorus and tungsten contents indicates a well-alloyed coating. At 240 s, the Ni content rose to 85.4 wt.%, and Fe content reduced to 5.8 wt.%, confirming almost complete coverage of the substrate. Phosphorus content reached 4.3 wt.%, contributing to the densification and enhancement of coating properties, such as improved hardness and wear resistance.

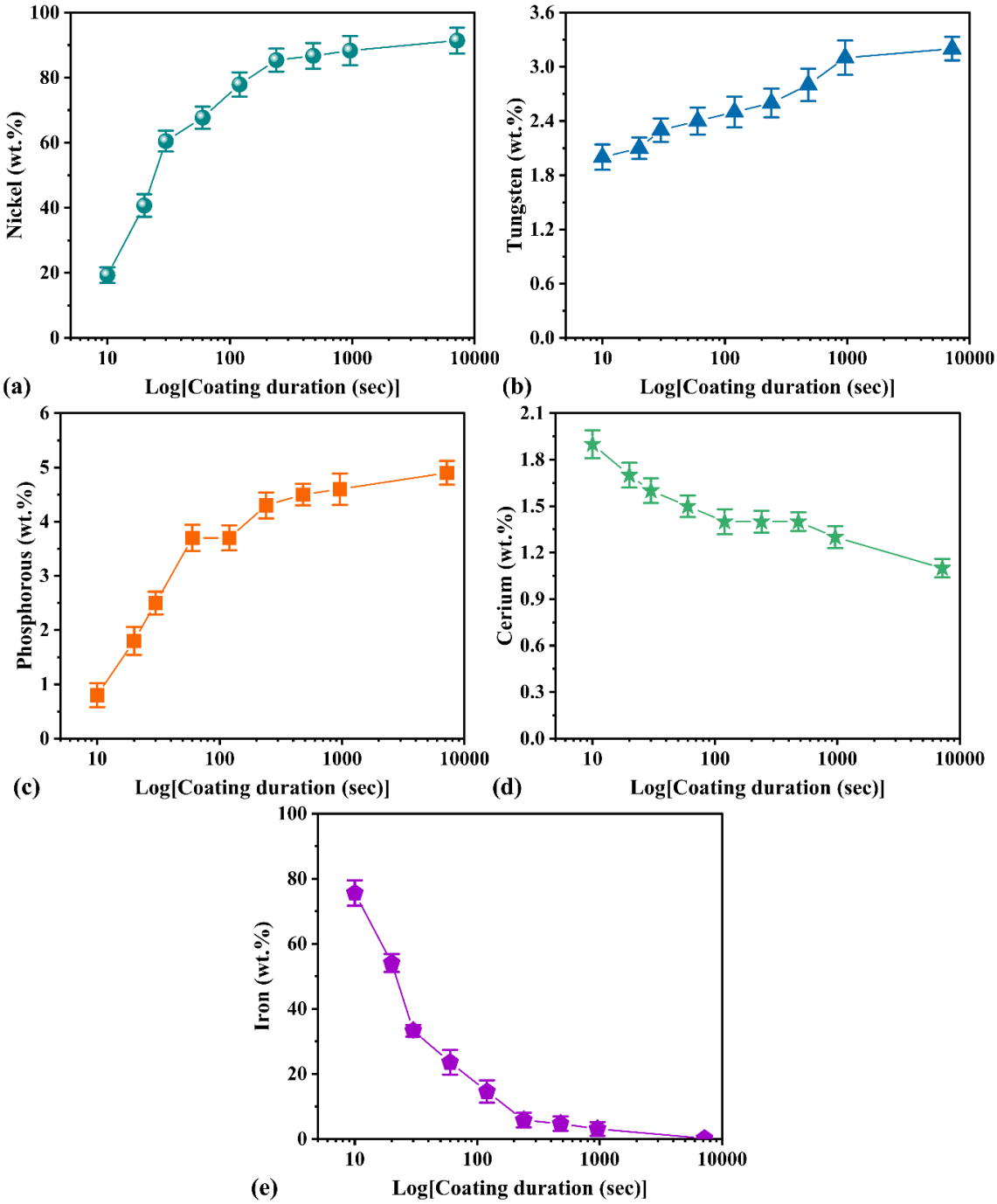

Figure 6.16. Elemental composition (wt.%) of coatings at different durations on 1200 grit polished substrates: (a) Ni, (b) W, (c) P, (d) Ce, (e) Fe.

As the coating process advanced, at 480 seconds, the nickel content stabilized at 86.7 wt.%, with Fe content decreasing further to 4.7 wt.%, indicating the coating had reached near full coverage with minimal substrate exposure. The phosphorus content increased to 4.9 wt.%, promoting a denser and defect-free coating structure, as seen in the SEM images. After 960 s, the Ni content increased to 88.3 wt.%, and Fe content further decreased to 3.1 wt.%, signifying further densification and coating maturity. The slight increase in phosphorus content suggests continued coating refinement. After 2 h (7200 s), the final coating composition was 91.4 wt.% Ni, with Fe content reduced to a negligible 0.2 wt.%, indicating complete substrate coverage. Phosphorus content remained stable at 4.5 wt.%, while tungsten and cerium contents were maintained at 2.5 wt.% and 1.4 wt.%, respectively, contributing to the improved mechanical and corrosion resistance of the coating.

The deposition behavior on the 1200 grit substrate revealed a slower initial coating process compared to the 400 and 800 grit substrates. A smoother surface results in delayed visible nucleation, which ultimately leads to a more uniform and well-distributed coating. The final nickel content was the highest among all the substrates, indicating a superior deposition efficiency over time. Controlled deposition led to a finer and more homogeneous coating structure free from defects and voids, as observed in the SEM images.

The elemental mapping of the electroless Ni-W-P-Ce coating after 10 s of deposition (Figure 6.17) confirms the early stage nucleation process, where Ni is sparsely distributed, while Fe remains dominant, indicating significant substrate exposure.

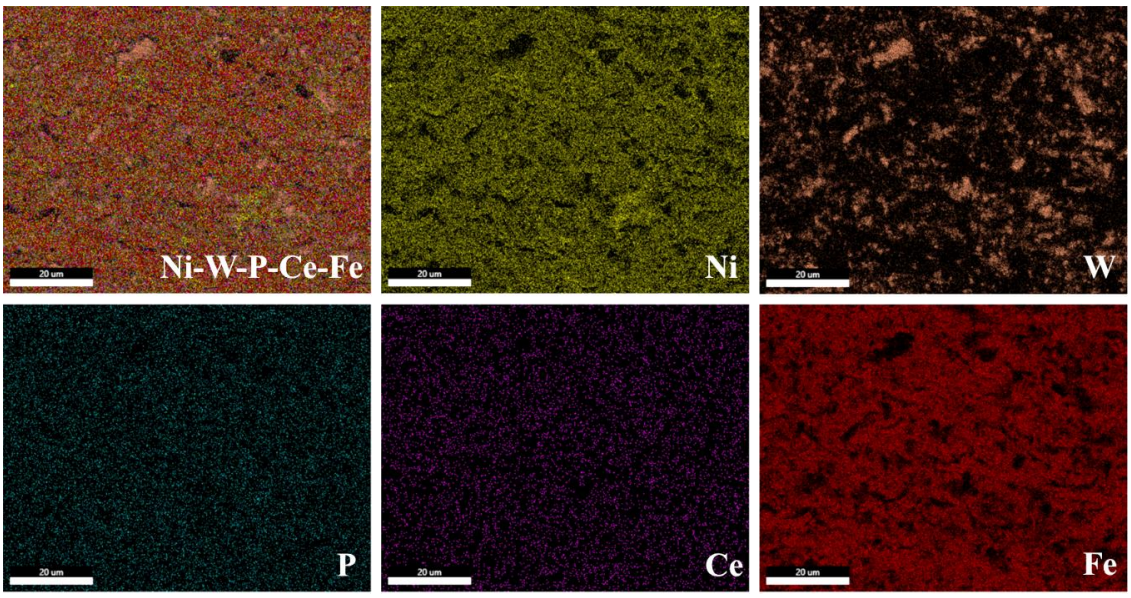

Figure 6.17. Elemental mapping of the electroless Ni-W-P-Ce coating after 10 s of deposition on the 1200 grit polished substrate.

The mappings of W, P, and Ce show their presence at lower concentrations, suggesting gradual incorporation as the deposition progresses. The combined elemental map visually illustrates patchy Ni-rich regions, confirming that the coating was still in its initial formation stage. This aligns with the SEM and EDS findings, supporting the gradual growth mechanism of the Ni-W-P-Ce coatings on the 1200 grit polished substrate toward a uniform and dense structure.

6.2.3.6 Coating characteristics on substrate polished with 1500 grit sandpaper

The evolution of the Ni-W-P-Ce coatings on the substrate polished with 1500 grit sandpaper was analyzed at various deposition durations, and the corresponding SEM images are presented in Figure 6.18. The coating behavior on this highly polished substrate exhibited significant differences compared to the substrates polished with coarser grits (400, 800, and 1200), highlighting the influence of finer surface roughness on coating nucleation and growth. After 10 s of deposition (Figure 6.18(a)), the substrate surface appeared smooth, resembling the surface characteristics observed for 400 and 800 grit substrates. Very few white dots, representing the initial deposition sites, were visible with an average dimension of 0.1 μm, which was the smallest observed among all the tested substrates. The lower density of deposition was further confirmed by EDS analysis, which showed only 7.9 wt.% nickel deposition, indicating that the smoother surface provided fewer nucleation sites for early-stage deposition. The lower deposition of other elements, such as tungsten and phosphorus, also suggests that a finer surface offers less favorable conditions for rapid nucleation.

After 20 s of deposition (Figure 6.18(b)), the number of deposited white dots slightly increased, mainly in the rougher regions of the substrate, with an average nodule size of 0.14 μm. This pattern suggests that coating initiation predominantly occurred at localized surface imperfections, where a higher surface energy facilitated the nucleation. After 30 s (Figure 6.18(c)), uniform-sized nodules with an average dimension of 0.18 μm were observed, covering a larger portion of the substrate surface. This stage marks the onset of a uniform coating spread across the surface, indicating a gradual and controlled nucleation process compared with the faster, more irregular growth observed on rougher substrates. At 60 seconds (Figure 6.18(d)), nodule size increased to 0.35 μm, and the formation of nodule columns was evident, signifying the transition from isolated nucleation sites to interconnected growth.

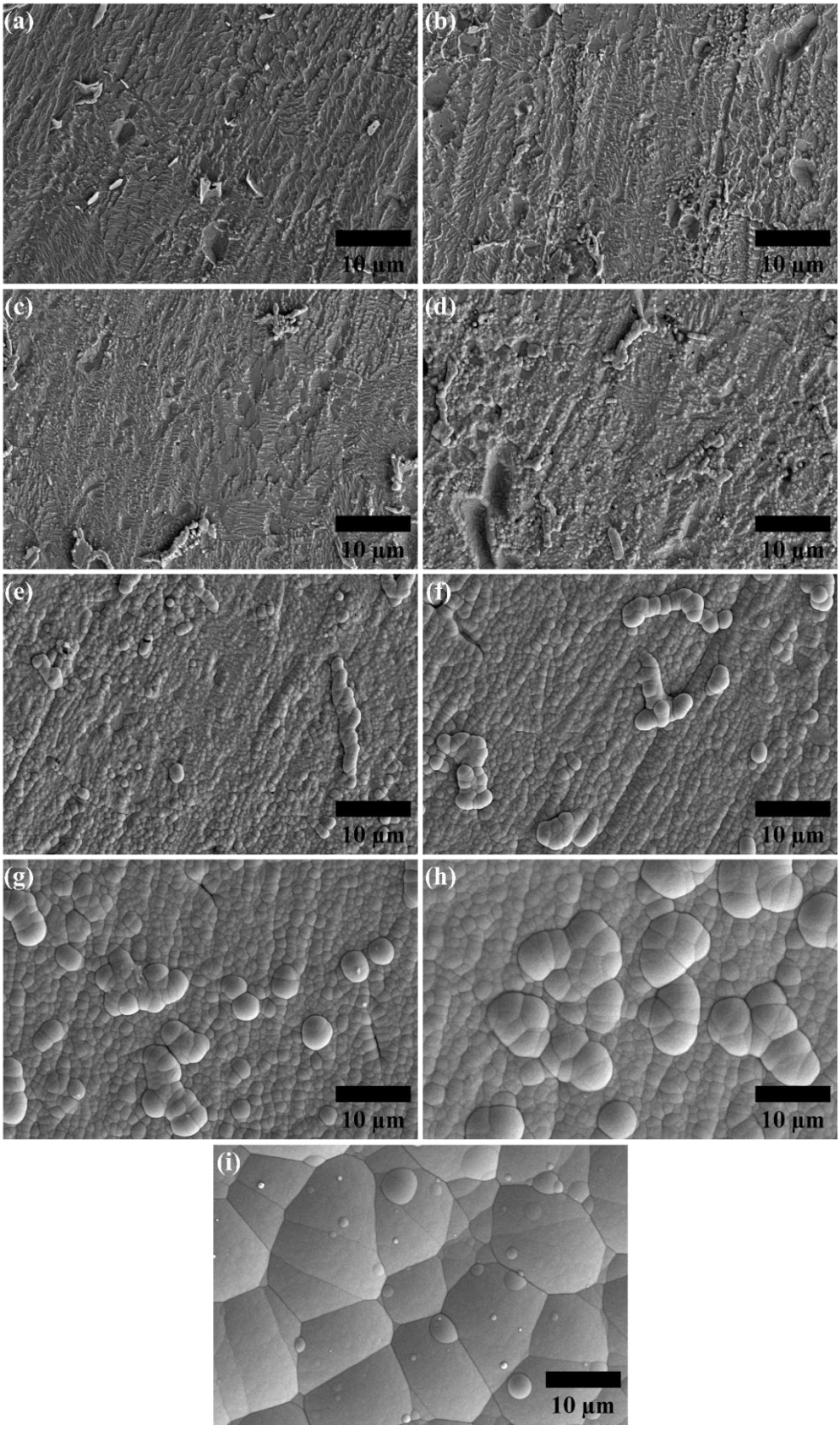

Figure 6.18. SEM images of coatings on 1500 grit polished substrates for different durations: (a) 10s, (b) 20s, (c) 30s, (d) 60s, (e) 120s, (f) 240s, (g) 480s, (h) 960s, and (i) 2h.

The more uniform growth pattern on this finer surface suggests that smoother substrates allow for a steady controlled deposition, resulting in a consistent nodule size. By 120 seconds (Figure 6.18(e)), the average nodule size further increased to 0.63 μm, with a more continuous and dense coverage. Despite the increase in coverage, the deposition pattern remained uniform with fewer large voids compared to coarser substrates, highlighting the benefits of finer substrate preparation for achieving a consistent coating structure. At 240 s (Figure 6.18(f)), the coating exhibited a more compact morphology, with nodules reaching an average size of 1.18 μm, covering the entire substrate surface with minimal voids. This stage signifies the completion of the initial coating layer and beginning of the densification process. With continued deposition, the coating morphology further evolved. At 480 s (Figure 6.18(g)), the nodule size increased to 2.05 μm, with a more refined and compact structure. The uniformity of the coating surface compared with the rougher substrates suggests that the smoother 1500 grit surface promoted a more controlled and even deposition process. By 960 s (Figure 6.18(h)), the nodules had grown to an average size of 3.14 μm, maintained a highly uniform structure. The absence of defects at this stage highlights the influence of the fine surface finish in ensuring defect-free deposition, unlike coarser substrates that exhibit larger voids and uneven growth. After 2 h of deposition (Figure 6.18(i)), the final coating exhibited an average nodule size of 9.35 μm, which is slightly smaller than that of the coatings observed on coarser substrates. The uniform nodule distribution and smooth coating morphology indicate that a finer surface roughness provides ideal conditions for homogeneous growth, minimizing irregularities, and ensuring a high-quality finish.

The coatings deposited on the 1500 grit polished substrate demonstrated the slowest initial nucleation rate among all the substrates, owing to the lower availability of surface imperfections. However, the growth was more uniform and controlled, leading to a coating with smaller, well-distributed nodules. The finer substrate surface limits the number of nucleation sites. However, once initiated, the deposition process results in a highly consistent coating layer. This uniformity contributes to better surface coverage with minimal defects, making the 1500 grit substrate an ideal choice for applications that require smooth and homogeneous coatings.

The elemental compositions of the Ni-W-P-Ce coatings deposited on the 1500 grit polished substrate at different time intervals, as obtained from EDS analysis, are presented in Table 6.8. Figure 6.19 graphically illustrates the variation in Ni, W, P, Ce, and Fe content

with increasing deposition time on substrates polished with 1500 grit sandpaper. In the early stages of the deposition, the Ni content was 7.9 wt.% after 10 seconds, which is significantly lower than that observed for substrates polished with coarser sandpaper. The high Fe content of 89.8 wt.% indicates that the substrate surface was still largely exposed, corroborating SEM observations where only a few deposits were visible. The tungsten (W) and phosphorus (P) contents were minimal at 0.8 wt.% and 0.3 wt.%, respectively, reflecting a slow initiation process due to the finer and smoother surface, which provided fewer nucleation sites. After 20 s, the Ni content increased to 19.9 wt.%, with Fe reducing to 76.6 wt.%, suggesting gradual substrate coverage.

Table 6.8. Elemental contents of coatings at different time durations on substrates polished with 1500 grit sandpaper.

Coating duration (sec)	Elements (wt.%)				
	Ni	W	P	Ce	Fe
10	7.9	0.8	0.3	1.6	89.8
20	19.9	1.6	0.5	1.6	76.6
30	33.4	1.8	0.9	1.5	62.4
60	62.5	2	1.8	1.4	32.6
120	80.8	2.3	2.6	1.4	12.8
240	82.3	2.5	4.1	1.3	8.2
480	84.8	3.4	4.5	1.3	7.1
960	86.6	3.6	4.6	1.2	4.2
7200	89.8	3.7	4.6	1.0	0.2

The increase in tungsten to 1.6 wt.% and phosphorus to 0.5 wt.% indicates progressive alloy incorporation, though the deposition remains slower compared to coarser substrates. After 30 s, the Ni content reached 33.4 wt.%, and Fe content reduced to 62.4 wt.%, confirming that the coating was spreading across the surface more uniformly. An increase in phosphorus content to 0.9 wt.% suggests improved stability and adhesion of the coating. The smoother surface delayed initial deposition. However, once nucleation occurs, the growth process becomes more uniform. At 60 s, a significant increase in the Ni content to 62.5 wt.% was observed, while Fe content dropped to 32.6 wt.%, indicating substantial coating formation. The phosphorus and tungsten content also increased to 1.8 wt.% and 1.8 wt.%, respectively, supporting densification and alloy uniformity. SEM observations at this

stage showed the formation of well-defined nodules covering more of the surface. After 120 s, the Ni content increased further to 80.8 wt.%, with Fe content reducing to 12.8 wt.%, signifying near-complete coverage of the substrate. The increase in phosphorus to 2.6 wt.% and cerium to 1.4 wt.% indicates the continued formation of a dense and well-structured coating. The smoother 1500 grit substrate facilitated the uniform distribution of the coating, albeit at a slower pace than the coarser substrates.

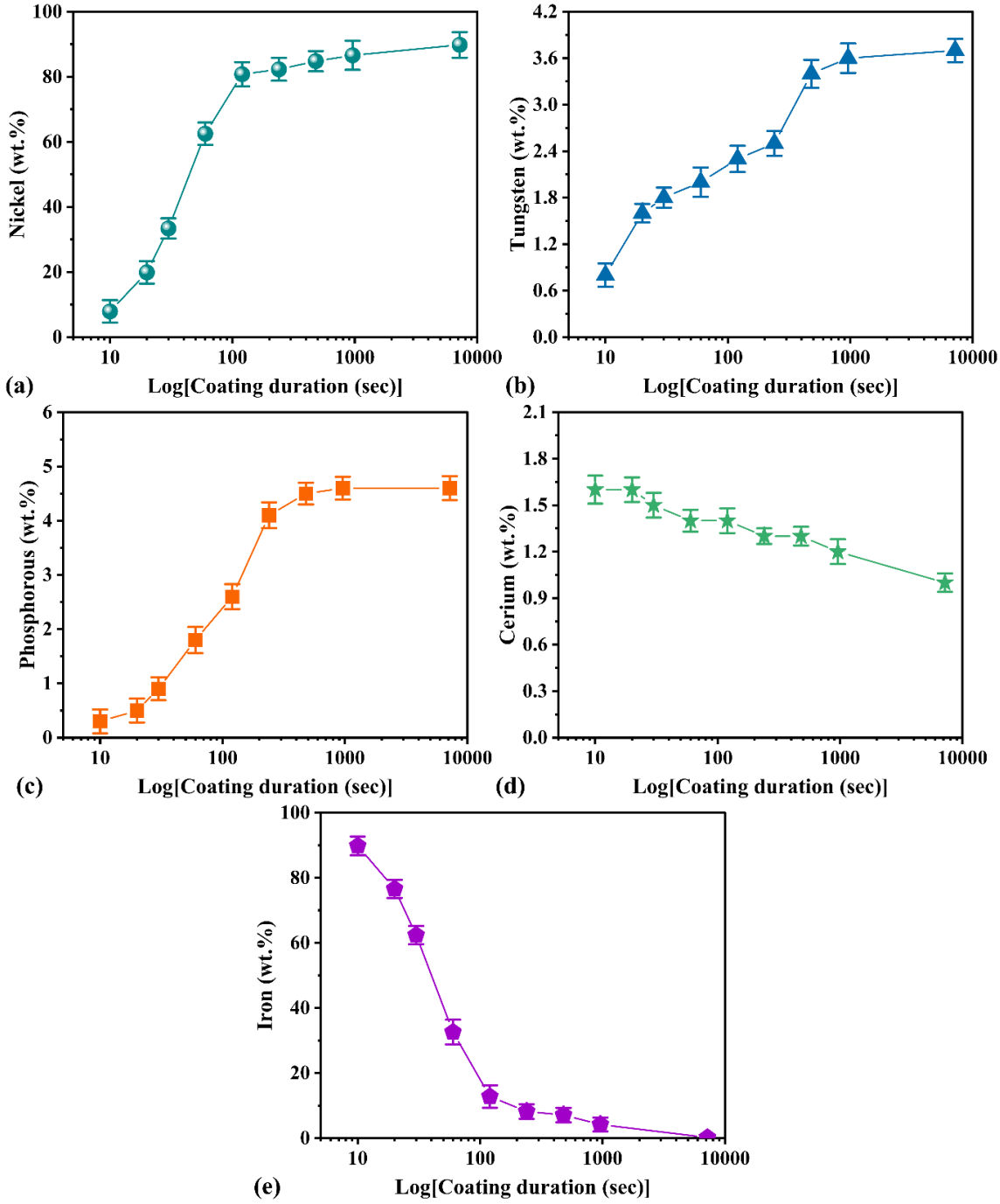

Figure 6.19. Elemental composition (wt.%) of coatings at different durations on 1500 grit polished substrates: (a) Ni, (b) W, (c) P, (d) Ce, (e) Fe.

At 240 s, the Ni content reached 82.3 wt.%, with Fe content reduced to 8.2 wt.%, reflecting an advanced stage of coating densification. The phosphorus content increased to 4.5 wt.%, indicating improved coating integrity and adhesion, consistent with the SEM images showing near-complete coverage with minimal voids. At 480 s, the Ni content stabilized at 84.8 wt.%, with a further reduction in Fe content to 7.1 wt.%, confirming the ongoing densification of the coating. The phosphorus and tungsten content increased steadily to 4.1 wt.% and 2.5 wt.%, respectively, reflecting continued refinement of the coating. After 960 s, the Ni content increased to 86.6 wt.%, with Fe content decreasing further to 4.2 wt.%, indicating almost complete substrate coverage. A steady increase in phosphorus to 4.6 wt.% and tungsten to 3.6 wt.% highlights the uniform incorporation of alloying elements, leading to enhanced coating properties. By the end of 2 hours (7200 seconds), the final coating composition reached 89.8 wt.% nickel, with Fe content reduced to a negligible 0.2 wt.%, confirming complete substrate coverage. The tungsten and phosphorus contents stabilized at 3.7 wt.% and 4.6 wt.%, respectively, indicating the formation of a dense, defect-free, and well-alloyed coating.

6.2.3.7 Adhesion performance of coatings on different substrates

The adhesion performance of the coatings deposited on substrates polished with different grit sandpapers (400, 800, 1200, and 1500 grit, denoted as S400, S800, S1200, and S1500, respectively) was evaluated using scratch testing at two different applied loads of 3 N and 6 N. These findings highlight the significant influence of substrate preparation on coating adhesion, mechanical integrity, and failure modes.

Figure 6.20 presents the variation in the scratch friction coefficient (SFC) over time for coating samples with different surface roughnesses tested under applied loads of 3 N (Figure 6.20(a)) and 6 N (Figure 6.20(b)) along with the corresponding average SFC values (Figure 6.20(c)). For comparison, the figure also shows the SFC trends for the uncoated substrate, which possessed the highest surface roughness and was polished using 400-grade sandpaper.

The coated samples demonstrated relatively stable SFC trends following an initial increase, indicating their capacity to withstand applied loads without significant material loss. The higher SFC values observed during the initial phase of scratching suggest localized plastic deformation because the indenter created considerable resistance owing to the rapid accumulation of plastic strain and the formation of shear bands within the coating.

This localized deformation increases friction because the material strongly resists the indenter, resulting in elevated SFC values. As scratching progressed, the deformation mechanisms transitioned to a more uniform state, allowing the material to accommodate the stress more effectively, leading to reduced frictional resistance and stabilization of the SFC as the indenter moved across the surface [273]. The SFC values obtained under both 3 N and 6 N loads exhibited distinct trends that were influenced by the substrate roughness. At a lower load of 3 N, the coated samples exhibited a significant reduction in SFC compared to the uncoated substrate, reflecting enhanced surface hardness.

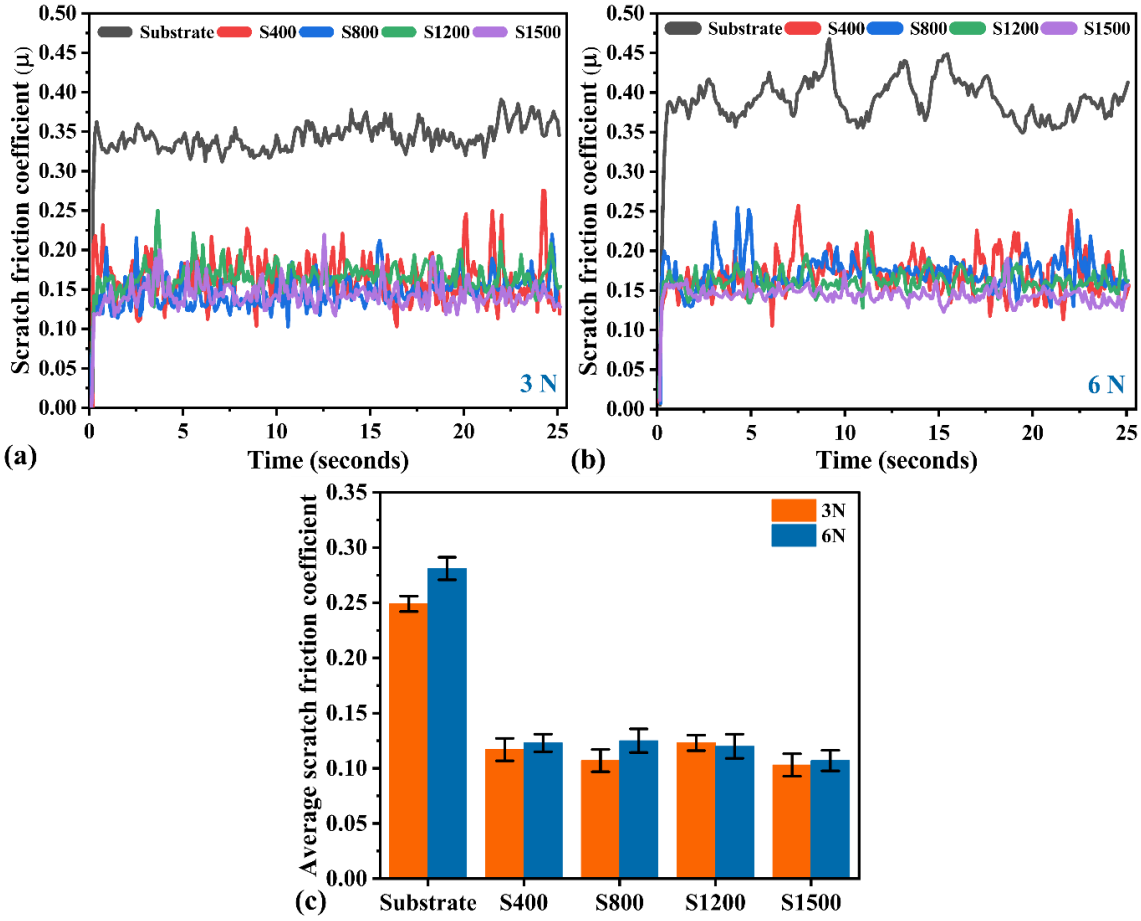

Figure 6.20. SFC variation over time for coatings under (a) 3 N and (b) 6 N loads and (c) the corresponding average SFC values.

S1500 had the lowest SFC value (0.103), indicating superior adhesion and resistance to scratch-induced deformation. In contrast, S1200, which had the highest surface roughness (S_a), showed a relatively higher SFC value of 0.123, likely owing to the increased friction caused by surface irregularities. The higher roughness enhances the actual contact area between the coating and counterpart material, resulting in more interaction points that

contribute to increased friction. Additionally, numerous surface asperities on the rougher coatings engaged more effectively with the indenter, leading to greater mechanical interlocking. This interaction may also induce cohesive cracking as the stress distributions around the asperities become complex, contributing to energy dissipation and ultimately increasing friction during scratching [274]. The average SFC values at 3 N for the uncoated substrate, S400, and S800 are 0.249, 0.117, and 0.107, respectively. At the higher applied load of 6 N, the SFC values followed a similar pattern. S1500 again demonstrated the lowest SFC value of 0.107, whereas S1200 exhibited a slightly lower SFC compared to its performance at 3 N. This reduction in SFC at higher loads can be attributed to increased strain rates, which facilitate the formation of additional shear bands that allow the coating to accommodate plastic deformation more effectively, reducing microfracture and chipping. Additionally, the larger contact area at higher loads enables better stress distribution, leading to a decrease in friction per unit area and contributing to an overall reduction in the SFC. These factors collectively resulted in lower friction coefficients at higher loads [275]. The average SFC values at 6 N for the uncoated substrate and the S400, S800, and S1200 were 0.281, 0.123, 0.125, and 0.120, respectively.

The scratch hardness and fracture toughness values (Figure 6.21) were determined from scratch tests conducted under a 6 N load, further emphasizing the influence of substrate roughness on the coating strength. S1500 exhibited the highest scratch hardness (8.84 GPa), indicating its superior ability to resist plastic deformation under the applied stress.

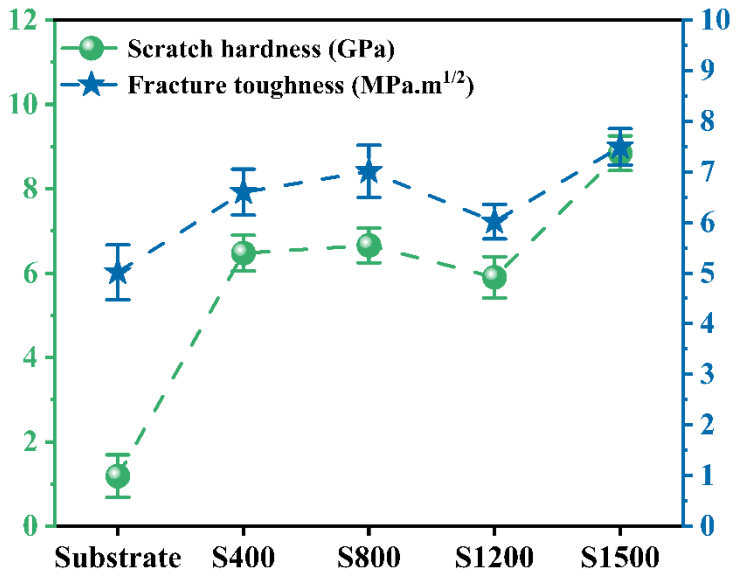

Figure 6.21. Scratch hardness and fracture toughness tested under a 6 N load.

The relatively smaller average nodule size of 9.35 μm, the lowest among all samples, suggests a more compact microstructure, which enhances the resistance to plowing by the indenter, directly contributing to the higher scratch hardness [276]. Similarly, S1500 exhibited the highest fracture toughness of 7.49 $MPa.m^{1/2}$, demonstrating its excellent resistance to crack propagation. The combination of low scratch friction coefficient and high fracture toughness in S1500 can be attributed to its smoother surface. Lower surface roughness reduces the impact of surface asperities during contact, leading to decreased friction and wear. This smoother interaction minimizes energy dissipation during loading, which translates into improved toughness because the coating can better absorb mechanical stress and resist crack propagation. Additionally, achieving a lower surface roughness often coincides with an optimized microstructure, where finer grain structures enhance the capacity of the coating to endure mechanical stress, further improving fracture toughness. These factors collectively contribute to the durability, resilience, and favorable frictional behavior of the coating [277]. On the other hand, S1200 exhibited lower values for both scratch hardness (5.90 GPa) and fracture toughness (6.02 $MPa.m^{1/2}$), which can be attributed to its relatively rougher surface. The increased surface roughness introduces stress concentration points, which facilitate crack initiation and propagation under the applied loads [278]. A higher substrate roughness often results in coating defects, such as increased porosity and non-uniform particle distribution, which compromise mechanical strength and adhesion. S400 and S800 exhibited intermediate scratch hardness and fracture toughness values, suggesting a balanced combination of mechanical strength and adhesion properties.

The scratch track analysis, based on the SEM images presented in Figure 6.22, revealed notable differences in the damage mechanisms among the samples. The uncoated substrate exhibited pronounced chevron-shaped tensile cracks, indicating brittle failure under the scratch-induced stress. In contrast, the coated samples displayed minimal tensile cracking, suggesting that the coatings effectively distributed the applied loads and enhanced crack resistance. In addition, substantial material removal was observed around the crack zones in the uncoated substrate, indicating adhesive failure, whereas the coated samples exhibited superior adhesion. At higher applied loads, tensile cracks and minor material detachment were observed in S800 and S1200, as shown in Figures 6.22(f) and 6.22(h), respectively. This indicated the presence of compressive residual stress within the coatings.

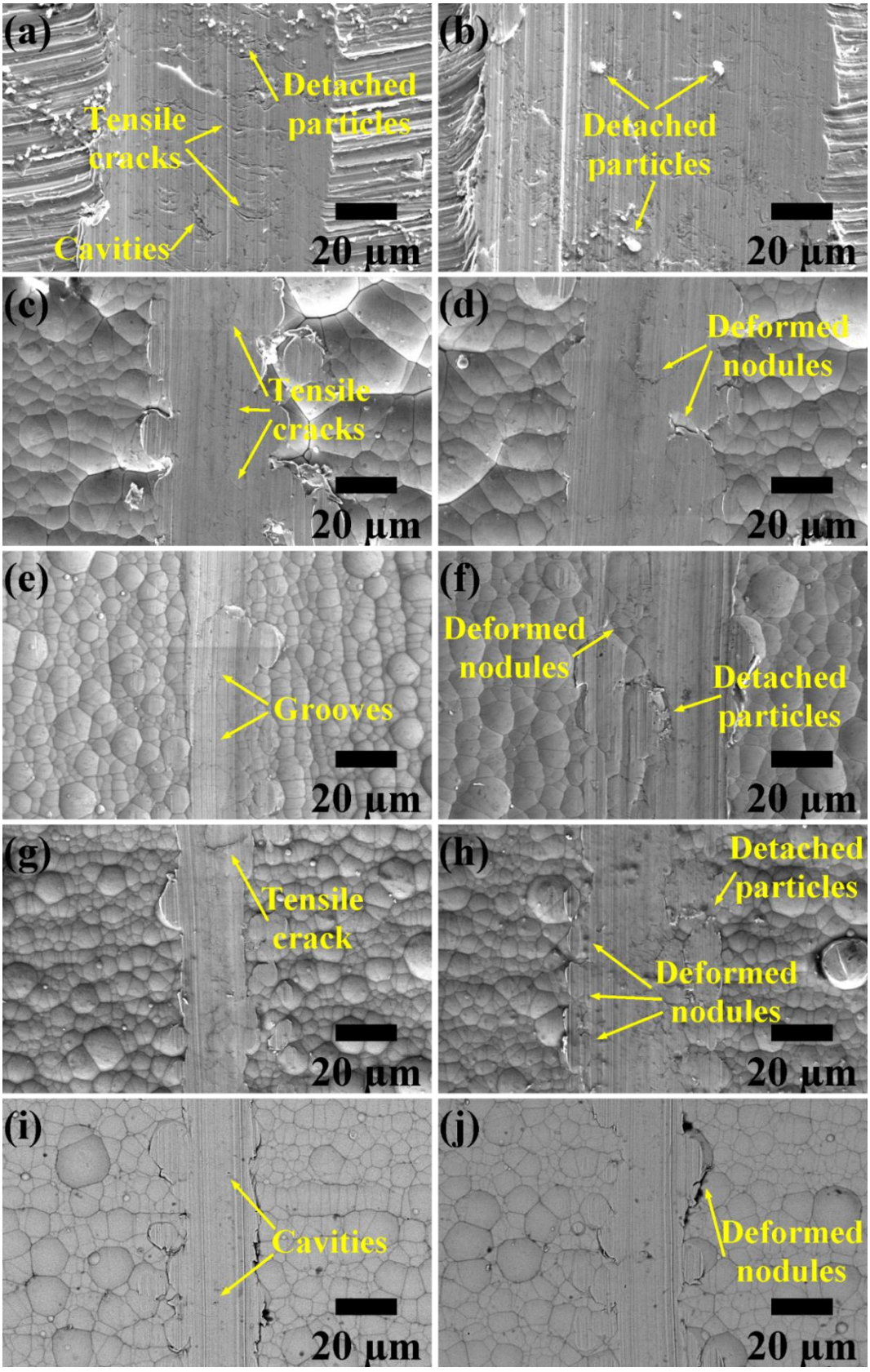

Figure 6.22. Surface morphology of scratch tracks under two distinct loads: (a) substrate, 3 N; (b) substrate, 6 N; (c) S400, 3 N; (d) S400, 6 N; (e) S800, 3 N; (f) S800, 6 N; (g) S1200, 3 N; (h) S1200, 6 N; (i) S1500, 3 N; and (j) S1500, 6 N.

It is important to note that crack formation is predominantly associated with tensile residual stresses [279]. Unlike the lower-load tests, the higher-load scratch tests resulted in particle detachment or spallation. A decrease in the surface roughness of the electroless coatings led to a reduction in the crack formation and particle detachment. Notably, in S1500, which exhibited the lowest roughness (S_a), no cracks or debris were observed. Instead, microscopic cavities and deformed spherical nodules are observed. The formation of these cavities is attributed to multiaxial stresses arising from tensile forces acting both parallel and perpendicular to the scratch direction [280]. The absence of cracks in S1500 indicates a stronger adhesion, which can be attributed to the increased attractive forces between the coating layers. S400 and S800 exhibited moderate damage, characterized by plowing effects, but without significant coating delamination, indicating a moderate adhesion strength. Across all coated samples, the scratch tracks showed pronounced plowing, resulting in the formation of scratch grooves. However, within these grooves, plastic deformation occurred without complete dislodgement of the coating material, further confirming the strong adhesion between the coating and substrate in all samples.

The scratch groove profiles obtained through non-contact optical profilometry, as shown in Figure 6.23, demonstrate the impact of the surface roughness on material removal. The corresponding scratch volume calculations, presented in Figure 6.24, further validated these findings. As expected, an increase in the applied load resulted in wider and deeper scratched grooves. S1200 exhibited the highest scratch volume loss, with values of 71.75 $\times 10^{-6}$ mm^3 at 3 N and 96.58 $\times 10^{-6}$ mm^3 at 6 N. The higher roughness of S1200 contributed to this increased material loss because surface irregularities created stress concentration points at the peaks and valleys, leading to localized stress intensification under mechanical loading. These localized stresses promote crack initiation and propagation, and accelerate material removal. Furthermore, the increased surface area owing to roughness amplifies frictional forces during scratching, generating more heat and wear, ultimately resulting in greater material loss [281].

In contrast, S1500, which exhibited the lowest surface roughness, recorded the smallest scratch volume loss, measuring 28.1 $\times 10^{-6}$ mm^3 at 3 N and 70.55 $\times 10^{-6}$ mm^3 at 6 N, highlighting its superior scratch resistance. The smoother coating surface minimized the stress concentration effects and reduced the frictional forces, leading to a lower material removal. Similarly, S800 followed a comparable pattern, with a lower material loss than S400 and S1200.

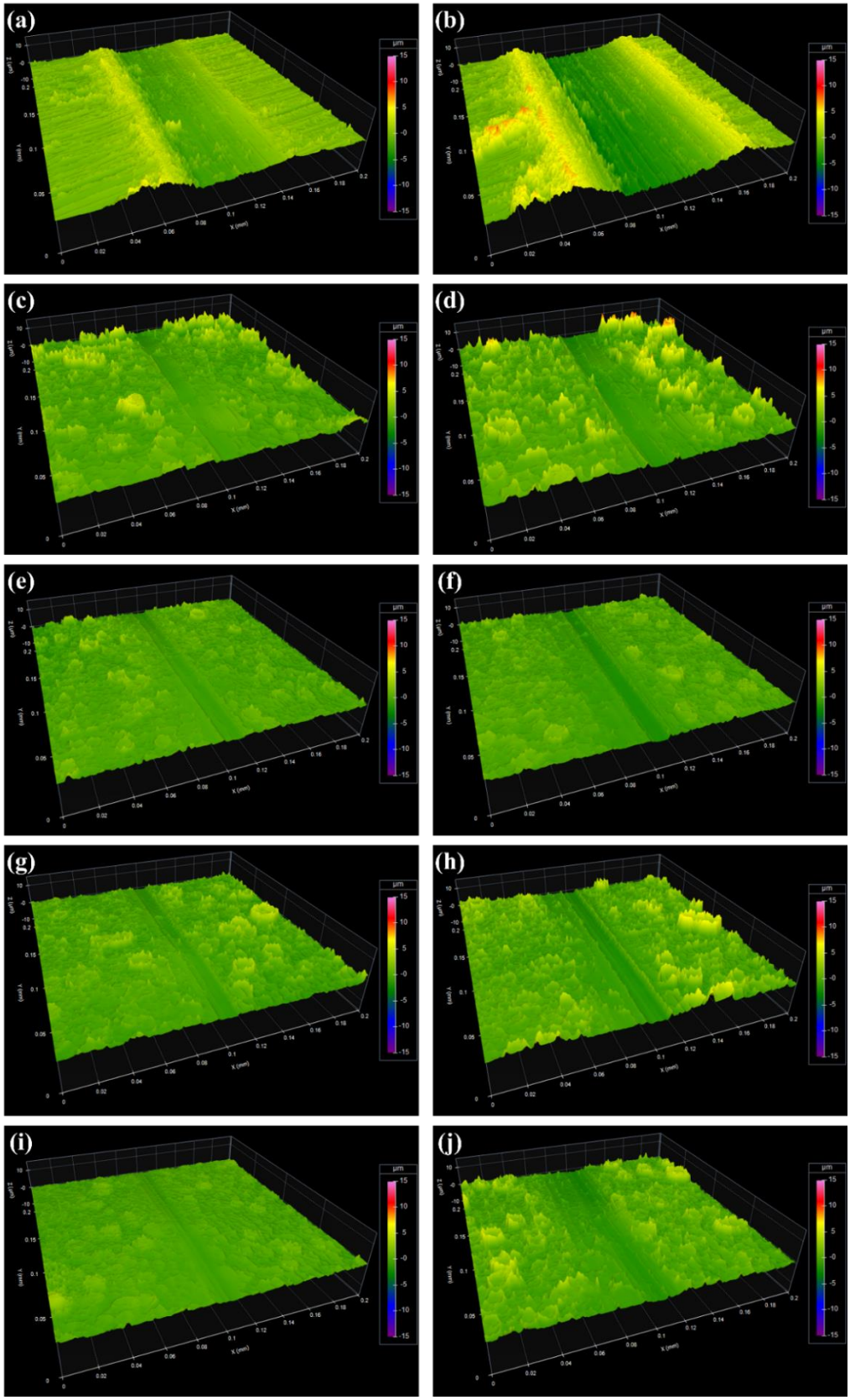

Figure 6.23. Surface topography of scratch tracks under two distinct loads: (a) substrate: 3 N; (b) substrate: 6 N; (c) S400: 3 N; (d) S400: 6 N; (e) S800: 3 N; (f) S800: 6 N; (g) S1200: 3 N; (h) S1200: 6 N; (i) S1500: 3 N; and (j) S1500: 6 N.

EDS analysis of the scratched regions, as presented in Table 6.9, revealed that the elemental composition remained largely unchanged compared to the unscratched areas. This consistency in the elemental distribution after the scratch test indicated the strong adhesion and resilience of the electroless coating.

Table 6.9. Elemental compositions (wt.%) of the scratched area under a 6 N load.

Sample	Nickel, Ni	Tungsten, W	Phosphorous, P	Cerium, Ce
S400	92.1	2.6	4.1	1.2
S800	90.7	3.1	4.4	1.8
S1200	90.5	3.6	4.8	1.1
S1500	91.6	3.1	3.8	1.4

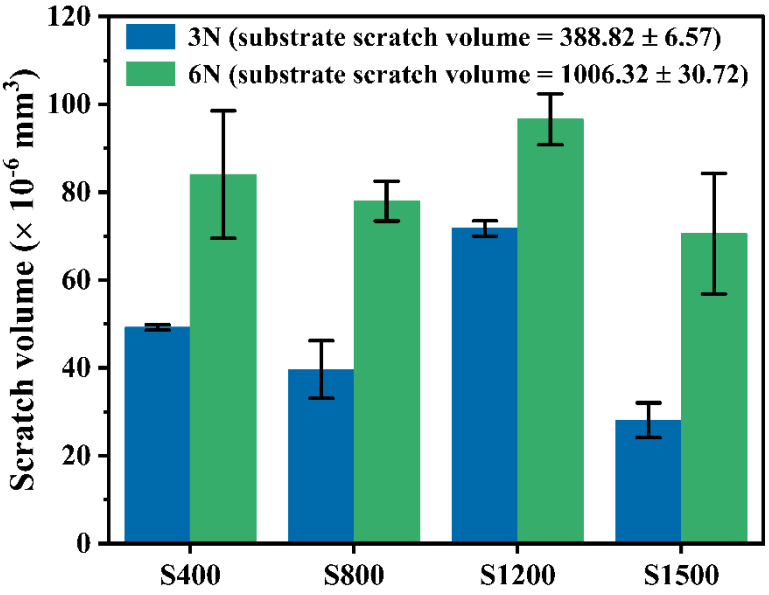

Figure 6.24. Comparison of the scratch volumes under two distinct loads.

The stable elemental composition suggests that the coating effectively withstands the mechanical stress without significant material loss. Furthermore, the surface texture of the substrate, which was enhanced by polishing with different grit sandpapers, likely contributed to the mechanical integrity of the coating, ensuring minimal disruption of the elemental distribution, even after exposure to mechanical forces. S1500 retained a Ni content of 91.6 wt.%, highlighting its superior adhesion properties, while S1200 exhibited slightly lower nickel retention, suggesting greater material loss due to mechanical stress. Given that these results were obtained for regions subjected to a higher load of 6 N, it is

reasonable to anticipate that the elemental composition of the regions tested under a lower load of 3 N would exhibit a similar trend.

The results clearly demonstrate a strong correlation between adhesion performance and substrate roughness. Coatings applied to smoother substrates, such as the 1500 grit polished surface, exhibit superior adhesion strength owing to the formation of a uniform and dense coating layer with minimal defects. In contrast, coatings on rougher substrates, like the 400 grit polished surface, experienced higher material loss and crack propagation, indicating weaker adhesion and increased brittleness. Although the 1200 grit polished substrate had a relatively lower surface roughness, the coating formed on it exhibited greater roughness than the other coated surfaces, leading to weaker adhesion. These findings highlight the necessity of optimizing substrate surface roughness to achieve coatings with superior adhesion and mechanical durability. Finer-polished substrates provide an ideal balance between the adhesion strength and surface integrity, making them more suitable for applications that require high-performance coatings with enhanced wear resistance and longevity.

6.2.4 Characterization of electroless Ni-W-P-Ce coatings

S1500, which exhibited the lowest surface roughness, lowest scratch friction coefficient, and highest scratch hardness and fracture toughness, was further analyzed through microstructural characterization.

The XRD pattern of the coating (Figure 6.25(a)) reveals a single peak corresponding to the face-centered cubic (FCC) structure of nickel in the (111) plane, located at 44.74°. Notably, no distinct diffraction peaks were observed for the other elements within the coating. The absence of visible peaks suggests that the presence of tungsten and phosphorus contributes to an amorphous structure, which lacks the long-range atomic order required to produce detectable peaks in XRD analysis. Additionally, the relatively low concentrations of tungsten and phosphorus compared to nickel may result in overshadowed signals. Moreover, the preferred orientation of the nickel crystals during the deposition process can enhance the intensity of the nickel peaks, further masking the presence of alloying elements and indicating that they may not form distinct crystalline phases within the coating [282]. The microstructural analysis of S1500 revealed a calculated crystallite size of 6.4 nm, with a full width at half maximum (FWHM) value of 1.34165° and a d-spacing of 2.03 Å. The crystallite size, which refers to the dimensions of coherent scattering domains within the

material, suggests that the coating falls into the ultrafine or nanocrystalline regime, as crystallites smaller than 10 nm are typically classified in this category [89]. Given a phosphorus content of less than 5 wt.%, the coating is categorized as a low-phosphorus type [283].

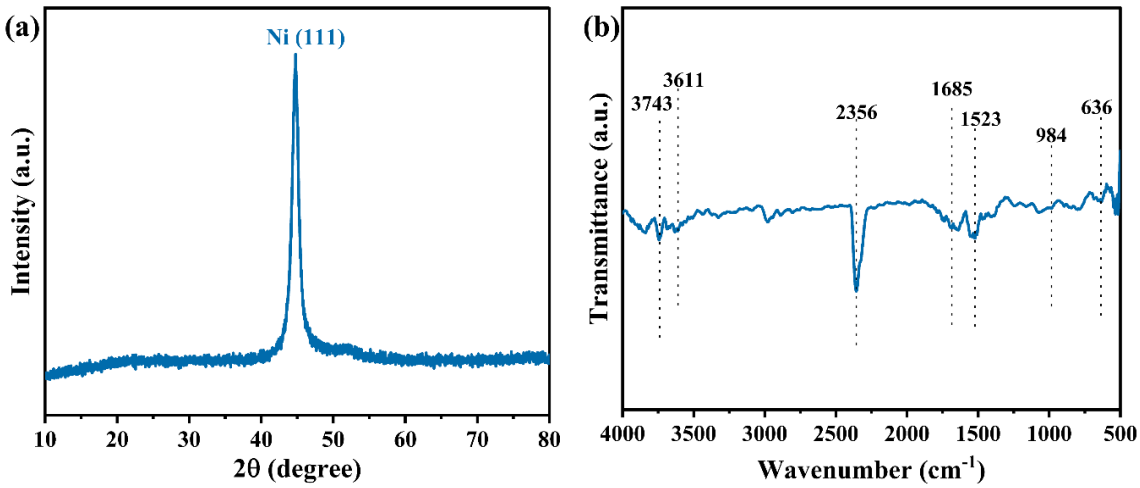

Figure 6.25. (a) XRD pattern and (b) FTIR spectra of Ni-W-P-Ce coating for S1500.

The relatively low phosphorus concentration alone was insufficient to significantly distort the nickel lattice structure, resulting in the observed nanocrystalline structure. However, the influence of tungsten and cerium on the microstructure is also significant. It is well established that tungsten, in conjunction with phosphorus, affects the microstructural characteristics of electroless Ni-W-P coatings, with up to 2 wt.% tungsten being incorporated into the nickel lattice to influence grain refinement [201]. Additionally, the incorporation of cerium, which has a considerably larger atomic radius (0.1824 nm) than Ni, W, and phosphorus (0.1246, 0.139, and 0.106 nm, respectively), can lead to lattice expansion. This expansion disrupts long-range atomic order, contributing to the amorphous nature of the coating [102].

The FTIR spectra of the electroless Ni-W-P-Ce coating of S1500, presented in Figure 6.25(b), provide valuable insights into the structural and bonding characteristics of Ce within the coating. Although present in minimal quantities, Ce plays a significant role in influencing the microstructure and properties of coatings. Spectral analysis revealed distinct peaks corresponding to cerium-oxygen interactions. The peak observed at 636 cm^{-1} is attributed to the presence of Ce-O bonds, confirming the incorporation of cerium oxide within the coating. Additionally, the peak located at 984 cm^{-1} corresponds to the Ce-O-Ce bond, further verifying the formation of cerium-based compounds in the coating matrix.

The presence of oxide-forming elements in electroless coatings has been found to greatly enhance fracture toughness and wear resistance [284]. Hydroxyl-related vibrations were identified in the spectrum, with prominent peaks at 1523 cm^{-1} and 1685 cm^{-1}, which correspond to the O-H stretching vibrations associated with adsorbed moisture. The broad absorption band between 2000 and 500 cm^{-1} further confirms the presence of hydroxyl stretching vibrations. The detection of a peak at 2356 cm^{-1} indicates CO_2 adsorption from the surrounding environment, suggesting surface interactions with atmospheric carbon dioxide. Moreover, the FTIR spectra revealed the presence of surface hydroxyl groups associated with cerium hydroxide (Ce-OH), as indicated by the peaks at 3611 cm^{-1} and a strong peak at 3743 cm^{-1}, which are characteristic of Ce-OH stretching vibrations. These findings, supported by previous studies [285–287], suggest that the coating microstructure is primarily characterized by two key functional groups: cerium-oxygen bonds and hydroxyl groups, which contribute to the unique chemical and physical properties of the coating.

The electrochemical characteristics of the electroless coating surface were affected by the presence of the four different elements. The reactivities of the substrate and coating (S1500) were evaluated using OCV, and the results are shown in Figure 6.26(a). The surface potential increased after coating. Both the substrate and coating displayed a decrease in potential, which shifted from -440 mV to -560 mV and -330 mV to -380 mV, respectively. The substrate potential initially decreased and stabilized in the final stage, whereas the coating potential continuously decreased steadily. The observed potential difference allows the determination of reaction rates, where more negative potentials suggest easier oxidation reactions [288]. Consequently, the substrate was expected to have a higher corrosion rate than that of the coating.

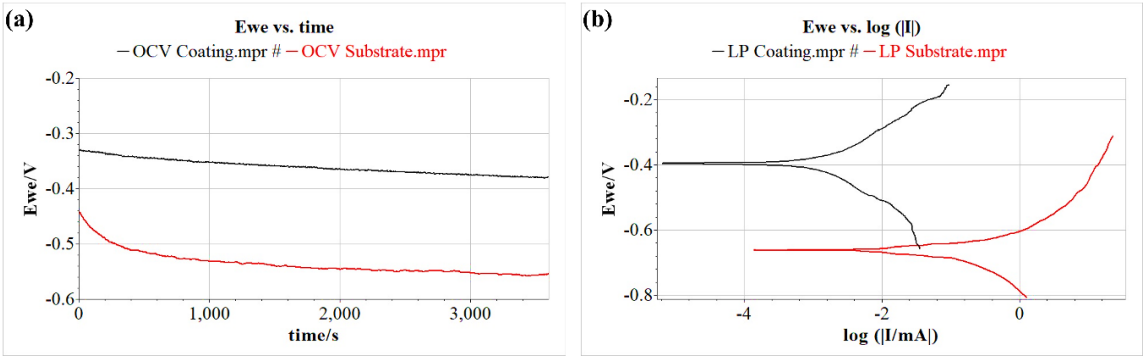

Figure 6.26. (a) OCV variation over 3600 s and (b) polarization plots for the substrate and coating (S1500).

The minimal variation in the open-circuit potential of S1500 suggested the presence of a uniform coating layer. To assess the corrosion behavior, a linear potentiodynamic polarization (LP) test was conducted, and the resulting Tafel plot is shown in Figure 6.26(b). The corrosion potential (E_{corr}), corrosion current density (I_{corr}), and Tafel slope (β_a, β_c) were determined using the Tafel slope extrapolation method [289], and are presented in Table 6.10.

Table 6.10. Tafel fitting results for the substrate and coating (S1500).

	E_{corr} (mV)	I_{corr} ($\mu A/cm^2$)	β_a (V/decade)	β_c (V/decade)
Substrate	-661.361	204.030	95.0	183.2
S1500	-394.862	1.622	134.5	143.1

The potentiodynamic polarization curves depicted in Figure 6.26(b) illustrate the corrosion behavior of both the electroless Ni-W-P-Ce coated sample (black curve) and the uncoated low-carbon steel substrate (red curve). The coated sample demonstrated a more positive corrosion potential (E_{corr}), whereas the uncoated substrate exhibited a more negative E_{corr}, indicating that the coating substantially improved the electrochemical stability of steel. The shift towards a nobler E_{corr} value for the coated sample suggests enhanced resistance to corrosion initiation and greater chemical inertness, making it less prone to anodic dissolution compared to the bare substrate. Furthermore, the coated sample exhibited a lower corrosion current density (I_{corr}) than the uncoated substrate did. The reduced current density in the coated sample indicates a lower current flow in the circuit, implying higher resistance and superior corrosion protection. Conversely, the uncoated substrate exhibited a significantly higher current density, indicating accelerated corrosion owing to the direct exposure of steel to the electrolyte. The polarization curves also reveal distinct anodic and cathodic slopes for both samples. The coated sample displayed a lower anodic slope, suggesting a slower dissolution rate of the coating material, whereas the uncoated substrate exhibited a steeper slope, indicating a more aggressive corrosion process and higher material degradation. In addition, the coated sample presented a broader passive region than the uncoated substrate, indicating the formation of a stable and protective oxide or hydroxide layer on the coating surface. This passive film acts as a barrier, effectively preventing further metal dissolution and safeguarding the underlying steel. In contrast, the uncoated substrate lacks a well-defined passive region, leading to continuous active corrosion across a wider potential range. The remarkably high corrosion protection

efficiency of 99.2% achieved by the electroless Ni-W-P-Ce coating confirms its excellent protective capability in aggressive environments. This superior performance can be attributed to the unique, compact, and defect-free microstructure of electroless coatings. Overall, potentiodynamic polarization analysis confirmed that the electroless Ni-W-P-Ce coating significantly enhanced the corrosion resistance of low-carbon steel, making it a viable option for applications under harsh environmental conditions.

6.3 Closure

This chapter explores the influence of key process variables on the initiation, growth, and properties of electroless Ni-W-P-Ce coatings applied to low-carbon steel substrates. The choice of activator solution significantly affected the coating adhesion. Hydrochloric acid (HCl) activation proved superior to palladium chloride ($PdCl_2$) activation, likely owing to the micro-roughening effect of HCl etching, which enhanced the mechanical interlocking between the coating and the substrate. Bath loading was another critical parameter, with an optimal value of 0.88 $dm^2.L^{-1}$ identified to balance the deposition rate and bath stability. Exceeding this value leads to the rapid depletion of reactants and accumulation of byproducts, adversely affecting the coating quality. Substrate roughness plays a vital role in the coating performance. The substrates polished to a finer grit (1500 grit) exhibited more uniform nucleation and growth, resulting in denser, more homogeneous coatings with better adhesion and mechanical properties. In contrast, coarser substrates showed faster initial deposition, but irregular growth. The coating process progressed through distinct stages of nucleation, growth, and densification. Finer substrates delayed visible nucleation but facilitated more controlled growth, yielding smoother coatings. Mechanical testing indicated that coatings applied to smoother substrates demonstrated superior scratch hardness, fracture toughness, and lower friction coefficients. Among the substrates, the 1500-grit polished surface produced coatings with the best overall mechanical performance. Microstructural analyses using XRD and FTIR revealed a nanocrystalline structure with amorphous characteristics, which were influenced by the incorporation of W, P, and Ce. The presence of Ce-O bonds and hydroxyl groups contributes to the enhanced coating properties. The optimized coatings also exhibited exceptional corrosion resistance, achieving 99.2% protection efficiency compared to the bare substrate.

Chapter 7 Conclusions, major contributions and future scope of work

7.1 Conclusions

This research comprehensively explored the development, characterization, and optimization of electroless Ni-W-P-Ce coatings on low-carbon steel (AISI 1010), offering insights into both the fundamental understanding and practical application of this surface engineering technique.

The initial part of the study showed that a neutral bath with a pH of 7 to 7.5, stabilized by thiourea, can deliver superior deposition rates and more uniform, high-performance coatings compared to both acidic and basic baths. SEM analyses showed that the neutral baths produced compact, nodular microstructures, whereas EDS confirmed a uniform elemental distribution. Microhardness measurements revealed values over four times greater than those of the substrate, primarily owing to the synergistic incorporation of tungsten, phosphorus, and cerium. XRD analysis identified the phases of nickel, cerium oxide, and cerium hydroxide with higher crystallinity in the neutral bath samples.

For the optimization of the Ni-W-P-Ce coating process parameters, the hybrid ANN-Red Fox algorithm yielded the most suitable results, as evident from the minimal deviation between the predicted and experimentally observed values of surface roughness, microhardness, fouling weight, surface energy, and corrosion resistance. Both RSM and sensitivity analyses identified the concentrations of nickel sulfate and sodium tungstate as the most critical factors influencing coating properties. The optimal coating achieved a surface roughness of 0.12 μm, a microhardness of 726 HV, a 64% reduction in fouling weight compared to the uncoated substrate, a surface free energy of 15.97 J/m^2, and a corrosion protection efficiency of 98.73%.

By exploring a range from 0 to 14 mg/L Ce, the study identified an optimal Ce concentration (8 mg/L) that yielded the highest deposition rate with smaller grains and significantly improved functional properties, such as scratch hardness, wear resistance, corrosion protection efficiency, and biofilm inhibition ability. However, the improvement in properties was not monotonic with increasing Ce; beyond 8 mg/L, a further increase in Ce concentration led to deterioration or plateauing of the benefits. Annealing the coating by heating it to a high temperature, followed by furnace cooling, helped augment the

coating properties to a greater extent. The coatings exhibited a silver-gray appearance, with color changes observed after annealing at different temperatures, indicating changes in the oxide films.

The final section of the study investigated the influence of key process variables, including activator type, bath loading, and substrate surface roughness. HCl activation was more effective than $PdCl_2$ activation in improving adhesion through micro-roughening. An optimal bath loading of 0.88 $dm^2 \cdot L^{-1}$ balanced the deposition efficiency and bath stability. Substrate surface preparation significantly influenced the coating morphology and performance. Finer grit polishing (1500 grit) led to more controlled nucleation, uniform growth, and superior mechanical properties, including higher scratch hardness, fracture toughness, and reduced friction. The coatings underwent distinct stages of nucleation, growth, and densification, resulting in dense nanocrystalline structures with amorphous features. XRD and FTIR confirmed the presence of Ce-O bonds and hydroxyl groups, contributing to the enhanced corrosion resistance, with protection efficiencies of up to 99.2%.

7.2 Major contributions

- Development of stable coating baths: The formulation and evaluation of four distinct Ni-W-P-Ce electroless coating baths identified a neutral pH bath stabilized with thiourea as the most effective for high-performance coatings.
- Optimization via hybrid ANN-metaheuristic techniques: A novel integration of ANN models with metaheuristic algorithms (RFO, TLBO, and WOA), enabling precise multi-objective optimization of coating parameters, with RFO showing the best results.
- Functional role of cerium: Demonstrated the beneficial effects of cerium addition on mechanical, corrosion, and antifouling properties while determining an optimal concentration threshold (8 mg/L $CeSO_4$).
- Influence of substrate preparation: The effects of the surface roughness, activation processes, and bath loading on the coating deposition, growth, and resulting properties were evaluated.
- Influence of post-treatment: Following coating, the samples underwent high-temperature heat treatment, followed by furnace cooling, after which various properties were evaluated.

- Comprehensive microstructural and mechanical characterization: SEM, EDS, XRD, XPS, FTIR, electrochemical, antibacterial, and mechanical testing to validate the coating performance and elucidate the structure-property relationships.

These findings provide a foundation for advancing electroless Ni-W-P-Ce coatings in multifunctional applications, particularly where corrosion, wear resistance, and biofouling are critical. The multifaceted optimization strategy and insights into material behavior open new avenues for future research and practical deployment.

7.3 Future scope of work

Building on the promising outcomes of the present study, several future research directions can be pursued to further advance the understanding and applicability of electroless Ni-W-P-Ce coatings. These coatings have demonstrated excellent functional properties in controlled environments. However, a more comprehensive evaluation is essential for establishing their performance and reliability under realistic service conditions.

First, the wear behavior of Ni-W-P-Ce coatings should be studied under various environmental conditions that mimic real-world applications. For instance, their resistance to fretting wear, which results from small-amplitude oscillatory motion between the contacting surfaces, has not yet been explored. Fretting wear is particularly relevant in applications that involve vibrations or repeated mechanical contact, such as aerospace joints, bolted assemblies, and automotive components. Understanding the ability of coatings to resist localized damage will expand their usability in high-performance mechanical systems.

The galvanic corrosion behavior of Ni-W-P-Ce coatings requires thorough investigation, particularly when paired with dissimilar metals in harsh environments, such as marine or industrial settings, where galvanic interactions can accelerate degradation. In addition, studying their tribo-corrosion performance, where wear and corrosion occur simultaneously, is vital for components such as valves, pumps, and rotating machinery.

Furthermore, the incorporation of advanced functional nanoparticles, such as carbon quantum dots, graphene, or metal-organic frameworks (MOFs), can be explored to introduce novel functionalities into the coating. These additives may offer properties such as self-healing ability, enhanced barrier protection, photocatalytic activity, or even antimicrobial resistance, thereby expanding the application spectrum of Ni-W-P-Ce

coatings into areas such as biomedical devices, food processing equipment, and marine coatings.

The substrate versatility of Ni-W-P-Ce coatings is another domain warranting further exploration. Although this study focused on low-carbon steel substrates, extending the coating process to a broader range of materials, including polymers such as ABS, engineering plastics, and lightweight metals such as aluminum, will help validate the adaptability of the coating system across various industrial domains.

Finally, the long-term performance evaluation of Ni-W-P-Ce coatings under industrial operating conditions is essential. While the current study focused on relatively short-term measurements of corrosion and wear, extended duration testing, including aging studies, accelerated corrosion tests, and real-time field exposure, will be crucial for assessing the practical viability of the coating. Investigating the coating behavior of functional components under actual load conditions will bridge the gap between laboratory-scale research and industrial implementation.

REFERENCES

[1] H.C. Barshilia, Surface Modification Technologies for Aerospace and Engineering Applications: Current Trends, Challenges and Future Prospects, Trans. Indian Natl. Acad. Eng. 6 (2021) 173–188. https://doi.org/10.1007/s41403-021-00208-z.

[2] V.B. Chintada, R. Koona, M.V.A. Raju Bahubalendruni, State of Art Review on Nickel-Based Electroless Coatings and Materials, J. Bio- Tribo-Corrosion. 7 (2021) 1–14. https://doi.org/10.1007/s40735-021-00568-7.

[3] A. Agarwal, T. Soga, Electroless Assisted Nanostructured Morphologies, in: Simple Chem. Methods Thin Film Depos., Springer, 2023: pp. 211–244. https://doi.org/10.1007/978-981-99-0961-2_5.

[4] Y. Shen, J. Guo, L. Wang, H. Han, Y. Ma, B. Xin, Z. Wang, Acceleration Mechanism of Triethanolamine in Electroless Bath for Pure Cobalt Deposition, J. Electrochem. Soc. 170 (2023) 112503. https://doi.org/10.1149/1945-7111/ad0a74.

[5] G.L. Tate, B.A.T. Mehrabadi, W. Xiong, A. Kenvin, J.R. Monnier, Synthesis of highly active pd@cu–pt/c methanol oxidation electrocatalysts via continuous, co-electroless deposition, Nanomaterials. 11 (2021) 1–15. https://doi.org/10.3390/nano11030793.

[6] L. Mielewczyk, V. Liebscher, J. Grothe, S. Kaskel, Sugar-Based Electroless Copper Deposition on Pectin-Coated Alumina Microparticles, Adv. Mater. Interfaces. 10 (2023) 2–7. https://doi.org/10.1002/admi.202300496.

[7] G. Barrera, F. Scaglione, F. Celegato, M. Coïsson, P. Tiberto, P. Rizzi, Electroless Cobalt Deposition on Dealloyed Nanoporous Gold Substrate: A Versatile Technique to Control Morphological and Magnetic Properties, Nanomaterials. 13 (2023). https://doi.org/10.3390/nano13030494.

[8] M. Lee, J. Park, K. Son, D. Kim, K. Kim, M. Kang, Electroless Ni-P-PTFE Composite Plating with Rapid Deposition and High PTFE Concentration through a Two-Step Process, Coatings. 12 (2022). https://doi.org/10.3390/coatings12081199.

[9] J. Song, M.R. Kim, Y. Kim, D. Seo, K. Ha, T.E. Song, W.G. Lee, Y. Lee, K.C. Kim, C.W. Ahn, H. Han, Fabrication of junction-free Cu nanowire networks via Ru-catalyzed electroless deposition and their application to transparent conducting

electrodes, Nanotechnology. 33 (2022). https://doi.org/10.1088/1361-6528/ac353d.

[10] D. Zhu, Q. Wang, J. Sun, X. Yang, X. Li, L. Wang, A Microporous Channel Copper Immersion Layer Promotes the Rapid Ni-P Electroless Plating Process on Aluminum Alloys at Medium and Low Temperatures, J. Electrochem. Soc. 171 (2024) 072503. https://doi.org/10.1149/1945-7111/ad6039.

[11] C.S. Rauta, G. Majumdar, S. Mukherjee, S. Sarkar, An eco-friendly one-step pretreatment method for the synthesis of electroless coating on magnesium alloy, Phys. Scr. 99 (2024). https://doi.org/10.1088/1402-4896/ad733c.

[12] Z. Gao, C. Zhang, Q. Wang, G. Xu, G. Gan, H. Zhang, Emerging Non-Noble-Metal Atomic Layer Deposited Copper as Seeds for Electroless Copper Deposition, Materials (Basel). 17 (2024). https://doi.org/10.3390/ma17071620.

[13] K. Pawar, P. Dixit, A critical review of copper electroless deposition on glass substrates for microsystems packaging applications, Surf. Eng. 38 (2022) 576–617. https://doi.org/10.1080/02670844.2022.2142002.

[14] K.S. Barros, E.M. Ortega, V. Pérez-Herranz, D.C.R. Espinosa, Evaluation of brass electrodeposition at RDE from cyanide-free bath using EDTA as a complexing agent, J. Electroanal. Chem. 865 (2020). https://doi.org/10.1016/j.jelechem.2020.114129.

[15] S. FRANCIS, Electroless Nickel Gets a 24/7 Helpline: A new helpline developed by Surface Technology Inc. provides EN finishers with troubleshooting and technical support in real time., Prod. Finish. (2025) 20–23. https://www.pfonline.com/articles/electroless-nickel-gets-a-247-helpline (accessed February 6, 2025).

[16] Electroless Nickel Plating, (2025). https://cbeplus.com/electroless-nickel/ (accessed February 22, 2025).

[17] Heat sink, (2025). https://en.wikipedia.org/wiki/Heat_sink (accessed February 22, 2025).

[18] Special Hydraulic Valves, (2025). https://www.hunger-group.com/products/special-hydraulic-valves (accessed February 22, 2025).

[19] Brake Piston, (2025). https://www.kamienbrake.com/what-happens-when-a-brake-

piston-goes-bad/ (accessed February 22, 2025).

[20] Actuators, (2025). https://sisto-aseptic.com/actuators/ (accessed February 22, 2025).

[21] EV Busbar, (2025). https://www.copper-components.com/sale-41341696-electric-vehicle-copper-busbar-ev-busbar-good-electrical-properties.html (accessed February 22, 2025).

[22] Steel tubes of compressors, (2024). https://www.mvt.be/en/operations/ (accessed January 5, 2024).

[23] Q. Barati, S.M.M. Hadavi, Electroless Ni-B and composite coatings: A critical review on formation mechanism, properties, applications and future trends, Surfaces and Interfaces. 21 (2020) 100702. https://doi.org/10.1016/j.surfin.2020.100702.

[24] V.B. Chintada, T.R. Gurugubelli, M.R. Tamtam, R. Koutavarapu, Advancements in Nickel-Phosphate/Boron Based Electroless Composite Coatings: A Comprehensive Review of Mechanical Properties and Recent Developments, Materials (Basel). 16 (2023). https://doi.org/10.3390/ma16186116.

[25] M. Khan, S. Yan, M. Ali, F. Mahmood, Y. Zheng, G. Li, J. Liu, X. Song, Y. Wang, Innovative Solutions for High-Performance Silicon Anodes in Lithium-Ion Batteries: Overcoming Challenges and Real-World Applications, Nano-Micro Lett. 16 (2024) 1–44. https://doi.org/10.1007/s40820-024-01388-3.

[26] G.E.M. Nasr, M.A. Baiomy, A.Z. Taieb, M.E.A. Razek, Assessment of the performance of Ni carbon nanotube nano composite coatings and activated carbon for diesel exhaust treatment, Sci. Rep. 15 (2025) 1–23. https://doi.org/10.1038/s41598-025-88823-6.

[27] X. Liang, S. Zhang, G.M. Gadd, J. McGrath, D.W. Rooney, Q. Zhao, Fungal-derived selenium nanoparticles and their potential applications in electroless silver coatings for preventing pin-Tract infections, Regen. Biomater. 9 (2022). https://doi.org/10.1093/rb/rbac013.

[28] H. Huang, J. Zhang, F. Bu, L. Jin, J. Wang, Y. Liu, C. Xu, Facile fabrication of magnetic-cobalt-nanoparticle-plated carbon aerogel by an electroless plating strategy, J. Mater. Res. 38 (2023) 2188–2202. https://doi.org/10.1557/s43578-023-00939-5.

[29] K. Gautam, D. Gogoi, T.D. Kongnyui, S. Devi, C. Kumar, M. Kumar, A comprehensive review on surface modifications of polymer-based 3D-printed structures: Metal coating prospects and challenges, Polym. Adv. Technol. 35 (2024) 1–29. https://doi.org/10.1002/pat.6369.

[30] S. Sharma, V. Gupta, D. Mudgal, Current trends, applications, and challenges of coatings on additive manufacturing based biopolymers: A state of art review, Polym. Compos. 43 (2022) 6749–6781. https://doi.org/10.1002/pc.26809.

[31] L. Zhang, Y. Chao, K. Yang, D. Xue, S. Zhou, Recent Advances in Metal/Alloy Nano Coatings for Carbon Nanotubes Based on Electroless Plating, Front. Chem. 9 (2022) 1–12. https://doi.org/10.3389/fchem.2021.782307.

[32] P. Siddikali, P.S.R. Sreekanth, Performance Evaluation of CNT Reinforcement on Electroless Plating on Solid Free-Form-Fabricated PETG Specimens for Prosthetic Limb Application, Polymers (Basel). 14 (2022). https://doi.org/10.3390/polym14163366.

[33] M. Molaei, M. Atapour, Nickel-based coatings as highly active electrocatalysts for hydrogen evolution reaction: A review on electroless plating cost-effective technique, Sustain. Mater. Technol. 40 (2024) e00991. https://doi.org/10.1016/j.susmat.2024.e00991.

[34] 5-unique-electroless-nickel-plating-processes, (2025). https://www.sharrettsplating.com/blog/5-unique-electroless-nickel-plating-processes/ (accessed February 26, 2025).

[35] J. Sudagar, J. Lian, W. Sha, Electroless nickel, alloy, composite and nano Coatings — A critical review, J. Alloys Compd. 571 (2013) 183–204. https://doi.org/10.1016/j.jallcom.2013.03.107.

[36] V. Genova, L. Paglia, F. Marra, C. Bartuli, G. Pulci, Pure thick nickel coating obtained by electroless plating: Surface characterization and wetting properties, Surf. Coatings Technol. 357 (2019) 595–603. https://doi.org/10.1016/j.surfcoat.2018.10.049.

[37] Delaunois F, Vitry V, Bonin L, Electroless nickel plating: fundamentals to applications, 2019. https://doi.org/10.1201/9780429466274.

[38] H. Gul, İ. Usta, Effect of Alumina Concentration on Morphology, Wear, and

Corrosion: Electroless Ni-W-P/Al2O3 Composite Coatings on Aluminum Surfaces, J. Mater. Eng. Perform. 32 (2023) 6107–6122. https://doi.org/10.1007/s11665-023-08184-x.

[39] S. Uppada, R. Koona, V.B. Chintada, R. Koutavarapu, Influence of Heat Treatment on Crystal Structure, Microhardness and Corrosion Resistance of Bilayer Electroless Ni-P-SiC/Ni-P-Al2O3 Coatings, Silicon. 15 (2023) 793–803. https://doi.org/10.1007/s12633-022-02042-6.

[40] H.M. Algailani, S.I. Al-Nassar, A.K. Mahmoud, H.A. Al-Kaisy, A.A.A.G. Alrubaiy, Study the Wear Characteristics for Ni-ZrO2 and Ni-Al2O3 Nanocomposite Coatings Produced by Electroless Deposition Technique, Mater. Des. Process. Commun. 2024 (2024). https://doi.org/10.1155/2024/4907211.

[41] T. Sharma, H. Bera, D.A. Brown, A. Schulze, R. Brüning, Thermal evolution, phase composition and fracture toughness of electroless Ni-P, Ni-W-P and Ni-Mo-W-P films for solderable surfaces on copper, Surf. Coatings Technol. 467 (2023) 129722. https://doi.org/10.1016/j.surfcoat.2023.129722.

[42] D. Jayabalakrishnan, S. Senthil Kumar, R. Suthan, P. Babu Aurtherson, J. Elanchezhian, V. Ramanareddy, S. Louies Praveen, Umamahesawari Kandasamy, Tribological Behavior of Ni-P Electroless Coating of Inconel 625 with Multiwall Nano Carbon Tubes, Adv. Mater. Sci. Eng. 2023 (2023). https://doi.org/10.1155/2023/7926006.

[43] S.K. Shetty, M. Nayak, M. Nagaral, F. Nalband, Inuence of Electroless Copper Coated B 4 C particles Addition on the Hardness, Density and Wear Behavior of Al2025 Alloy Composites, J. Bio- Tribo-Corrosion. 10 (2024) 1–16. https://doi.org/10.1007/s40735-024-00916-3.

[44] A. Biswas, S.K. Das, P. Sahoo, Oxidation issues during heat treatment and effect on the tribo-mechanical performance of electroless Ni-P–Cu deposits, Proc. Inst. Mech. Eng. Part L J. Mater. Des. Appl. 235 (2021) 1665–1685. https://doi.org/10.1177/1464420721999823.

[45] S. Bhattacharyya, P. Kumar, D. Choudhary, S.K. Pal, S. Chakraborty, Development of Electroless Ni-P-Cu Composite Coating: A Characterisation, Corrosion and Thermal Study on AISI-1040 Used in Heat Exchangers, Jom. 76 (2024) 6600–6614.

https://doi.org/10.1007/s11837-024-06817-7.

[46] N. Saha, J. Basu, S. Mondal, B. Satpati, G. Majumdar, Effect of Electroless NiP/PTFE Composite Coating on Mechanical Properties of AISI 420 SS and Its Corrosion Behaviour in Human Blood, J. Bio- Tribo-Corrosion. 10 (2024) 1–8. https://doi.org/10.1007/s40735-024-00825-5.

[47] G. Liu, B. Zhang, H. Wang, Q. Ma, G. Lv, X. Zhang, Y. Wu, D. Li, The Corrosion Resistance Study of Ni-P-CS Coating Improved by Carbon Nanoparticle, Mater. Corros. (2025) 1–9. https://doi.org/10.1002/maco.202414735.

[48] I. Paul, S. Ghosh, Al-induced electroless Co/Sn bi-layered deposition and evaluation of corrosion resistance, Bull. Mater. Sci. 47 (2024). https://doi.org/10.1007/s12034-023-03073-4.

[49] S.Y. Ahmed, S.B. Mahmoud, M.A. Shoeib, Synthesis, structure characterization, and corrosion properties of duplex electroless Ni-P/Ni-B and Ni-P/Ni-B-W coatings on mild steel, Sci. Rep. 14 (2024) 1–12. https://doi.org/10.1038/s41598-024-75883-3.

[50] Z. Wang, Y. Li, G. Zhang, Influences of La3+ Concentrations on Properties of Electroless Nickel–Phosphorus–Boron Coatings, Prot. Met. Phys. Chem. Surfaces. 59 (2023) 956–963. https://doi.org/10.1134/S2070205123700909.

[51] W. Hao, X. Ma, L. Wang, Y. Guo, Q. Bi, J. Fan, H. Li, G. Li, Surface Corrosion-Resistant and Multi-Scenario MoNiP Electrode for Efficient Industrial-Scale Seawater Splitting, Adv. Energy Mater. 2403009 (2024) 1–18. https://doi.org/10.1002/aenm.202403009.

[52] S. Bhattacharyya, D. Choudhary, P. Kumar, S. Chakraborty, Microstructure and Corrosion Changes Due to Spray Cooling: How Synthesized Wastewater Effects the Electroless Composite Coating, Arab. J. Sci. Eng. (2024). https://doi.org/10.1007/s13369-024-09165-5.

[53] W.S. Barakat, A. Samir, O.A. Elkady, M. Abu-Okail, A.Y.A. Mohamed, A. EL-Nikhaily, A.M.I. Abu-Oqail, Improved properties of hybrid Al-CNTs via h-BNs coated with ag and ni for ball bearings, Sci. Rep. 15 (2025) 1–27. https://doi.org/10.1038/s41598-024-84249-8.

[54] S.A. Lone, A. Rahman, Electroless nanoceria films on nickel-based superalloy, Surf. Eng. 36 (2020) 936–943. https://doi.org/10.1080/02670844.2019.1662225.

[55] X. Wu, J. Cao, H. Liang, H. Tang, Y. Liao, G. Meng, W. Huang, Silver nanoparticles-coated 2D glass-flakes reinforced polyurea composites with high thermal conductivity, acceptable toughness and thermal stability, Iran. Polym. J. (English Ed. 31 (2022) 1347–1359. https://doi.org/10.1007/s13726-022-01082-4.

[56] B.Z. Tian, X.P. Jiang, J. Chen, H. Gao, Z.G. Wang, J. Tang, D.L. Zhou, L. Yang, Z.G. Chen, Low lattice thermal conductivity and enhanced thermoelectric performance of SnTe via chemical electroless plating of Ag, Rare Met. 41 (2022) 86–95. https://doi.org/10.1007/s12598-021-01805-1.

[57] M. Arefpour, M. Almasi Kashi, M. Bagheli, High Chemical and Thermal Stability of Ag Nanowire-Based Transparent Conductive Electrodes Induced by Electroless Ag Nanoparticle Decoration, Phys. Status Solidi Appl. Mater. Sci. 217 (2020) 1–11. https://doi.org/10.1002/pssa.201900957.

[58] Q. Zhang, K. Wang, X. Chen, X. Tang, Q. Zhao, Q. Fu, Improving the Thermal Stability and Functionality of Bamboo Fibers by Electroless Plating, ACS Sustain. Chem. Eng. 10 (2022) 16935–16947. https://doi.org/10.1021/acssuschemeng.2c06017.

[59] N. Xiao, Y.Q. Qiao, N.K. Shi, Y.Z. Song, S.Q. Deng, J. Chen, Realization of high thermal conductivity and tunable thermal expansion in the ScF3@Cu core-shell composites, Sci. China Technol. Sci. 64 (2021) 2057–2065. https://doi.org/10.1007/s11431-020-1758-5.

[60] E.M. Fayyad, P.A. Rasheed, N. Al-Qahtani, A.M. Abdullah, F. Hamdy, M.A. Sharaf, M.K. Hassan, K.A. Mahmoud, A.M. Mohamed, G. Jarjoura, Z. Farhat, Microbiologically-influenced corrosion of the electroless-deposited NiP-TiNi – Coating, Arab. J. Chem. 14 (2021) 103445. https://doi.org/https://doi.org/10.1016/j.arabjc.2021.103445.

[61] F. Nabhan, E.M. Fayyad, M.H. Sliem, F.M. Shurrab, K. Eid, G. Nasrallah, A.M. Abdullah, ZnO-Doped gC3N4 Nanocapsules for Enhancing the Performance of Electroless NiP Coating─Mechanical, Corrosion Protection, and Antibacterial Properties, ACS Omega. 8 (2023) 22361–22381. https://doi.org/10.1021/acsomega.2c07288.

[62] D. Lu, Y. Ning, X. Liu, S. Ren, B. Ni, Y. Song, J. Li, Z. Li, W. Liu, Preparation and

properties of antibacterial food-preservative paper incorporating ceramic pigments, Packag. Technol. Sci. 37 (2024) 273–282. https://doi.org/10.1002/pts.2797.

[63] L. Jiang, Y. Zhou, Y. Guo, Z. Jiang, S. Chen, J. Ma, Preparation of silver nanoparticle functionalized polyamide fibers with antimicrobial activity and electrical conductivity, J. Appl. Polym. Sci. 136 (2019) 1–9. https://doi.org/10.1002/app.47584.

[64] S. Restrepo, M.P. Duque, S. Bello, L.M. Tirado, F. Echeverría, A.A. Zuleta, J.G. Castaño, E. Correa, Antibacterial evaluation of electroless Ni–P coating with ZnO nanoparticles on 3D printed ABS, Int. J. Adv. Manuf. Technol. 128 (2023) 209–220. https://doi.org/10.1007/s00170-023-11751-0.

[65] K. An, Y. Wang, Y. Sui, Y. Qing, W. Tong, X. Wang, C. Liu, Recent advances of cerium compounds in functional coatings: Principle, strategies, and applications, J. Rare Earths. 43 (2024) 227–245. https://doi.org/10.1016/j.jre.2024.03.017.

[66] S. Bhaskar, V. Srinivasan, S.S. Ramamurthy, Nd2O3-Ag Nanostructures for Plasmonic Biosensing, Antimicrobial, and Anticancer Applications, ACS Appl. Nano Mater. 6 (2023) 1129–1145. https://doi.org/10.1021/acsanm.2c04643.

[67] X. Shu, Y. Wang, X. Lu, C. Liu, W. Gao, Parameter optimization for electroless Ni-W-P coating, Surf. Coatings Technol. 276 (2015) 195–201. https://doi.org/10.1016/j.surfcoat.2015.06.068.

[68] V. Genova, L. Paglia, G. Pulci, G. Pedrizzetti, A. Pranzetti, M. Romanelli, F. Marra, Medium and High Phosphorous Ni-P Coatings Obtained via an Electroless Approach: Optimization of Solution Formulation and Characterization of Coatings, Coatings. 13 (2023). https://doi.org/10.3390/coatings13091490.

[69] A. Mukhopadhyay, S. Sahoo, A Grey-Fuzzy Based Approach for the Optimization of Corrosion Resistance of Rebars Coated with Ternary Electroless Nickel Coatings, J. Soft Comput. Civ. Eng. 6 (2022) 107–127. https://doi.org/10.22115/SCCE.2022.326903.1401.

[70] R. Mandal, A. Ghosh, S. Sarkar, J. De, T. Mandal, R.S. Sen, G. Majumdar, Parametric Optimization to Maximize Microhardness of Electroless Ni-Sn-P Coating Using Taguchi and Evolutionary Approaches, J. Inst. Eng. Ser. C. 105 (2024) 1217–1231. https://doi.org/10.1007/s40032-024-01094-4.

[71] B.B. Mandal, V. Kumar, B. Oraon, Optimization, Prediction, and Characterization of Electroless Ni-W-P-nanoTiO2 Composite Coatings on Pipeline Steel, Arab. J. Sci. Eng. (2023). https://doi.org/10.1007/s13369-023-07928-0.

[72] S. Lamichaney, R. Mandal, N. Mondal, S. Sarkar, B. Oraon, G. Majumdar, Impact of Coating Variables on Micro-hardness in Ni–W–P Electroless Coatings: Experimental Assessment, Modelling and Optimization, J. Inst. Eng. Ser. C. (2024). https://doi.org/10.1007/s40032-024-01070-y.

[73] B. Liu, Q. Zhang, Y. Li, Y. Yang, T. Zhang, Y. Wang, Y. Shao, H. Sun, Z. Wang, F. Wang, Optimization of the Corrosion Resistance of Electroless Ni–W–P Coatings on Magnesium Alloys by the Response Surface Methodology, Coatings. 11 (2021) 1–14. https://doi.org/10.3390/coatings11010018.

[74] Z. Zhang, Y. Bai, Y. He, H. Li, Y. Fan, T. He, Using RSM optimization to fabricate Ni–Fe–P ternary alloy electroless coating and explore its corrosion properties, J. Mater. Sci. Mater. Electron. 32 (2021) 26412–26424. https://doi.org/10.1007/s10854-021-07020-z.

[75] S. Sarkar, R.K. Baranwal, A. Mukherjee, I. Koley, C. Biswas, J. Haider, G. Majumdar, Optimisation & minimisation of corrosion rate of electroless Ni-Co-P coating, Adv. Mater. Process. Technol. 6 (2020) 487–508. https://doi.org/10.1080/2374068X.2019.1709326.

[76] T. Hassan, A. Mallick, S. Lamichaney, S. Das Mandal, S. Sarkar, N. Mondal, G. Majumdar, Modelling and optimization of corrosion rate of Ni-Co-P coating using box-behnken design, gradient descent with RMSprop & metaheuristic algorithm, Int. J. Interact. Des. Manuf. (2024). https://doi.org/10.1007/s12008-024-02156-8.

[77] M. Vijayanand, R. Varahamoorthi, P. Kumaradhas, S. Jayabal, Process Modeling and Intuitive Search Based Optimization of Average Surface Roughness in Citrate Stabilized Electroless Nickel-Boron Coatings, Jom. 74 (2022) 563–573. https://doi.org/10.1007/s11837-021-05072-4.

[78] C.S. Rauta, G. Majumdar, S. Sarkar, Parametric Optimization of Microhardness of Electroless Ni-Zn-Cu-P Coating Using Taguchi Design and Artificial Neural Network, Jom. 74 (2022) 4564–4574. https://doi.org/10.1007/s11837-022-05489-5.

[79] D. Połap, M. Woźniak, Red fox optimization algorithm, Expert Syst. Appl. 166

(2021) 114107. https://doi.org/10.1016/j.eswa.2020.114107.

[80] Z. Zhou, Y. Du, G. He, L. Xu, L. Shu, Optimization and Characterization of Laser Cladding of 15-5PH Coating on 20Cr13 Stainless Steel, J. Mater. Eng. Perform. 32 (2023) 962–977. https://doi.org/10.1007/s11665-022-07157-w.

[81] R. Agrawal, A. Mukhopadhyay, Wear Behaviour and Mechanisms of Electroless Lead Free Ni–B–W Coatings Using Artificial Neural Networks in Conjunction with Genetic Algorithms, Arab. J. Sci. Eng. 49 (2024) 15611–15628. https://doi.org/10.1007/s13369-024-09141-z.

[82] A.M. Sadoun, I.M.R. Najjar, A. Fathy, M. Abd Elaziz, M.A.A. Al-qaness, A.W. Abdallah, M. Elmahdy, An enhanced Dendritic Neural Algorithm to predict the wear behavior of alumina coated silver reinforced copper nanocomposites, Alexandria Eng. J. 65 (2023) 809–823. https://doi.org/10.1016/j.aej.2022.09.036.

[83] I.R. Najjar, A.M. Sadoun, A. Fathy, A.W. Abdallah, M.A. Elaziz, M. Elmahdy, Prediction of Tribological Properties of Alumina-Coated, Silver-Reinforced Copper Nanocomposites Using Long Short-Term Model Combined with Golden Jackal Optimization, Lubricants. 10 (2022). https://doi.org/10.3390/lubricants10110277.

[84] J. Yuan, J. Wang, Y. Gao, J. Mao, W. Hu, Preparation and magnetic properties of Ni-Co-P-Ce coating by electroless plating on silicon substrate, Thin Solid Films. 632 (2017) 1–9. https://doi.org/10.1016/j.tsf.2017.04.038.

[85] W. Qian, H. Wei, H. Chen, L. Zhu, Y. Sun, S. Han, H. Lin, J. Jiang, The effect of heat treatment on Ni–B–Ce electroless coatings, Surf. Eng. 35 (2019) 145–153. https://doi.org/10.1080/02670844.2018.1442697.

[86] J. De, S. Sarkar, P. Roy, R.S. Sen, G. Majumdar, B. Oraon, Synthesis and characterization of electroless Ni-Co-P coating, Sadhana - Acad. Proc. Eng. Sci. 47 (2022). https://doi.org/10.1007/s12046-022-01933-z.

[87] L. Liu, J. Peng, X. Du, H. Zheng, Z. Chen, P. Gong, Y. Xiao, X. Cao, Synthesis, composition, morphology, and wettability of electroless Ni-Fe-P coatings with varying microstructures, Thin Solid Films. 706 (2020) 138080. https://doi.org/10.1016/j.tsf.2020.138080.

[88] K. Wang, Y. Si, Z. Lv, T. Yu, X. Liu, G. Wang, G. Xie, L. Jiang, Efficient and stable Ni–Co–Fe–P nanosheet arrays on Ni foam for alkaline and neutral hydrogen

evolution, Int. J. Hydrogen Energy. 45 (2020) 2504–2512. https://doi.org/10.1016/j.ijhydene.2019.11.154.

[89] S. Roy, B.M. Mishra, G.K. Bose, Characterization of Ni-P based poly-alloy and composite coatings involving nanoindentation and nanoscratch tests, Mater. Today Commun. 29 (2021). https://doi.org/10.1016/j.mtcomm.2021.102991.

[90] P.W. Li, C.W. Hsu, C.S. Yan, C.Y. Hsu, C.H. Hung, J.Y. Kao, Structure and fatigue behavior of electroless plated Ni-Zn-P films using pretreatments, annealing and an applied magnetic field, Int. J. Fatigue. 167 (2023) 107369. https://doi.org/10.1016/j.ijfatigue.2022.107369.

[91] M. Heshmati, D. Seifzadeh, P. Shoghi, M. Gholizadeh-Gheshlaghi, Duplex Ni-Zn-Cu-P/Ni-P electroless coating on magnesium alloy via maleic acid pretreatment, Surf. Coatings Technol. 328 (2017) 20–29. https://doi.org/10.1016/j.surfcoat.2017.08.027.

[92] Y.P. Jia, W.C. Sun, Y.R. Dong, Y. Xiao, J.P. Liu, C.X. Zhang, Preparation, Microstructures, and Corrosion Resistance of Ni-Mo-P Ternary Amorphous Coating, J. Mater. Eng. Perform. 32 (2023) 2476–2487. https://doi.org/10.1007/s11665-022-07288-0.

[93] S.S. Tian, W.C. Sun, Y.W. Liu, Y. Xiao, Y.P. Jia, Microstructures and corrosion resistance of conversion film-electroless Ni-W-P ternary coatings on AZ91D magnesium alloy, Trans. Inst. Met. Finish. 99 (2021) 292–298. https://doi.org/10.1080/00202967.2021.1930722.

[94] M. Asgari, G. Barati Darband, M. Monirvaghefi, Electroless deposition of Ni-W-Mo-Co-P films as a binder-free, efficient and durable electrode for electrochemical hydrogen evolution, Electrochim. Acta. 446 (2023) 142001. https://doi.org/10.1016/j.electacta.2023.142001.

[95] W. Cheng, P. Wen, T. Wang, H. Yu, M. Jiang, H. Wen, B. Wang, A study of Ni–P electroless coating modified by rare earth oxide (La2O3, Y2O3 and Ce2O3) on pre-phosphorized zirconium alloy, Ferroelectrics. 606 (2023) 161–174. https://doi.org/10.1080/00150193.2023.2189832.

[96] Y.-P. Jia, W.-C. Sun, Y. Xiao, J.-P. Liu, C.-X. Zhang, T.-Q. Zhang, Z.-F. Hou, Effect of rare earth on microstructure and corrosion behavior of electroless Ni-W-P

composite coatings, Anti-Corrosion Methods Mater. (2022). https://doi.org/10.1108/ACMM-11-2021-2575.

[97] Y.P. Jia, W.C. Sun, Y. Xiao, Y.W. Liu, S.S. Tian, Effect of Rare Earth on the Corrosion Resistance of Electroless Ni-Mo-P Composite Coatings, Mater. Res. 25 (2022). https://doi.org/10.1590/1980-5373-MR-2021-0278.

[98] Y. Zhu, B. Chen, T. Cheng, C. Du, S. Zhang, Deposit amorphous Ni-Co-B-RE (RE = Ce, Gd and Nd) on nickel foam as a high performance and durable electrode for hydrogen evolution reaction, J. Electroanal. Chem. 878 (2020) 114552. https://doi.org/10.1016/j.jelechem.2020.114552.

[99] P. Zhang, Z. Xu, G. Meng, Y. Wang, J. Wang, Y. Shao, F. Wang, Efficiently Improved Corrosion Resistance of Electrodeposition Ni–Cu Coatings via Site-Blocking Effect of Ce, Adv. Eng. Mater. 24 (2022) 1–15. https://doi.org/10.1002/adem.202200109.

[100] D. Li, X. Cui, X. Wen, L. Feng, Y. Hu, G. Jin, E. Liu, W. Zheng, Effect of CeO2 nanoparticles modified graphene oxide on electroless Ni-P coating for Mg-Li alloys, Appl. Surf. Sci. 593 (2022). https://doi.org/10.1016/j.apsusc.2022.153381.

[101] A. Krishnan, Malavika, A. Prasannan, M. Yoosuf, Tailoring of a novel high conductive, hydrophilic cum aerophobic CeO2-MoS2/PANI core-shell composite for enhancing the catalytic property of Ni-P electrode for hydrogen production, J. Alloys Compd. 1010 (2025) 178307. https://doi.org/10.1016/j.jallcom.2024.178307.

[102] V. Kumar, B.B. Mandal, S. Das, B. Oraon, S. Mukherjee, Tailoring electroless Ni-W-P polyalloy coatings: Unveiling the synergistic impact of cerium addition and annealing on surface functional properties, Surf. Coatings Technol. 485 (2024) 130874. https://doi.org/10.1016/j.surfcoat.2024.130874.

[103] D.Y. Liu, L.G. Li, L.S. Liu, Effect of rare earth cerium on the synthesis and wear-resistance of electroless Ni-P-PTFE coatings, in: Adv. Mater. Res., 2013: pp. 1996–2002. https://doi.org/10.4028/www.scientific.net/AMR.750-752.1996.

[104] D. Gültekin, E. Duru, H. Akbulut, Improved wear behaviors of lead-free electroless Ni–B and Ni-B/CeO2 composite coatings, Surf. Coatings Technol. 422 (2021). https://doi.org/10.1016/j.surfcoat.2021.127525.

[105] J.K. Pancrecious, J.P. Deepa, V. Jayan, U.S. Bill, T.P.D. Rajan, B.C. Pai, Nanoceria induced grain refinement in electroless Ni-B-CeO2 composite coating for enhanced

wear and corrosion resistance of Aluminium alloy, Surf. Coatings Technol. 356 (2018) 29–37. https://doi.org/10.1016/j.surfcoat.2018.09.046.

[106] S.A. Lone, A. Rahman, Hot Corrosion Behaviour of Electroless Deposited Nano-structured Cerium Oxide Coatings on Superalloy, J. Inst. Eng. Ser. D. 101 (2020) 81–92. https://doi.org/10.1007/s40033-020-00220-7.

[107] R. Andreeva, D. Stoychev, Phosphate sealing improvement of the corrosion resistance of thin cerium oxides coatings electroless deposited on aluminium, J. Phys. Conf. Ser. 2240 (2022). https://doi.org/10.1088/1742-6596/2240/1/012001.

[108] W. Qian, H. Chen, C. Feng, L. Zhu, H. Wei, S. Han, G. Li, H. Lin, J. Jiang, Microstructure and properties of the Ni-B and Ni-B-Ce ultrasonic-Assisted electroless coatings, Surf. Rev. Lett. 25 (2018) 1–11. https://doi.org/10.1142/S0218625X19500069.

[109] E. Valova, S. Armyanov, G. Hristova, T. Vassilev, O. Steenhaut, J. Dille, A. Hubin, I. Vandendael, Electroless deposited Ni-Ce-P Coatings, Surf. Coatings Technol. 304 (2016) 468–475. https://doi.org/10.1016/j.surfcoat.2016.07.054.

[110] J. Yuan, J. Wang, Y. Gao, J. Mao, W. Hu, Preparation and magnetic properties of Ni-Co-P-Ce coating by electroless plating on silicon substrate, Thin Solid Films. 632 (2017) 1–9. https://doi.org/10.1016/j.tsf.2017.04.038.

[111] B. Liu, Q. Zhang, Y. Li, Y. Yang, T. Zhang, Y. Wang, Y. Shao, H. Sun, Z. Wang, F. Wang, Optimization of the corrosion resistance of electroless ni–w–p coatings on magnesium alloys by the response surface methodology, Coatings. 11 (2021) 1–14. https://doi.org/10.3390/coatings11010018.

[112] S. Yazdani, V. Vitry, RSM models approach for optimization of the mechanical properties of electroless Ni-B-nanodiamond coating: An experimental and molecular dynamic simulation study, Surf. Coatings Technol. 452 (2023) 129133. https://doi.org/10.1016/j.surfcoat.2022.129133.

[113] M. Vijayanand, R. Varahamoorthi, P. Kumaradhas, S. Sivamani, Modelling and optimisation of hardness in citrate stabilised electroless nickel boron (ENi-B) coatings using back propagation neural network–Box Behnken design and simulated annealing–genetic algorithm, Trans. Inst. Met. Finish. 99 (2021) 253–264. https://doi.org/10.1080/00202967.2021.1898172.

[114] M. Vijayanand, R. Varahamoorthi, P. Kumaradhas, S. Sivamani, M. V. Kulkarni, Regression-BPNN modelling of surfactant concentration effects in electroless Ni[sbnd]B coating and optimization using genetic algorithm, Surf. Coatings Technol. 409 (2021) 126878. https://doi.org/10.1016/j.surfcoat.2021.126878.

[115] A.S. Nateri, A. Hajipour, S. Balarak, G. Khayati, Prediction of the concentration of dye and nanosilver particle on silk fabric using artificial neural network, Pigment Resin Technol. 46 (2017) 433–439. https://doi.org/10.1108/PRT-11-2016-0114.

[116] J. De, T. Banerjee, R.S. Sen, B. Oraon, G. Majumdar, Multi-objective optimization of electroless ternary Nickel–Cobalt–Phosphorous coating using non-dominant sorting genetic algorithm-II, Eng. Sci. Technol. an Int. J. 19 (2016) 1526–1533. https://doi.org/10.1016/j.jestch.2016.04.011.

[117] E. Ergul, H.I. Kurt, M. Oduncuoglu, N.F. Yilmaz, Electroless nickel–phosphorus and cobalt–phosphorus coatings on multi-walled carbon nanotubes, Mater. Res. Express. 7 (2020) 115604. https://doi.org/https://doi.org/10.1088/2053-1591/abcc3f.

[118] Y.H. Cheng, H.Y. Chen, Z.C. Zhu, T.C. Jen, Y.X. Peng, Experimental study on the anti-fouling effects of Ni-Cu-P-PTFE deposit surface of heat exchangers, Appl. Therm. Eng. 68 (2014) 20–25. https://doi.org/10.1016/j.applthermaleng.2014.04.003.

[119] Y. Zhang, X. Shen, Facile fabrication of robust superhydrophobic coating for enhanced corrosion protection on AZ91 magnesium alloy by electroless Ni-B/GO plating, Surf. Coatings Technol. 455 (2023) 129213. https://doi.org/10.1016/j.surfcoat.2022.129213.

[120] A.R. Subhani, D.K. Mondal, C. Mondal, J. Maity, Synthesis of Nano-Particle Dispersed Highly Substructured Strong and Ductile Low Carbon Steel Possessing Structural Hierarchy, Steel Res. Int. 90 (2019) 1–7. https://doi.org/10.1002/srin.201800519.

[121] W. chang Sun, J.M. Xu, Y. Wang, F. Guo, Z.W. Jia, Effect of Cerium Oxide on Morphologies and Electrochemical Properties of Ni-W-P Coating on AZ91D Magnesium, J. Mater. Eng. Perform. 26 (2017) 5753–5759. https://doi.org/10.1007/s11665-017-3038-3.

[122] V. Kumar, B. Baran Mandal, B. Oraon, Synthesis and characterization of electroless

Ni–W-Ce-P coating on AISI 1010 substrate, in: Mater. Today Proc., Elsevier Ltd, 2022: pp. 1183–1188. https://doi.org/10.1016/j.matpr.2022.03.267.

[123] B. Oraon, G. Majumdar, B. Ghosh, Improving hardness of electroless Ni-B coatings using optimized deposition conditions and annealing, Mater. Des. 29 (2008) 1412–1418. https://doi.org/10.1016/j.matdes.2007.09.005.

[124] T. Radu, M. Vlad, F. Potecaşu, G.G. Istrate, Preparation and characterization of electroless Ni–P–Al2O3 nanocomposite coatings, Dig. J. Nanomater. Biostructures. 10 (2015) 1055–1065.

[125] D.F. Liu, H. Wang, Affects of citric acid concentration and system pH on the speed and the stability of nickel electroless plating, Adv. Mater. Res. 239–242 (2011) 1813–1818. https://doi.org/10.4028/www.scientific.net/AMR.239-242.1813.

[126] R. Janik, N.J. Micyus, Electroless nickel plating solution and method, U.S. Patent 10,246,778, 2019.

[127] J.I. Martins, M.C. Nunes, On the kinetics of copper electroless plating with hypophosphite reductant, Surf. Eng. 32 (2016) 363–371. https://doi.org/10.1179/1743294415Y.0000000066.

[128] W. Wang, X. Jü, C. Xu, W. Zhang, N. Mitsuzaki, Z. Chen, Study on Electroless Plating Ni-W-P Ternary Alloy with High Tungsten from Compound Complexant Bath, J. Mater. Eng. Perform. 29 (2020) 8213–8220. https://doi.org/10.1007/s11665-020-05312-9.

[129] A. Oni, The mode of action of thiourea in electroless nickel plating, Trans. IMF. 66 (1988) 47–49. https://doi.org/10.1080/00202967.1988.11870803.

[130] M. Czagany, P. Baumli, Effect of pH on the characteristics of electroless Ni-P coatings, J. Min. Metall. Sect. B Metall. 53 (2017) 327–332. https://doi.org/10.2298/JMMB170530020C.

[131] M. Selvam, Electroless silver deposition on ABS plastic using Co(II) as reducing agent, Trans. Inst. Met. Finish. 88 (2010) 198–203. https://doi.org/10.1179/002029610X12694310988964.

[132] R.N. Duncan, The effect of solution age on corrosion resistance of electroless nickel deposits, in: Plat. Surf. Finish., 1996: pp. 64–68.

[133] J. Cao, X. Wang, W. Zhao, Y. Zhao, J. Wang, W. Jiang, G. Song, Effect of pH on Microstructure and Properties of Ultrasonic-Assisted Electroless Ni–P Coatings on Titanium Alloy, Integr. Ferroelectr. 225 (2022) 255–265. https://doi.org/10.1080/10584587.2021.1911370.

[134] J.D. Lin, C. Te Chou, The influence of phosphorus content on the microstructure and specific capacitance of etched electroless Ni-P coatings, Surf. Coatings Technol. 368 (2019) 126–137. https://doi.org/10.1016/j.surfcoat.2019.04.009.

[135] W. Wu, J. Liu, N. Miao, J. Jiang, Y. Zhang, L. Zhang, N. Yuan, Q. Wang, L. Tang, Influence of thiourea on electroless Ni–P films deposited on silicon substrates, J. Mater. Sci. Mater. Electron. 30 (2019) 7717–7724. https://doi.org/10.1007/s10854-019-01088-4.

[136] J. Sun, X.W. Zhang, Effect of cerium addition on properties of electroless nickel-phosphorus coatings, Anti-Corrosion Methods Mater. 60 (2013) 194–198. https://doi.org/10.1108/ACMM-May-2012-1177.

[137] J.N. Balaraju, Kalavati, K.S. Rajam, Surface morphology and structure of electroless ternary NiWP deposits with various W and P contents, J. Alloys Compd. 486 (2009) 468–473. https://doi.org/10.1016/j.jallcom.2009.06.173.

[138] J.N. Balaraju, M. Chembath, Electroless ternary NiCeP coatings: Preparation and characterisation, Appl. Surf. Sci. 258 (2012) 9692–9700. https://doi.org/10.1016/j.apsusc.2012.06.012.

[139] S. Kundu, S.K. Das, P. Sahoo, Friction and wear behavior of electroless Ni-P-W coating exposed to elevated temperature, Surfaces and Interfaces. 14 (2019) 192–207. https://doi.org/10.1016/j.surfin.2018.12.007.

[140] J. Wojewoda-Budka, A. Wierzbicka-Miernik, M. Szczerba, H. Kazimierczak, I. Kwiecien, J. Morgiel, K. Stan-Glowinska, F. Valenza, The effect of Re addition on the thermal stability and structure of Ni–P electroless coatings, Mater. Charact. 171 (2021) 1–9. https://doi.org/10.1016/j.matchar.2020.110811.

[141] S.A. Hassanzadeh-Tabrizi, Precise calculation of crystallite size of nanomaterials: A review, J. Alloys Compd. 968 (2023) 171914. https://doi.org/10.1016/j.jallcom.2023.171914.

[142] M.L. Xu, S.M. Kang, T.T. Chen, Coating properties of electroless Ni-P plating on

magnesium alloy with cerium chloride, Metalurgija. 58 (2019) 106–108.

[143] C.Y. Wang, G.W. Wen, G.H. Wu, Improving corrosion resistance of aluminium metal matrix composites using cerium sealed electroless Ni-P coatings, Corros. Eng. Sci. Technol. 46 (2011) 471–476. https://doi.org/10.1179/147842209X12489567719509.

[144] Y.H. Cheng, Y. Zou, L. Cheng, W. Liu, Effect of the microstructure on the anti-fouling property of the electroless Ni-P coating, Mater. Lett. 62 (2008) 4283–4285. https://doi.org/10.1016/j.matlet.2008.07.002.

[145] Q. Zhao, Y. Liu, E.W. Abel, Surface free energies of electroless Ni-P based composite coatings, Appl. Surf. Sci. 240 (2005) 441–451. https://doi.org/10.1016/j.apsusc.2004.07.013.

[146] S. Mukherjee, Laser Surface Modification of Ti6Al4V Implants, (2014).

[147] D.C. Montgomery, Design and analysis of experiments, 8th ed., John Wiley & Sons, 2012. https://doi.org/10.1002/ep.11743.

[148] B. Shi, T. Lookman, D. Xue, Multi-objective optimization and its application in materials science, Mater. Genome Eng. Adv. 1 (2023). https://doi.org/10.1002/mgea.14.

[149] B. Li, X. Fan, D. Li, P. Jiang, Design of Thermal Barrier Coatings Thickness for Gas Turbine Blade Based on Finite Element Analysis, Math. Probl. Eng. 2017 (2017). https://doi.org/10.1155/2017/2147830.

[150] H. Xi, H. Gao, W. Hou, B. Yin, J. Zuo, H. Zhao, Multi-Objective Optimization for Winter Heating Retrofit in Rural Houses of Cold Regions: A Case Study in the Wusu Area, Appl. Sci. 14 (2024). https://doi.org/10.3390/app14093760.

[151] M. Hemmat Esfe, D. Toghraie, Cascade forward Artificial Neural Network to estimate thermal conductivity of functionalized graphene-water nanofluids, Case Stud. Therm. Eng. 26 (2021) 101194. https://doi.org/10.1016/j.csite.2021.101194.

[152] A. Ibrahim, S. Rahnamayan, M.V. Martin, K. Deb, 3D-RadVis: Visualization of Pareto front in many-objective optimization, in: 2016 IEEE Congr. Evol. Comput. CEC 2016, 2016: pp. 736–745. https://doi.org/10.1109/CEC.2016.7743865.

[153] H. Liang, W. Li, Y. Li, Y. Li, Machine learning-based multi-objective optimization

and physical-geometrical competitive mechanisms for 3D woven thermal protection composites, Int. J. Heat Mass Transf. 232 (2024). https://doi.org/10.1016/j.ijheatmasstransfer.2024.125920.

[154] M. Črepinšek, S.H. Liu, L. Mernik, A note on teaching-learning-based optimization algorithm, Inf. Sci. (Ny). 212 (2012) 79–93. https://doi.org/10.1016/j.ins.2012.05.009.

[155] G. Waghmare, Comments on "a note on teaching-learning-based optimization algorithm," Inf. Sci. (Ny). 229 (2013) 159–169. https://doi.org/10.1016/j.ins.2012.11.009.

[156] Z. Rajabi, F. Afshar Taromi, S. Pourmahdian, H. Eivaz Mohammadloo, Maximizing Corrosion Resistance of HA+Ce Coated Mg Implants Using Random Forest and Whale Optimization Algorithm, Processes. 12 (2024). https://doi.org/10.3390/pr12030490.

[157] M. Zaborski, M. Woźniak, J. Mańdziuk, Multidimensional Red Fox meta-heuristic for complex optimization, Appl. Soft Comput. 131 (2022) 109774. https://doi.org/10.1016/j.asoc.2022.109774.

[158] M. Islam, M.R. Azhar, N. Fredj, T.D. Burleigh, O.R. Oloyede, A.A. Almajid, S. Ismat Shah, Influence of SiO2 nanoparticles on hardness and corrosion resistance of electroless Ni-P coatings, Surf. Coatings Technol. 261 (2015) 141–148. https://doi.org/10.1016/j.surfcoat.2014.11.044.

[159] Y. Cheng, S. Cao, Q. Hou, D. Han, Z. Han, Effect of tungsten addition on the anti-fouling property of the electroless Ni-W-P deposits, Xiyou Jinshu Cailiao Yu Gongcheng/Rare Met. Mater. Eng. 45 (2016) 1931–1937. https://doi.org/10.1016/s1875-5372(16)30149-7.

[160] H. Ashassi-Sorkhabi, M. Moradi-Haghighi, M.G. Hosseini, Effect of rare earth (Ce, La) compounds in the electroless bath on the plating rate, bath stability and microstructure of the nickel-phosphorus deposits, Surf. Coatings Technol. 202 (2008) 1615–1620. https://doi.org/10.1016/j.surfcoat.2007.07.019.

[161] E. Onofre-Bustamante, M.A. Domínguez-Crespo, A.M. Torres-Huerta, A. Olvera-Martínez, J. Genescá-Llongueras, F.J. Rodríguez-Gómez, Characterization of cerium-based conversion coatings for corrosion protection of AISI-1010 commercial

carbon steel, J. Solid State Electrochem. 13 (2009) 1785–1799. https://doi.org/10.1007/s10008-009-0871-9.

[162] S.K. Das, P. Sahoo, Influence of process parameters on microhardness of electroless Ni-B coatings, Adv. Mech. Eng. 2012 (2012). https://doi.org/10.1155/2012/703168.

[163] J.D. Costa, M.B. de Sousa, J.J.N. Alves, B. de O. Evaristo, R.A. Queiroga, A.X. dos Santos, T.M. Maciel, A.R.N. Campos, R.A.C. de Santana, S. Prasad, Effect of electrochemical bath composition on the preparation of Ni-W-Fe-P amorphous alloy, Int. J. Electrochem. Sci. 13 (2018) 2969–2985. https://doi.org/10.20964/2018.03.36.

[164] K. Huang, J. Chen, S.R. Nugen, J.M. Goddard, Hybrid Antifouling and Antimicrobial Coatings Prepared by Electroless Co-Deposition of Fluoropolymer and Cationic Silica Nanoparticles on Stainless Steel: Efficacy against Listeria monocytogenes, ACS Appl. Mater. Interfaces. 8 (2016) 15926–15936. https://doi.org/10.1021/acsami.6b04187.

[165] L. Ren, Y. Cheng, J. Yang, Q. Wang, Study on heat transfer performance and anti-fouling mechanism of ternary Ni-W-P coating, Appl. Sci. 10 (2020) 1–20. https://doi.org/10.3390/app10113905.

[166] Y.S. Huang, X.T. Zeng, X.F. Hu, F.M. Liu, Corrosion resistance properties of electroless nickel composite coatings, Electrochim. Acta. 49 (2004) 4313–4319. https://doi.org/10.1016/j.electacta.2004.04.023.

[167] M. Czagány, P. Baumli, G. Kaptay, The influence of the phosphorous content and heat treatment on the nano-micro-structure, thickness and micro-hardness of electroless Ni-P coatings on steel, Appl. Surf. Sci. 423 (2017) 160–169. https://doi.org/10.1016/j.apsusc.2017.06.168.

[168] P. Salehikahrizsangi, K. Raeissi, F. Karimzadeh, L. Calabrese, E. Proverbio, Highly hydrophobic nickel and nickel-tungsten coatings: Microstructural and surface properties, Appl. Surf. Sci. 520 (2020) 146319. https://doi.org/10.1016/j.apsusc.2020.146319.

[169] M. Hanachi, Z.S. Seyedraoufi, M. Samiee, Y. Shajari, Effect of Phosphorus Content and Heat Treatment Temperature on Microstructure and Corrosion Resistance of Ni–(X)P–GO Nanocomposite Coating on AZ31D Alloy, J. Bio- Tribo-Corrosion. 7 (2021) 1–12. https://doi.org/10.1007/s40735-020-00468-2.

[170] N.P. Wasekar, N. Hebalkar, A. Jyothirmayi, B. Lavakumar, M. Ramakrishna, G. Sundararajan, Influence of pulse parameters on the mechanical properties and electrochemical corrosion behavior of electrodeposited Ni-W alloy coatings with high tungsten content, Corros. Sci. 165 (2020) 108409. https://doi.org/10.1016/j.corsci.2019.108409.

[171] D. Liu, L. Zhou, J. Yu, Y. Yan, K. Lee, Effects of rare earth cerium addition on the synthesis and corrosion resistance of electroless Ni-PTFE-P coating, Mater. Corros. 62 (2011) 926–931. https://doi.org/10.1002/maco.200905523.

[172] A. Ataki, H. Kiepfer, H.J. Bart, Investigations on crystallization fouling on PEEK films used as heat transfer surfaces: experimental results, Heat Mass Transf. Und Stoffuebertragung. 56 (2020) 1443–1452. https://doi.org/10.1007/s00231-019-02769-w.

[173] L. Ren, Y. Cheng, Q. Wang, X. Tian, J. Yang, D. Zhang, Relationship between corrosion product and fouling growth on mild steel, copper and brass surface, Colloids Surfaces A Physicochem. Eng. Asp. 591 (2020) 124502. https://doi.org/10.1016/j.colsurfa.2020.124502.

[174] X. Chen, H. Wang, C. Wang, W. Zhang, C. Lv, Y. Zhu, A novel antiscaling and anti-corrosive polymer-based functional coating, J. Taiwan Inst. Chem. Eng. 97 (2019) 397–405. https://doi.org/10.1016/j.jtice.2019.01.016.

[175] M. Sahadat Hossain, S. Ahmed, Crystallographic characterization of naturally occurring aragonite and calcite phase: Rietveld refinement, J. Saudi Chem. Soc. 27 (2023) 101649. https://doi.org/10.1016/j.jscs.2023.101649.

[176] Y. Zhang, S. Cao, Y. Wang, G. Wang, T. Sun, Application of alternating electric field scale inhibition device in heat exchange station, Int. J. Heat Mass Transf. 185 (2022). https://doi.org/10.1016/j.ijheatmasstransfer.2021.122321.

[177] J. Xu, J. Zhao, Y. Jia, Experimental study on the scale inhibition effect of the alternating electromagnetic field on CaCO3 fouling on the heat exchanger surface in different circulating cooling water conditions, Int. J. Therm. Sci. 192 (2023) 108388. https://doi.org/10.1016/j.ijthermalsci.2023.108388.

[178] W. Riedel, Electroless nickel plating, ASM International, 1991.

[179] P. Jokinen, K. Korpiola, A. Mahiout, Duplex coating of electroless nickel and HVOF

(high-velocity oxygen fuel) sprayed WC-Co, J. Therm. Spray Technol. 9 (2000) 241–244. https://doi.org/10.1361%2F105996300770349980.

[180] W.M. Haynes, CRC handbook of chemistry and physics, 95th ed., CRC press, 2014. https://doi.org/10.1201/b17118.

[181] V. Nemane, S. Chatterjee, Scratch and Sliding Wear Testing of Electroless Ni-B-W Coating, J. Tribol. 142 (2020) 1–9. https://doi.org/10.1115/1.4045165.

[182] D. Zhang, Y. Sun, C. Gao, M. Liu, Measurement of fracture toughness of copper via constant-load microscratch with a spherical indenter, Wear. 444–445 (2020) 203158. https://doi.org/10.1016/j.wear.2019.203158.

[183] K.U. Mahto, S. Das, Microscopic techniques to evaluate the biofilm formation ability of a marine bacterium Pseudomonas aeruginosa PFL-P1 on different substrata, Microsc. Res. Tech. 84 (2021) 2451–2461. https://doi.org/10.1002/JEMT.23799.

[184] G. Pedrizzetti, L. Paglia, V. Genova, S. Cinotti, M. Bellacci, F. Marra, G. Pulci, Microstructural, mechanical and corrosion characterization of electroless Ni-P composite coatings modified with ZrO2 reinforcing nanoparticles, Surf. Coatings Technol. 473 (2023). https://doi.org/10.1016/j.surfcoat.2023.129981.

[185] F.H.H. Constable, Spectrophotometric observations on the growth of oxide films on iron, nickel, and copper, Proc. R. Soc. Lond. A Math. Phys. Sci. 117 (1928) 376–387. https://doi.org/10.1098/rspa.1928.0005.

[186] Y.-P. Jia, W.-C. Sun, Y. Xiao, Y.-W. Liu, S.-S. Tian, Effect of rare earth on the corrosion resistance of electroless Ni-mo-P composite coatings, Mater. Res. 25 (2022). https://doi.org/10.1590/1980-5373-mr-2021-0278.

[187] A. Akyol, H. Algul, M. Uysal, H. Akbulut, A. Alp, A novel approach for wear and corrosion resistance in the electroless Ni-P-W alloy with CNFs co-depositions, Appl. Surf. Sci. 453 (2018) 482–492. https://doi.org/10.1016/j.apsusc.2018.05.152.

[188] T.J. Hardwick, THE REDUCTION OF CERIC SULPHATE SOLUTIONS BY IONIZING RADIATION', Can. J. Chem. 30 (1952) 23–38. https://doi.org/10.1139/v52-004.

[189] G. Dai, S. Wu, X. Huang, M. Wang, R. Wu, Research on the coating formation of

Al-induced electroless plating on metallic surfaces, J. Mater. Sci. 58 (2023) 3768–3789. https://doi.org/10.1007/s10853-023-08238-4.

[190] X. Liu, P.C. Okafor, X. Pan, D.I. Njoku, K.J. Uwakwe, Y. Zheng, Corrosion inhibition and adsorption properties of cerium-amino acid complexes on mild steel in acidic media: Experimental and DFT studies, J. Adhes. Sci. Technol. 34 (2020) 2047–2074. https://doi.org/10.1080/01694243.2020.1749474.

[191] X. Li, S. Deng, Ce(SO4)2 as an efficient corrosion inhibitor for cold rolled steel in citric acid solution, J. Taiwan Inst. Chem. Eng. 122 (2021) 273–283. https://doi.org/10.1016/j.jtice.2021.04.057.

[192] F. Cotting, I.V. Aoki, Octylsilanol and Ce(III) ions – alternative corrosion inhibitors for carbon steel in chloride neutral solutions, J. Mater. Res. Technol. 9 (2020) 8723–8734. https://doi.org/10.1016/j.jmrt.2020.06.011.

[193] V. Vitry, A. Sens, A.-F. Kanta, F. Delaunois, Experimental study on the formation and growth of electroless nickel–boron coatings from borohydride-reduced bath on mild steel, Appl. Surf. Sci. 263 (2012) 640–647. https://doi.org/10.1016/j.apsusc.2012.09.126.

[194] S. Bi, H. Zhao, L. Hou, Y. Lu, Enhanced Electromagnetic Interference Shielding Effects of Cobalt-Nickel Polyalloy Coated Fabrics with Assistance of Rare Earth Elements, Fibers Polym. 19 (2018) 1084–1093. https://doi.org/10.1007/s12221-018-1084-6.

[195] D. Gültekin, E. Duru, H. Akbulut, Improved wear behaviors of lead-free electroless Ni-B and Ni-B/CeO2 composite coatings, Surf. Coat. Technol. 422 (n.d.). https://doi.org/10.1016/j.surfcoat.2021.127525.

[196] V. Vitry, A.F. Kanta, F. Delaunois, Initiation and formation of electroless nickel-boron coatings on mild steel: Effect of substrate roughness, Mater. Sci. Eng. B. 175 (2010) 266–273. https://doi.org/10.1016/j.mseb.2010.08.003.

[197] D. Ekmekci, F. Bülbül, Preparation and characterization of electroless Ni–B/nano-SiO2, Al2O3, TiO2 and CuO composite coatings, Bull. Mater. Sci. 38 (2015) 761–768. https://doi.org/10.1007/s12034-015-0912-1.

[198] H. Ashassi-Sorkhabi, M. Moradi-Haghighi, M.G. Hosseini, Effect of rare earth (Ce, La) compounds in the electroless bath on the plating rate, bath stability and

microstructure of the nickel-phosphorus deposits, Surf. Coatings Technol. 202 (2008) 1615–1620. https://doi.org/10.1016/j.surfcoat.2007.07.019.

[199] G. Liu, Z. Huang, L. Wang, W. Sun, S. Wang, X. Deng, Effects of Ce4+ on the structure and corrosion resistance of electroless deposited Ni-Cu-P coating, Surf. Coatings Technol. 222 (2013) 25–30. https://doi.org/10.1016/j.surfcoat.2013.01.053.

[200] J.N. Balaraju, S.M. Jahan, A. Jain, K.S. Rajam, Structure and phase transformation behavior of electroless Ni-P alloys containing tin and tungsten, J. Alloys Compd. 436 (2007) 319–327. https://doi.org/10.1016/j.jallcom.2006.07.045.

[201] E. Valova, S. Armyanov, A. Franquet, K. Petrov, D. Kovacheva, J. Dille, J.-L. Delplancke, A. Hubin, O. Steenhaut, J. Vereecken, Comparison of the structure and chemical composition of crystalline and amorphous electroless Ni-W-P coatings, J. Electrochem. Soc. 151 (2004) C385. https://doi.org/10.1149/1.1705661.

[202] J.N. Balaraju, Kalavati, K.S. Rajam, Surface morphology and structure of electroless ternary NiWP deposits with various W and P contents, J. Alloys Compd. 486 (2009) 468–473. https://doi.org/10.1016/j.jallcom.2009.06.173.

[203] J.N. Balaraju, K.S. Rajam, Electroless deposition of Ni–Cu–P, Ni–W–P and Ni–W–Cu–P alloys, Surf. Coat. Technol. 195 (2005) 154–161. https://doi.org/10.1016/j.surfcoat.2004.07.068.

[204] L. Che, M. Xiao, H. Xu, B. Wang, Y. Jin, Enhanced corrosion resistance and micro-hardness of titanium with electroless deposition Ni-W-Cr-P coating, Mater. Manuf. Process. (2013) 130709115809008. https://doi.org/10.1080/10426914.2013.792412.

[205] L. Wang, Z. Li, Y. Zhang, T. Zhang, G. Xie, Hydrogen generation from alkaline NaBH4solution using electroless-deposited Co–Ni–W–P/γ-Al2O3as catalysts, J. Alloys Compd. 702 (2017) 649–658. https://doi.org/10.1016/j.jallcom.2017.01.295.

[206] J. Zhong, S. Zhang, Y. He, Z. Zhang, H. Li, R. Song, Preparation, corrosion resistance and mechanical properties of electroless Ni-W-P-eGO composite coatings, Colloids Surfaces A Physicochem. Eng. Asp. 651 (2022). https://doi.org/10.1016/j.colsurfa.2022.129704.

[207] H. Liu, H.L. Yao, Y. Liu, G.E. Thompson, Z. Liu, Crystallisation and performance characteristics of high-temperature annealed electroless Ni-W-P coatings, Cryst.

Res. Technol. 49 (2014) 178–189. https://doi.org/10.1002/crat.201300375.

[208] R. Wang, Z. Li, Z. Li, M. Wen, G. Wang, G. Xie, X. Liu, L. Jiang, Electroless deposition synthesis of composite catalysts Ni-Fe-P-WO3/NF with superior oxygen evolution performance, Int. J. Hydrogen Energy. 47 (2022) 29305–29314. https://doi.org/10.1016/j.ijhydene.2022.06.266.

[209] P. Van Der Heide, X-Ray Photoelectron Spectroscopy; An Introduction to Principles and Practices, John Wiley & Sons, 2011. https://doi.org/10.1002/9781118162897.

[210] Y. Hou, Z. Yuan, X. Yu, B. Ma, L. Zhao, D. Kong, Directly preparing well-dispersed ultra-hydrophilic NiFeP nanoparticle/Mxene complexes from spent electroless Ni plating solution as efficient hydrogen evolution catalysts, J. Environ. Chem. Eng. 11 (2023) 109738. https://doi.org/10.1016/j.jece.2023.109738.

[211] A. Shaikh, B.K. Singh, K. Purnendu, P. Kumari, P.R. Sankar, G. Mundra, S. Bohm, Utilization of the nickel hydroxide derived from a spent electroless nickel plating bath for energy storage applications, RSC Sustain. (2023). https://doi.org/10.1039/d2su00036a.

[212] J.-Z. Hao, J.-J. Xu, H.-L. Cao, H. Miao, S.-A. Xu, The effects of P and metal elements in electroless nickel-based alloys on the formation of Ti/Zr conversion coating, J. Alloy. Compd. 982 (2024) 173761. https://doi.org/10.1016/j.jallcom.2024.173761.

[213] R.L. Zeller lll, L. Salvati Jr, Effects of Phosphorus on Corrosion Resistance of Electroless Nickel in 50% Sodium Hydroxide, Corrosion. 50 (1994) 457–467. https://doi.org/10.5006/1.3293524.

[214] M.A. Kamde, Y. Mahton, J. Ohodnicki, M. Roy, P. Saha, Effect of cerium-based conversion coating on corrosion behavior of squeeze cast Mg-4 wt% Y alloy in 0.1 M NaCl solution, Surf. Coatings Technol. 421 (2021) 127451. https://doi.org/10.1016/j.surfcoat.2021.127451.

[215] S.M.A. Shibli, M. Ameen Sha, Development and characterization of electro active CeO2–RuO2 mixed oxide and its role in alkaline hydrogen evolution reaction, J. Alloys Compd. 749 (2018) 250–261. https://doi.org/10.1016/j.jallcom.2018.03.274.

[216] T.V.H. Luu, M.D. Luu, N.N. Dao, V.T. Le, H.T. Nguyen, V.D. Doan, Immobilization of C/Ce-codoped ZnO nanoparticles on multi-walled carbon nanotubes for

enhancing their photocatalytic activity, J. Dispers. Sci. Technol. 42 (2021) 1311–1322. https://doi.org/10.1080/01932691.2020.1740728.

[217] M. Dumpalapally, S. Boggala, R.C. Nappuni, S. Varimalla, V. Akula, Cerium sulfate doped ZrO2 as a solid acid catalyst for the synthesis of polyoxymethylene dimethyl ethers: Influence of Brønsted acidity on the catalytic activity and product selectivity, Chem. Eng. Sci. 278 (2023) 118922. https://doi.org/10.1016/j.ces.2023.118922.

[218] M. Eslami, M. Fedel, G. Speranza, F. Deflorian, N.E. Andersson, C. Zanella, Study of selective deposition mechanism of cerium-based conversion coating on Rheo-HPDC aluminium-silicon alloys, Electrochim. Acta. 255 (2017) 449–462. https://doi.org/10.1016/j.electacta.2017.09.182.

[219] E. Saei, B. Ramezanzadeh, R. Amini, M.S. Kalajahi, Effects of combined organic and inorganic corrosion inhibitors on the nanostructure cerium based conversion coating performance on AZ31 magnesium alloy: Morphological and corrosion studies, Corros. Sci. 127 (2017) 186–200. https://doi.org/10.1016/j.corsci.2017.08.017.

[220] G.-S. Song, S. Sun, Z.-C. Wang, C.-Z. Luo, C.-X. Pan, Synthesis and Characterization of Electroless Ni–P/Ni–Mo–P Duplex Coating with Different Thickness Combinations, Acta Metall. Sin. (English Lett. 30 (2017) 1008–1016. https://doi.org/10.1007/s40195-017-0603-6.

[221] A. Shaikh, B.K. Singh, K. Purnendu, P. Kumari, P.R. Sankar, G. Mundra, S. Bohm, Utilization of the nickel hydroxide derived from a spent electroless nickel plating bath for energy storage applications, RSC Sustain. 1 (2023) 294–302. https://doi.org/10.1039/d2su00036a.

[222] A.F. Kanta, V. Vitry, F. Delaunois, Wear and corrosion resistance behaviours of autocatalytic electroless plating, J. Alloys Compd. 486 (2009). https://doi.org/10.1016/j.jallcom.2009.07.038.

[223] H.D. Johansen, C.M.A. Brett, A.J. Motheo, Corrosion protection of aluminium alloy by cerium conversion and conducting polymer duplex coatings, Corros. Sci. 63 (2012) 342–350. https://doi.org/10.1016/j.corsci.2012.06.020.

[224] E.A. Clark, R. Yeske, H.K. Birnbaum, The effect of hydrogen on the surface energy of nickel, Metall. Trans. A. 11 (1980) 1903–1908.

https://doi.org/10.1007/BF02655107.

[225] A. Harvey, X. He, I.J. Godwin, C. Backes, D. McAteer, N.C. Berner, N. McEvoy, A. Ferguson, A. Shmeliov, M.E.G. Lyons, V. Nicolosi, G.S. Duesberg, J.F. Donegan, J.N. Coleman, Production of Ni(OH)2 nanosheets by liquid phase exfoliation: from optical properties to electrochemical applications, J. Mater. Chem. A. 4 (2016) 11046–11059. https://doi.org/10.1039/C6TA02811J.

[226] J. Tam, B. Feng, Y. Ikuhara, H. Ohta, U. Erb, Crystallographic orientation–surface energy–wetting property relationships of rare earth oxides, J. Mater. Chem. A. 6 (2018) 18384–18388. https://doi.org/10.1039/C8TA04938F.

[227] S. Hayun, S. V Ushakov, A. Navrotsky, Direct measurement of surface energy of CeO2 by differential scanning calorimetry, J. Am. Ceram. Soc. 94 (2011) 3679–3682. https://doi.org/10.1111/j.1551-2916.2011.04843.x.

[228] O. Matz, M. Calatayud, H2 Dissociation and Oxygen Vacancy Formation on Ce2O3 Surfaces, Top. Catal. 62 (2019) 956–967. https://doi.org/10.1007/s11244-019-01183-0.

[229] A. Biswas, S.K. Das, P. Sahoo, Investigation of the tribological behavior of electroless Ni-W-P coating pre and post phase transformation regime, Mater. Res. Express. 6 (2019). https://doi.org/10.1088/2053-1591/ab33bd.

[230] A. AlZahrani, Y. Alhamed, L. Petrov, S. Armyanov, E. Valova, J. Georgieva, J. Dille, Mechanical and corrosion behavior of amorphous and crystalline electroless Ni–W–P coatings, J. Solid State Electrochem. 18 (2014) 1951–1961. https://doi.org/10.1007/s10008-014-2437-8.

[231] S. Chen, T. Liang, N. Wen, F.-H. Liu, C.-C. Tsao, C.-Y. Hsu, Electro-less plating nickel-phosphorus of low carbon steel using various pretreatments and an external magnetic field, J. Saudi Chem. Soc. 24 (2020) 704–714. https://doi.org/https://doi.org/10.1016/j.jscs.2020.07.008.

[232] M. Buchtík, L. Doskočil, R. Brescher, P. Doležal, J. Másilko, J. Wasserbauer, The effect of crystallization and phase transformation on the mechanical and electrochemical corrosion properties of Ni-P coatings, Coatings. 11 (2021) 447. https://doi.org/10.3390/coatings11040447.

[233] V. Nemane, S. Chatterjee, Evaluation of microstructural, mechanical, and

tribological characteristics of Ni-B-W-SiC electroless composite coatings involving multi-pass scratch test, Mater. Charact. 180 (2021) 111414. https://doi.org/10.1016/j.matchar.2021.111414.

[234] D. Ahmadkhaniha, F. Eriksson, C. Zanella, Optimizing heat treatment for electroplated nip and NiP/SiC coatings, Coatings. 10 (2020) 1–19. https://doi.org/10.3390/coatings10121179.

[235] Z. Zhang, C. Ma, Q. Dai, W. Huang, X. Wang, A two-stage approach to Ni-P-SiC coatings and their friction against SiC in water, Surf. Coatings Technol. 457 (2023). https://doi.org/10.1016/j.surfcoat.2023.129268.

[236] L. Liu, J. Peng, X. Du, H. Zheng, Z. Chen, P. Gong, Y. Xiao, X. Cao, Synthesis, composition, morphology, and wettability of electroless Ni-Fe-P coatings with varying microstructures, Thin Solid Films. 706 (2020) 138080. https://doi.org/10.1016/j.tsf.2020.138080.

[237] N.A. Bin Masripan, Y. Miyahira, H. Nishimura, T. Tokoroyama, N. Umehara, Y. Fuwa, Effect of Transfer Layer on Ultra Low Friction of CN<I>$_x$</I> Coating under Blowing Dry Ar, Tribol. Online. 8 (2013) 219–226. https://doi.org/10.2474/trol.8.219.

[238] V. Vitry, M. Yunacti, A. Megret, H.A. Khalid, M.H. Staia, A. Montagne, Selection of New Heat Treatment Conditions for Novel Electroless Nickel-Boron Deposits and Characterization of Heat-Treated Coatings, Coatings. 13 (2023). https://doi.org/10.3390/coatings13010001.

[239] M.S. Jagatheeshwaran, A. Elayaperumal, S. Arulvel, Impact of nano zinc oxide on the friction – Wear property of electroless nickel-phosphorus sea shell composite coatings, Mater. Sci. Eng. B Solid-State Mater. Adv. Technol. 225 (2017) 160–172. https://doi.org/10.1016/j.mseb.2017.08.026.

[240] S. Kundu, S.K. Das, P. Sahoo, Friction and wear characteristics of heat treated electroless Ni–P–W coatings under elevated temperature, in: Lect. Notes Multidiscip. Ind. Eng., Springer International Publishing, Cham, 2019: pp. 59–82. https://doi.org/10.1007/978-3-319-96968-8_4.

[241] S. Roy, P. Sahoo, Optimization of electroless Ni-P-W coatings for minimum friction and wear using grey-Taguchi method, J. Coat. 2013 (2013) 1–13.

https://doi.org/10.1155/2013/608140.

[242] G. Chen, J. Wang, L. Xue, Z. Huang, Enhancement of wear and corrosion resistance of M2052 damping alloys by electroless plating Ni–P coating, ISIJ Int. 60 (2020) 2276–2284. https://doi.org/10.2355/isijinternational.isijint-2019-797.

[243] R. Agrawal, A. Mukhopadhyay, Inclusion of W in electroless Ni–B coating developed from a stabilizer free bath and investigation of its tribological behaviour, J. Indian Chem. Soc. 100 (2023). https://doi.org/10.1016/j.jics.2023.100966.

[244] A. Biswas, S.K. Das, P. Sahoo, Hardness, friction and wear trends of electroless Ni-W-P coating heat-treated at different temperatures, in: Lect. Notes Multidiscip. Ind. Eng., Springer International Publishing, Cham, 2019: pp. 83–105. https://doi.org/10.1007/978-3-319-96968-8_5.

[245] X. Zheng, Y. Huang, C. Cai, H. Huang, F. Yang, High temperature tribological behavior of electroless plating Ni-P-Si3N4-WS2 composite coatings, Coatings. 13 (2023) 723. https://doi.org/10.3390/coatings13040723.

[246] S. Mukherjee, S. Dhara, P. Saha, Enhanced corrosion, tribocorrosion resistance and controllable osteogenic potential of stem cells on micro-rippled Ti6Al4V surfaces produced by pulsed laser remelting, J. Manuf. Process. 65 (2021) 119–133. https://doi.org/10.1016/J.JMAPRO.2021.03.023.

[247] A. Królikowski, B. Karbownicka, O. Jaklewicz, Anodic dissolution of amorphous Ni–P alloys, Electrochim. Acta. 51 (2006) 6120–6127. https://doi.org/10.1016/j.electacta.2006.01.070.

[248] H. Luo, X. Wang, S. Gao, C. Dong, X. Li, Synthesis of a duplex Ni-P-YSZ/Ni-P nanocomposite coating and investigation of its performance, Surf. Coat. Technol. 311 (2017) 70–79. https://doi.org/10.1016/j.surfcoat.2016.12.075.

[249] O. Kohmoto, H. Nakagawa, Y. Isagawa, A. Chayahara, Effect of heat treatment on the oxygen content and resistivity in sputtered NiO films, J. Magn. Magn. Mater. 226–230 (2001) 1629–1630. https://doi.org/10.1016/s0304-8853(00)01043-x.

[250] M.A.A.M. van Wijck, M.A.J. Verhoeven, E.M.C.M. Reuvekamp, G.J. Gerritsma, D.H.A. Blank, H. Rogalla, CeO2 as insulation layer in high T c superconducting multilayer and crossover structures, Appl. Phys. Lett. 68 (1996) 553–555. https://doi.org/10.1063/1.116397.

[251] X. Zhou, Y. Shen, Beneficial effects of CeO2 addition on microstructure and corrosion behavior of electrodeposited Ni nanocrystalline coatings, Surf. Coat. Technol. 235 (2013) 433–446. https://doi.org/10.1016/j.surfcoat.2013.07.070.

[252] D. Li, X. Cui, X. Wen, L. Feng, Y. Hu, G. Jin, E. Liu, W. Zheng, Effect of CeO2 nanoparticles modified graphene oxide on electroless Ni-P coating for Mg-Li alloys, Appl. Surf. Sci. 593 (n.d.). https://doi.org/10.1016/j.apsusc.2022.153381.

[253] I.A. Shozib, A. Ahmad, A.M. Abdul-Rani, M. Beheshti, A.A. Aliyu, A review on the corrosion resistance of electroless Ni-P based composite coatings and electrochemical corrosion testing methods, Corros. Rev. 40 (2022) 1–37. https://doi.org/10.1515/corrrev-2020-0091.

[254] A.C. Lazanas, M.I. Prodromidis, Electrochemical Impedance Spectroscopy-A tutorial, ACS Meas. Sci. Au. 3 (2023) 162–193. https://doi.org/10.1021/acsmeasuresciau.2c00070.

[255] Y.-P. Zhao, G.-C. Wang, T.-M. Lu, G. Palasantzas, J.T.M. De Hosson, Surface-roughness effect on capacitance and leakage current of an insulating film, Phys. Rev. B Condens. Matter. 60 (1999) 9157–9164. https://doi.org/10.1103/physrevb.60.9157.

[256] E. Pütz, A. Gazanis, N.G. Keltsch, O. Jegel, F. Pfitzner, R. Heermann, T.A. Ternes, W. Tremel, Communication Breakdown: Into the Molecular Mechanism of Biofilm Inhibition by CeO2 Nanocrystal Enzyme Mimics and How It Can Be Exploited, ACS Nano. 16 (2022) 16091–16108. https://doi.org/10.1021/acsnano.2c04377.

[257] S. Zheng, M. Bawazir, A. Dhall, H.-E. Kim, L. He, J. Heo, G. Hwang, Implication of surface properties, bacterial motility, and hydrodynamic conditions on bacterial surface sensing and their initial adhesion, Front. Bioeng. Biotechnol. 9 (2021) 643722. https://doi.org/10.3389/fbioe.2021.643722.

[258] M.C.L. De Oliveira, O.V. Correa, B. Ett, I.J. Sayeg, N.B. de Lima, R.A. Antunes, Influence of the tungsten content on surface properties of electroless Ni-W-P coatings, Mater. Res. 21 (2018). https://doi.org/10.1590/1980-5373-mr-2017-0567.

[259] P. Verdi, S.M. Monirvaghefi, Electroless Ni-P Plating of Carbon Steel via Hot Substrate Method and Comparison of Coating Properties with those for Conventional Method, J. Mater. Eng. Perform. 29 (2020) 7915–7928.

https://doi.org/10.1007/s11665-020-05286-8.

[260] M. Novák, D. Vojtěch, T. Vítů, Influence of heat treatment on microstructure and adhesion of Al 2O3 fiber-reinforced electroless Ni-P coating on Al-Si casting alloy, Mater. Charact. 61 (2010) 668–673. https://doi.org/10.1016/j.matchar.2010.03.014.

[261] B. Oraon, Some studies on the parametric optimization of electroless nickel composite coating and its impact on mechanical properties, Jadavpur University, 2005. http://hdl.handle.net/10603/184888 (accessed September 24, 2023).

[262] R.-D. Sun, D.A. Tryk, K. Hashimoto, A. Fujishima, Adhesion of Electroless Deposited Cu on ZnO-Coated Glass Substrates: The Effect of the ZnO Surface Morphology, J. Electrochem. Soc. 146 (1999) 2117–2122. https://doi.org/10.1149/1.1391901.

[263] N. Latha, V. Raj, M. Selvam, Effect of plating time on growth of nanocrystalline Ni-P from sulphate/glycine bath by electroless deposition method, Bull. Mater. Sci. 36 (2013) 719–727. https://doi.org/10.1007/s12034-013-0501-0.

[264] H. Ashassi-Sorkhabi, S.H. Rafizadeh, Effect of coating time and heat treatment on structures and corrosion characteristics of electroless Ni-P alloy deposits, Surf. Coatings Technol. 176 (2004) 318–326. https://doi.org/10.1016/S0257-8972Ž03.00746-1.

[265] V.K. Bulasara, H. Thakuria, R. Uppaluri, M.K. Purkait, Effect of process parameters on electroless plating and nickel-ceramic composite membrane characteristics, Desalination. 268 (2011) 195–203. https://doi.org/10.1016/j.desal.2010.10.025.

[266] M.R. Kalantary, K.A. Holbrook, P.B. Wells, Optimisation of a bath for electroless plating and its use for the production of nickel-phosphorus-silicon carbide coatings, Trans. Inst. Met. Finish. 71 (1993) 55–61. https://doi.org/10.1080/00202967.1993.11870987.

[267] T.H. Oh, S. Kwon, Effect of bath composition on properties of electroless deposited Co-P/Ni foam catalyst for hydrolysis of sodium borohydride solution, Int. J. Hydrogen Energy. 37 (2012) 17027–17039. https://doi.org/10.1016/j.ijhydene.2012.08.083.

[268] M.W. Jung, S.K. Kang, J.H. Lee, Effects of sodium citrate concentration on electroless Ni-Fe bath stability and deposition, J. Electron. Mater. 43 (2014) 290–

298. https://doi.org/10.1007/s11664-013-2838-y.

[269] M.F. González, N. Saadatkhah, G.S. Patience, Experimental methods in chemical engineering: X-ray fluorescence—XRF, Can. J. Chem. Eng. 102 (2024) 2004–2018. https://doi.org/10.1002/cjce.25218.

[270] Y. Jiao, Y. Zhu, Z. Wang, X. Hu, Y. Guo, J. Ji, K. Liu, Effect of the surface peak-valley features on droplet splash dynamics, Phys. Fluids. 35 (2023). https://doi.org/10.1063/5.0165689.

[271] W. Liao, X. Liu, G. Li, T. Chen, Evaluation of thermal-hydraulic performance of dimpled tube from the perspective of skewness and kurtosis, Int. J. Therm. Sci. 156 (2020) 106469. https://doi.org/10.1016/j.ijthermalsci.2020.106469.

[272] B. Liu, X. Yu, X. Jiang, Y. Qiao, L. You, Y. Wang, F. Ye, Effect of deposition substrates on surface topography, interface roughness and phase transformation of the Al/Ni multilayers, Appl. Surf. Sci. 546 (2021) 149098. https://doi.org/10.1016/j.apsusc.2021.149098.

[273] A. Kumar, S.K. Nayak, A. Pathak, A. Banerjee, T. Laha, Investigation of nanomechanical deformation behavior in plasma sprayed Fe-based amorphous/ nanocrystalline composite coating via multi-scale indentation and nanotribology, J. Non. Cryst. Solids. 545 (2020) 120244. https://doi.org/10.1016/j.jnoncrysol.2020.120244.

[274] P. Terek, L. Kovačević, V. Terek, Z. Bobić, A. Miletić, B. Škorić, M. Čekada, A. Drnovšek, Surface Roughness and Its Effect on Adhesion and Tribological Performance of Magnetron Sputtered Nitride Coatings, Coatings. 14 (2024). https://doi.org/10.3390/coatings14081010.

[275] A. Kumar, S.K. Nayak, T. Laha, Deformation behavior of plasma sprayed Fe-based amorphous/ nanocrystalline coating under multi-scale tribological contact, J. Non. Cryst. Solids. 609 (2023). https://doi.org/10.1016/j.jnoncrysol.2023.122281.

[276] A.K. Karn, R. Agrawal, A. Kumar, A. Mukhopadhyay, Deposition and process parameter optimization of electroless Ni-B coating from a stabilizer free bath to achieve enhanced microhardness, scratch-hardness and adhesion using taguchi's methodology, Eng. Res. Express. 5 (2023). https://doi.org/10.1088/2631-8695/acecdf.

[277] Z. Wang, S. Zhou, G. Ma, Y. Dong, X. Zhang, Y. Liu, Z. Wang, A. Wang, Achieving ultrastrong-tough CrAlN coatings with low friction coefficient by Y incorporating, Ceram. Int. 50 (2024) 23621–23633. https://doi.org/10.1016/j.ceramint.2024.04.086.

[278] M. Xiao, S. Huang, H. Wu, K. Chen, D. Wu, H. Yang, Effect of matrix roughness on microstructure and properties of electroless Ni-P plating, Dig. J. Nanomater. Biostructures. 13 (2018) 1019–1029.

[279] S. Arulvel, D. Dsilva Winfred Rufuss, J. Kandasamy, P. Kumaravelu, R. Raychoudhury, S. Raghul, Hydrophobic electroless nickel phosphorus-graphene carbon nitride coating on AISI 4140 steel with enhanced hardness and scratch resistance, Surf. Coatings Technol. 473 (2023). https://doi.org/10.1016/j.surfcoat.2023.130023.

[280] S. Yazdani, V. Vitry, RSM models approach for optimization of the mechanical properties of electroless Ni-B-nanodiamond coating: An experimental and molecular dynamic simulation study, Surf. Coatings Technol. 452 (2023). https://doi.org/10.1016/j.surfcoat.2022.129133.

[281] S. Sneddon, Y. Xu, M. Dixon, D. Rugg, P. Li, D.M. Mulvihill, Sensitivity of material failure to surface roughness: A study on titanium alloys Ti64 and Ti407, Mater. Des. 200 (2021) 109438. https://doi.org/10.1016/j.matdes.2020.109438.

[282] M. Asgari, B. Abedi, A. Ashrafi, G. Barati Darband, M. Monirvaghefi, Electroless deposition of Ni-W-P films as binder-free, efficient and durable electrode for electrochemical hydrogen evolution, Mater. Res. Bull. 166 (2023) 112318. https://doi.org/10.1016/j.materresbull.2023.112318.

[283] A. Salicio-Paz, I. Ugarte, J. Sort, E. Pellicer, E. García-Lecina, Full optimization of an electroless nickel solution: Boosting the performance of low-phosphorous coatings, Materials (Basel). 14 (2021). https://doi.org/10.3390/ma14061501.

[284] A. Mabrouk, Z. Farhat, Novel Ni-P-Tribaloy Composite Protective Coating, Materials (Basel). 16 (2023). https://doi.org/10.3390/ma16113949.

[285] E. Kızılkonca, F.B. Erim, Development of Anti-Aging and Anticorrosive Nanoceria Dispersed Alkyd Coating for Decorative and Industrial Purposes, Coatings. 9 (2019). https://doi.org/10.3390/coatings9100610.

[286] S.M.A. Shibli, L. Thushara, S.R. Archana, Development of nano CeO2–Fe2O3 mixed oxide based electro catalytic electrodes for hydrogen evolution reaction, Int. J. Hydrogen Energy. 42 (2017) 1919–1931. https://doi.org/10.1016/j.ijhydene.2016.11.092.

[287] M.A. Kamde, Y. Mahton, J. Ohodnicki, M. Roy, P. Saha, P.N. Kumta, Effect of cerium-based conversion coating on corrosion behavior of squeeze cast Mg-4 wt% Y alloy in 0.1 M NaCl solution, Surf. Coatings Technol. 424 (2021). https://doi.org/10.1016/j.surfcoat.2021.127683.

[288] S. Oh, D. Kim, K.C. Kim, D.I. Kim, W. Chung, B.H. Shin, Electrochemical properties of electroless Ni plated super duplex stainless in 3.5% NaCl solution, Int. J. Electrochem. Sci. 18 (2023). https://doi.org/10.1016/j.ijoes.2023.100287.

[289] S. Samanta, K. Mondal, M. Dutta, S.B. Singh, Electroless NiP coatings over API X70 steel: Effect of composition on the H-permeation and corrosion resistance, Surf. Coatings Technol. 409 (2021) 126928. https://doi.org/10.1016/j.surfcoat.2021.126928.

APPENDIX

The MATLAB codes used for the multi-objective optimization work presented in Chapter 4 are available at the following Google Drive link:

https://drive.google.com/drive/folders/170xRFoW8Kcro3H_R8AZt1pS4VbBSoq2y?usp=drive_link

All relevant files should be opened in the editor window. Before running the **main.m** file, the input and target datasets must be loaded into the MATLAB workspace and saved as variables named **inputData** and **targetData**, respectively.

The functionality of each code file is outlined below:

trainANN.m: Contains the code for training the ANN, as described in Section 4.4.

sTLBO.m, **WOA.m**, **RFO.m**: Implement the metaheuristic algorithms TLBO, WOA, and RFO, corresponding to Sections 4.4.1, 4.4.2, and 4.4.3, respectively.

objectiveFunction.m: Defines the objective function, as utilized in the optimization process described in Section 4.4.

findNonDominated.m: Identifies non-dominated solutions, as explained in Section 4.4.

performSensitivityAnalysis.m: Executes sensitivity analysis, as described in Section 4.4.

visualizeSensitivity.m: Visualizes sensitivity results, corresponding to Subsections 4.5.3.3 and 4.5.3.4.

plot3DRadVisEnhanced.m: Generates plots for Pareto front and trade-off visualizations, as shown in Subsection 4.5.3.2.

CURRICULUM VITAE

Name VIKASH KUMAR

Contact Address
Ph.D. Scholar
Surface Engineering Laboratory
Department of Mechanical Engineering
Jadavpur University, Kolkata-700032, India
Phone: +918544119573
Email: vkkr58@gmail.com / vikashk.mech.rs@jadavpuruniversity.in
https://www.linkedin.com/in/talk2vikash/ https://x.com/vikashPhD

SUMMARY OF QUALIFICATIONS, SKILLS, AND EXPERIENCES

- Successfully completed Ph.D. pre-submission on March 25, 2025 in the Department of Mechanical Engineering, Jadavpur University, Kolkata on the topic: "Development, characterization and optimization of electroless Ni-W-P-Ce coatings for multifunctional applications."
- Verified Peer Reviewer of Tribology - Materials, Surfaces & Interfaces (Taylor & Francis), Web of Science Researcher ID: AAM-9988-2021
- Completed M.Tech project at CSIR-Central Mechanical Engineering Research Institute, Durgapur from 28.09.2018 to 31.07.2019 in the area of Laser Cladding.
- Proficient in conducting comprehensive materials analysis through techniques such as SEM, EDX, XRD, XPS, FTIR, Corrosion (OCP, LP, EIS), Wettability, Microhardness, Roughness, Wear, Scratch, Annealing, with advanced skills in data interpretation and result analysis utilizing Taguchi, RSM, ANN, and other metaheuristic optimization techniques.

EDUCATIONAL QUALIFICATIONS

Degree	Year of passing	Specialization	Percentage	University/Institute/Board
Ph.D.	2025	Mechanical Engineering	83.50	Jadavpur University, Kolkata
M.Tech	2019	Mechanical Engineering (Production Technology)	89.70	Birsa Institute of Technology, Sindri, Dhanbad
B.Tech	2017	Mechanical Engineering	80.79	Motihari College of Engineering, Motihari
12^{th}	2013	Science	67	Bihar School Examination Board, Patna
10^{th}	2011		76	Bihar School Examination Board, Patna

THESIS/PROJECT TITLE

Ph.D.: Development, characterization and optimization of electroless Ni-W-P-Ce coatings for multifunctional applications

M.Tech: Microstructural and mechanical analysis of multi-layer deposited Ni-5Mo-5Al by laser cladding

PUBLICATIONS

Papers published in journals

1. **V. Kumar**, B.B. Mandal, S. Das, B. Oraon, S. Mukherjee, Tailoring electroless Ni-W-P polyalloy coatings: Unveiling the synergistic impact of cerium addition and annealing on surface functional properties, Surf. Coatings Technol. 485 (2024) 130874. https://doi.org/10.1016/j.surfcoat.2024.130874.

2. B.B. Mandal, **V. Kumar**, B. Oraon, Optimization, Prediction, and Characterization of Electroless Ni-W-P-nanoTiO2 Composite Coatings on Pipeline Steel, Arab. J. Sci. Eng. (2023). https://doi.org/10.1007/s13369-023-07928-0.
3. **V. Kumar**, B.B. Mandal, B. Oraon, Statistical analysis of activator and poly-alloy electroless coating on plain carbon steel by Full Factorial Design, NeuroQuantology 20 (2022) 9396–9405. https://doi.org/10.14704/nq.2022.20.10.NQ55917.
4. **V. Kumar**, B. Baran Mandal, B. Oraon, Synthesis and characterization of electroless Ni-W-Ce-P coating on AISI 1010 substrate, in: Mater. Today Proc., Elsevier Ltd, 2022: pp. 1183–1188. https://doi.org/10.1016/j.matpr.2022.03.267.

Papers published in conference proceedings

1. **V. Kumar**, A. Shrivastava, D. Patra Karmakar, S. Shekhar Chakraborty, H. Roy, M. Gopinath, P. Kumar, S. Mukherjee, Effect of process parameters on geometrical aspects in direct metal laser deposition of Ni5Mo5Al hardface coating, in: IOP Conf. Ser. Mater. Sci. Eng., Institute of Physics Publishing, 2019: p. 012063. https://doi.org/10.1088/1757-899X/561/1/012063.
2. A. Shrivastava, **V. Kumar**, V. Singh, S. Mukherjee, P. Kumar, S.S. Chakraborty, Estimation of residual stress and deformation of laser deposited tracks of Ni-5Mo-5Al powder using thermo-mechanical finite element simulation, in: IOP Conf. Ser. Mater. Sci. Eng., Institute of Physics Publishing, 2019. https://doi.org/10.1088/1757-899X/561/1/012059.

Book chapter

1. **V. Kumar**, A. Shrivastava, S.S. Chakraborty, S. Mukherjee, Directed Energy Deposition of Ni-Based Hard-Facing Alloy, in: Laser Appl. Manuf., CRC press, 2023: pp. 81–98. https://doi.org/10.1201/9781003279501-5.

MEMBERSHIPS

- AMPP: Association for Materials Protection and Performance (Credential ID: 113904051)
- Royal Society of Chemistry (Affiliate Member, Credential ID: 770483)

SOFTWARE SKILL

Conversant with software like Siemens NX, MATLAB, AutoCAD, Minitab, Origin, ImageJ, Microsoft Office, etc.

SCHOLARSHIPS RECEIVED

- Received AICTE **Doctoral Fellowship** (ADF) (provided by All India Council for Technical Education (AICTE), Department of Higher Education) at Jadavpur University, Kolkata during my Ph.D. course as a Research Scholar from August 2019 to July 2023.
- AICTE **PG scholarship** (provided by All India Council for Technical Education (AICTE), Department of Higher Education) at BIT, Sindri during the M.Tech course from July 2017 to July 2019.

NOTABLE PERFORMANCE IN COMPETITIVE EXAMINATION

Cleared the Graduate Aptitude Test in Engineering (GATE) examination with a score of 500 in the Mechanical Engineering paper in 2017 and with a score of 467 in the same paper in 2018.

WORKSHOPS/CONFERENCES

- Attended the DST-SERB sponsored workshop "Microstructural Characterization: A Hands-On Workshop on SEM, EDS, and EBSD (MCWS-2024)" organized by the Department of Metallurgical and Materials Engineering at Visvesvaraya National Institute of Technology (VNIT), Nagpur, Maharashtra, India, from March 12th to 21st, 2024.
- Participated in the Young Scientist Conference of 9th India International Science Festival (IISF) 2023 held at DBT THSTI-RCB Campus, NCR Biotech Science Cluster, Faridabad, Haryana from January 17-20, 2024, and presented my research work through a poster presentation.
- Delivered an oral presentation at the 5th International Conference on Processing and Characterization of Materials (ICPCM 2023), held by the Department of Metallurgical and Materials Engineering at the National Institute of Technology, Rourkela, from December 8th to 10th 2023.
- Showcased my research findings at the Young Scientists Colloquium 2023 through a poster presentation, an event organized by the Materials Research Society of India (MRSI), Kolkata chapter, hosted at Jadavpur University in Kolkata on December 1, 2023.
- Successfully participated in the online Computational Materials Science Summer School (CMS^3) hosted by the Department of Materials Science & Engineering at Texas A&M University from July 23 to August 4, 2023.
- Attended DST-SERB sponsored High-End Workshop (Karyashala) on “Industrial Tribology: Towards Sustainable Approaches” from 15-22 May 2023 at SRM Institute of Science & Technology, Kattankulathur, Chennai.
- Attended ACS ON CAMPUS seminar at IISER, Kolkata on April 11, 2023.
- Participated in the Young Scientist Conference of IISF 2022 held at MANIT, Bhopal from January 22-24, 2023, and presented my research work through poster presentation.
- Attended DST-STUTI one week Hands-on Training Workshop on “Uses of Sophisticated Mechanical Characterization Instruments” from 4th - 10th July 2022 at IIT (ISM), Dhanbad.
- Skill Initiative Program on “Characterization and Non-Destructive Evaluation of Materials” (Organized by Industrial Services and Research Group & Materials Processing and Microsystems Laboratory) from 09.12.2019 to 13.12.2019 at CSIR-CMERI, Durgapur.
- Completed the “Essentials for NX Designers” course from 19.03.2018 to 12.04.2018 at Birsa Institute of Technology Sindri, Dhanbad.

NAMES AND CONTACT DETAILS OF SUPERVISORS

Dr. Buddhadeb Oraon (Professor)
Department of Mechanical Engineering
Jadavpur University
Kolkata - 700032, India
Mobile number: +918017803005
E-mail: buddhadeb.oraon@jadavpuruniversity.in

Dr. Sumanta Mukherjee (Assistant Professor)
Department of Production & Industrial Engg
BIT Sindri
Dhanbad- 828123, India
Mobile number: +918637396668
E-mail: sumanta.prod@bitsindri.ac.in

PERSONAL PROFILE:
Date of Birth: 05th August, 1995
Gender: Male
Nationality: Indian
Marital Status: Single
Languages Known: English, Hindi

PERMANENT ADDRESS:
Vill-Shankarpur, P.O+P.S-Indrapuri
Dist-Rohtas, State-Bihar,
PIN- 821308

I certify that the information given above is true to the best of my knowledge.

Date: June 13, 2025
Place: Kolkata

Vikash Kumar

Signature of the Candidate: Vikash Kumar

(VIKASH KUMAR)

Date: 16-06-2025

1. 17/6/25

(Dr. Buddhadeb Oraon)

Signature of the Supervisor
and date with Office Seal

Professor
Dept. of Mechanical Engineering
Jadavpur University, Kolkata-32

2. Sumanta Mukherjee 16.06.25

(Dr. Sumanta Mukherjee)

Signature of the Supervisor
and date with Office Seal

Assistant Professor
Production & Industrial Engg. Dept.
BIT Sindri, Dhanbad